Active Mountain–building in Mongolia and Iran

by

Edwin Karl Nissen

Thesis submitted to the University of Oxford
for the degree of Doctor of Philosophy
in Earth Sciences

Department of Earth Sciences, University of Oxford

Trinity, 2008

Supervised by Prof. Barry Parsons, Prof. Philip England
& Dr. Richard Walker

Declaration

The contents of this thesis are all my own work, except where otherwise stated. The views and opinions expressed herein are mine and not necessarily those of any other person or body unless so attributed.

Abstract

In this thesis I use a multi-disciplinary approach to investigate two areas of active mountain–building within the Alpine–Himalayan belt: the Altai range in western Mongolia, and the Zagros mountains in southern Iran. I begin by studying a clustered earthquake sequence that struck a previously unrecognised fault zone in the NW Altai mountains in 2003. By combining seismology and field observations with satellite radar interferometry (InSAR), I attempt to unravel the detailed history of faulting in time and space. Differences between body-wave and InSAR-based models prevent me from matching individual seismic events with individual fault segments, and I explore the cause of these discrepancies. In the following two chapters, I establish late Quaternary slip-rates on major right-lateral and thrust faults in the eastern part of the Altai. In particular, I explore the use of *in situ*-produced cosmogenic ^{10}Be and Optically Stimulated Luminescence (OSL) for dating offset alluvial fans and river terraces. My results suggest that faulting has migrated toward the eastern margin of the range from the high, interior Altai, presumably in response to stresses introduced by topography. In the final, main chapter, I investigate a link between buried reverse faulting and surface folding in the Zagros Simply Folded Belt. Using surface displacements measured with InSAR, I show that a major anticline on Qeshm Island was uplifted during an earthquake in 2005. However, the pattern of uplift is discordant with the growth of neighbouring folds, preventing us from establishing a simple connection between faulting and folding. All in all, my work demonstrates the importance of using several techniques in parallel when studying regions of active continental deformation.

Extended Abstract

In Chapter 1, I introduce continental tectonics and outline the scope of this thesis, before summarizing previous work on the active tectonics of Mongolia.

In Chapter 2, I study a sequence of large earthquakes which struck the Siberian part of the Altai mountains in September and October 2003. The M_w 7.2 mainshock was the largest earthquake to have struck the Altai mountains in more than seventy years, and was closely followed by two M_w 6.2 and 6.6 aftershocks. I use radar interferometry, seismic bodywaves and field investigations to examine the source processes of these earthquakes. The mainshock of the initial earthquake ruptured a subvertical, ∼NW-SE striking dextral strike-slip fault. The fault was previously unrecognised; although it approximately follows the south-western boundaries of two intermontane depressions within the interior northwestern Altai, it has very little topographic expression. A ∼NE-dipping M_w ∼6.7 reverse sub-event, possibly triggered by shear waves from the mainshock, occurred ten seconds afterwards, along strike to the south-east. The later M_w 6.2 and 6.6 aftershocks were dextral strike-slip events which contributed further to deformation in the north-west part of the fault zone. However, interferometric and bodywave models disagree significantly on the source parameters of the earthquakes, in particular the total moment released and the dip of the fault planes. Trade-offs of fault dip with moment and centroid depth in the bodywave modelling can account for some, but not all, of these discrepancies.

The interferometric data are unevenly distributed, containing many more datapoints on one side of the fault zone than the other; however, on the basis of calculations with synthetic data I rule this out as a reason for the discrepancies in fault parameters. The lower moment predicted by interferometry could be explained by the lack of coherent data close to the faulting, if slip was concentrated at very shallow depths. The dip yielded by the interferometric modelling might be influenced by lateral changes in elastic properties, although these would also affect the bodywave solutions. The earthquake sequence occurred close to recent paleomagnetic measurements of late Cenozoic anticlockwise rotations. These suggest that the right-lateral strike-slip faulting that ruptured in the 2003 earthquakes accommodates regional ∼NNE-SSW shortening by rotating anticlockwise over time. The reverse sub-event is a rare case of pure shortening perpendicular to the trend of the Altai range.

In Chapter 3, I address questions about the active fault slip-rates and initial timing of deformation in the Altai. I study the major, right-lateral Har-Us-Nuur fault in the eastern Altai, focusing on a series of abandoned alluvial fans that have been displaced right-laterally by ∼155 m from their feeder catchments. To constrain fan ages, I combine two independent dating methods – vertical profiles of *in situ*-produced cosmogenic ^{10}Be (averaged over many clasts) and Optically Stimulated Luminescence (OSL). Assuming no erosion, the exposure age for one surface is ∼70 ka (although I cannot rule out older ages, possibly around 120 ka, with higher erosion rates). However, OSL measurements from the same sampling pit yield burial ages of ∼19 ka. These figures yield right-lateral slip-rates of ∼2 mm yr^{-1} and ∼8 mm yr^{-1}, respectively. A terrace riser preserved above a younger fan surface, which I date at ∼6 ka with OSL, provides a slip-rate of ∼1–3 mm yr^{-1}, consistent with the lower of the two estimates from the older fan. Paleo-ruptures from the previous earthquake on the fault indicate coseismic slip of 2–3 m, implying an average repeat time of around

1100 years using a 2 mm yr^{-1} slip-rate. If these late Quaternary rates are representative over the longer term, movement on the fault initiated at 1–4 Ma, significantly later than the late Oligocene or Miocene (25–5 Ma) onset of shortening in the Altai region. These results suggest that active deformation is migrating away from the high, interior part of the Altai, onto structures at the margins of the range such as the Har-Us-Nuur fault. This may be because older faults in the range interior have rotated about vertical axes into orientations that require work to be done against gravity.

In Chapter 4, I investigate mountain building at Baatar Hyarhan, a NW-trending massif bounded by active thrust faults in the eastern Altai. My primary aims are to describe how thrusting has evolved over time, to calculate late Quaternary slip rates by dating offset alluvial markers with optically stimulated luminescence (OSL), and to compare these late Quaternary rates with measurements of deformation on decadal and geological timescales. Patterns of topography and drainage suggest that Baatar Hyarhan has grown in length, and has propagated laterally from the SE towards the NW over time. On the NE side of the massif, the range-bounding Zereg fault appears active only along younger parts of Baatar Hyarhan; next to the oldest, SE part of the massif faulting has migrated into the adjacent Zereg Basin where it has uplifted low, linear ridges of folded sediment, known locally as forebergs. On the SW side of the massif, only the range-bounding Tsetseg fault appears active. Using OSL, I establish ages of ∼15 ka, ∼20 ka and ∼85 ka for alluvial deposits cut by these faults. These ages are close to those of alluvial markers in the separate Gobi Altai range, suggesting that periods of fan and terrace formation may correlate over wide tracts of Mongolia, presumably under the primary control of climate. Combining these OSL ages with offsets measured with differential GPS, I calculate Late Quaternary slip rates across forebergs in the Zereg Basin and across the range-bounding Zereg and

Tsetseg faults. Uncertainties in fault dip (due to lack of clear fault exposures) and burial ages (due to incomplete resetting of the luminescence clock) mean that the exact slip rates are poorly constrained. Nevertheless, the vertical displacement rates calculated across the Zereg and Tsetseg range-front faults – 0.2–0.6 mm yr^{-1} and 0.1–0.4 mm yr^{-1}, respectively – are at the lower end of long-term ($\sim$5 Ma) estimates of 0.4–0.8 mm yr^{-1} and 0.3–0.7 mm yr^{-1}. Vertical rates of deformation may, therefore, have remained constant over the past $\sim$5 Ma, but equally the late Quaternary rates might be lower than the geological ones. This possible discrepancy could be accounted for if some of the shortening has shifted away from the range-front faults onto other nearby structures. The forebergs in the eastern Zereg Basin are an obvious candidate, but they show at least 10 km cumulative shortening (which would take a few Ma to accumulate at late Quaternary rates) and cannot simply be regarded as the latest stage of outward mountain growth. The total late Quaternary shortening rate across all three areas of faulting is 0.7–2.4 mm yr^{-1}, making up between one tenth and one third of the $\sim$7 mm yr^{-1} convergence across the whole Altai range.

In Chapter 5, I investigate the 2005 November 27 Qeshm Island earthquake (M_w 6.0), which provides an excellent opportunity to study coseismic deformation in the Zagros Simply Folded Belt with Synthetic Aperture Radar interferometry (InSAR). Typical of reverse faulting in the Zagros, slip in the Qeshm Island earthquake did not rupture the surface. However, ascending and descending track interferograms spanning the earthquake both show an elliptical pattern of surface deformation in the central part of the island. I invert the interferometric data to attain a set of source parameters; these show $\sim$1 m slip on a steep ($\sim$50°), north-dipping reverse fault, extending from a maximum depth of $\sim$8 km up to $\sim$4 km below the surface. Limited aeromagnetic data suggests the fault ruptured the sedimentary cover; whether its deepest parts also affected the crystalline basement is not clear. Source parameters from seismic bodywave modelling agree with those from the interferometric modelling. Using the InSAR-derived model, I produce a map of coseismic vertical displacements, with which I compare the surface structure of the island. Coseismic uplift is centred on the eastern end of a major anticline, which trends E–W, parallel with the fault. The long-term growth of this fold may be controlled primarily by repeated earthquakes on this fault. However, the uplifted region extends to parts of other nearby folds, whose long-term growth must have other controls; moreover, a region of coseismic subsidence lies very close to a part of the Qeshm island coastline that displays raised beaches, evidence of Quaternary uplift. Therefore the link between reverse faulting and surface folding is not wholly evident from this earthquake alone. The local structure is complicated by orthogonal fold axes; it may take a large earthquake in a simpler structural setting within the Zagros to establish convincingly whether a one-to-one correlation between faulting and folding exists.

Although detailed conclusions are provided at the end of each chapter, I also provide some more general concluding remarks in Chapter 6.

Acknowledgments

Firstly, I would like to thank my supervisors, Barry, Philip and Richard, for providing a great environment in which to develop as a scientist. My other colleagues in the COMET group have also been a huge source of advice, and friendship, during my time in Oxford. In particular I would like to thank Gareth, John and Mike for helping me out of numerous scrapes with ROI_PAC, GMT and MATLAB. I am also very grateful to my examiners, Conall Mac Niocaill and Jean-François Ritz, for constructive reviews of my work and for an enjoyable viva.

For my thesis I have tried to throw as many different techniques at a problem as I can. This has given me the opportunity to collaborate with many scientists, covering a variety of fields, and I would like to thank all of these people for their input. In Chapter 2, I was helped in the field by Anatoly Mistrukov, while Eugene Rogozhin kindly provided me his own map of surface ruptures; Brian Emmerson helped me produce the body-wave solutions and David Robinson the joint hypocentre relocations. Luminescence measurements in Chapters 3 & 4 were carried out by Morteza Fattahi. In Chapter 3, Christophe Schnabel took the final ^{10}Be measurements, Josh West helped me model these results, and Andy Carter contributed the AFT analysis. Chapters 5 was greatly improved by field contributions from Morteza Talebian, Manoucher Ghorashi and James Jackson, who also provided the body-wave models.

The highlight of my time at Oxford has been my time outside Oxford, namely my three trips to Mongolia. I am really grateful to all those involved – Rich (again), Bayasgalan, Molor, Chimgee, Altan, Ganbold, and a host of students and drivers – for making these trips such a unique experience. My fondest memories are of sitting down to discuss the day's work over a glorious sunset, a can of warm lager and a bowl of steaming mutton stew.

That is not to say I have not enjoyed my time *in* Oxford, and I feel fortunate to have made so many good friends here at the Department. In particular I would like to thank those I have lived with in Marlborough Road. In this regard, contributions from Eggwina et al. (2007, 2008) are also gratefully acknowledged.

Finally, I would like to thank my family for their support throughout education and for encouraging me to do a D. Phil. in the first place. And lastly, Louise: tack så mycket för allt.

Contents

List of Figures

List of Tables

Chapter 1

Introduction

1.1 Continental Tectonics

Plate tectonics provides a useful framework for describing and explaining the deformation of the Earth's oceans. Here, narrow bands of earthquakes define tight plate boundaries, and the type of faulting directly reflects the relative motions of the rigid plates on either side. Plate tectonics is less helpful for understanding the deformation of the continents, where seismicity is spread over areas hundreds or even thousands of kilometers wide – distances that far exceed the thickness of the lithosphere itself (e.g. McKenzie, 1972). Moreover, the type of faulting observed in these zones does not always reflect (in any simple way) the relative motions of the rigid plates on either side of it. For instance, the collision zone between India and Eurasia contains all three types of faulting – thrust, normal and strike-slip.

These observations led to the development of a new field, continental tectonics, which aimed to describe and explain this behaviour. In the intervening forty years this has expanded into a wide-ranging and rich subject of research, though there are several unresolved issues which are actively debated today. These arguments are often divided into those that aim to characterize the deformation ("kinematics") and those that then try to account for it ("dynamics").

One important debate in continental tectonics regards a choice of framework used to describe the kinematics. One approach describes the movements of rigid blocks, or "microplates", using rotations about Euler poles – the central tenet of plate tectonics (e.g. Thatcher, 1995). By measuring the relative motions across the boundaries of each block, this approach aims to provide a complete picture of the kinematics. There are indeed many large, rigid regions within the deforming parts of continents which could be described as microplates – for instance, the Tarim Basin in the India-Eurasia collision zone. However, in many regions of continental deformation active faults are spaced only tens of kilometers apart; taking this approach to its logical conclusion results in blocks that are so numerous, and so small, that describing continental regions hundreds or thousands of kilometers wide becomes impractical (e.g. McKenzie, 1972; Molnar, 1988).

An alternative approach describes the deformation in terms of a continuum. This method relies on smoothly varying velocity fields calculated from records of earthquakes (Molnar & Qidong, 1984; Jackson & McKenzie, 1988) or estimates of fault slip-rates (England & Molnar, 1997a) over large regions. As such, this approach is concerned with length-scales larger than the thickness of the lithosphere ($\sim$100 km) and does not attempt to characterize deformation on smaller length-scales in the upper crust, where strain is clearly focused onto narrow fault zones. Continuum models of continental deformation can be compared to these velocity fields to investigate the forces responsible for the observed deformation (e.g. England & Molnar, 1997b).

Central to both of these approaches is the need to map, and then quantify, the active faulting present within these continental regions. Earthquakes still offer important information about the location, depth and style of faulting, but the $\sim$100 year record of instrumental seismology limits their use at providing rates of deformation. To overcome this problem, earthquake studies are increasingly complemented by new geodetic techniques that map strain over months, years and decades ($<10^2$ yr), and modern geochemical dating methods that do so on millenial (10^2–10^4), Quaternary

(10^4–10^6 yr) and geological (>10^6 yr) timescales.

These new tools have thrown up many interesting questions regarding the relationship between deformation on these different timescales. For instance, how does the pattern of faulting in the upper crust evolve over time, and can activity shift temporarily between one fault zone and another? How do neighbouring faults interact, and is there any use in the concept of an earthquake repeat interval?

1.2 Scope of this thesis

Clearly, if the questions posed at the end of the previous section are to be answered then the full range of observational techniques, covering each different timescale, must be embraced. Furthermore, it is useful to study not just one but many areas of active faulting, so that patterns emerge which can highlight the underlying processes. In this thesis I will investigate active shortening within two mountainous regions of the Alpine-Himalayan earthquake belt – Mongolia and Iran (Fig. 1.1).

Why choose these two areas? Relatively little is known about the deformation of Mongolia at present, but its pristine environment and superb preservation of landforms offer key advantages for investigating fault geomorphology. Iran has a long history of destructive earthquakes and is much more widely studied as a result, but large earthquakes here continue to provide new insights into continental tectonics (e.g. Jackson et al., 2006). Both countries have semi-arid environments, with sparse vegetation, low rates of erosion and little human activity – factors which greatly help interpretation of satellite imagery.

I will use a combination of geodesy, field observations and seismology to study individual earthquakes, and remote sensing, Quaternary dating and thermochronology to investigate Quaternary and geological deformation. Wherever possible, I will try to establish links between the two. The aim of the thesis is not to advance any one particular technique, but rather to contribute to an understanding of continental deformation by applying a multi-disciplinary approach. As such there is no “methods” chapter; however I do provide brief introductions to some of the newer techniques in the places where they are first used – namely Synthetic Aperture Radar Interferometry (InSAR), optically-stimulated luminescence (OSL) dating and *in situ*-produced cosmogentic ^{10}Be exposure dating.

- In the remainder of this chapter I summarise the active tectonics of Mongolia, focusing in particular on the Altai mountains (which concern the majority of the thesis).

- In chapter 2 I study a sequence of earthquakes which struck the north-western Altai in 2003 – including the largest in the region for over seventy years. The earthquakes were clustered in space and time, and using InSAR, seismology and field observations I try to discriminate the effects of each individual event.

- In chapter 3 I estimate the late Quaternary slip-rate and average earthquake repeat interval on a major strike-slip fault in the eastern Altai. My results have implications for the evolution of faulting within the range; they also provide a rare opportunity to compare OSL and ^{10}Be dating.

- In chapter 4 I study a series of clearly-exposed thrust faults in the south-eastern Altai. I describe how faulting has evolved over time, and compare late Quaternary displacement rates – determined with OSL dating – to geological estimates of range uplift.

- In chapter 5 I use InSAR and seismology to investigate the 2005 Qeshm Island earthquake in southern Iran. This event provides a good opportunity to constrain the long-debated relationship between buried faulting and surface folding in the Zagros Simply Folded Belt.

- Although specific conclusions are provided at the end of each chapter, I also provide some brief, more general concluding remarks in chapter 6.

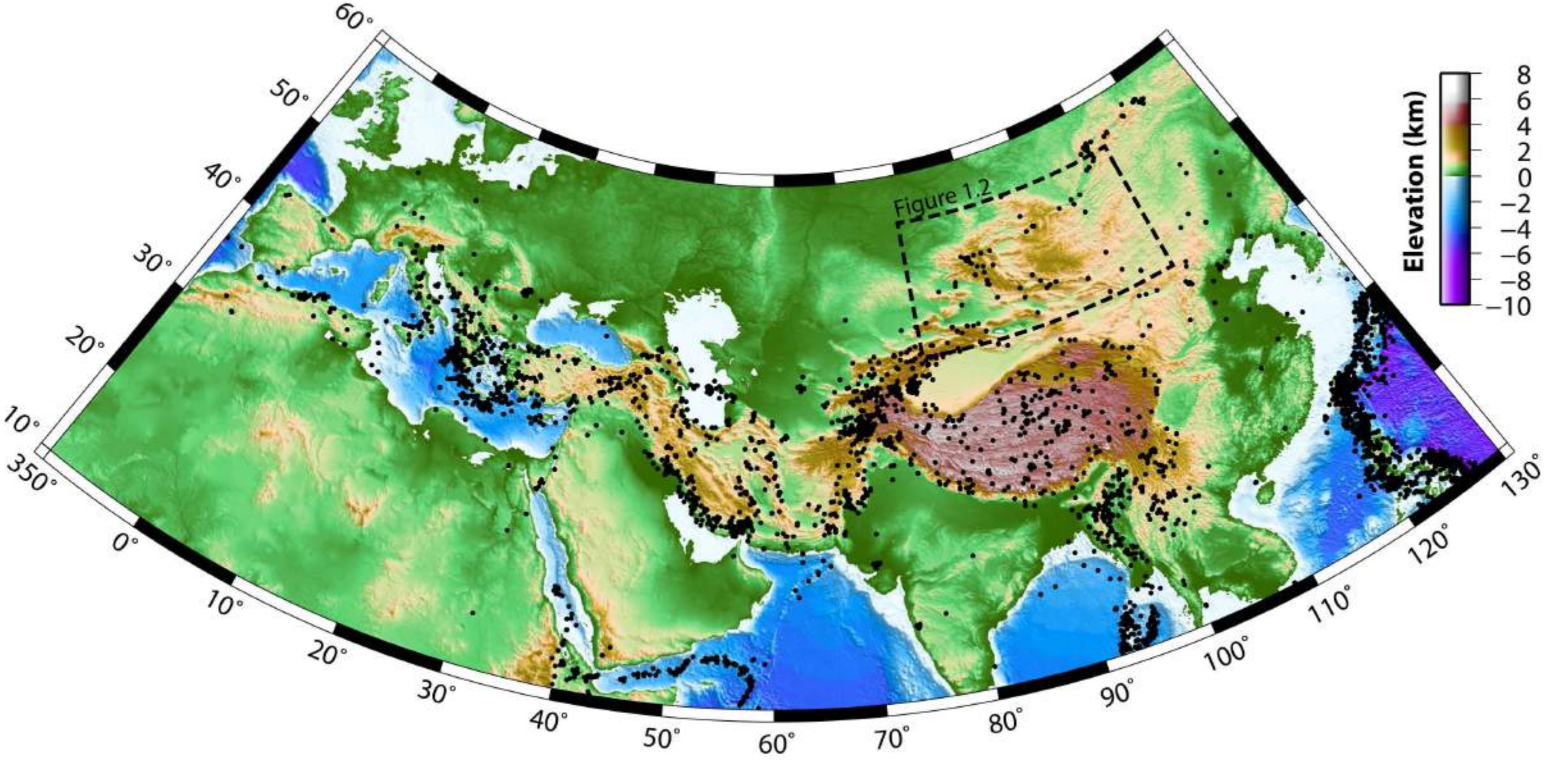

Figure 1.1: The Alpine-Himalayan earthquake belt, stretching from the Moroccan Atlas to eastern Siberia. Black dots represent medium and large-sized earthquakes (mostly $M_w \geq 5$) from 1976–2007, as listed in the Global CMT catalogue (formally called the Harvard CMT catalogue). These are plotted on topography artifically sun-shaded from the NE and in an Albers equal-area conic projection.

1.3 Active Tectonics of Mongolia

Mongolia lies at the very northern edge of the India-Eurasia collision zone, around 2500 km north of the Himalaya (Fig. 1.1). The country is well-known amongst seismologists for three very large earthquakes that struck here during the 20th Century – the M_s 8.2 Tsetserleg (1905 July 9), M_s 8.3 Bulnay (1905 July 23) and M_s 8.3 Gobi-Altai (1957 December 4) earthquakes. In addition, a fourth event – the M_s 8.0 Fu-Yun (1931 August 10) earthquake – struck a neighbouring part of China during the same period. Each of these earthquakes involved several metres of slip and ruptured fault lengths of more than 100 km (Baljinnyam et al., 1993).

Early work on the regional tectonics by Russian and Mongolian geologists focused on mapping the surface breaks of these great earthquakes (e.g. Florensov & Solonenko, 1963; Khil'ko et al., 1985), while others identified active faults with satellite imagery (Molnar & Tapponnier, 1975; Tapponnier & Molnar, 1979). Political changes during the early 1990's greatly eased access to the country, and a proliferation of new field research has been accomplished during the past two decades.

This previous work has drawn on a number of advantages Mongolia holds over other actively deforming continental areas. Firstly, the low population density means there is relatively little anthropogenic impact on the landscape while the cold, semi-arid environment results in low rates of erosion. These factors allow subtle features in the landscape to be preserved exceptionally well and for long periods of time. In particular, historical earthquake ruptures can still be observed many hundreds of years, and perhaps even thousands, after the original event (e.g. Khil'ko et al., 1985; Baljinnyam et al., 1993; Walker et al., 2006). This is illustrated in Fig. 1.2, which shows the ruptures of three strike-slip earthquakes a few years, one hundred years and about one thousand years old, respectively.

It is important to note the scale of surface rupturing depends largely on the type of earthquake. Strike-slip ruptures in Mongolia are often particularly impressive,

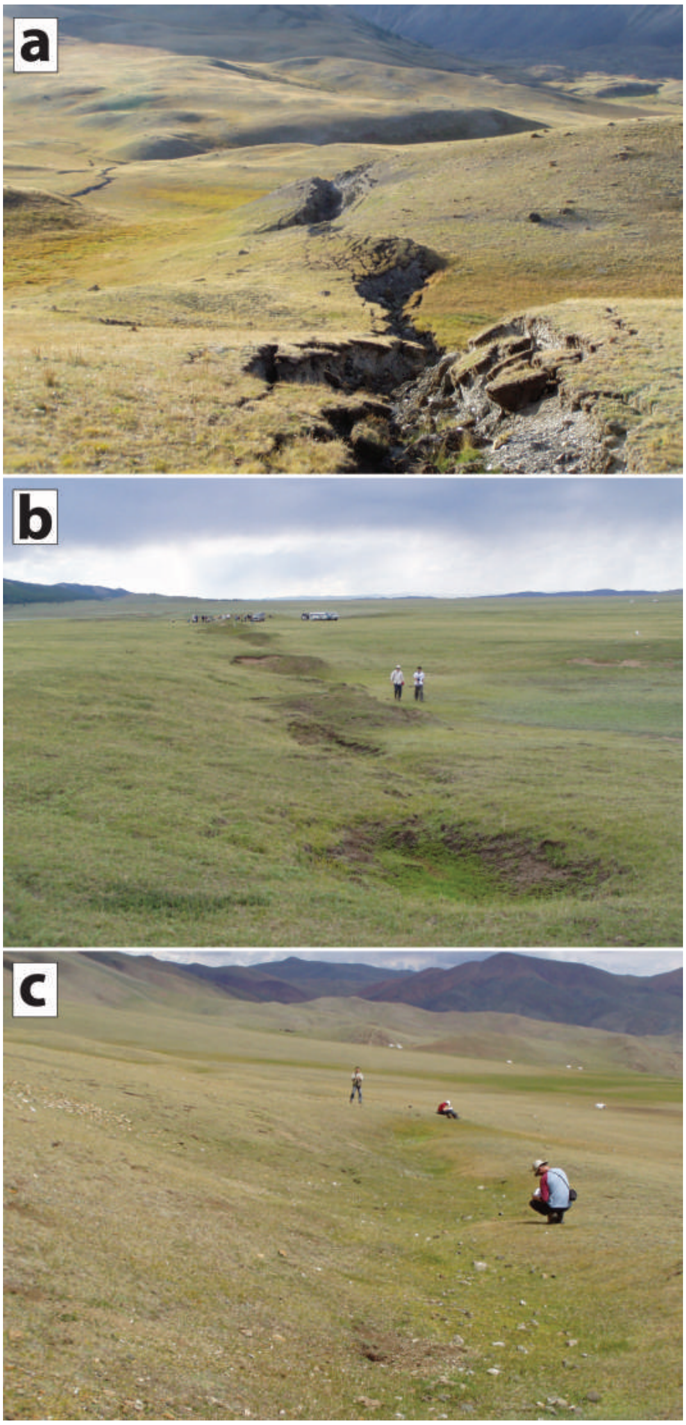

Figure 1.2: Photographs showing ruptures from earthquakes (a) 2 years, (b) 100 years and (c) ∼900 years in age, illustrating the exceptional preservation of surface deformation made possible by western Mongolia's cold, semi-arid climate and its sparse population. (a) En echelon tension fissures from the right-lateral, M_w 7.2 2003 Siberian Altai earthquake (photographed in 2005 at ∼49°59'N 87°59'E, facing ∼NW). (b) En echelon tension fissures from the left-lateral, M_s 8.3 1905 Bulnay earthquake, now partly infilled. (c) En echelon tension fissures from a right-lateral, M_w 7.5 earthquake on the Jid fault which occurred 870–980 years ago (Walker et al., 2006); the fissures are now largely infilled but their approximate size and orientation can still be picked out by the dense vegetation growing within them.

tending to form a clear, en echelon pattern of tension cracks (sometimes accompanied by pressure ridges, or "moletracks"). Using the orientation and scale of these fissures, the sense and amount of slip that occurred in the event can be established; in addition, where high-resolution satellite imagery is available (such as Quickbird images on Google Earth) many of these ruptures can be identified and mapped entirely remotely. In contrast, reverse faulting is known to not always form clear breaks at the surface (e.g. Stein & King, 1984). So while paleo-earthquake ruptures are very useful, they should in no way be viewed as a complete record of historical activity.

A second advantage Mongolia has over other parts of the India-Eurasia collision zone is that Cenozoic deformation probably started here significantly later than further south (e.g. De Grave et al., 2007; Vassallo et al., 2007a). As a result, late Cenozoic faulting and the resulting tectonic structures are at a relatively youthful stage of development and may be simpler to interpret. In addition a widespread peneplain, preserved on numerous flat-topped mountain summits across the western half of the country, acts as a convenient marker of cumulative vertical strain (Fig. 1.3). According to apatite fission-track studies, this vast erosional surface formed during the Jurassic or Cretaceous period (De Grave & Van den haute, 2002; Yuan et al., 2006; Vassallo et al., 2007a) and has since undergone more than 100 million years of tectonic quiescence before the onset of late Cenozoic deformation (Jolivet et al., 2007).

A better comprehension of the active tectonics here, where these advantages can be exploited, could greatly benefit studies of other regions of intracontinental shortening. However, the styles and rates of deformation in many parts of the country remain relatively unknown. In the first part of my thesis, I will concentrate on active faulting in the Altai mountains in far western Mongolia. But first, in the section below, I will provide a brief summary of the tectonics of the whole region, moving in a clockwise direction from northern Mongolia, through central and southern parts of

Figure 1.3: View ∼W from from 47°15’41”N 91°55’10”E toward the interior part of the Altai range in far western Mongolia. The high mountain forming the horizon is Monkh Hyarhan Uul (see Fig. 1.5). Like many peaks across the country, a widespread Jurassic or Cretaceous peneplain surface is preserved as a distinctive summit plateau; in this case, it can be seen across the full width of the photograph.

the country, and finally to western Mongolia.

1.3.1 Northern Mongolia

Northern Mongolia was the location of two magnitude ∼8 earthquakes in 1905. The first of these earthquakes (M_s 8.2) ruptured a 130 km length of the NE-trending Tsetserleg fault, and involved left-lateral and vertical (reverse faulting) components of up to 2.5 m and 2 m, respectively. Two weeks later the nearby E-W trending Bulnay fault ruptured in a second left-lateral strike-slip event (M_s 8.3); with a total rupture length of 375 km and an average slip of 5–10 m, this remains one of the very

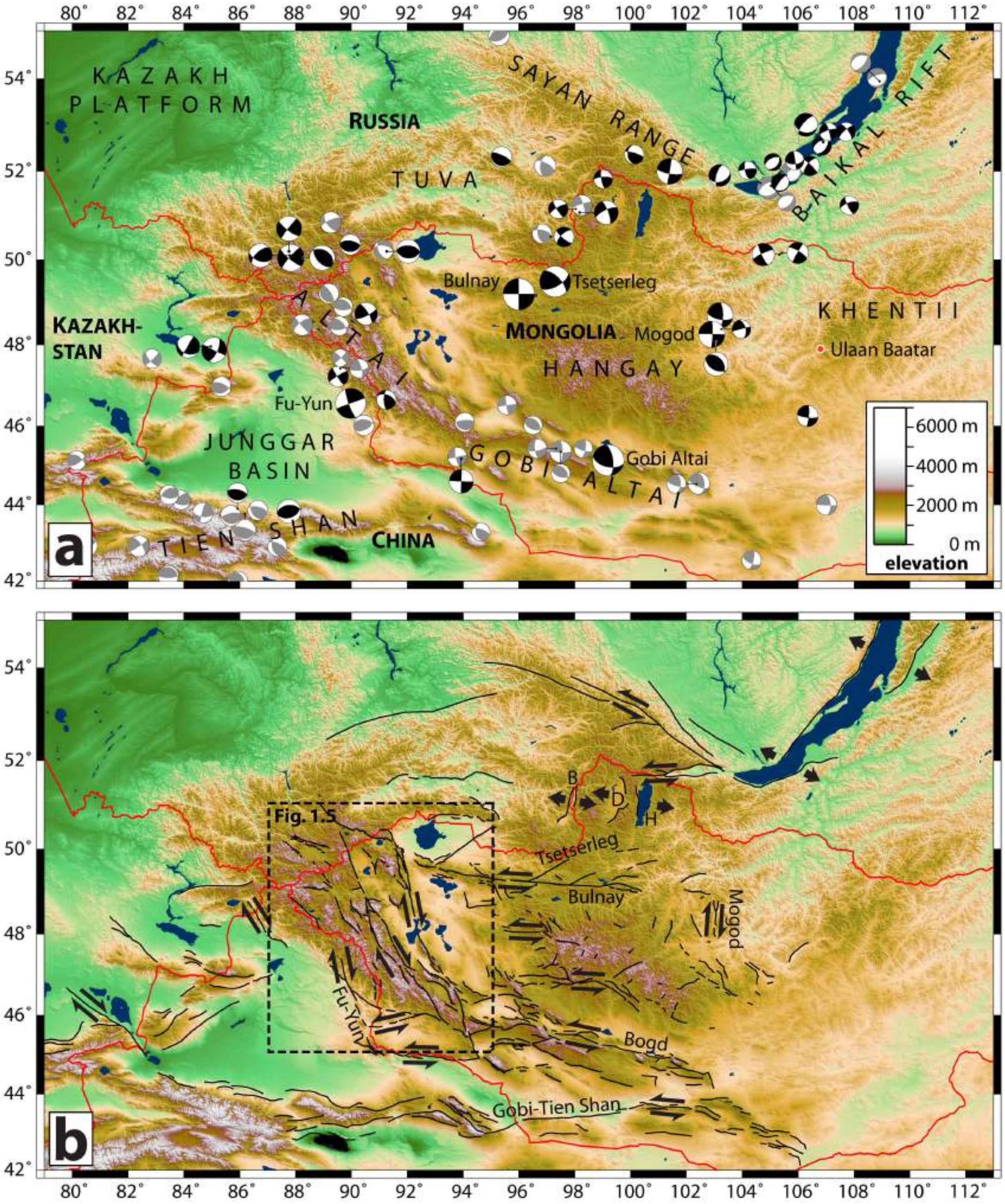

Figure 1.4: (a) Earthquake focal mechanisms ($M_w \geq 5$) in Mongolia and its surroundings, plotted on topography artificially shaded from the NE, in a Mercator projection. Black mechanisms represent earthquakes modelled with seismic waveforms or first motions (1905–2003), from Bayasgalan et al. (2005) (and references therein) and Chapter 2 of this thesis. Grey mechanisms are from the Global CMT catalogue (1977–2007), though for simplicity I exclude six M_w 5.0–5.2 aftershocks of the 2003 Siberian Altai sequence. All earthquakes are plotted at the latitude and longitude given in the updated version of the Engdahl et al. (1998) catalogue. Earthquakes discussed in the text are labelled. (b) Active faults in Mongolia (note that not all faults in the surrounding Tien Shan, Tuva, Sayan and Baikal areas are plotted, and that scattered faulting in the Khentii mountains remains largely unmapped). Those mentioned in the text are labelled; in northern Mongolia, B = Busiin Gol, D = Darhad and H = Hövsgöl grabens.

largest known continental earthquakes. The ruptures of both events are described in detail by Khil'ko et al. (1985) and Baljinnyam et al. (1993) and seismological perspectives are provided by Okal (1977) and Schlupp & Cisternas (2007). It has also been suggested that stress changes caused by these earthquakes – principally by postseismic relaxation of the lower crust – contributed toward triggering other large Twentieth Century earthquakes in Mongolia and its surroundings (Chéry et al., 2001; Pollitz et al., 2003).

These left-lateral faults, together with parallel structures in the Sayan range to the north (Delouis et al., 2002; Arjannikova et al., 2004), cause eastward motion of central Mongolia with respect to Siberia. North-east of the Bulnay fault, this eastward motion opens up a series of N–S grabens – Busiin Gol, Darhad and Hövsgöl – situated at the SW end of the Baikal rift. Interestingly, recent earthquake focal mechanisms in this area are all strike-slip, although it is not clear whether they involve E-W left-lateral or N-S right-lateral faulting.

1.3.2 Central Mongolia

In central Mongolia, the dome-shaped Hangay range rises to elevations of around 4000 m. Unusually for a major mountain belt within the India-Eurasia collision zone, its elevated topography is not thought to be caused by shortening and associated crustal thickening. Low upper-mantle seismic velocities and scattered Miocene–Quaternary volcanism have lead some to suggest that a mantle plume dynamically supports the range (e.g. Windley & Allen, 1993), although the absence of any corresponding gravity anomalies implies an alternative cause, perhaps magmatic underplating of the crust (Petit et al., 2002; Bayasgalan et al., 2005).

Although there were no large earthquakes in the Hangay during the past century, the range contains several active faults (Fig. 1.4). The easiest to identify in satellite imagery are a scattered set of normal faults, which have been described as resulting from localised stresses caused by the uplifted topography (Baljinnyam et al., 1993; Cunningham, 2001). However, recent field and remote-sensing studies show that some of these faults represent releasing-bend segments of much larger, left-lateral strike-slip faults, which follow an E–W trend, like the Bulnay fault to the north (Walker et al., 2007, 2008). Just to the east of the Hangay, the 1967 Mogod earthquake (M_w 7.0) involved right-lateral strike-slip on a N–S fault (Bayasgalan & Jackson, 1999).

1.3.3 Southern Mongolia

In southern Mongolia, the Gobi-Altai range consists of a number of separate massifs uplifted to heights of up to 4000 m by left-lateral transpression on the E-W trending Gurvan Bogd fault system. This fault zone ruptured in the 1957 Gobi-Altai earthquake (M_s 8.3); wide-ranging research since then, summarised below, makes it by far the best studied fault in Mongolia (and probably one of the best-studied in continental Asia).

The 1957 earthquake produced a complex set of surface breaks within the Gurvan Bogd fault zone, involving left-lateral displacements of up to 7 m on a 250 km section of the Bogd fault and dip-slip displacements of up to 5 m on nearby thrusts (Florensov & Solonenko, 1963; Kurushin et al., 1997). Paleoseismlogical excavations indicate average repeat times of a few thousand years on these faults, but also suggest that the 1957 rupture pattern may not have been charasteristic (Bayasgalan, 1999; Prentice et al., 2002; Ritz et al., 2007). Exposure ages of offset alluvial fans yield late Quaternary horizontal slip-rates of $\sim$1.5 mm yr^{-1} on the Bogd fault, and vertical slip-rates of 0.1–0.2 mm yr^{-1} on the nearby thrusts (Ritz et al., 2006 and references therein). Modelling of apatite-fission track data implies that the uplift of the Gobi-Altai range – and presumably slip within the Gurvan Bogd fault zone – began during the late Miocene or Pliocene, at 5±3 Ma (Vassallo et al., 2007a), while geomorphological studies have shown how faulting is likely to have evolved over time during this period (e.g. Bayasgalan et al., 1999b).

Further south, another set of left-lateral transpressive structures – the Gobi-Tien Shan fault system – provides a kinematic link with the eastern Tien Shan range in China (Cunningham et al., 1996). However, compared to the main Gobi-Altai range there have been very few recent earthquakes here, and the characteristics of this fault zone remains largely unknown.

1.3.4 Western Mongolia

In western Mongolia active faulting is concentrated within the Altai mountains, a major, NW-trending mountain belt which encroaches into neighbouring parts of China, Kazakhstan and Russia. The range averages ∼2500 m in elevation and reaches a maximum height of 4506 m. It is surrounded by flat, low-lying and apparently undeforming regions – the vast Kazakh Platform to the north and west, the Junggar Basin to the south, and a collection of smaller basins known as the Depression of Great Lakes to the east. The main part of the Altai are shown in more detail in Fig. 1.5.

Basement Geology and Onset of Cenozoic shortening

The basement geology of the Altai primarily consists of Proterozoic and Paleozoic metamorphic and igneous rocks. These have been categorised as Precambrian continental fragments and Paleozoic subduction and arc complexes (Badarch et al., 2002). These terranes were accreted onto the southern margin of the Siberian (or Angara) craton during a prolonged interval of continental growth during the Paleozoic (Sengör et al., 1993). In western Mongolia this accretion imparted a strong NW-trending structural fabric, which plays an important role in the tectonics of the Altai today (Cunningham, 2005).

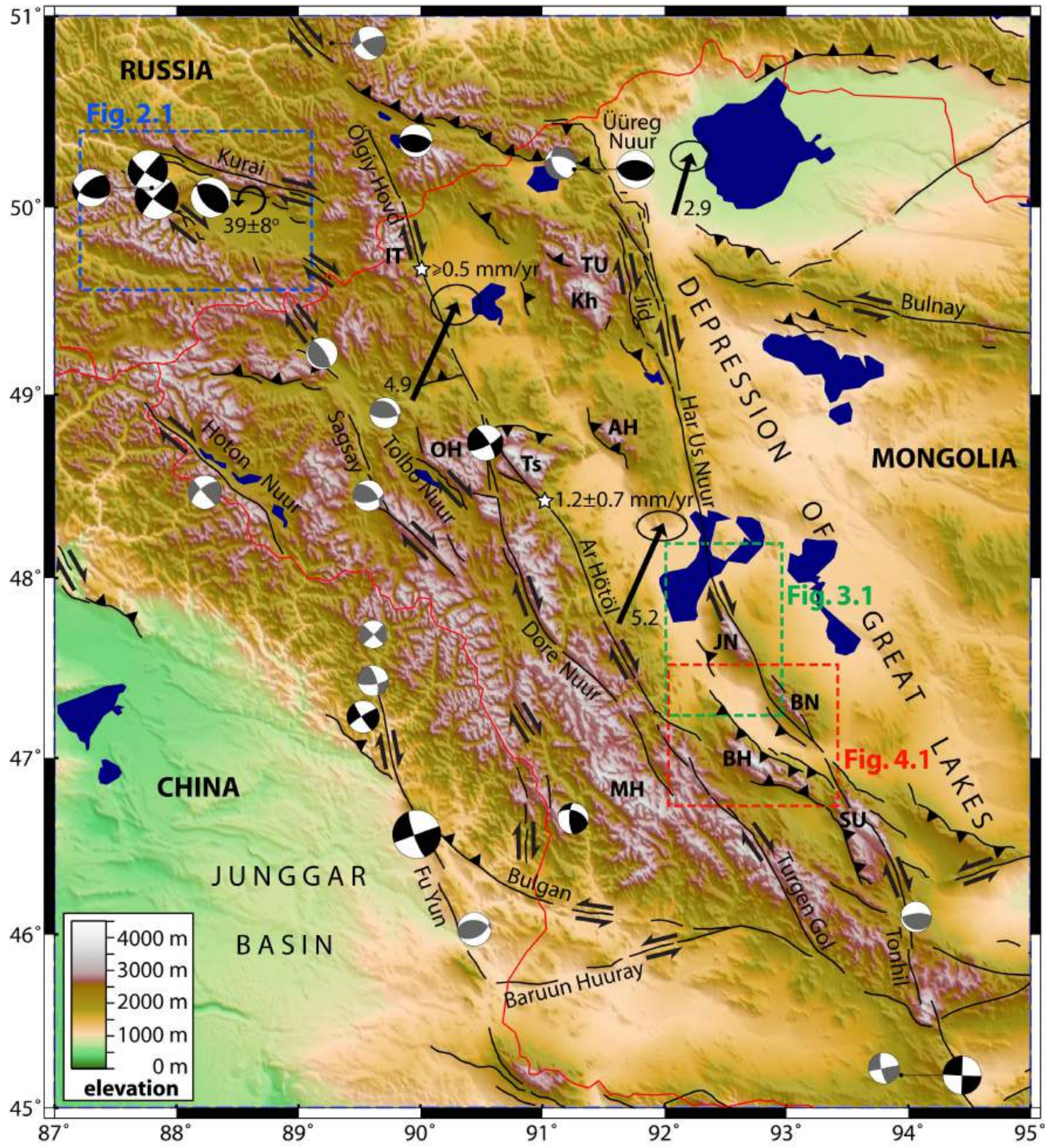

Figure 1.5: Earthquake focal mechanisms (M_w ≥5), GPS vectors and major active faults faults in the Altai mountains, plotted on Shuttle Radar Topography Mission (SRTM) topography, artificially shaded from the NE, in a Mercator projection. Earthquake focal mechanisms and GPS velocities are the same as in Figs. 1.4 & 1.6, respectively, and once more the smaller aftershocks from the 2003 Siberian Altai sequence are not plotted. The circular arrow shows the location of paleomagnetic measurements of anticlockwise rotations within Neogene sediments in the NW Altai (Thomas et al., 2002). Abbreviations of individual massifs within the Mongolian part of the range are as follows: AH = Altun Hühay Uul, BH = Baatar Hyarhan, BN = Bumbat Nuruu, IT = Ih Türgen Uul, JN = Jargalant Nuruu, Kh = Kharkhiraa, MH = Monkh Hyarhan Uul, OH = Ömnö Hayrhan Uul, SU = Sutai Uul, Ts = Tsambagarav Uul, TU = Türgen Uul.

Jurassic or Cretaceous clastic rocks are present locally within basins along the eastern margin of the range. Howard et al. (2003, 2006) interpret these Mesozoic basins as extensional in origin, although there is no widespread evidence for large-scale rifting at this time.

The onset of India-related deformation in the Altai is poorly constrained. Coarsening sedimentation in basins in and around the Altai points to initial range uplift some time during the late Oligocene or early Miocene ($\sim$28–15 Ma; Devyatkin, 1974, 1981; Howard et al., 2003), whilst apatite fission-track modelling places it some time during the Miocene ($\sim$23–5 Ma) or Pliocene ($\sim$5–2 Ma) for the Chinese and Russian parts of the range, respectively (Yuan et al., 2006; De Grave & Van den haute, 2002).

GPS constraints on shortening

There is little GPS data by which to constrain the present-day deformation of the Altai, the three arrows plotted on Fig. 1.5 representing the only measurements taken within the range (Calais et al., 2003). However, the difference between velocities (relative to Eurasia) at Urumqi, in the southern Junggar Basin ($\sim$10 mm yr^{-1}) and at Ulaangom, in the Depression of Great Lakes ($\sim$3 mm yr^{-1}), suggests the Altai currently accommodates $\sim$7 mm yr^{-1} of NNE-directed shortening (Calais et al., 2003). The Altai thus makes a significant contribution toward the 35–40 mm yr^{-1} total India-Eurasia convergence, also constrained by GPS (e.g. Chen et al., 2000; Wang et al., 2001; Sella et al., 2002).

Earthquakes and faulting

During the Twentieth century, the Altai range was the most seismically active region in Mongolia. Most earthquakes involved right-lateral strike-slip on N–NW striking faults. The largest of these events was the 1931 Fu-Yun earthquake (M_s 8.0), which ruptured a 180 km length of the Fu-Yun fault (in the Chinese Altai) and involved an average slip of about 8 m (Zhang, 1982; Shi et al., 1984). The ruptures of large historical earthquakes have been mapped on a number of faults within the Mongolian part of the range, too (Khil'ko et al., 1985; Baljinnyam et al., 1993; Walker et al., 2006). These include a probable magnitude ∼8 event on the Ar Hötöl fault, which has been tentatively ascribed to an earthquake felt in western Mongolia and southern Siberia in 1761 (Baljinnyam et al., 1993).

These dextral strike-slip faults are distributed in an anastomosing pattern across the full width of the Altai, and for the most part the range lacks the clear frontal faulting observed at the margins of many other intracontinental mountain belts (Cunningham, 2005). The orientation of the faults is thought to be governed by the NW-SE structural grain of the range (Cunningham, 1998). Many include a significant reverse component, which has uplifted numerous peaks of around 4 km elevation, often with very flat summits preserving remnants of the Mesozoic peneplain.

Thrust faulting also plays a role in the kinematics of the Altai range. In the northern Altai, a M_w 6.3 earthquake at Üureg Nuur ruptured a north-dipping thrust, which probably relates to the northern termination of the Har-Us-Nuur fault (Baljinnyam et al., 1993). Other terminal thrusts have been mapped in the Siberian part of the range; many of the high mountains in this area are uplifted along them. Elsewhere in the range thrust faulting is poorly documented, although a number of isolated massifs in the eastern Altai show clear scarps through Quaternary deposits at their margins (Fig. 1.5). I return to one of these ranges, Baatar Hyarhan, in Chapter 4.

At the far southern end of the Altai, the N-S striking right-lateral faults intersect with E-W striking left-lateral faulting at the western end of the Gobi Altai mountains. The kinematics of this area, and the interactions between these conjugate strike-slip faults, are not well understood.

Mechanism of convergence

The discrepancy between earthquake slip vectors and the overall convergence direction suggests that shortening across the Altai is achieved by anticlockwise, vertical-axes rotations of the right-lateral strike-slip faults and the slivers of crust between them (Baljinnyam et al., 1993; Bayasgalan et al., 2005). The limited paleomagnetic data currently available, from a single study of Neogene sediments in the Siberian part of the range (Thomas et al., 2002, Fig. 1.5), support this kinematic model.

A cartoon representation of this mechanism is shown in Fig. 1.6a & b. The anticlockwise rotation of the Altai may promote the left-lateral shear observed on E-W faults in areas to the east. This shear moves southern and central parts of the country eastwards with respect to Siberia, motions that are clear in the GPS velocity field of Calais et al. (2003), shown in Fig. 1.6c.

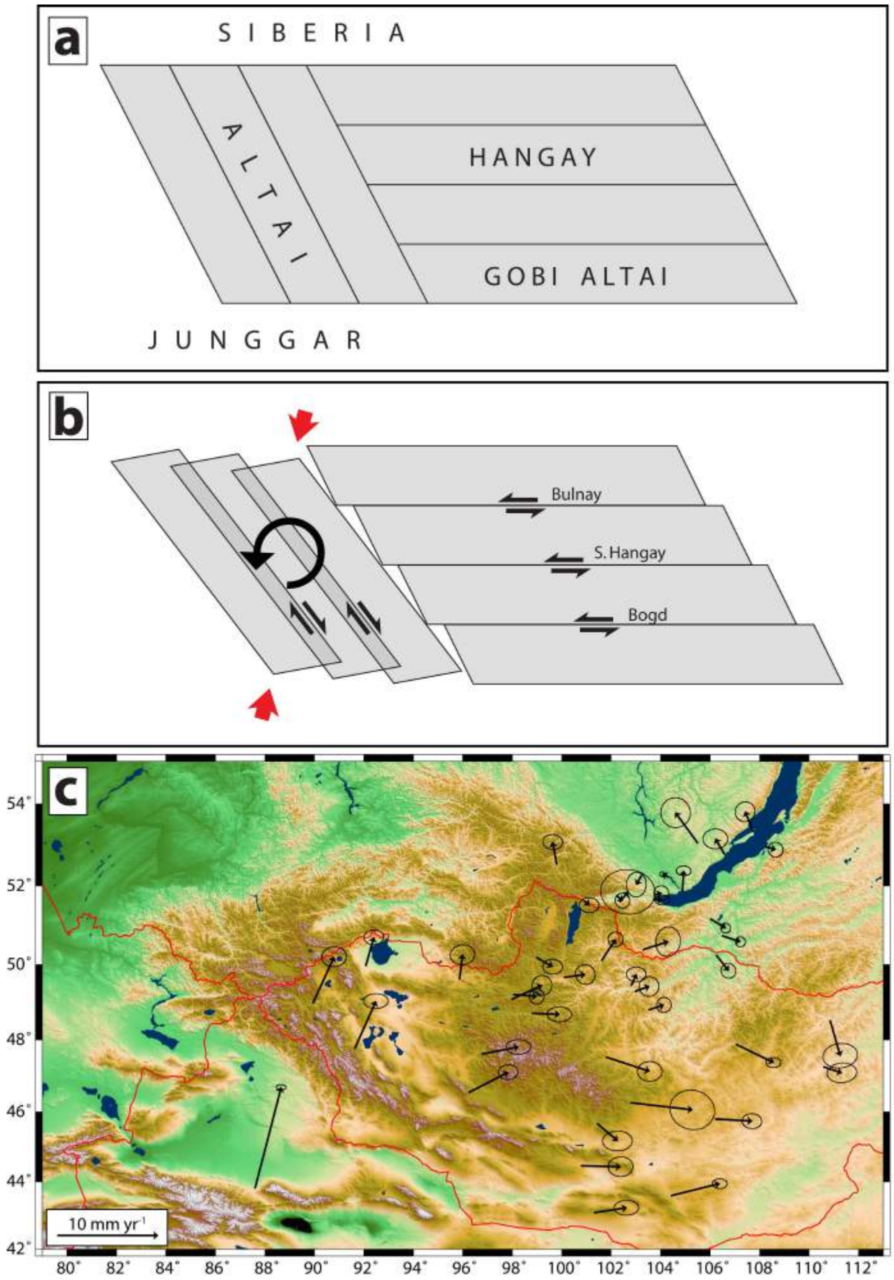

Figure 1.6: (a) & (b) Cartoon model for the active deformation of Mongolia, adapted from Bayasgalan et al. (2005). The situation before India-Eurasia shortening is shown in (a), and that afterwards in (b): the Junggar Basin has moved NNE with respect to Siberia; faults in the Altai have undergone right-lateral transpression, and the slivers of crust between them have rotated anticlockwise. These rotations induce left-lateral shear on faults to the east of the Altai. (c) GPS velocities (mm yr^{-1}) relative to stable Eurasia with 95% confidence ellipses, from Calais et al. (2003), with a scale provided in the bottom left of the figure. The velocities in western and central Mongolia qualitatively fit the convergence mechanism described in (a) and (b), although in northern parts of the country the Baikal Rift appears to exert more of an influence.

Chapter 2

The 2003 Siberian Altai earthquakes

2.1 Introduction

On 27 September 2003, a M_w 7.2 earthquake struck the north-western Altai mountains in southern Siberia, close to the Russian borders with Mongolia, Kazakhstan and China (Fig. 1.5). It was the largest earthquake to have hit the Altai since the M_s 8.0 Fu-Yun earthquake of 1931, and the first major event in the region since the advent of Synthetic Aperture Radar Interferometry (InSAR). In addition, it occurred further north-west than any large event in the Altai during the period of instrumental seismology, and thus provides important evidence for how shortening is accommodated in this area.

Two large (M_w 6.2 and M_w 6.6) aftershocks occurred within four days of the mainshock, and six smaller (M_w ~5.0) events in the following weeks. As well as the close temporal association, these earthquakes were clustered spatially, all within a ~60 km long fault zone (Fig. 2.1). Conventionally, such an earthquake sequence is studied using a combination of seismology and field observations. However, errors in hypocentral location can make it difficult to link individual seismic events with particular features of the surface deformation. In recent years, InSAR has provided a potential way around this problem. InSAR can provide a detailed map of surface deformation which, through modelling, can yield a set of earthquake source parameters. By comparing these source parameters with those determined using seismology, the matching of detailed surface displacements to individual seismic events can be attempted. But just as seismology is limited by its poor spatial resolution, so interferometry lacks good temporal resolution. Because of the long intervals between consecutive passes used in interferometry, interferograms provide maps of total displacements over 35 days, or periods that are multiples of 35 days, for European Space Agency (ESA) satellites. When several earthquakes have occurred within this repeat interval, and are spatially close together, it can be difficult to distinguish individual coseismic ground movements.

I investigate the 2003 Siberian Altai earthquakes to see if it is possible, by combining the spatial resolution of InSAR with the temporal resolution of seismology, to decipher the detailed history of a large, clustered earthquake sequence.

2.2 Setting of the 2003 Siberian Altai earthquakes

The 2003 earthquake and its aftershocks struck the interior part of the north-western Altai, just south-west of the Chuya and Kurai intermontane depressions (Fig. 2.1). The Chuya depression contains a good Cenozoic stratigraphic record, which has been used to infer its origins as an extensional basin in the Oligocene and Pliocene, and subsequent inversion along bounding thrusts starting in the late Pliocene (Delvaux et al., 1995). The clearest of these bounding faults, on Landsat images and in the topography, is the Kurai fault zone, which is described as undergoing sinistral transpressional deformation (Delvaux et al., 1995). Within the two depressions themselves several late Cenozoic faults have been mapped; palaeoseismological work has revealed that some of these faults ruptured in large earthquakes during the Holocene (Devyatkin, 2000; Rogozhin et al., 1998a,b). Nevertheless, the faults on which the 2003 earthquakes occurred had not previously been recognized.

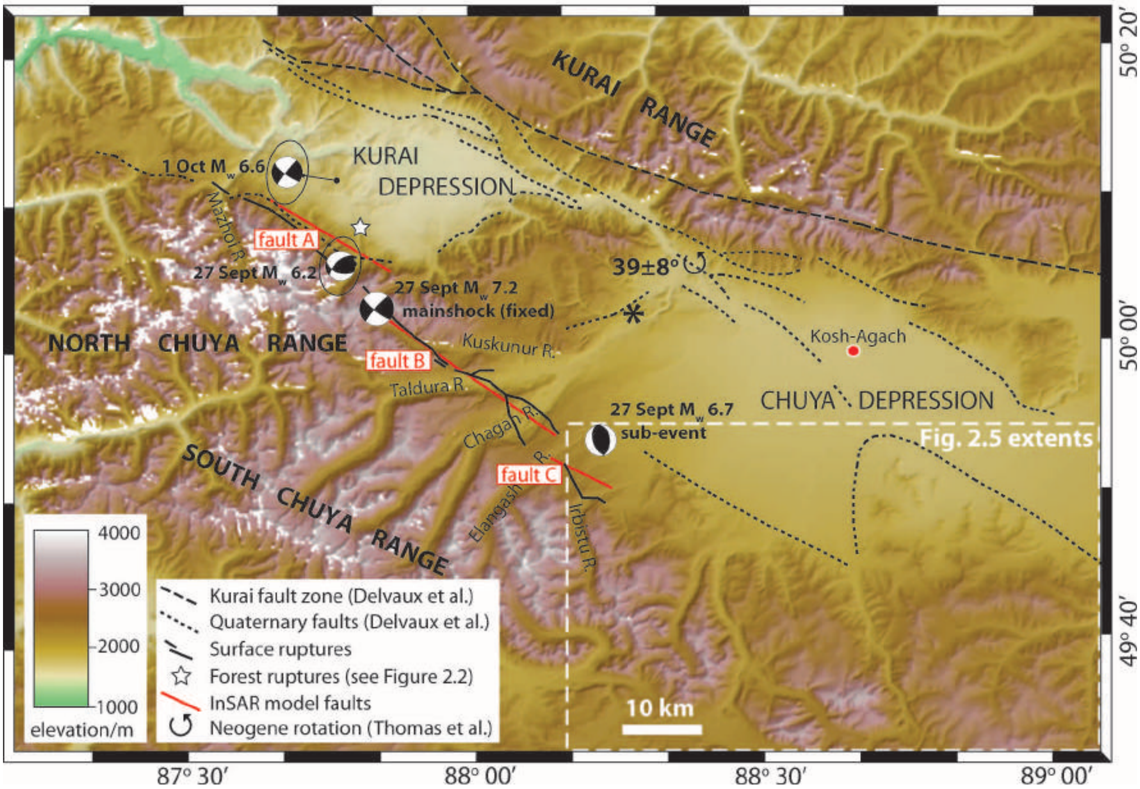

Figure 2.1: Shaded Shuttle Radar Topographic Mission (SRTM) digital topography of the epicentral region of the 2003 Siberian Altai earthquakes, in the local UTM zone (45) projection. The location of this map is shown as a blue, dashed box on Fig. 1.5. The focal mechanisms are my bodywave solutions for the four M_w 6.2–7.2 events. The 27 September M_w 7.2 mainshock is plotted in the position given in the updated version of the Engdahl et al. (1998) catalogue. Relative locations between this event and the 27 September M_w 6.2 and 1 October M_w 6.6 aftershocks were calculated using the Joint Hypocentral Determination (JHD) method (Douglas, 1967; Dewey, 1972). For the latter two events, arrows connect hypocentres from the updated version of the Engdahl et al. (1998) catalogue to 90% confidence ellipses, relative to the fixed mainshock, attained by the JHD method. Meanwhile the 27 September M_w 6.7 sub-event is plotted in a fixed location, 32km ESE of the mainshock (see Section 2.4.3); its minimum-misfit location 32 km E of the mainshock (marked with an asterisk) does not correspond with any significant interferometric deformation. Also shown are ruptures of the 2003 earthquakes mapped in the field, the surface traces of my InSAR model faults, and other Quaternary faults mapped in the area (Delvaux et al., 1995). The circular arrow shows where anticlockwise paleomagnetic rotations were measured within Miocene–Pliocene sediments ((Thomas et al., 2002)); also marked is the Kurai fault zone, described in the same study as sinistral transpressional (see Discussion).

The Chuya depression was also the focus of a paleomagnetic study in which 39° ± 8 anticlockwise rotations were measured in middle Miocene to early Pliocene sediments (Thomas et al., 2002). These measurements were taken just ∼30 km from the 2003 earthquakes, in the north-west part of the basin (Fig. 2.1). It has been proposed that ∼NW striking dextral strike-slip faults accommodate the NNE–SSW shortening across the Altai by rotating anticlockwise about vertical axes over time (Baljinnyam et al., 1993; Bayasgalan et al., 1999a, 2005). So far, the Thomas et al. (2002) study is the only direct evidence that rotations do indeed occur in the Altai.

The first and largest of the 2003 earthquakes (M_w 7.2) happened on 27 September at 11:33 GMT, 17:33 local time. It was felt throughout southern Siberia and in much of Kazakhstan, as far away as Almaty, more than 1000 km to the south-west. Reports vary as to the extent of the resulting damage. It appears not to have directly led to a loss of life (unconfirmed reports claim 3 people died from heart attacks) or a great number of injuries, but according to some reports it left ∼1800 homeless in a number of villages in the Chuya and Kurai depressions. It also triggered landsliding in the mountains south of these basins, and flooding of the Chuya river. The first large aftershock (M_w 6.2) struck at 18:52 GMT on the same day, and a second major aftershock (M_w 6.6) followed on 1 October at 01:03 GMT. The M_w 6.6 event caused further damage to local villages and like the first earthquake was felt over a large part of southern Siberia. Several smaller events occurred in the following weeks, including six earthquakes of M_w 5.0–5.2. Hypocentres for all the $M_w > 5.0$ events are available in the updated version of the Engdahl et al. (1998) catalogue. The M_w 7.2 hypocentre is located in the mountains just south of the Kurai depression, with the two largest aftershocks ∼6 km (M_w 6.2) and ∼17 km (M_w 6.6) to the NNW (Fig. 2.1). Most of the M_w ∼5 aftershocks are also placed in or close to the Kurai depression, with the exception of one event in the southern Chuya depression.

2.3 Fieldwork and Landsat Imagery

Field-based mapping of surface deformation revealed three principal sections of earthquake ruptures (Fig. 2.1). In the western part of the fault zone, ruptures were mapped across the southern Kurai depression; it is likely that some of the deformation in this section was missed due to the dense forest vegetation in this area. In the central part, Eugene Rogozhin mapped deformation between the Kuskunur and Chagan valleys in the SW Chuya depression; this work was undertaken immediately after the earthquakes and is already published in Rogozhin et al. (2003). I later revisited this same section of surface faulting. Finally, further east in the SW Chuya depression, Eugene Rogozhin mapped ruptures between the Elangash and Irbistu rivers.

In the southern Kurai depression I used the InSAR measurements (Section 2.4.1) as a guide to search for earthquake ruptures. A heavily forested, ∼5 km wide incoherent area divides positive and negative line-of-sight displacements along the southern flank of the depression. Traversing this region, I found a number of en echelon, left-stepping extensional fissures (Fig. 2.2). Individual fissures trended ∼N–S and were up to ∼50 m long; they displayed vertical offsets of up to ∼50 cm and openings of up to ∼40 cm. The orientation of these fissures is consistent with right-lateral strike-slip on a ∼NW striking fault. Unfortunately I could only follow them for ∼3 km along the overall strike of the fault zone before they were lost in the dense forest vegetation, and it is likely that more ruptures are present further NW and SE. The location of these ruptures is plotted as a star on Fig. 2.1 (and subsequent figures). Ruptures are also present further west, along the northern flank of the North Chuya range. These were mapped as far west as the Mazhoi valley, where Eugene Rogozhin measured oblique displacements with a dextral component of ∼20 cm and a vertical component of ∼20 cm, up to the SW.

The most continuous section of ruptures, described already in Rogozhin et al.

Figure 2.2: Field photos of earthquake ruptures in the southern Kurai depression, denoted by a star in Figures 2.1, 2.6 & 2.8. (a) 50° 08.273' N 87° 48.577' E, facing 030°. The fissure strikes 030° and is offset vertically by 40 cm, up to the SE. (b) 50° 08.342' N 87° 48.582' E, facing 180°. These fissures strike N–S along a small ridge. (c) Detail of a fissure on the same ridge as (b) with a pen for scale, pointing N (up). The fissure is 35 cm wide and offset vertically by 10 cm, up to the E. (d) Photo at 50° 08.532' N 87° 48.632' E, facing 005°, with notebook for scale. This fissure strikes ∼NW for 30 m along the western flank of another small ridge.

(2003), lies in the far south-west of the Chuya depression (Fig. 2.1). This fault section does not follow a topographic break of any sort, but cuts obliquely across the Kuskunur, Taldura and Chagan valleys and the spurs between them; its overall strike is 300° and its length is about 30 km. In the main part, these ruptures consist of spectacular ∼N–S striking extension fissures, up to 100 m long, 10 m wide and 3 m deep, and sometimes showing ∼0.5 m dextral offsets. Smaller ∼E–W striking pressure ridges (or push-ups), up to 50 m long and 2 m high, are also present. Rather than forming a neat 'zig-zag' pattern, these fissures and ridges are scattered across a zone up to 100 m wide (Fig. 2.3). The orientation of this zone and the en echelon arrangement of extensional and compressional features again suggests an overall mechanism of right-lateral strike-slip on a NW–SE-striking fault.

In one place, on a high plateau between the Kuskunur and Taldura rivers, the ruptures can be followed more or less uninterrupted for ∼4 km. Here, I used the trace of the fault across the topography to estimate the dip of the fault (Fig. 2.4). Following the fault from a high saddle south-east of the plateau, down to and across the plateau itself, and up another saddle further north-west, I measured GPS positions and elevations of the earthquake ruptures. The plane defined by these x, y, z coordinates strikes 295° and dips 55–85° NE. Although there is a large uncertainty in the absolute value of dip (due to the ruptures being distributed over a ∼100 m wide zone on the plateau), the field evidence does at least support a fault plane that dips to the north-east, rather than to the south-west. However, it should be noted that a curved fault plane that changes strike as it crosses the plateau could have produced the same pattern of ruptures, without requiring a dip to the north-east.

Finally, in the far eastern part of the fault zone Eugene Rogozhin observed ruptures on the spur between the Elangash and Irbistu rivers. These display up to ∼1.2 m dextral offset and uplift of the north-east side by ∼0.65 m. In map view the trace of these ruptures is kinked, one segment striking ∼N–S and another striking ∼E–W.

In order to identify geomorphic indicators of active faulting, I also studied Landsat images of the fault zone. Interestingly, there are no obvious features in the immediate vicinity of the ruptures mapped in the field (which explains why the fault

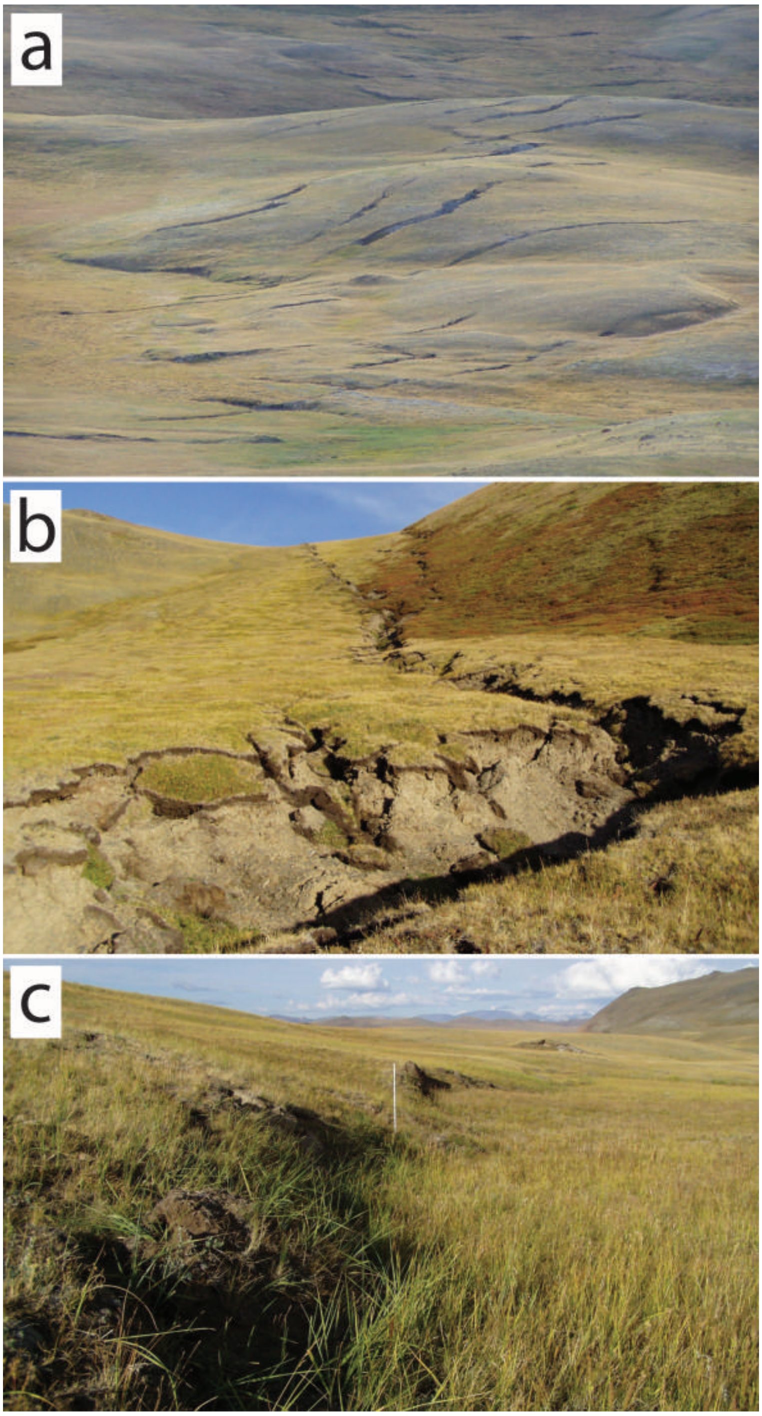

Figure 2.3: Field photos of earthquake ruptures in the southwestern Chuya depression. (a) Photograph taken at 49° 59.067' N E87° 58.733' E, facing ∼NW, showing earthquake ruptures on the plateau between the Kuskunur and Taldura rivers. Here they consist of ∼N–S tension fissures and ∼E–W pressure ridges scattered across a zone up to ∼100 m wide. (b) Photograph taken from the same point as (a) but facing ∼SE. In the foreground the rupture consists of a single fissure, about 10 m wide and 5 m deep. In the background the rupture splits into two strands as it crosses a prominent saddle. (c) Close-up view of an ENE-trending pressure ridge, taken at 49° 59.175' N 87° 58.047' E, facing 060°, with a 1 m ruler for scale.

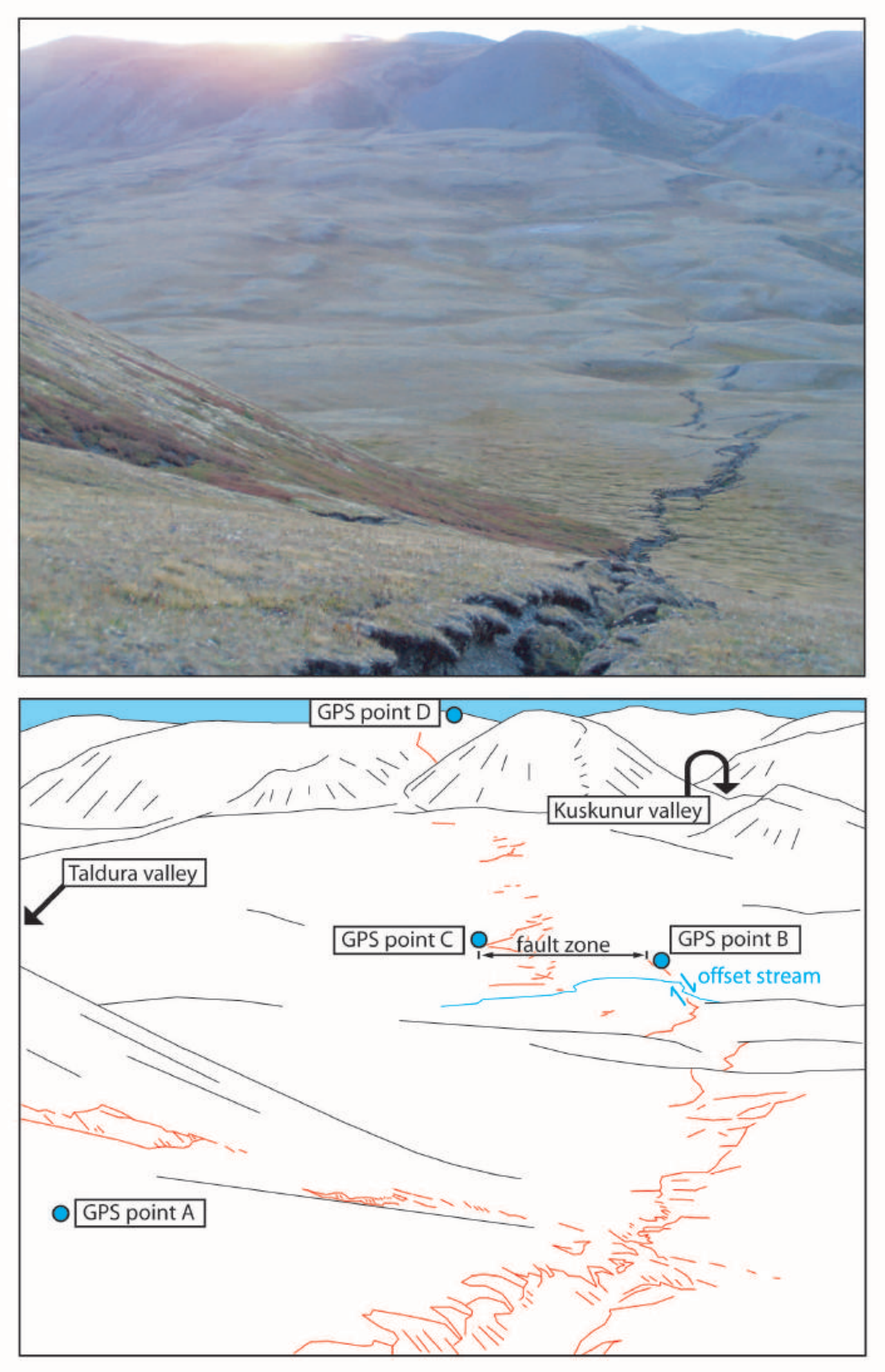

Figure 2.4: Field photo of earthquake ruptures on the plateau between the Kuskunur and Taldura rivers, taken from 49° 58.856' N 87° 59.223' E and facing 285°. Annotations are given on the sketch below the photo. The ruptures make a broad arc as they cross the plateau and rise to high saddles (at GPS points A and D) on either side. Such a pattern could be produced by a planar fault dipping to the right in the picture (to the NNE). On the plateau there is no single strand to the ruptures, which instead form en echelon fissures and push-ups over a ∼100 m wide zone between GPS points B and C. As a result I can calculate only a range of dip estimates, between 55° NNE (using the triangle ABD) and 85° NNE (triangle ACD).

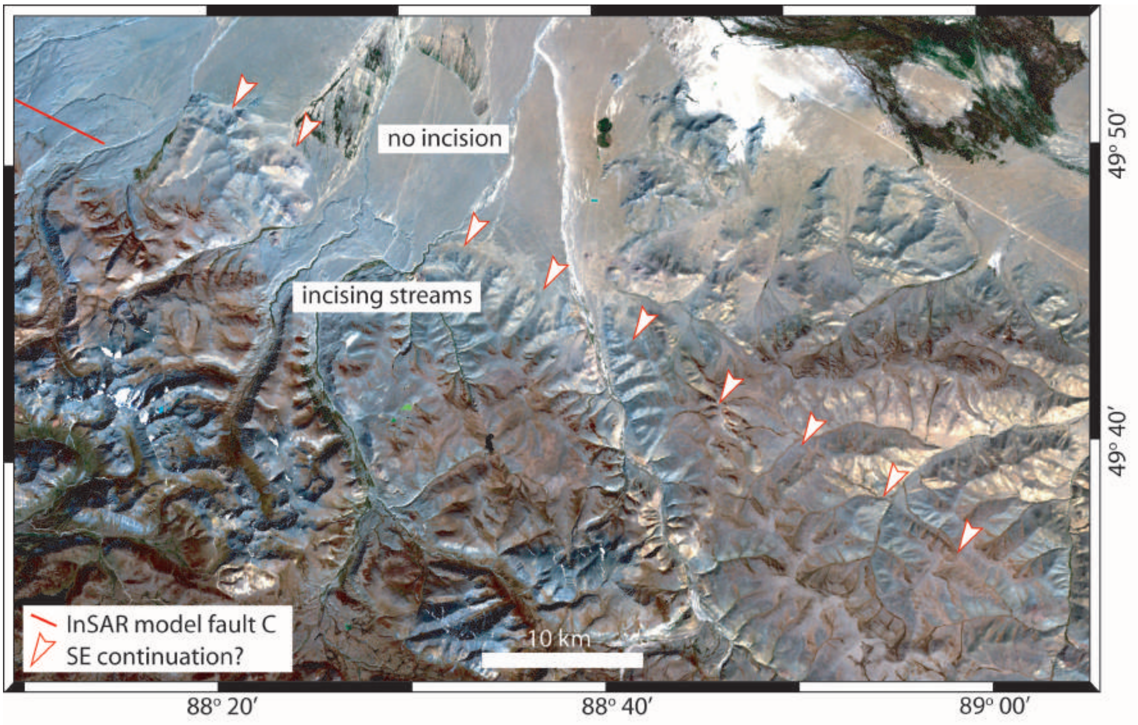

Figure 2.5: Landsat image (RGB 321) of the southern Chuya depression, south-east of the surface ruptures and InSAR model faults. A possible continuation to the active fault is picked out by arrows. In the north-west part of the map, the fault follows a N-facing scarp and streams only incise to the south-west. Further south-east, the fault follows a number of very straight valleys.

had not previously been mapped). However, following their strike to the south-east, a distinct ∼50 km long lineation is visible, perhaps indicating the continuation of the active faulting which ruptured in the 2003 earthquakes (Fig. 2.5). In the north-west, it consists of a straight, north-facing scarp dividing hills to the south-west from a low, flat plain to the north-east (the southernmost part of the Chuya depression). Some streams appear to be incising south-west of the scarp, but stop doing so to the north-east, suggesting active uplift of the south-west side of the fault. If there is a reverse component to this part of the fault, this would indicate a fault dip to the south-west. Further south-east, the lineation enters hilly ground and is marked out by a series of very straight valleys.

2.4 Earthquake source parameters

In this section I investigate the source parameters of the 27 September 2003 earthquake and its two largest aftershocks using Synthetic Aperture Radar Interferometry (InSAR) and seismology.

2.4.1 Synthetic Aperture Radar Interferometry (InSAR)

A brief introduction to InSAR

Since pioneering studies fifteen to twenty years ago (e.g. Gabriel et al., 1989; Massonnet et al., 1993), InSAR has developed into a powerful tool for studying the deformation of the Earth's surface. I begin this section with a short summary of the technique; more detailed reviews of InSAR and its applications are available elsewhere (e.g. Gens & Van Genderen, 1996; Massonnet & Feigl, 1998; Bürgmann et al., 2000).

Like conventional radar, Synthetic Aperture Radar (SAR) derives information about a target by illuminating it with electromagnetic waves of microwave frequency and measuring the back-scattered signal. SAR satellites operate at altitudes of around 800 km, and signal processing techniques – in which the returns of consecutive radar pulses from the same patch of ground are combined to simulate an antenna many times larger than the real one – must be used to achieve a high spatial resolution at the Earth's surface – typically $\sim$4 m in along-track ('azimuth') direction and $\sim$20 m in the cross-track ('range') direction.

SAR satellites measure the amplitude and phase of radiation back-scattered from each target pixel. The phase signal from a given pixel depends on its back-scattering characteristics (produced by the individual point scatterers within that pixel) and, taken on its own, is effectively random. However, by differencing two SAR images of the same area, the random phase contribution from each pixel is cancelled and a coherent interference signal can be observed.

If the two images are taken from slightly different viewpoints, the pattern of interference provides information about the range between the satellite and ground, and thus the topography. In February 2000, the Shuttle Radar Topographic Mission (SRTM) used this principle to produce a 3 arcsecond ($\sim$90 m) resolution digital elevation model (DEM) covering the vast majority of the Earth's land surface between 56° S and 60° N (for a detailed review of this dataset, see Farr et al., 2007). If, on the other hand, the two images are acquired with the same viewing geometry but at different times, then the interference pattern reflects a change in the path length between satellite and target pixel during this interval – in other words, the displacement of the target toward or away from the satellite (or 'line-of-sight' displacement). In reality, there is usually a significant difference (or 'baseline separation') between the position of the SAR antenna for the first and second images. As a result, most interferograms contain both topographic and surface displacement effects; to view the latter, the topographic signal must first be removed using a DEM (today, SRTM is widely used for this step).

Interferograms are usually displayed in cycles of colour, with each cycle (or fringe) representing a phase change of 2π radians ($\sim$2.8 cm, for the most commonly-used InSAR satellites). These *modulo* 2π phase measurements can be converted into continuous line-of-sight displacements by adding up these fringes, a process known as 'unwrapping'. If possible, data from both ascending (moving north) and descending (moving south) satellite orbit tracks are used, thus providing an additional component of the displacement vector.

There are a number of factors which can limit the effectiveness of InSAR. Firstly, the back-scattering properties of the pixels must not change significantly between the first image and the second. This is problematic in areas of dense vegetation, seasonal snow cover or landsliding, as well as for interferograms that span long time intervals. Secondly, even if the individual point scatterers do not change, their summed response can be significantly altered if there is too large a change in the viewing geometry between one image and the other. This limits the use of InSAR to image pairs with perpendicular baselines of up to about 200 m (and even then, the problem can persist in areas of steep terrain). Thirdly, if the phase difference across the width of a pixel is greater than 2π then the phase will not appear to vary continuously between adjacent pixels. In interferograms spanning large earthquakes, this can prevent displacements from being measured close to the location of active faulting.

Even if the interference pattern is coherent, the Earth's atmosphere provides a final limitation upon the accurate measurement of ground displacements. Atmospheric path delays often produce apparent displacements of a few millimeters (up to a maximum of a few centimeters), reducing the precision of ground displacements from millimetre to centimetre-level.

Application to the Siberian Altai earthquakes

At present the principal satellite acquiring regular SAR measurements is the ESA Envisat platform, which was launched in 2002 but became fully operational only in 2003. The Siberian Altai earthquake was the first large continental earthquake for which prior Envisat Advanced Synthetic Aperture Radar (ASAR) data was available and interferometry possible.

Using the Envisat ASAR data itemised in Table 2.1, I produce three adjacent, descending track interferograms, each with a centre-scene incidence angle of 23° measured from the vertical (beam mode IS2). Unfortunately, there is no suitable ascending-track data for an additional component of ground displacements. Interferograms are constructed with the JPL/Caltech Repeat Orbit Interferometry Package (ROI_PAC) processing software (Rosen et al., 2004). Delft precise orbits are used to make an initial correction of the orbital contribution to phase (Scharroo & Viser, 1998), and the topographic phase contribution is removed using the 3-arcsecond (90 m) resolution SRTM DEM (Farr & Kobrick, 2000). Interferograms are then cleaned with a power spectrum filter (Goldstein & Werner, 1998) and unwrapped using the branch-cut unwrapper in ROI_PAC (Goldstein et al., 1988). Because the deformation signal covers a large proportion of the interferograms – and so as not to risk removing some of this signal – I choose not to make further orbital corrections at this point (although I do allow orbital adjustments to be made when modelling the earthquakes, later on).

The interferograms are shown in Fig. 2.6a, overlaid on one other, and unwrapped and then rewrapped such that adjacent fringes differ by 10 cm in line-of-sight displacement. All three interferograms span the whole earthquake sequence and so cannot be used to distinguish between different aftershocks in time. Correlation is best in the low-lying, flat and sparsely vegetated Chuya depression, and in parts of the Kurai depression. However, the southern part of the Kurai depression is heavily forested and suffers from temporal decorrelation, while the mountains south of both depressions are very steep and display only patchy coherence. As a result, and with the added effects of steep deformation gradients, coseismic ground-shaking and land-sliding near the fault, the precise location of faulting within this area cannot be ascertained. Nevertheless, a ~5 km wide, ~60 km long strip of incoherence can be made out striking north-west across the southern margin of the Chuya and Kurai depressions; this strip separates line-of-sight displacements that are towards the satellite from those that are away from the satellite, and thus gives a rough indication of where the surface faulting must lie.

	Pass	*Track*	*Frame*	*Date 1*	*Orbit 1*	*Date 2*	*Orbit 2*	Δt *(days)*	$B_\perp$ *(m)*	H_a *(m)*
Western	Desc.	434	2596	11-Sep-03	08003	22-Jul-04	12512	315	50	189
Central	Desc.	162	2601	23-Aug-03	07731	06-Dec-03	09234	105	166	57
Eastern	Desc.	391	2600	08-Sep-03	07960	19-Jul-04	12469	315	130	73

Table 2.1: Summary of Envisat data used to produce interferograms. The first image of each pair was acquired on Date 1, and the second on Date 2, separated by Δt days. $B_\perp$ is the perpendicular baseline between the positions of the SAR antenna for the first and second image acquisitions (in other words, the component of the baseline separation perpendicular to the look direction). H_a is the altitude of ambiguity, which is the vertical error in the DEM that would result in a single interference fringe; because SRTM heights are accurate to better than ~9 m (Rodriguez et al., 2006), any remaining topographic signal in the interferograms will be negligible.

On the north-east side of this fault zone, line-of-sight displacements are towards the satellite and form a two-lobed pattern. The south-eastern lobe, in the Chuya depression, contains the largest line-of-sight displacements, up to 1.9 m. In the north-western lobe, in the Kurai depression, displacements reach 0.3 m, while the area between the two lobes contains displacements of up to 0.8 m. South-west of the fault zone there is much less interferometric data, something I must bear in mind when modelling the earthquakes. Line-of-sight displacements in this part of the interferogram are away from the satellite and up to 0.3 m in magnitude. The overall pattern is consistent with dextral strike-slip, or uplift to the north-east and subsidence to the south-west, on a fault plane striking NW–SE. In addition, the greater number and closer spacing of fringes north-east of the faulting (a feature shown in more detail in Fig. 2.7) suggests that the fault plane dips to the north-east.

To prepare the data for modelling I first resample each interferogram, using a quadtree decomposition algorithm to concentrate sampling in areas of high phase gradients (e.g. Jónsson et al., 2002). This reduces the size of each dataset from an initial $\sim$2 million datapoints to a more manageable $\sim$2000. Using the formulation of (Okada, 1985), I represent faults as rectangular dislocations in an elastic half-space, with an elastic shear modulus of 3.23×10^{10} Pa and a Poisson ratio of 0.25. I solve for the strike, dip, rake, slip, latitude, longitude, length, and top and bottom depths of the faults, systematically varying these parameters and finding a global minimum misfit using a Powell minimization algorithm with multiple Monte Carlo restarts to avoid local minima (Wright et al., 1999). In addition to the fault plane parameters, I also solve for a static shift in the measured displacements (to account for ambiguities in the zero-displacement level) and for gradients of displacement in the N–S and E–W directions (to account for any residual orbital phase ramps).

I find that a single fault plane cannot reproduce the interferometric data. This result is unsurprising for two reasons. Firstly, it is impossible to draw a single straight

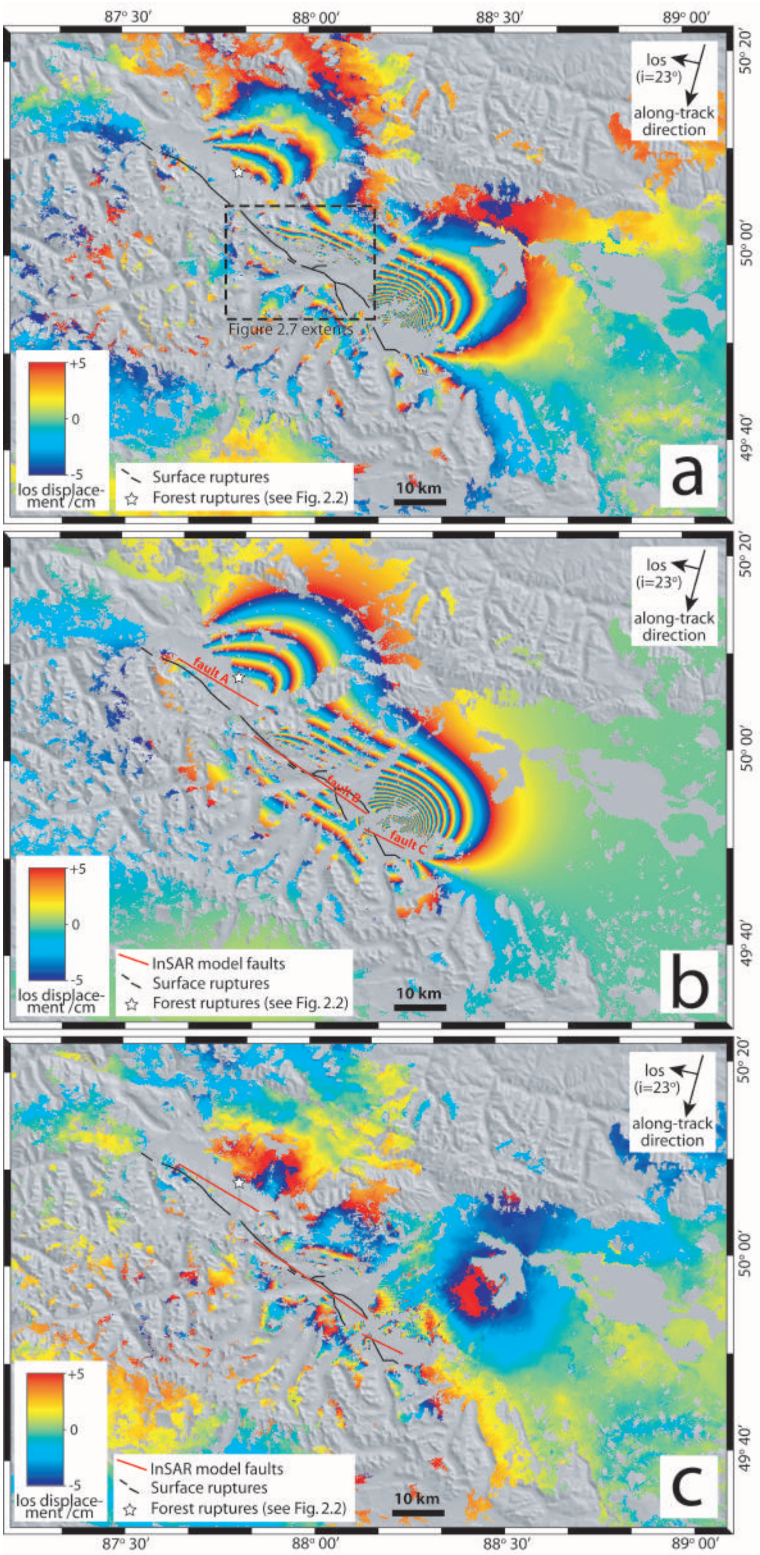

Figure 2.6: (a) Interferogram, unwrapped and then re-wrapped such that adjacent fringes differ by 10 cm in line-of-sight displacement. The figure actually contains three separate interferograms, each only covering part of the epicentral region, but because these have very similar line-of-sight vectors I plot them together. They are overlaid on shaded SRTM topography. (b) Model and (c) residual interferograms, also shown wrapped such that adjacent fringes differ by 10 cm in line-of-sight displacement.

line through the fault zone which can cleanly divide areas of positive displacements from areas of negative ones. Secondly, uniform slip on a single plane cannot reproduce the distinctive double-lobed pattern of positive displacements north-east of the fault.

Next, I experiment inverting the data using different numbers of faults, with all parameters free to vary. My preferred model contains three faults; this model is significantly better a two-fault model, but is not much further improved by the addition of a fourth fault. In this three-fault model, one segment accounts for the north-western lobe of positive displacements, a second segment accounts for the central portion, and a third the south-eastern lobe. The model parameters are given in Table 2.2, where (and from here on in) the north-western model fault segment is called fault A, the central segment B and the south-eastern segment C. Each fault segment has a moment of between $\sim$10 and $\sim 14 \times 10^{18}$ Nm, with the total moment ($\sim 39 \times 10^{18}$ Nm) equivalent to a M_w 7.0 earthquake. The strikes (295–305°) and dips (57–70° NE) of the three faults are similar, and each involves oblique slip with right-lateral and reverse components. However, the reverse component on fault C is much higher than on the other two faults, lying closer to pure dip-slip than pure strike-slip. Because the model faults dip NE, the reverse components result in uplift to the north-east and subsidence to the south-west of the faults.

Standard deviations in the model parameters are also given in Table 2.2. These were estimated by inverting 100 datasets perturbed by realistic noise (with the same statistical properties as the atmospheric noise present in undeformed parts of the interferograms), one fault at a time (Wright et al., 2003; Parsons et al., 2006). Model source parameters for faults B and C are well constrained, partly because they are covered by two interferograms (tracks 162 and 391). In contrast, fault A is only covered by the western interferogram (track 434) and its 1σ errors are greater.

The model interferogram is shown in Fig. 2.6b and the residuals (a map of the difference between real and model interferograms) in Fig. 2.6c. Like the interferograms

	Fault A	*Fault B*	*Fault C*
Strike	300.6° ± 2.2	304.7° ± 0.3	295.9° ± 0.3
Dip	59.5° ± 3.4	70.3° ± 0.5	56.6° ± 0.3
Rake	155.0° ± 6.5	140.1° ± 1.8	101.3° ± 1.3
Slip (m)	1.06 ± 0.14	1.54 ± 0.03	4.37 ± 0.04
Top (km)	0.7 ± 0.4	0.0 ± 0.0	1.3 ± 0.1
Eastings (km)	553.7 ± 0.6	571.4 ± 0.1	585.5 ± 0.1
Northings (km)	5553.9 ± 0.5	5536.2 ± 0.1	5524.0 ± 0.1
Bottom (km)	15.3 ± 1.1	10.4 ± 0.2	11.1 ± 0.1
Length (km)	17.6 ± 0.7	26.3 ± 0.3	8.5 ± 0.1
Moment (Nm)	$10.2 \pm 0.7 \times 10^{18}$	$14.4 \pm 0.2 \times 10^{18}$	$14.0 \pm 0.2 \times 10^{18}$
M_w	6.67	6.77	6.76

Table 2.2: Fault plane parameters from the inversion of interferometric data, shown with 1σ errors. *Fault A* is the north-western segment, *fault B* the central segment and *fault C* the south-eastern segment in the model. *Eastings* and *Northings* represent the centre of the fault plane projected to the surface, and are in UTM zone 45 co-ordinates. *Top* and *Bottom* refer to the top and bottom depths of the fault plane.

in Fig. 2.6a, they are shown wrapped such that adjacent fringes differ in line-of-sight displacement by 10 cm. There are few residual fringes, except for two areas; very close to the western end of fault C, and along the eastern half of fault B. In both cases, a fault whose slip could vary along strike, rather than ending abruptly as in the uniform slip model, might account for the residuals.

The surface traces of my model faults agree very well with the location of mapped ruptures (Fig. 2.6b). The best fit is between fault B and ruptures mapped in the far western Chuya depression. Fault A's location lies in between the two sets of surface ruptures mapped in the southern Kurai depression, around 2–3 km from either one, and the location of the mapped ruptures may reflect the splitting of this fault into parallel strands at shallow depths. Fault C's location lies very close to ruptures mapped SE of the Elangash river, although the kinked geometry of these ruptures is not required for my model to successfully reproduce the interferometric data.

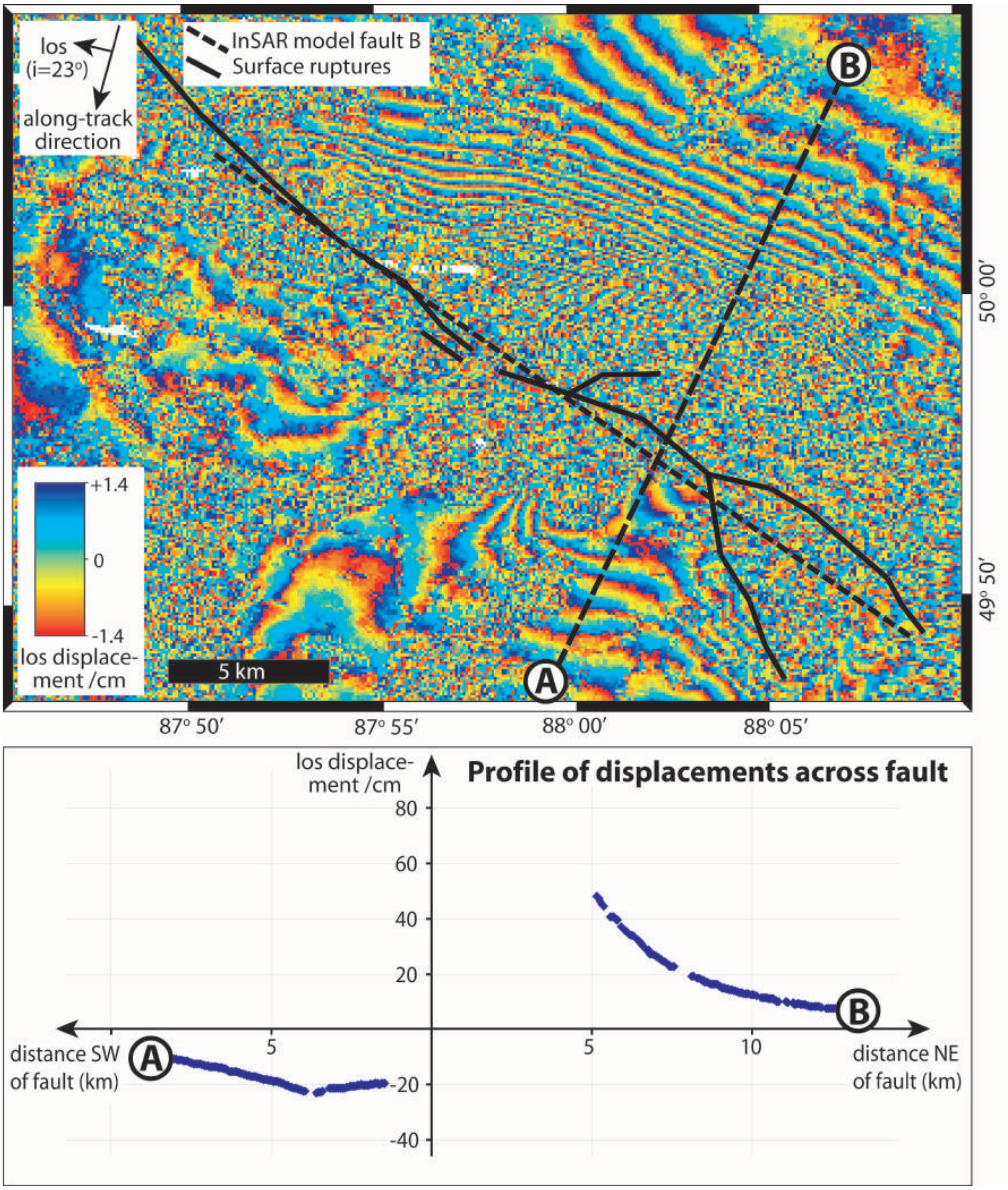

Figure 2.7: Detail of part of the western interferogram, before filtering and unwrapping (adjacent fringes differing by 2.8 cm in line-of-sight displacement). The amplitude of line-of-sight diplacements north-east of the faulting is much greater than that to the south-west; this is demonstrated on the profile below the interferogram, which shows unwrapped line-of-sight displacements along a transect from A to B. The asymmetry of this profile is consistent with a fault that dips to the north-east.

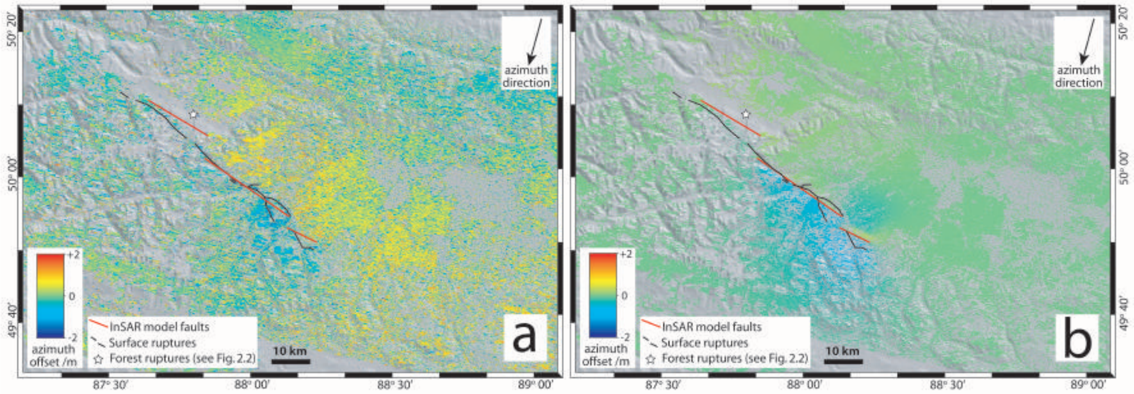

Figure 2.8: (a) Azimuth offsets, plotted over shaded SRTM topography. (b) Azimuth offsets predicted by the three fault InSAR model.

2.4.2 Azimuth offsets

In addition to the ASAR phase measurements used in interferometry, the amplitudes of radar returns can also be used to study ground deformation (e.g. Michel et al., 1999). Azimuth offsets are the positional shifts required to align amplitude pixels in the along-track direction for a pair of SAR images, and can be calculated to sub-pixel precision. These horizontally-resolved displacements provide a further constraint on ground motion, independent of the line-of-sight phase changes measured by InSAR.

I measure azimuth offsets for the three Envisat ASAR pairs used to calculate the interferograms. The along-track displacements are shown in Fig. 2.8a, next to those predicted by my InSAR model (Fig. 2.8b). The data are noisy, due to false matches between slave and master pixels, and I cannot invert them as I did the interferograms. However, the azimuth offsets do not suffer from patchy coherence and the location of the faulting can be seen relatively precisely. I find that jumps in the values of azimuth offset agree with the location of faulting predicted by my InSAR model and mapped in the field.

2.4.3 Teleseismic bodywave modelling and earthquake relocations

The M_w 7.2 earthquake and the M_w 6.2 and M_w 6.6 aftershocks were widely recorded by stations of the Global Digital Seismic Network (Butler et al., 2004). I consider only those waveforms recorded teleseismically (in the distance range 30°–90°) in order to avoid complications from the Earth's crust and outer core. For each of the three events, I use the MT5 program (Zwick et al., 1994) to invert P and SH waveforms by a weighted least-squares method (McCaffrey & Abers, 1988). Following the procedure of (Molnar & Lyon-Caen, 1989) I obtain the strike, dip, rake, centroid depth, seismic moment and source-time function of the best double-couple solutions. The focal mechanisms are shown in Figs 2.9, 11 & 12; the source parameters are given in Table 2.3 alongside those listed in the Harvard CMT catalogue, for comparison.

Date	*Time*	*Study*	*Strike1*	*Dip1*	*Rake1*	*Strike2*	*Dip2*	*Rake2*	*Depth*	*Moment (Nm)*	M_w
27 Sep.	11:33:35	Harvard CMT	*131°*	*71°*	*158°*	*228°*	*70°*	*20°*	*15 km*	93.8×10^{18}	*7.2*
		this study	132°	82°	173°	223°	83°	7°	18 km	70.7×10^{18}	7.2
	+10 secs	this study	163°	51°	82°	356°	40°	98°	6 km	16.2×10^{18}	6.7
27 Sep.	18:52:47	Harvard CMT	*117°*	*67°*	*156°*	*217°*	*68°*	*25°*	*15 km*	4.5×10^{18}	*6.4*
		this study	111°	51°	143°	226°	62°	45°	12 km	2.5×10^{18}	6.2
01 Oct.	01:03:25	Harvard CMT	*129°*	*85°*	*157°*	*221°*	*67°*	*5°*	*15 km*	11.3×10^{18}	*6.6*
		this study	127°	78°	176°	218°	86°	12°	7 km	8.5×10^{18}	6.6

Table 2.3: Source parameters of the three largest events in the 2003 sequence determined through seismology; the depth listed is the centroid depth. Harvard CMT mechanisms are written in itallic (their centroid depths fixed), whilst those determined by inversion of P and SH bodywaves (Section 2.4.3) are in plain text. Origin times (GMT) are from an updated version of the Engdahl *et al.* (1998) catalogue, with the exception of the 27 September M_w 6.7 sub-event. This was not listed separately in the catalogue and its timing was estimated along with its source parameters in the waveform inversion; its location was fixed relative to the M_w 7.2 mainshock (see text).

For the 27 September M_w 7.2 earthquake, the best fit to the data is achieved when I model it as a double event, the mainshock being followed, 10 seconds later, by a smaller sub-event. I allow the location of the sub-event (the distance and azimuth between sub-event and mainshock) to vary in the inversion. In the minimum misfit solution, the sub-event lies ∼32 km from the mainshock at a bearing of 089° (the asterisk on Fig. 2.1). This places it in an area lacking in significant interferometric deformation (comparing Fig. 2.1 with Fig. 2.6a), so the minimum misfit location is unlikely. By running several inversions for a variety of fixed offsets, I find that the sub-event location is indeed poorly constrained; we see good matches between synthetic and real waveforms for offsets of 25–40 km, over which the azimuth changes from 120° to 088°.

I run another inversion with the sub-event azimuth fixed to 120° and the distance fixed to 32 km; this places the sub-event where I would expect it to plot, given the InSAR model and surface deformation. This model is shown in Fig. 2.9 and is my preferred solution. Waveforms for this model (plotted on the bottom line of Fig. 2.10) are not significantly degraded compared to the minimum misfit solution (middle line), but are significantly better than the best single event model (top line). This demonstrates the importance of including a sub-event; although the sub-event has a negligible effect on SH waveforms (YKW3 and UGM), it considerably improves the fit to the P waveforms (PET, UGM, FURI and DRLN), adding a second peak to the synthetic waveform which matches a peak present in the P-wave data.

The difference in the sub-event mechanism between the minimum misfit solution and my preferred model reflects a broad minimum in the sub-event misfit, with strong trade-offs in strike and depth (and to a lesser extent, rake) with distance and azimuth. A further point of note is that the distance/time between the mainshock and sub-event yields ∼3.2 kms^{-1}, a believable shear wave speed. The timing and position of the sub-event are therefore consistent with rupture initiated by shear

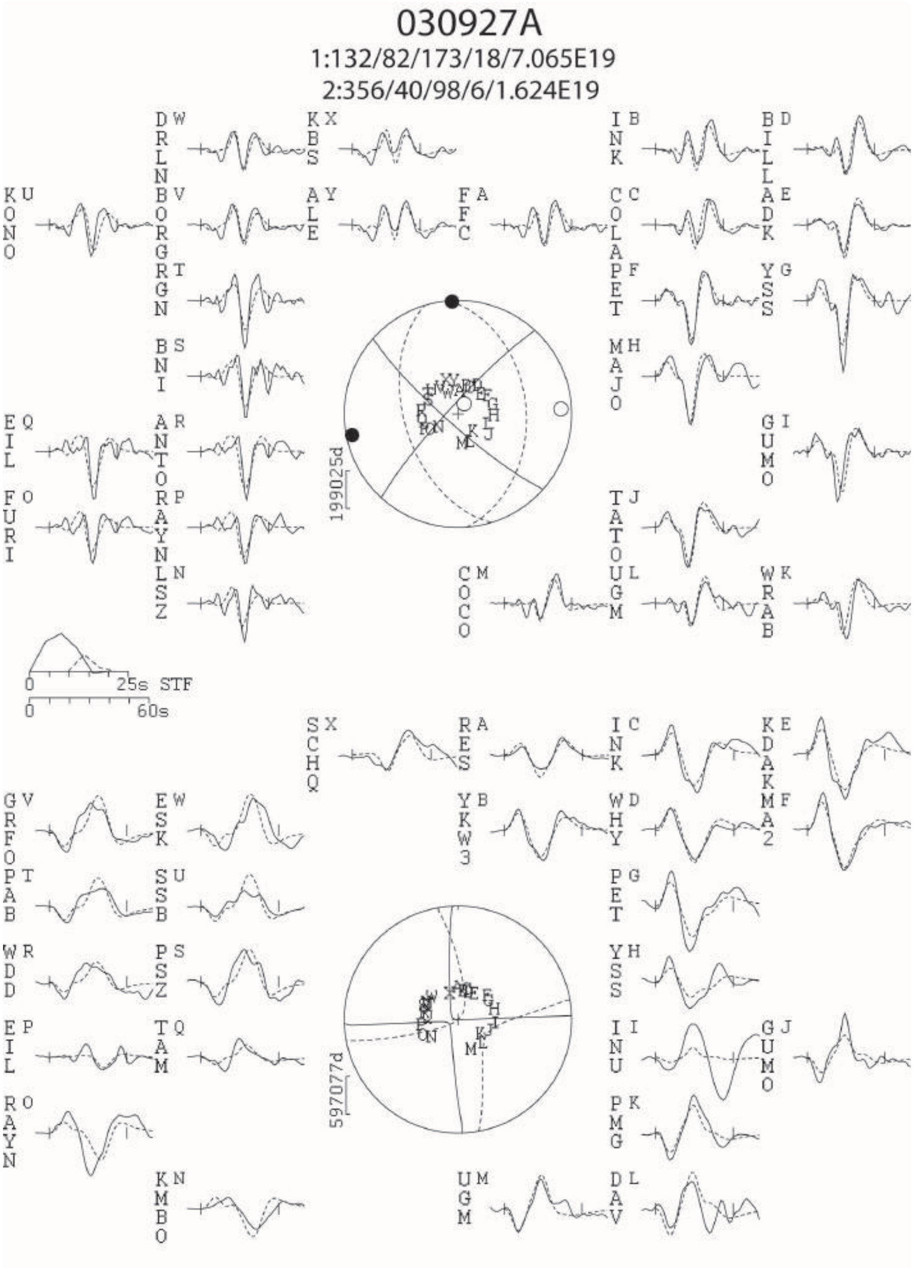

Figure 2.9: Preferred model for the 27 September M_w 7.2 earthquake, calculated by inverting P and SH bodywaves for a point source in a half space of $V_p = 5.9$ ms^{-1} and $V_s = 3.4$ ms^{-1}. A sub-event was included, fixed to a location 32 km from the mainshock at an azimuth of 120° (see text). The focal spheres show P (top) and SH (bottom) nodal planes in lower hemisphere projections; solid nodal planes represent the mainshock and dotted nodal planes represent the sub-event, while the closed and open circles represent the P-axes and T-axes respectively. Numbers beneath the header line are strike, dip, rake, centroid depth (km) and moment (Nm) of the mainshock (1) and sub-event (2). Observed (solid) and synthetic (dashed) waveforms are plotted around the focal spheres; the inversion window is indicated by vertical ticks, station codes are written vertically and station positions denoted by capital letters. The STF is the source time function, and the scalebar below it (in seconds) is that of the waveforms.

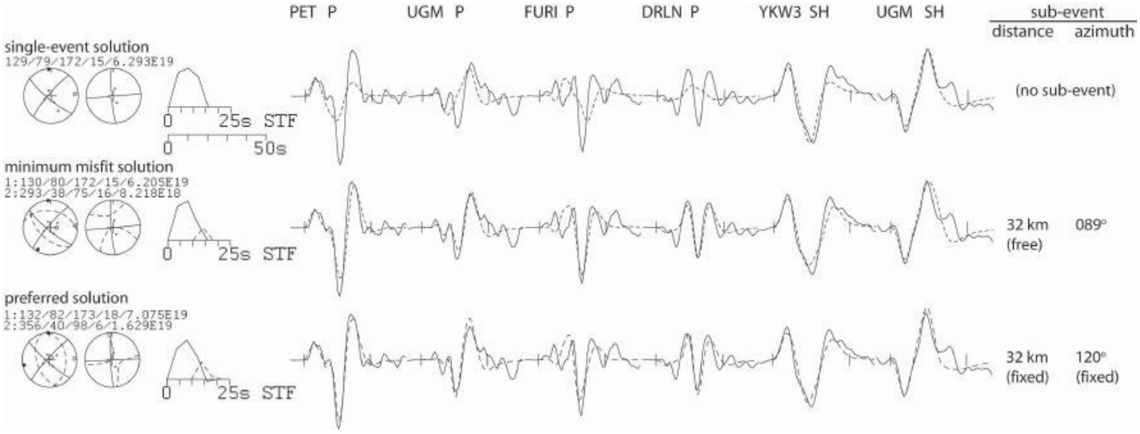

Figure 2.10: Bodywave models of the 27 September M_w 7.2 earthquake, showing the match between real (solid line) and synthetic (dashed line) waveforms for a selection of four P and two SH stations, indicated at the top of the figure. On the left-hand side, each model's P and SH nodal planes are plotted, in lower hemisphere projections and with solid and dashed lines again indicating the mainshock and sub-event respectively. The model's strike, dip, rake, centroid depth (km) and moment (Nm) are written above the focal spheres and the STF (source time function) to the immediate right of them. The top line of waveforms shows the best-fit solution for a single event, while the second line shows the minimum misfit solution, improved with the addition of a sub-event. The bottom line shows my favoured model, in which the sub-event location has been fixed to the location suggested by InSAR measurements and surface ruptures.

waves from the mainshock.

From the fieldwork and InSAR, it is clear that faulting will correspond to nodal planes striking ~NW–SE. The mainshock thus involves mainly right-lateral strike-slip on a fault plane dipping very steeply to the south-west. The sub-event involves mainly reverse motion, with only a small strike-slip component. Both nodal planes strike ~NNW–SSE, with the ENE-dipping plane probably representing the fault (because all interferometric displacements towards the satellite lie north-east of the faulting).

The first large aftershock, also on 27 September, is modelled as a single event (Fig. 2.11). In general there is a good fit between synthetic and observed waveforms, although for stations in the west the amplitudes of the two do not match well. The fault plane again strikes SE and dips to the SW, though less steeply than the largest

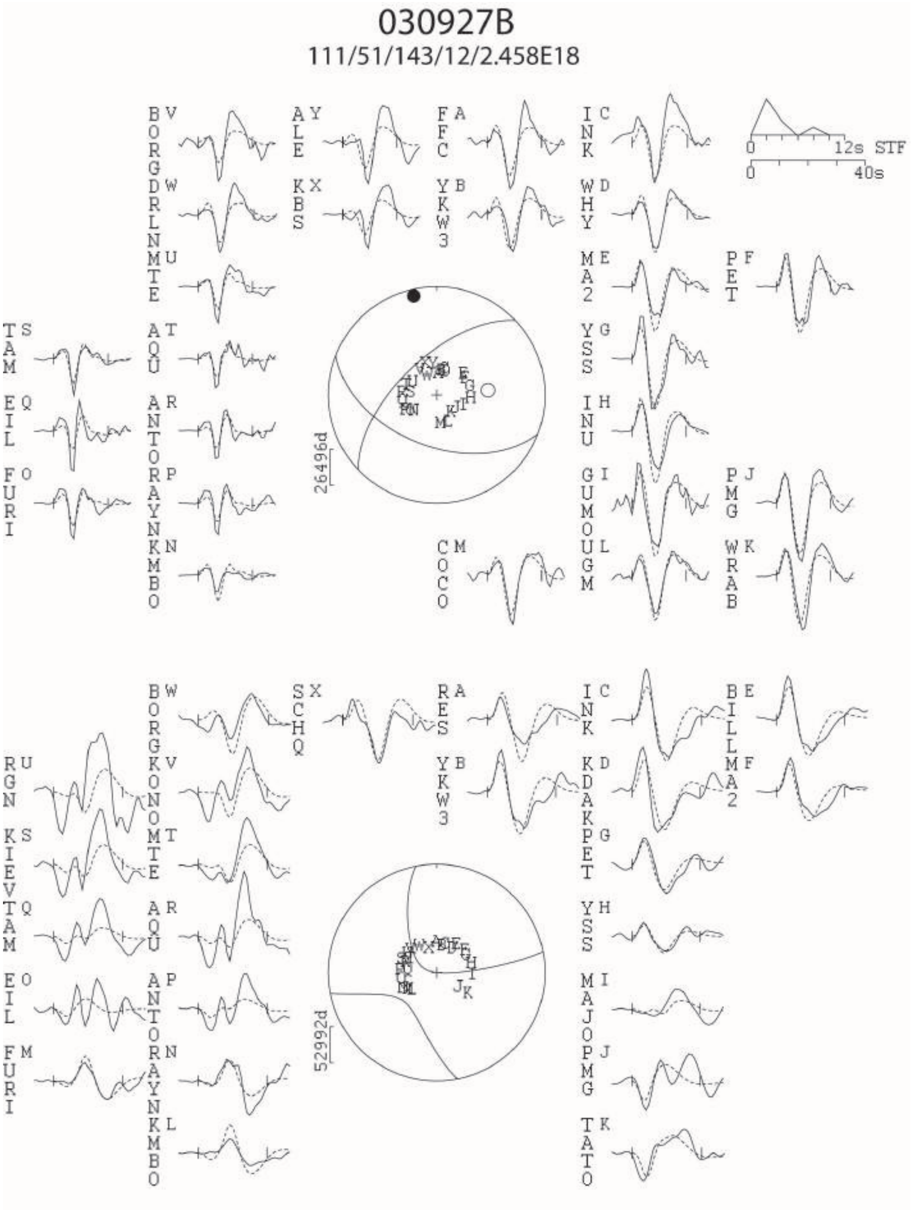

Figure 2.11: Minimum misfit solution for the 27 September M_w 6.2 earthquake. Layout is the same as in Fig. 2.9.

event. The rake is intermediate between right-lateral strike-slip and reverse faulting.

The fit to the data for the bodywave model of the 1 October aftershock is worse than for the earlier earthquakes, especially for P waves in the west (Fig. 2.12). However, the solution cannot be significantly improved by adding a sub-event of the same orientation and so I keep the single mechanism. Its minimum misfit solution is

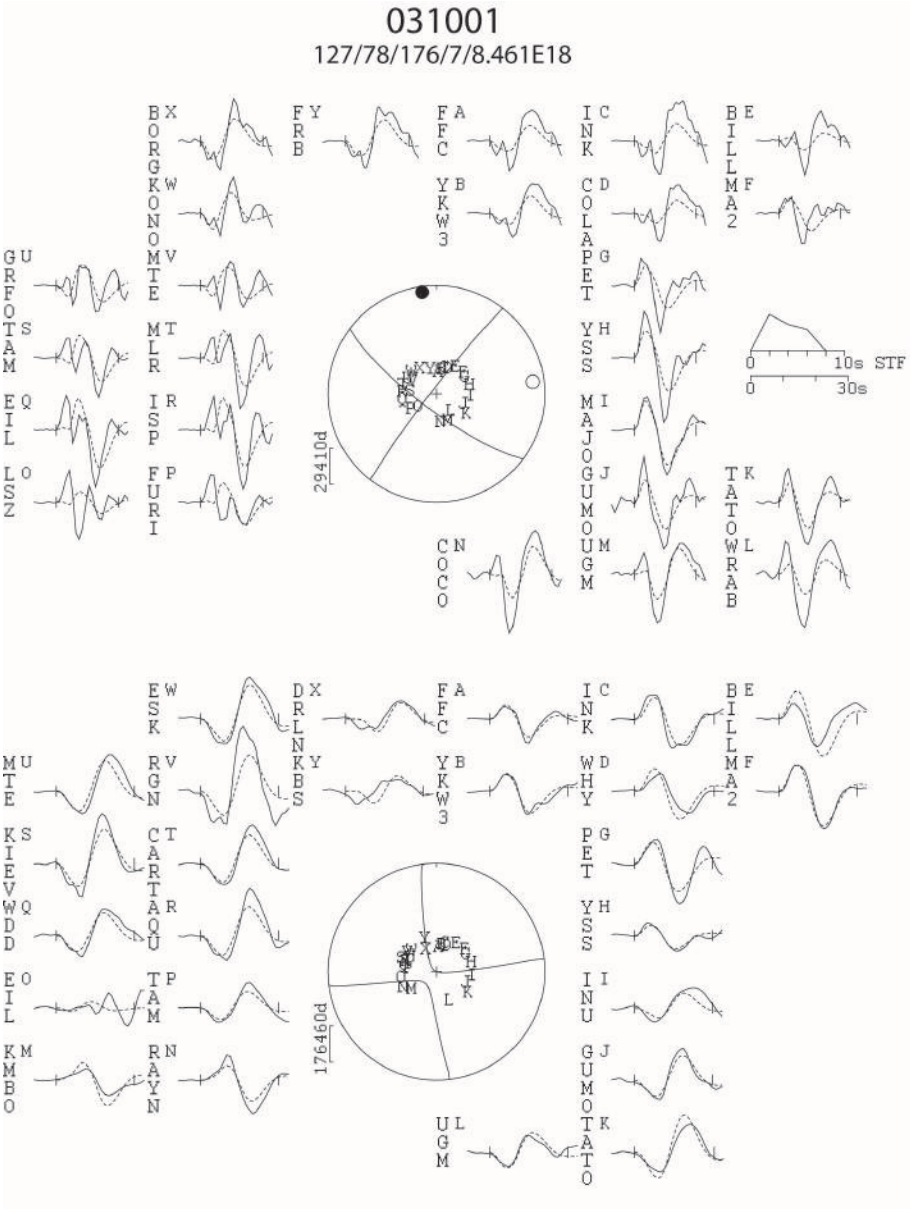

Figure 2.12: Minimum misfit solution for the 1 October M_w 6.6 earthquake. Layout is the same as in Fig. 2.9.

very similar to that of the largest event, but at a shallower depth. However, I find there to be a number of local minima close to this solution, within a few degrees of dip and rake and a few km of depth, and so the model is less well constrained than those of the earlier earthquakes.

Hypocentres for the 2003 earthquake sequence are available in the updated version of the Engdahl et al. (1998) catalogue. In this catalogue, the three largest earthquakes (modelled above) all lie in the north-western part of the fault zone revealed by InSAR. However, these locations may be erroneous, perhaps through an inaccurate representation of the Siberian shield in the earth model used or some irregularity in local crustal structure. I use Joint Hypocentral Determination (Dewey, 1972) to calculate improved relative locations of the large earthquakes. These are shown, relative to the M_w 7.2 mainshock and with 90% confidence ellipses, in Fig. 2.1. Both M_w 6.2 and M_w 6.6 aftershocks lie north-west of the M_w 7.2 mainshock, at distances of ∼7 km and ∼20 km respectively.

2.4.4 Comparing interferometric and seismic models

I can now try to assign individual seismic events in the earthquake sequence to different parts of the fault zone. The M_w 7.2 mainshock hypocentre lies ∼20 km SE of the M_w 6.6 aftershock and ∼32 km WNW of the M_w 6.7 sub-event, so probably initiated in the central part of the fault zone. It most likely ruptured the entire length of the faulting (∼50 km, not unreasonable for a M_w 7.2 earthquake). The M_w 6.7 thrust sub-event contributed further to deformation in the south-east part of the fault zone, while the M_w 6.2 and 6.6 aftershocks added to deformation in the north-west. For this reason, and because the interferometry measures the cumulative deformation spanning the whole earthquake sequence, I am unable to isolate individual seismic events in the interferometric displacements. As a result I cannot directly compare the bodywave models of any individual event with the source parameters of any one InSAR model fault.

However, a more general comparison between the source parameters of the two models is still useful, and reveals some striking discrepancies. The combined moment of the three InSAR model faults (39×10^{18} Nm) is less than half that of the four seismic bodywave models (98×10^{18} Nm), despite the interferometric displacements including up to 9 months of post-seismic deformation (Table 2.1). In the central and north-western parts of the fault zone, there are also striking discrepancies in fault dip and rake; the bodywave models of the M_w 7.2 mainshock and M_w 6.6 and 6.2 aftershocks dip steeply south-west and two of these events are almost purely strike-slip, while InSAR model faults A and B dip steeply north-east and include a significant reverse component. Furthermore, the bodywave centroid depths (6–18 km) are generally deeper than the equivalent centroid depths of the InSAR model faults (5–8 km).

It is interesting and unusual to find such significant differences between interferometric and seismic models of the same earthquake sequence, and it is important to investigate the cause of these differences. I begin by investigating whether trade-offs between different source parameters (which affect both type of model) might account for the some of the differences in fault dip. I estimate the bounds of dip for each bodywave solution using the procedure of Molnar & Lyon-Caen (1989), inverting the data with fault dip fixed to a new value and seeing whether the fit between the synthetic and observed waveforms is noticeably degraded. When this is done for a series of fixed dip values, trade-offs with other source parameters will become apparent. Fig. 2.13 shows the dip test for the M_w 7.2 mainshock as an example; from this I estimate a $\sim$10° uncertainty in fault dip, with a dip of 90° (20° from that of InSAR fault B) within the bounds of error. This slightly reduces the discrepancy in fault dip between bodywave and InSAR models. Furthermore, I find that values of centroid depth and moment decrease significantly as the dip is forced towards the north-east. These trade-offs with fault dip could account for the discrepancy in centroid depth and some (but not all) of the discrepancy in moment. For the M_w 6.2 aftershock I estimate an upper bound of 61° SW for dip, which this time trades off positively with rake as well as with strike. For the M_w 6.6 aftershock, I estimate an upper bound of 90° in dip (the fit degrades as soon as the dip is forced towards the SW); trade-offs

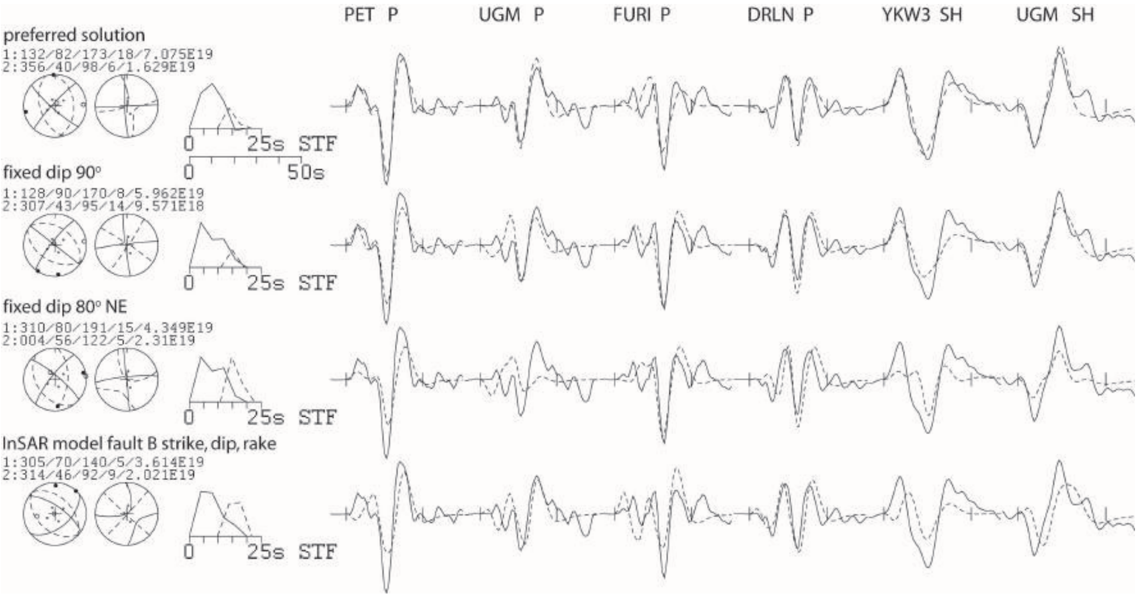

Figure 2.13: Dip test for the September 27 M_w 7.2 main shock, showing the match between real (solid line) and synthetic (dashed line) waveforms for a selection of four P and two SH stations. The top line shows our preferred solution (with subevent location fixed), in which the fault plane dips 80° SW. The second and third lines show solutions for fixed dips of 90° and 80° NE, respectively; in the third line (dip fixed to 80° NE) the depth was also fixed, to 5 km (the equivalent centroid of InSAR model fault B) because otherwise it was forced to zero. We estimate that the dip could lie as much as 10° from the minimum misfit solution.although the match for P waves at UGM is worse for a fixed dip of 90° than for the minimum misfit solution, the match at FURI is actually significantly better. The final line shows a model with strike, dip and rake fixed to the values of the InSAR solution for fault B; the fit between observed and synthetic waveforms is now significantly worse than in the first three lines.

are difficult to ascertain because the differences in fit as a function of azimuth are so large (Fig. 2.12).

Trade-offs in InSAR model dip are also qualitatively assessed, by plotting the distribution of dips yielded by inverting 100 perturbed datasets against the distributions of other parameters. Only for fault A are clear trade-offs in dip observed; positively, with rake, slip, minimum depth and latitude, and negatively with length and longitude. However, these trade-offs are not large enough to explain the difference in fault dip.

The InSAR model faults are forced to dip towards to north-east because there are more fringes north-east of the faulting than to the south-west (Fig. 2.7). However, there is also much better coherence north-east of the faulting (in the Chuya and Kurai depressions) than to the south-west (in the steep Chuya ranges). As a result, more data points going into the inversion are from north-east of the faulting than from south-west of it. Such a bias in data coverage might influence the parameter values yielded by interferometric modelling, and I now investigate whether this could be so for the case of fault dip.

I start by inverting the interferometric data three more times, but with the dips of fault segments A and B fixed to values of 80° NE, 90° and 80° SW. All other parameters are free to vary in the inversions, including the dip of fault segment C. I also produce a fourth model, constraining the strike, dip and rake of faults A, B and C to lie very close to (within 5° for strike and dip, and 10° for rake) the values yielded by the bodywave inversions of the M_w 6.6 aftershock, the M_w 7.2 mainshock and the M_w 6.7 sub-event respectively; other parameters are largely free to vary. The model parameters yielded by all four of these inversions are shown in Table 2.4.

InSAR model	(i)			(ii)			(iii)			(iv)		
Fault	A	B	C	A	B	C	A	B	C	A	B	C
Strike (°)	322	305	295	327	305	294	151	125	293	129^c	135^c	351^c
Dip (°)	80^c	80^c	57	90^c	90^c	58	80^c	80^c	61	79^c	77^c	45^c
Rake (°)	145	146	96	161	152	94	185	186	90	172^c	171^c	88^c
Slip (m)	1.27	1.61	4.63	2.10	1.79	4.81	2.22	3.43	5.06	4.90	3.08	5.43
Top depth (km)	1.8	0.0	1.4	2.6	0.0	1.5	0.7	0.0	1.7	0.0	0.0	3.1
Bottom depth (km)	25.9	9.7	11.4	15.3	8.9	11.5	15.3	6.1	11.9	13.7	15.0^f	12.0
Length (km)	12.3	25.3	8.2	14.6	25.2	8.0	14.4	26.3^f	8.1	18.3	29.8	7.7
Moment ($Nm \times 10^{18}$)	12.3	12.9	14.4	12.7	12.9	14.7	15.4	18.0	15.4	40.3	46.0	17.1
M_w	6.66	6.68	6.71	6.67	6.68	6.72	6.73	6.77	6.73	7.01	7.04	6.76
RMS misfit (W) (cm)		2.65			2.72			3.47			11.53	
RMS misfit (C) (cm)		4.02			4.25			4.73			11.75	
RMS misfit (E) (cm)		5.55			6.01			6.98			14.88	

^{c} parameters constrained during inversion to lie close to bodywave solution

^{f} parameters fixed during inversion

Table 2.4: Fault plane parameters for four models of the 2003 Siberian Altai earthquakes, produced by inverting the interferometric data but with the dips of some faults fixed. Once again, fault A is the north-western segment, fault B the central segment and fault C the south-eastern segment in each model. In (i), the dip of faults A and B is fixed to 80° NE, in (ii), 90° and in (iii), 80° SW. In model (iv), the strike, dip and rake of all three fault segments were constrained to be close to the values of the corresponding bodywave models; strike and dip were allowed to vary by up to 5° and rake by 10° from the bodywave solutions. For (iii) and (iv), the length and bottom depth respectively had to be fixed at sensible values to ensure a realistic solution. The bottom three lines of the table show Root Mean Square (RMS) misfits for the Western, Central and Eastern interferograms. For comparison, the equivalent RMS misfits for the best-fit model (Fig.2.6) are 2.77 cm, 3.92 cm and 5.25 cm respectively.

Using the results of these fixed-dip inversions I produce model interferograms. These are shown in Fig. 2.14 alongside residuals, which increase progressively as the dip is forced further from the InSAR best-fit solution and are especially large for model *iv*, where the strike, dip and rake are constrained to lie close to the bodywave solutions. Data corresponding to the incoherent parts of the real interferograms is masked from these synthetic datasets, and I add noise with the same statistical properties as the atmospheric noise present in the real interferograms. I then invert them in exactly the same fashion as was done in Section 2.4.1. In all four cases, the results of the inversions match the parameters (strike, dip, rake, slip, length, and top and bottom depths) used to make the synthetic data very closely. I am therefore confident that the bias in the data coverage does not affect the results of the interferometric modelling.

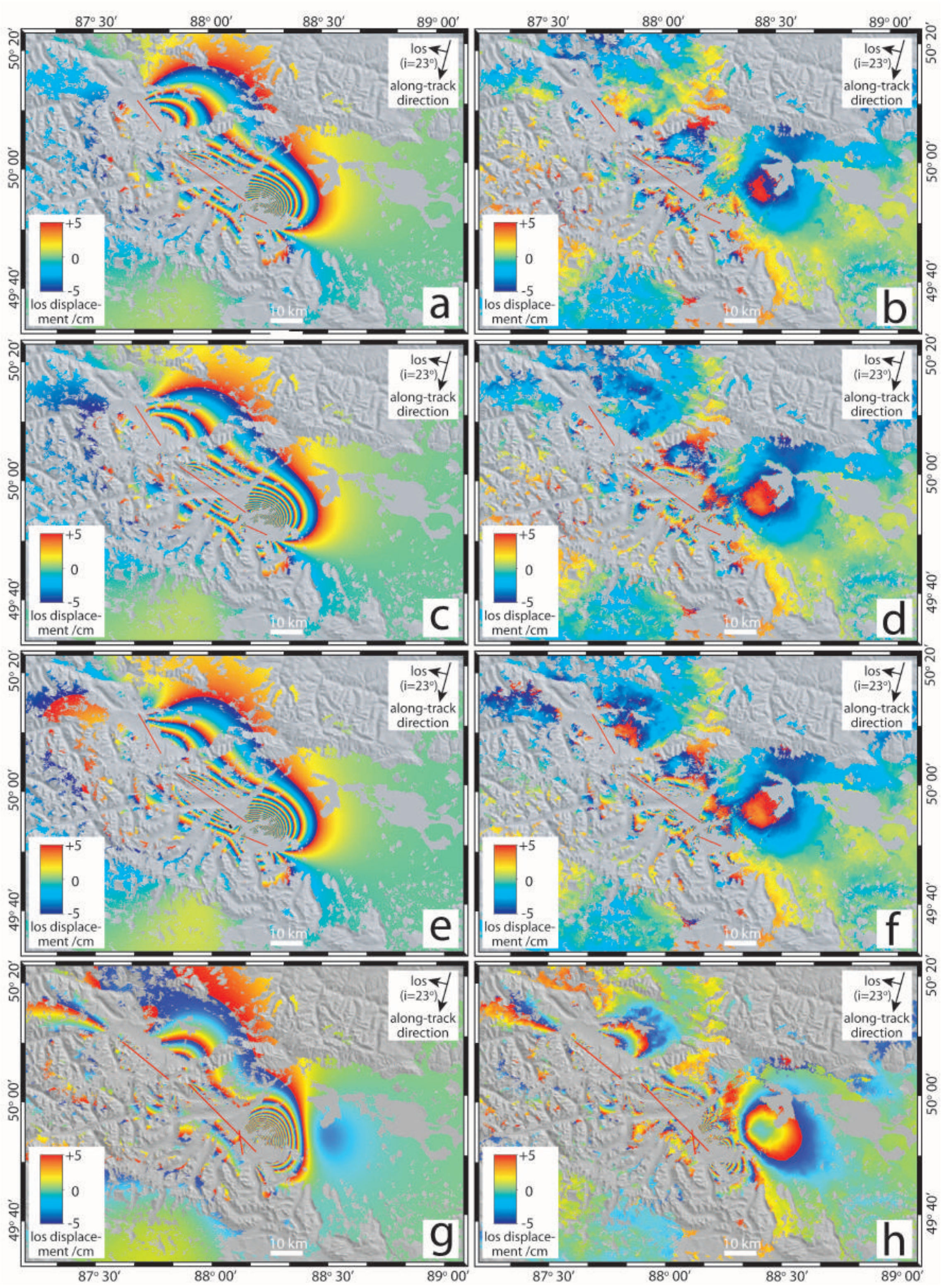

Figure 2.14: Model and residual interferograms produced by the inversion of interferometric data, and corresponding to the parameters given in Table 2.4. Faults A and B are constrained to dip 80° NE (a & b), 90° (c & d) and 80° SW (e & f). In g & h, faults A, B and C are constrained to have values of strike, dip and rake close to the corresponding bodywave solutions (see text).

2.5 Discussion

Although I have identified, for the first time, a large reverse slip event in the south-east of the fault zone, it has not been possible to match individual seismic events with detailed interferometric displacements. Moreover, the seismic bodywave and interferometric models of the earthquakes disagree significantly on the earthquake source parameters, most strikingly in the values for moment (with the combined InSAR moment less than half that of the bodywave models) and dip (InSAR faults A and B dip steeply north-east, but minimum misfit bodywave solutions of the three strike-slip events dip steeply south-west). Trade-offs in the bodywave modelling can only partly account for these discrepancies, while the uneven interferometric data coverage cannot account for them at all. Instead, I should look at the assumptions made in the modelling.

In the interferometric modelling I have assumed uniform slip on each fault plane. One limitation of the interferometry is the ~5 km wide strip of incoherence close to the surface faulting; if slip was not uniform but concentrated at very shallow depths (down to perhaps 2 km), then displacements within this incoherent area would be higher than expected. However, the greater moment resulting from these higher displacements would be missed by the InSAR modelling. This is one obvious way to account for some of the discrepancy in moment. However, it does seem unlikely that enough slip could be concentrated at such shallow depths to account for all of the discrepancy in moment.

In the interferometric modelling I solve for slip in an elastic half-space; the elastic shear modulus is assumed to be a constant 3.23×10^{10} Pa. In reality, however, the elastic modulus is not uniform throughout the upper crust but will vary with lithology. There is a distinct change in lithology across the southern margins of the Chuya and Kurai depressions – to the south, the Chuya ranges are made of crystalline bedrock, while to the north, the Chuya and Kurai depressions contain

~1,200 m and ~500m of Cenozoic sediments respectively (Delvaux et al., 1995). The surface faulting approximately follows this change in lithology, so there is a higher elastic modulus south of the faulting than north of it, at least in the top ~1 km of the crust. This might influence the number of fringes present either side of the faulting, with potentially more fringes than expected in the Chuya and Kurai depressions, where the elastic modulus is lower. If this was the case, the variation in elastic modulus could be forcing the apparent dip of the InSAR faults to the north-east, even if the real faulting was vertical or dipped steeply south-west.

A lateral variation in the elastic modulus of the upper crust would also influence take-off angles of seismic bodywaves, and so would affect the bodywave solutions too. Upper mantle anisotropies are also known to exist beneath the Altai (Dricker et al., 2002) and these might also influence the seismology, although it is not clear exactly how.

Other observations of dip, from field measurements and the study of Landsat images (Section 2.3), are ambiguous. In different parts of the fault zone, there is evidence for both a dip to the north-east (between the Kuskunur and Taldura valleys, in Fig. 2.4) and a dip to the south-west (in the Mazhoi valley, and south-east of the surface ruptures, in Fig. 2.5). It is, therefore, possible that the strike-slip faulting changes dip along strike. A similar scenario has been envisaged for other large, continental strike-slip faults. Bodywave models of the 1997 May 10 Zirkuh, Iran earthquake (M_w 7.2) show four sub-events varying in orientation along the strike of the fault (Berberian et al., 1999); this change in orientation is also seen at the surface, in observations of earthquake ruptures and geomorphology. Reversals in dip have also been identified along the Manyi fault in Tibet, in InSAR measurements of the 1997 November 8 Manyi earthquake (M_w 7.5) and in the geomorphology (Funning et al., 2007). In both these cases the bodywave solution of the mainshock alone says little about the orientation of the fault as a whole.

Irrespective of the dip, the faulting reactivated in the 2003 earthquakes lacks a clear topographic expression, explaining why it was previously unmapped. While the large strike-slip faults bounding the Altai range (such as the Ölgiy-Hovd, Har-Us-Nuur and Fu-Yun faults) are obvious in the topography, there may well be other active faults in the interior of the Altai which have yet to have been mapped. The M_w 6.7 reverse sub-event is also interesting because it acted as if to invert the Chuya depression; more normally, reverse-faulting in active continental mountain belts uplifts high ground relative to low ground.

Right-lateral strike-slip faults can accommodate shortening across the Altai if they and the slivers of crust between them rotate anticlockwise over time (Baljinnyam et al., 1993; Bayasgalan et al., 1999a, 2005). The only study to have looked for paleomagnetic rotations in the Altai mountains sampled upper Oligocene to Pleistocene clays and sandstones about 30 km north-east of the 2003 earthquake in the north-west Chuya depression (Thomas et al., 2002). Anticlockwise rotations of 39° ±8 were recorded in middle Miocene to early Pliocene sediments, though the authors suggest that most of this occurred during the last 5 million years. They attribute the anticlockwise rotations to the influence of the Kurai fault zone, which strikes E-W across the mountains north of the Chuya and Kurai depressions (Fig. 2.1). Although stream offsets across the Kurai fault in the north-east Chuya depression are consistent with dextral strike-slip, it is described in the literature as a sinistral transpressional fault (Delvaux et al., 1995); left-lateral motion on this fault zone is meant to have caused a domino-style rotation of the Chuya depression, giving rise to the paleomagnetic rotations. However, the 2003 earthquakes strongly suggest that the rotations are instead associated with right-lateral shear along a fault zone striking ~WNW-ESE across the southern margins of the Chuya and Kurai depressions. This style of deformation has been attributed to the Altai mountains further SE, in Mongolia and China, and should now be extended to the Siberian part of the range.

There is one clear difference between the faults reactivated in the 2003 sequence and active faults further south-east, in the Mongolian and Chinese parts of the Altai; the former strike ∼300°, whereas the latter strike ∼NNW. However, this probably reflects to the different orientation of structural grain in the Siberian part of the Altai (Dehandschutter, 2001), rather than a change in the style of deformation.

2.6 Conclusions

The 2003 Siberian Altai earthquakes occurred on a segmented fault zone that had not previously been recognised. It is possible that there are other unmapped faults in the Altai capable of producing large earthquakes, particularly in the interior part of the range where their expression is not obvious in the topography. The 2003 sequence involved both right-lateral strike-slip and reverse movements, on fault segments striking ∼NW. The strike-slip segments rotate anticlockwise over time to accommodate the regional ∼NNE-directed shortening, while the reverse faulting represents a rare case of pure shortening perpendicular to the strike of the Altai range.

Chapter 3

Late Quaternary slip-rate of the Har-Us-Nuur fault

3.1 Introduction

Late Quaternary fault slip-rates are important indicators of seismic hazard and provide valuable constraints for models of continental deformation. The collision between India and Eurasia is a key testing ground for these models (e.g. England & Molnar, 1997a; Thatcher, 2007), but quantitative data on the rates of deformation are primarily concentrated in the southern half of this zone, in and around the Tibetan plateau (e.g. Ryerson et al., 2006). The style of faulting and occurrence of large magnitude earthquakes in the Altai are well documented (e.g. Baljinnyam et al., 1993), but until now very little is known about how fast these faults move on late Quaternary time-scales, the frequency at which these large events happen, or how the distribution of faulting has evolved through time. These questions are the motivation for this chapter.

I focus on the Har-Us-Nuur fault, a major strike-slip fault bounding the eastern margin of the Altai mountains. My first aim is to calculate the late Quaternary slip-rate on this fault. To measure slip-rates accurately, robust ages and displacements of offset geomorphic markers must be determined. A number of techniques are available to date these landforms; the choice of which to use depends on the type, lithology and approximate age of the feature under consideration, and often only one is applicable at a particular site. As such, it is rare for separate dating methods to be used in parallel and tested against one another. In this study I am given an opportunity to compare, directly, two dating methods – *in situ*-produced cosmogenic ^{10}Be and optically stimulated luminescence (OSL) – used to determine the age of alluvial fans offset by the fault. Next, I use ruptures preserved from a prehistoric earthquake – described here for the first time – to deduce the size and average recurrence time of earthquakes on this section of the fault. Finally, I use the cumulative vertical displacement across the fault to estimate its age. My results have significant implications for the evolution of faulting in an important part of the Alpine-Himalayan belt.

3.2 Overview of the Har-Us-Nuur fault

Around 500 km long, the Har-Us-Nuur fault strikes SSE through relatively low terrain along the eastern margin of the Altai, adjacent to the Depression of Great Lakes (Fig. 1.5). At its northern end, the fault splits into a number of parallel strands. Walker et al. (2006) provide a detailed geomorphological study of the westernmost of these, known as the Jid fault. The authors describe an en echelon, left-stepping arrangement of partially-infilled tension fissures which probably result from the most recent earthquake here. These features are observed for at least 55 km but may continue along the entire 90 km length of the Jid fault. The age of the earthquake is bracketed at 870–980 years from OSL dating of material found in a trench, and slip of $\sim$5 m is determined from the size and orientation of the fissures. Using simple scaling relationships, the rupture length and displacement are consistent with a moment magnitude of 7.5 (Scholz, 1982).

Khil'ko et al. (1985) describe a 25 km section of the southernmost Har-Us-Nuur fault – known as the Tonhil fault – along which another series of en echelon tension

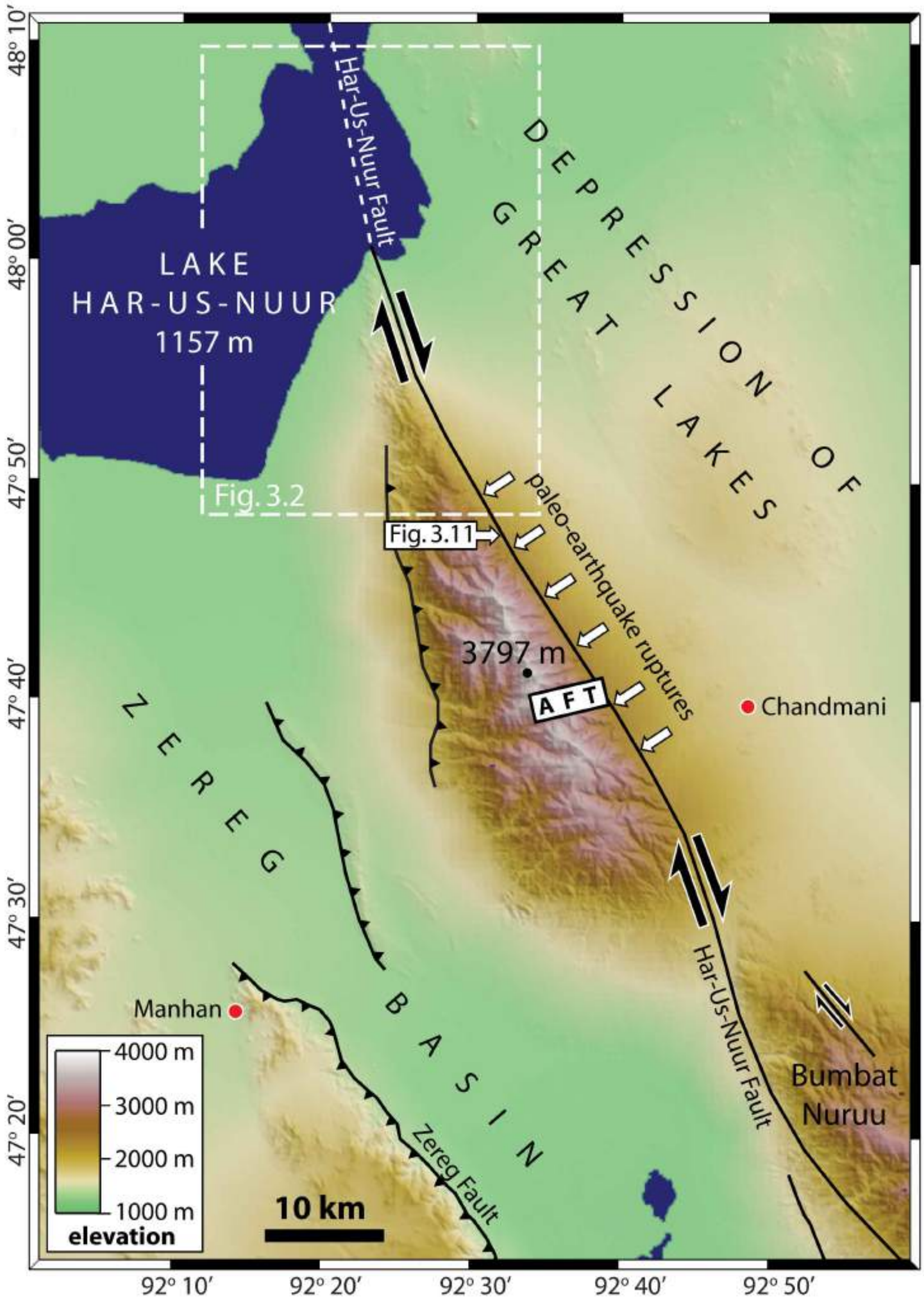

Figure 3.1: SRTM topography and faulting around the Jargalant-Nuruu massif, displayed in the local UTM zone (46) projection (as are subsequent maps) and artificially sun-shaded from the NE. The extents of the paleo-earthquake ruptures described in Section 3.4 are indicated by white arrows, and the location of Fig. 3.11 is also shown. Apatite fission track samples were taken from a transect of the Jargalant Nuruu range covered by the white rectangle labelled AFT. The location of this map is shown as a green, dashed box on Fig. 1.5.

cracks are preserved. The size of these fissures indicates coseismic slip of ∼2.5 m, consistent with a moment magnitude of around 6.9, assuming 25 km represents the full length of the rupture. Based on their level of preservation (rather than actual geochemical dating), the ruptures are assigned an age of 500–1000 years.

In contrast with the northern and southern sections, the central part of the Har-Us-Nuur fault has until now been overlooked. This central section represents a significant source of seismic hazard for Hovd (the largest town in western Mongolia, around 50 km to the west), so it important to establish the magnitude and frequency of earthquakes here. I focus on the area south of Har-Us-Nuur lake, where a major restraining-bend (introduced by a change in fault strike) has uplifted the ∼3800 m-high Jargalant-Nuruu massif (Fig. 3.1). The Har-Us-Nuur fault bounds the eastern margin of these mountains.

3.3 Late Quaternary slip-rate

3.3.1 Site descriptions and offsets

South of Har-Us-Nuur lake, the Har-Us-Nuur fault beheads a series of alluvial fans deposited along the eastern margin of the Jargalant-Nuruu mountains (Fig. 3.2). Streams exiting the range bend sharply to the north, toward Har-Us-Nuur lake, which constitutes the local base-level. In the northern part of this section, 15 m-pixel Advanced Spaceborne Thermal Emission and Reflection Radiometer (ASTER) and 2.5 m-pixel Satellite Pour l'Observation de la Terre (SPOT-5) images show six light-coloured fan systems sourced from granitic bedrock in the interior part of the Jargalant-Nuruu range (Fig. 3.3).

Within these systems, incised, abandoned fan surfaces have been displaced right-laterally from the catchment outlets that fed them. The elevation of the range-front increases southwards so these displacements are in an uphill direction and can

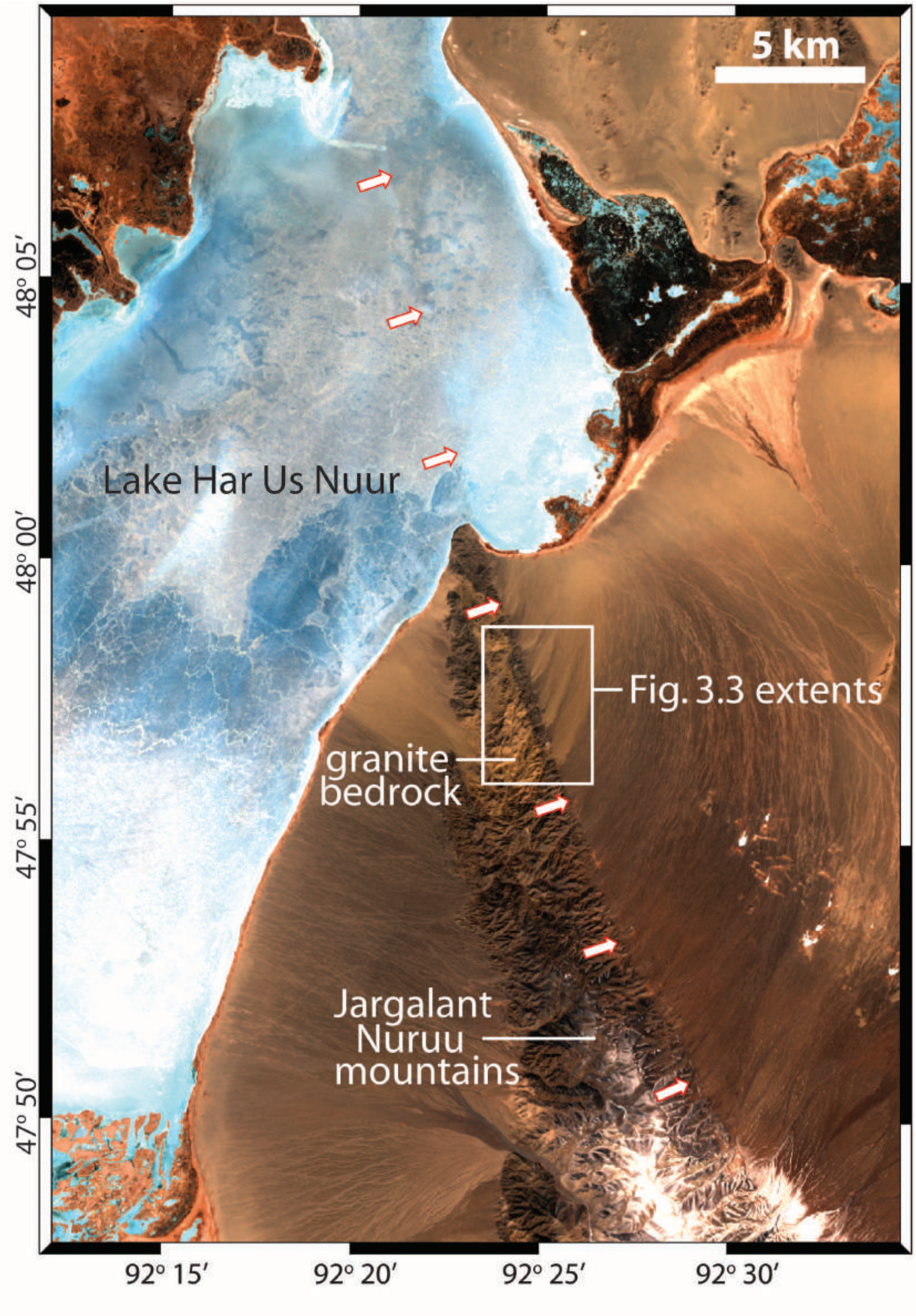

Figure 3.2: ASTER image (RGB 321) of the Har-Us-Nuur fault (picked out by white arrows) just south of the Har-Us-Nuur lake. In the northern part of the image the lake is completely frozen through, and the fault can be made out as it crosses the lake bed. Because there is no topography associated with the fault here, its 166° strike represents the fault slip vector.

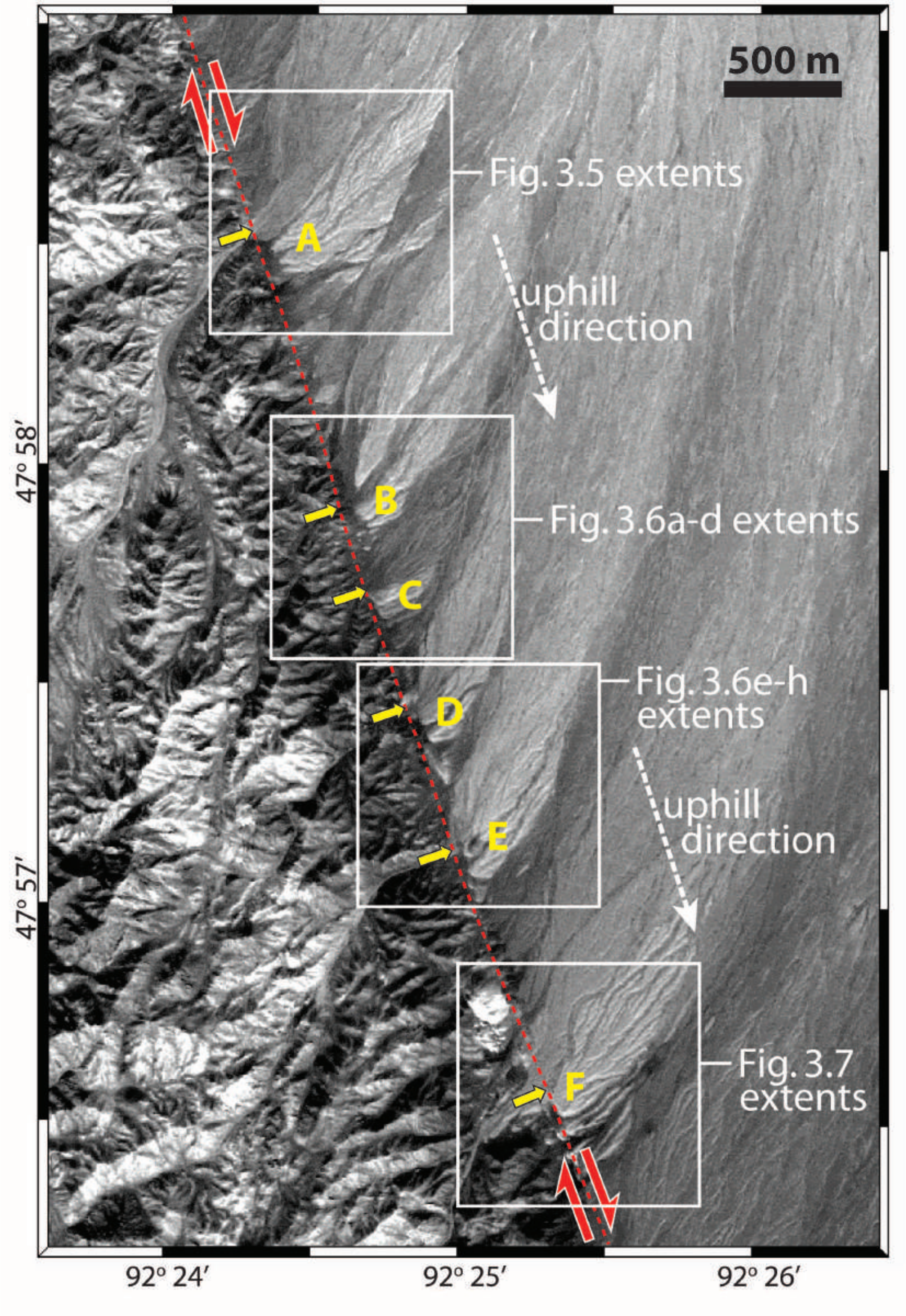

Figure 3.3: SPOT-5 image (2.5 m resolution) of a series of six light-coloured alluvial fan systems (labeled A to F) along the eastern margin of the Jargalant-Nuruu mountains. The range-front outlets of the catchments feeding these fans are denoted by yellow arrows, and the trace of the Har-Us-Nuur fault by a dashed red line.

only have been caused by right-lateral slip on the Har-Us-Nuur fault. Sourced from granitic bedrock the displaced surfaces are quartz-rich and thus an obvious target for exposure dating with *in situ*-produced cosmogenic ^{10}Be.

During fieldwork in June 2006 I visited each of the six granitic alluvial fan systems, which I label A–F. Photographs of the northermost (A) and southernmost (F) fan system are provided in Fig. 3.4, whilst detailed SPOT 5 images of all six systems are shown in Figs. 3.5–3.7. Most systems contain an active fan (labeled A1, B1 *etc.*), although the youngest surface in the southernmost system (F1) shows minor incision by the active channel (Fig. 3.7d). In contrast, the older, abandoned set of surfaces – A2, B2 *etc.* – are crossed by networks of incised runnels. These channels, up to a few metres wide and one or two deep, contain dark material sourced from mafic bedrock along the adjacent range-front.

Away from the runnels the older fan surfaces are typically composed of gravel-sized clasts, although there are some rare boulders up to ∼50 cm in diameter. These boulders show desert varnish that decreases in development only in the lowest few centimetres of exposure, suggesting that the tops of the abandoned surfaces have undergone only minor erosion (possibly by deflation of fine-grained material). The surface-tops are planar in form, also consistent with only minor erosion. In fan system F the eroded remnants of an even older surface (F3), with deeper and wider runnels, are also preserved (Figs. 3.4b & 3.7). Small, isolated remnants of surfaces equivalent to F3 may also be preserved within some of the other, more northerly systems.

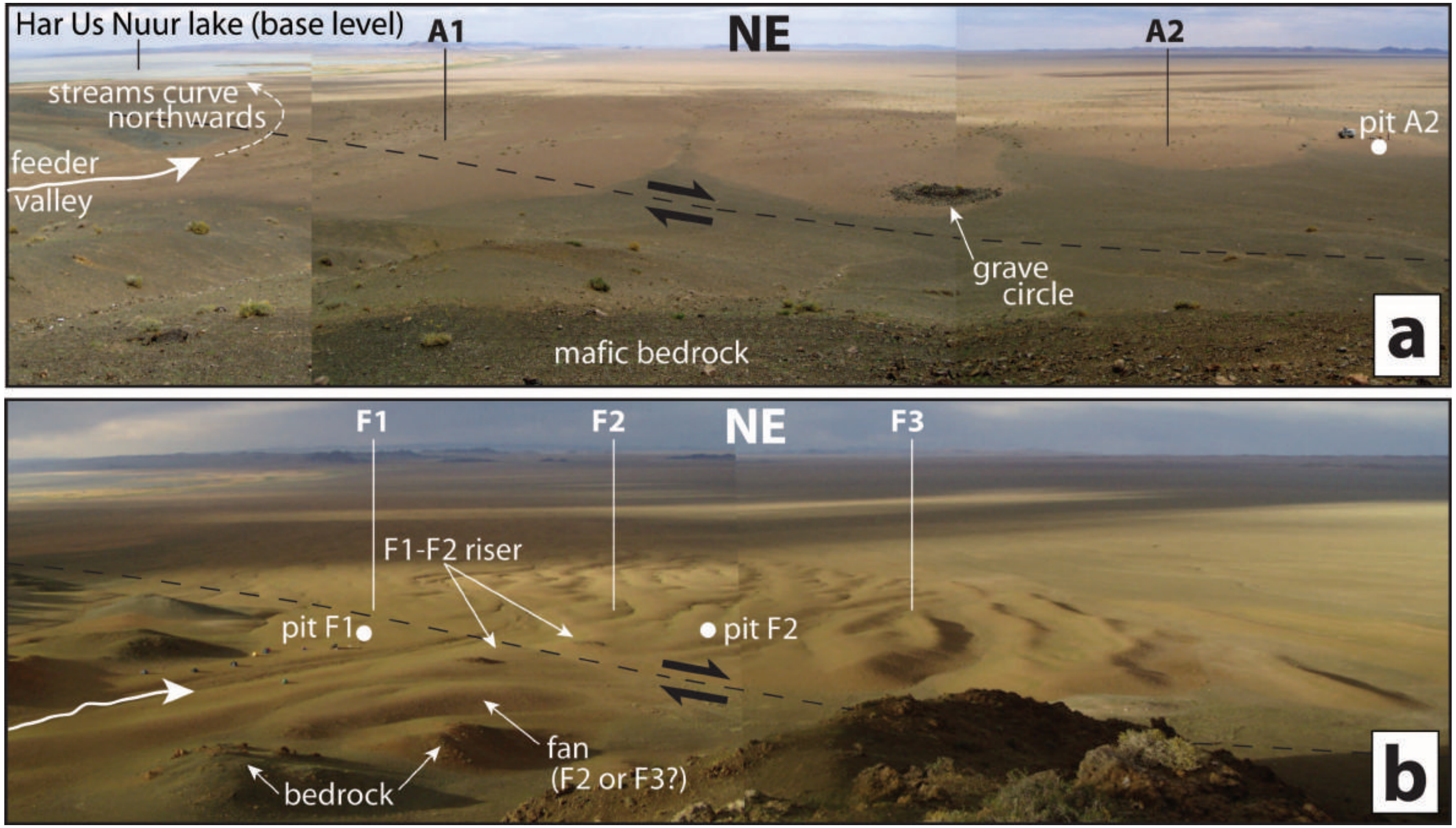

Figure 3.4: (a) Panoramic photographs facing ∼NE from 47° 58’ 28” N 92° 24’ 16” E. Mafic bedrock can be seen in the foreground, and material eroded from this has been washed into the runnels crossing A2. (b) Panorama facing ∼NE from 47° 56’ 25” N 92° 25’ 10” E. Tents in left of picture give scale.

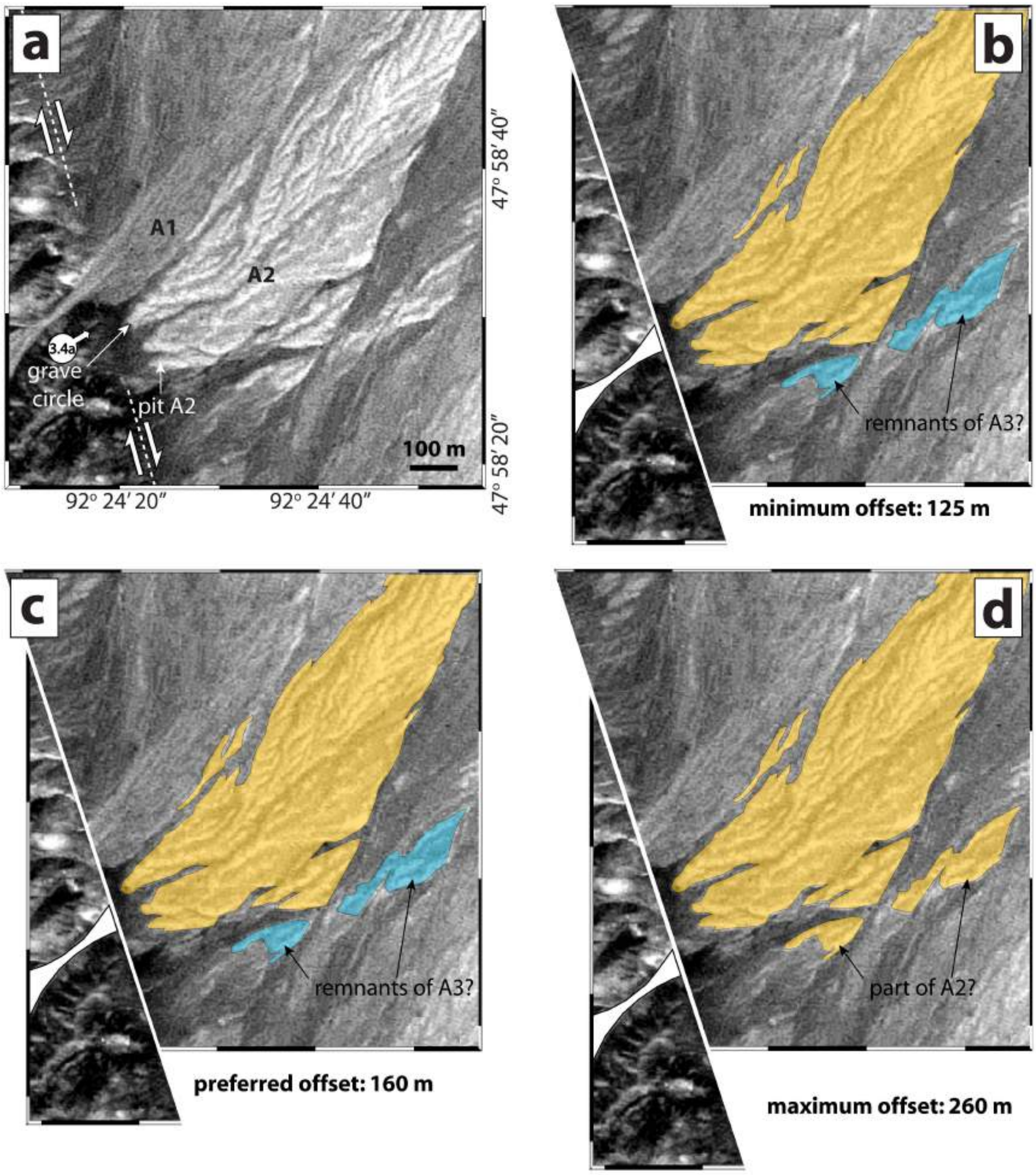

Figure 3.5: (a) SPOT-5 image of fan system A. A1 is a younger and slightly darker surface, and is still being deposited by the active stream channel. A2 is older and lighter, and is crossed by several runnels filled with dark material shed from mafic bedrock along the range-front. (b) Reconstruction made by restoring A2 along the Har-Us-Nuur fault. Here, I use my minimum estimate of the A2 offset; two patches of light-coloured alluvial material further SE are assumed to be remnants of an older surface, A3. (c) A second reconstruction, using my preferred estimate of the A2 offset. Here, the southern edge of A2 lines up with the southern edge of the feeder valley. (d) A third reconstruction, using my maximum estimate of the A2 offset; here the two patches of light material are assumed to be remnants of the A2 surface.

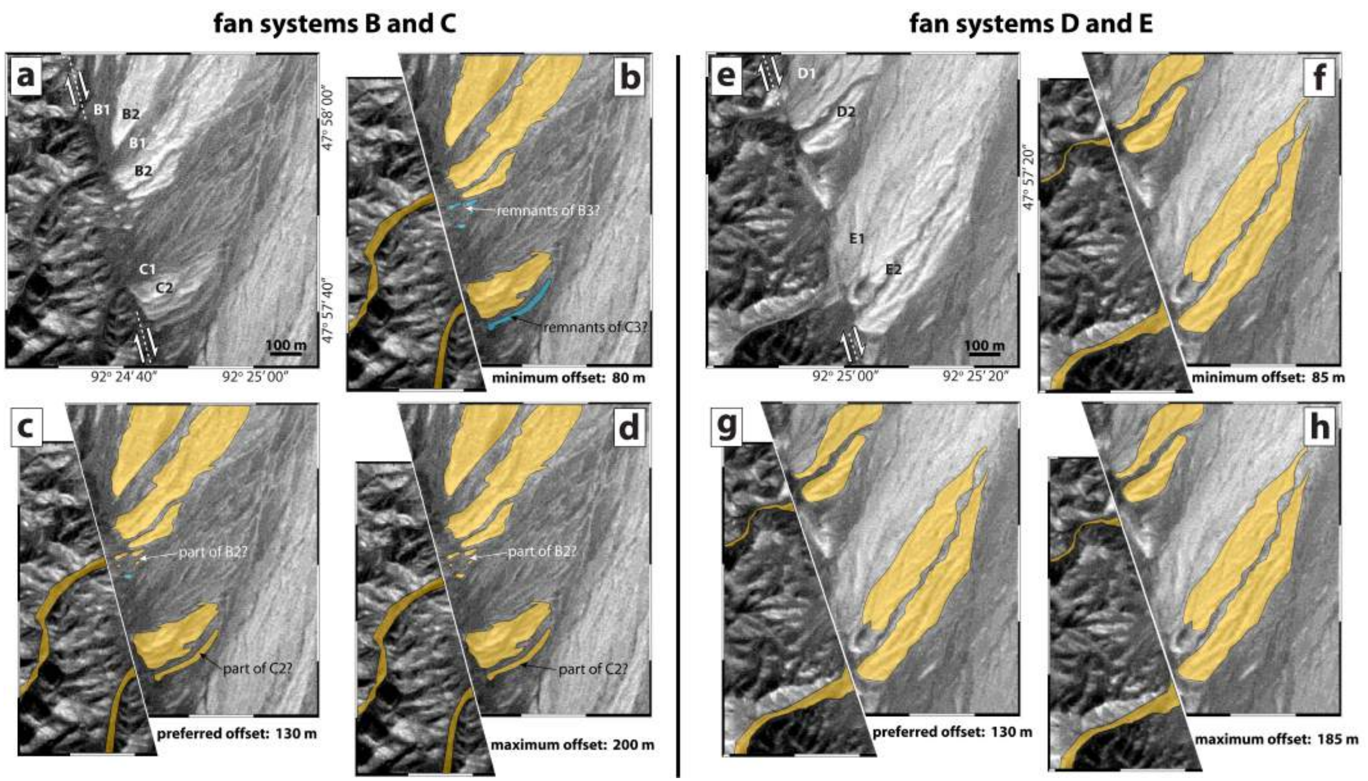

Figure 3.6: (a) SPOT-5 image of fan systems B & C. Next to this, I show reconstructions made by restoring (b) minimum, (c) preferred and (d) maximum estimates of the offset between the B2 & C2 surfaces and their feeder valleys along the Har-Us-Nuur fault. Small, isolated patches of light-coloured material may or may not be remnants of older surfaces B3 and C3; this uncertainty leads to the large bounds in my displacement estimates. (e) SPOT image of fan systems D & E. Again, I also show reconstructions made by restoring (f) minimum, (g) preferred and (h) maximum estimates of the offset between the D2 & E2 surfaces and their feeder catchments.

The older set of surfaces (A2–F2) all show clear right-lateral offsets from the catchment outlets that supplied them. Measuring these displacements is not trivial, because the extents of each fan may have been altered by erosion since they were originally deposited. This is of particular concern along their northern margins, which are exposed to the active feeder streams. I therefore focus on reconstructing the southern margins of the surfaces (which are likely to be more intact), estimating their displacements relative to the southern edges of the feeder valleys at their outlets. For each fan I provide a preferred value for this offset, as well as cautious upper and lower bounds (Figs. 3.5–3.7); details of all of the reconstructions are given in the relevant figure captions.

For A2, my preferred offset is 160 m, with bounds of 125–260 m. For B2 and C2, my preferred offset is 130 m with bounds of 80–200 m, while for D2 & E2, my preferred offset is also 130 m, but with bounds of 85–185 m. Finally, for F2 my preferred offset is 145 m with bounds of 55–190 m. Interestingly, for many of the surfaces (A2–E2, though not F2) my preferred reconstructions place major runnels adjacent to the feeder valley outlets. These runnels may be exploiting channels cut into the fan apices when they were first abandoned (equivalent to the active channel cut into the F1 surface).

Although the error bounds for individual fans are large, my preferred values lie in a relatively narrow range and in each case a displacement of 125–185 m is bracketed. The offsets are therefore consistent with the simultaneous deposition of these six surfaces. This implies that periods of fan-building are controlled by climate, which is unlikely to vary significantly over the small geographical area and narrow elevation range ($\sim$1275–1400 m) represented by the fan systems. Similar relationships between climate and periods of alluvial fan deposition and abandonment are observed elsewhere in central Asia. For instance, in both the Qilian Shan mountains in NE Tibet and the Gobi-Altai range of S Mongolia, periods of fan aggradation are thought to be

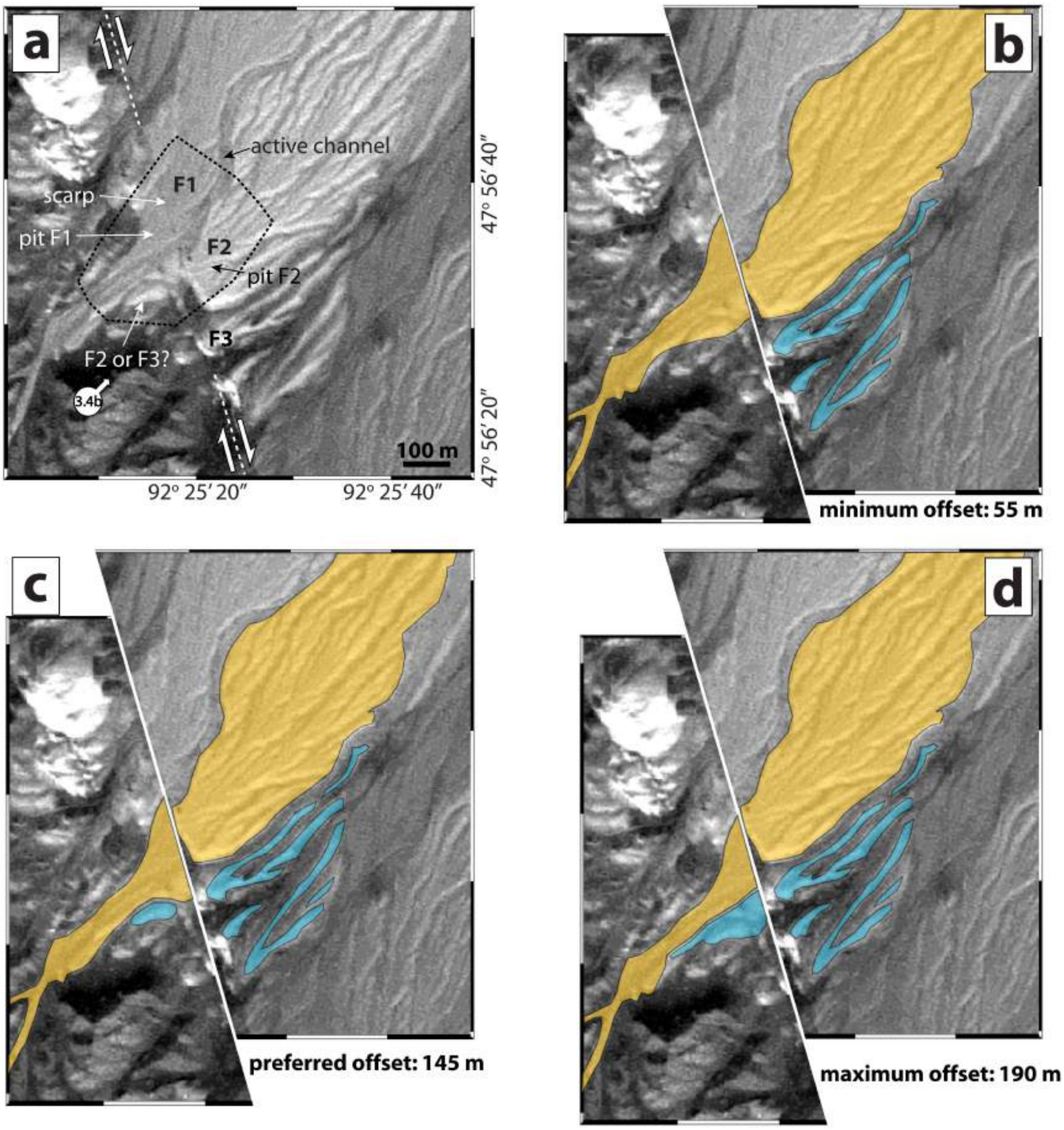

Figure 3.7: (a) SPOT-5 image of fan system F. The dashed black line marks the extents of the DEM in Fig. 3.8a. Next, I show reconstructions based on restoring the southern margin of F2 next to the southern edge of the feeder valley, using (b) minimum, (c) preferred and (d) maximum estimates of F2 displacement. Uncertainties in the extents of the F2 and F3 surfaces SW of the fault give rise to the large error bounds on this offset. (e) Panorama facing ∼NE from 47° 56' 25" N 92° 25' 10" E. Tents in left of picture provide scale.

promoted at the transitions from cold and dry glacial periods to warmer and wetter interglacials (Pan et al., 2003; Vassallo et al., 2005); in the latter case, these pulses can be correlated over areas many tens of kilometres wide.

I assume, therefore, that each set of surfaces (A1–F1, A2–F2) was deposited and abandoned roughly simultaneously. A displacement of 155 ± 30 m on the older surfaces satisfies all of the bounds (Figs. 3.5c, 3.6c, 3.6g & 3.7c); later on I use this figure to calculate the late Quaternary slip-rate in Section 3.3.4. These older surfaces all appear lighter in colour than the younger set (Figs. 3.5–3.7). This colour difference may reflect soil development over time, or, alternatively, a systematic change in sediment supply between one pulse of aggradation and the next.

On the southernmost fan system I also observe some younger displacements. Firstly, a clear scarp is preserved across the F1 surface, along the line of the fault (this can be picked out as a faint, dark line crossing the SPOT image in Fig. 3.7a). Secondly, the riser between F1 and F2 preserves a right-lateral displacement along the fault (Fig. 3.8c). This offset is much smaller than the overall 55–190 m displacement of the southern edge of F2 (Fig. 3.7); the riser must have been refreshed since F2 was abandoned, and I assume that the offset dates from the abandonment of F1, instead.

To measure these displacements, I first construct a digital elevation model (DEM) of fan system F using differential GPS (Fig. 3.8a). From a series of elevation profiles through this DEM (e.g. 3.8c) the vertical offset across the scarp is constrained to lie in the range 0.4–0.8 m. Parallel profiles taken either side of the fault across the F1–F2 riser show an apparent dextral offset of 12 ± 2 m (Fig. 3.8d). However, these profiles also show that the riser on the eastern side of the fault (profile E–F) is somewhat steeper than that on the western side (C–D), suggesting that the riser has been more recently refreshed on the eastern side. The true displacement of the F1–F2 riser may, therefore, be somewhat lower than the apparent offset measured from these profiles.

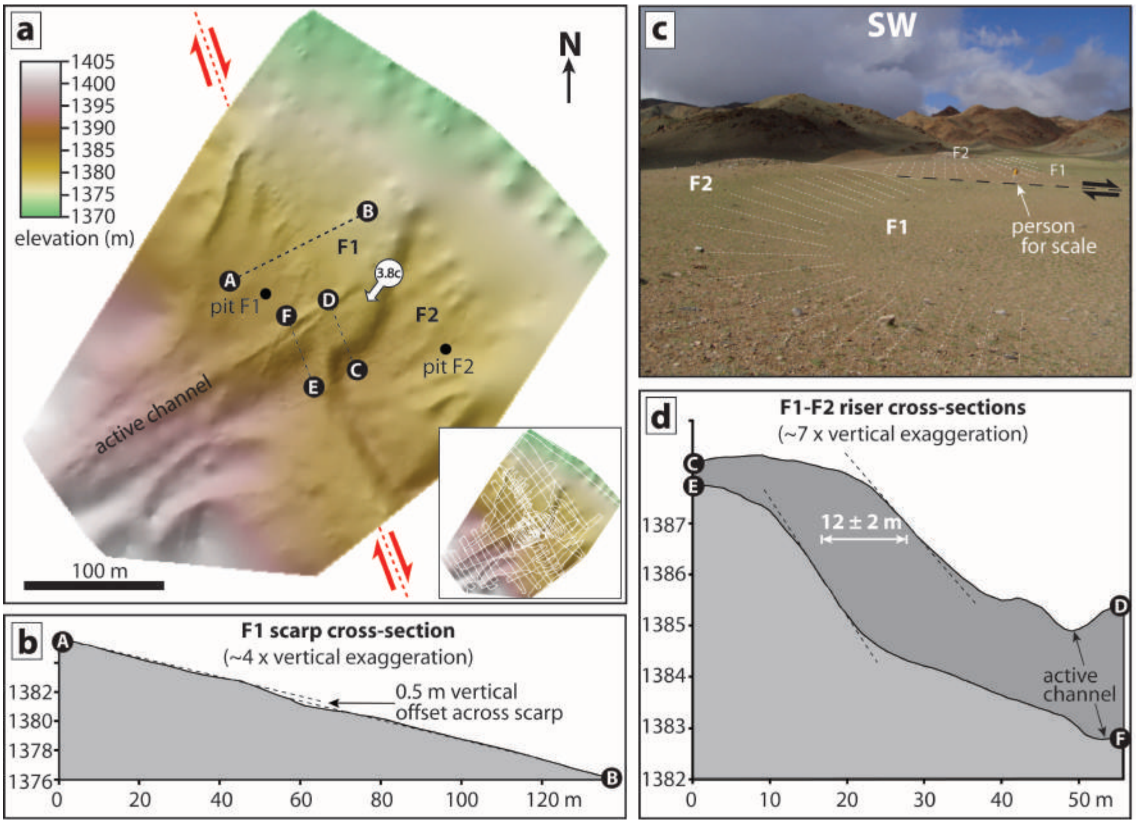

Figure 3.8: (a) Digital elevation model (DEM) of fan system F, artificially sun-shaded from the south-east. Its extents are marked on Fig. 3.7a as a dashed black line. The DEM was made by fitting a surface of minimum curvature to the differential GPS points shown on the inset map. (b) An example of an elevation profile across the scarp on F1. In this case, the surface is displaced, vertically, by 0.5 m; by producing several of these profiles, I bracket the offset at 0.4–0.8 m. (c) Photo facing ∼SW from 47° 56' 37" N 92° 25' 21" E, showing the F1–F2 riser with a person for scale. (d) Parallel topographic profiles through the F1–F2 riser, taken either side of the fault. The steepest part of the riser (picked out by a dashed line) is displaced, right-laterally, by 12 ± 2 m.

3.3.2 *In situ*–produced cosmogenic ^{10}Be exposure dating

A brief introduction to ^{10}Be exposure dating

To calculate the slip-rate of the Har-Us-Nuur fault, I constrain the timing of alluvial fan abandonment using exposure dating with *in situ*-produced cosmogenic ^{10}Be (e.g. Nishiizumi et al., 1986). This rare, long-lived isotope is generated within surficial quartz grains by interactions with cosmic rays. Its production rate is a function of latitude and altitude, and also decreases exponentially with overlying mass so that at depths of a few metres negligible amounts are generated. After a quartz-bearing rock is exposed its ^{10}Be content will increase over time until eventually a steady-state equilibrium between production and decay (plus loss through erosion) is reached. Providing this equilibrium is not yet achieved, measurements of ^{10}Be concentrations can therefore be used to establish the age at which the rock was exposed. This method has become an important way of determining the timing of alluvial fan abandonment in arid, mountain environments where organic material (for ^{14}C dating) or fine-grained sediment (for luminescence dating) may be unavailable (e.g. Ritz et al., 1995; Bierman et al., 1995).

The ^{10}Be contained in any one quartz grain may include a significant portion obtained prior to deposition – during hillslope exhumation and transport within the catchment area – and the age of fan abandonment can be over-estimated if this inherited component is not recognized (Anderson et al., 1996). There are two methods by which this can be done. In the first method, samples are taken from the bed of the active feeder stream, which is not yet abandoned and whose ^{10}Be concentration is effectively derived entirely from pre-depositional exposure. These measurements are then used to correct for the concentrations of individual boulders sampled from the surface of the alluvial fan (Brown et al., 1998). This approach relies on an assumption that the pre-depositional history of clasts in the active river bed is similar to that of the material making up the older, abandoned surfaces. As a result, this method may be unsuitable for the Jargalant Nuruu fans, where erosional conditions at the time at the time of fan deposition were probably more intense that at present.

A second strategy involves samples being taken not just from the surface, but from several depths within the deposit to be dated (Repka et al., 1997). In this method, each sample should consist of many separate, small clasts so that individual clast exposure histories are averaged. Providing there is no significant variation in inherited ^{10}Be over time, concentrations should decrease exponentially with depth. The average inherited component can then be determined from the asymptotic value that the profile tends to at depth.

In addition to the inherited ^{10}Be, one must also account for any surface erosion the deposit has undergone between deposition and the time of sampling. A high surface erosion rate equates to an increased level of shielding in the past, and will act to reduce the ^{10}Be content of the material now exposed. If the surface erosion rate is not known, a minimum exposure age can be established by assuming no erosion. Otherwise the erosion rate can be estimated by comparing the shape of vertical profiles of ^{10}Be with theoretical curves calculated with known erosion rates (Siame et al., 2004; Ritz et al., 2006).

Sampling and laboratory procedures

In this chapter I aim to establish exposure ages for the A2, F1 and F2 fans using the vertical distribution of ^{10}Be, averaged over many individual clast exposure histories. On each of these surfaces a 2 m-deep sampling pit was excavated (at 47° 58' 27.0" N 92° 24' 24.5" E, 47° 56' 35.7" N 92° 25' 15.3" E and 47° 56' 34.2" N 92° 25' 21.9" E, respectively). These locations were carefully chosen to avoid signs of recent erosion or deposition – in particular the runnels crossing A2 and F2, and the active stream incising into F1 (as well as some small debris flows that overtopped this channel, depositing clasts on the F1 surface).

Clasts were extracted from the pit wall into sampling bags at eight depths within each pit, at 25 cm intervals from the surface down to 1.75 m. The lack of cementation made it difficult to detach a block of fan material to establish the bulk density of the *in situ* sediment. Instead, average clast densities of 2.57–2.59 g cm^{-3} were measured in the laboratory and, with an assumption of 20–30% porosity – typical for poorly sorted, unconsolidated gravels (Fraser, 1935) – I estimate a bulk density of 1.935 ± 0.135 g cm^{-3}.

Each sample was crushed and sieved to yield 250–750 μm grains, which were cleaned in an ultrasound tank and then submerged in aqua regia for a day to remove traces of organic matter. To remove the bulk of the non-quartz fraction, samples were heated to $\sim$300^{o}C in concentrated phosphoric acid; the remaining (mostly quartz) grains were then heated to $\sim$100^{o}C in sodium hydroxide and washed to remove traces of acid. The samples were then put through a Frantz magnetic separation to remove any remaining magnetic minerals.

Samples were then etched for 48 hours in Hexafluorosilicic acid and a further 24 hours in 2% HF, to eliminate any leftover impurities and remove any atmospheric ^{10}Be contaminating the surfaces of the quartz grains. The remaining quartz grains were dissolved in analytical grade HF and a ^{9}Be carrier was added. After carrier addition, further sample preparation was carried out as described by (Wilson et al., 2008). Finally, the ^{10}Be/^{9}Be ratios were measured at the SUERC AMS facility in East Kilbride. NIST SRM4325 with a calibrated ^{10}Be/^{9}Be ratio of 3.06×10^{-11} was used as primary standard. ^{10}Be concentrations therefore agree with Nishiizumi (2002) but disagree with Nishiizumi et al. (2007). The exposure ages presented here of less than 100 ka are unaffected by the currently ongoing discussion on the half-life of ^{10}Be because the production rates used are consistent with the half-life of 1.5 Ma used here. Details of the AMS measurement of ^{10}Be are given in Maden et al. (2007) and Schnabel et al. (2007).

Final ^{10}Be concentrations are displayed in Table 3.1. It should be noted that I was not able to measure concentrations for all 24 samples; those at 150 cm in F1 and at 25 cm in F2 contained biotite inclusions such that pure quartz could not be extracted, while those at 100 cm and 150 cm in F2 yielded too little quartz.

Surface	*Depth (cm)*	^{10}*Be* ($\times$ *10* ^{5} *at g* $^{-1}$)
A2	0	11.84 ± 0.35
A2	25	10.24 ± 0.32
A2	50	8.08 ± 0.24
A2	75	6.19 ± 0.19
A2	100	5.33 ± 0.17
A2	125	4.42 ± 0.16
A2	150	6.89 ± 0.21
A2	175	7.20 ± 0.21
F1	0	4.46 ± 0.20
F1	30	2.59 ± 0.08
F1	50	4.52 ± 0.17
F1	75	4.49 ± 0.25
F1	102.5	3.72 ± 0.12
F1	125	4.78 ± 0.17
F1	175	4.09 ± 0.13
F2	0	8.44 ± 0.24
F2	50	9.22 ± 0.33
F2	75	6.12 ± 0.25
F2	125	4.04 ± 0.13
F2	175	6.81 ± 0.21

Table 3.1: *In situ*-produced cosmogenic ^{10}Be concentrations from sampling pits in the A2, F1 and F2 fans. Analytical errors are given at the 1σ level and include the standard uncertainty of the AMS measurement and 2% for the uncertainty of the concentration of the carrier solution used.

Chi-square inversion

To determine the A2 exposure age I use a chi-squared inversion that minimises the difference between the observed ^{10}Be concentrations and vertical profiles predicted by theory (Siame et al., 2004):

$$\chi^2 \;=\; \sum_{i=1}^{n} \left[\frac{C_i - C)}{\sigma_i}\right]^2 \tag{3.1}$$

where C_i is the measured ^{10}Be concentration (at g^{-1}) at depth x_i; σ_i is the analytical uncertainty at that depth; n is the total number of samples in the profile. C is the predicted ^{10}Be concentration (at g^{-1}) as a function of depth x (g cm^{-2}), surface erosion rate ϵ (g cm^{-2} yr^{-1}) and exposure time t (yr):

$$\begin{aligned}
C(x,\epsilon,t) &= C_{inh}\cdot e^{-\lambda t} \\
&+\frac{P_0\cdot p_n}{\lambda+\epsilon/\Lambda_n}\cdot e^{-x/\Lambda_n}(1-e^{-t(\lambda+\epsilon/\Lambda_n})\\
&+\frac{P_0\cdot p_s}{\lambda+\epsilon/\Lambda_s}\cdot e^{-x/\Lambda_s}(1-e^{-t(\lambda+\epsilon/\Lambda_s})\\
&+\frac{P_0\cdot p_f}{\lambda+\epsilon/\Lambda_f}\cdot e^{-x/\Lambda_f}(1-e^{-t(\lambda+\epsilon/\Lambda_f}).
\end{aligned} \tag{3.2}$$

Here, C_{inh} is the initial inherited ^{10}Be concentration (at g^{-1}); λ is the ^{10}Be decay constant (yr^{-1}); P_0 is the total surface production rate (at g^{-1} yr^{-1}); p_n, p_s and p_f are the relative contributions to this total from neutrons, slow muons and fast muons, respectively; and Λ_n, Λ_s and Λ_f are the effective attenuation lengths of these same particles (g cm^{-2}). The first line of this equation gives the portion resulting from inherited ^{10}Be, while the second, third and fourth lines give the contributions from neutrons, slow muons and fast muons, respectively.

For my calculations I use a decay constant of 4.59×10^{-7} yr^{-1}. P_0 is calculated from the scaling factors of Stone (2000), using a sea-level, high-latitude surface production rate of 5.1 at g^{-1} yr^{-1}. The relative contributions and attenuation lengths are taken from Braucher et al. (2003) – p_n, p_s and p_f are 97.85%, 1.50% and 0.65%, and Λ_n, Λ_s and Λ_f are 150, 1500 and 5300 g cm^{-2}, respectively. Finally, I use my estimated bulk density of 1.935 g cm^{-3} to convert depths from cm to g cm^{-2}. (For the A2 fan, I find that the age is not significantly altered when I use my maximum or minimum estimates of bulk density – 1.80 g cm^{-3} and 2.07 g cm^{-3}, respectively – although the best match to the data is achieved at different values of inheritance – 2.5×10^{5} atoms g^{-1} and 1.9×10^{5} atoms g^{-1}, respectively).

A2 fan profile

Sediment exposed in the A2 pit comprises angular to sub-angular coarse gravels and pebbles of quartz-rich granite or mafic composition. The material is uncemented and shows only subtle stratification, although there is a clear layer of soft sand with occasional pebbles exposed in one pit wall at 50–70 cm depth (I use this fine-grained material for OSL dating in Section 3.3.3).

Averaged ^{10}Be concentrations decrease steadily from $\sim 12 \times 10^{5}$ at g $^{-1}$ at the surface down to $\sim 4 \times 10^{5}$ atoms g^{-1} at a depth of 125 cm, but then rise to $\sim 7 \times 10^{5}$ atoms g^{-1} for the 150 cm and 175 cm samples (Fig. 3.9a). The pit was situated close to the southern edge of the fan, and I probably excavated through A2 into an older deposit below, from which this final pair of samples was taken. There is no well-developed paleosol at the boundary of these two layers (at 125–150 cm), suggesting that the surface of the older deposit was removed when the younger material was deposited.

To determine the A2 exposure age I use a chi-squared inversion that minimises the difference between the observed ^{10}Be concentrations and vertical profiles predicted by theory (Siame et al., 2004). Details of this technique, together with the values I used for the production rates, attenuation lengths, decay constant and sediment density are provided in the supplementary material. Whatever the reason for the relatively high ^{10}Be concentrations in the deepest pair of samples, they are unlikely to reflect the exposure history of the fan surface and only the upper six samples are used in the inversion. Material collected from the surface may have a more complex history than the buried clasts (for instance, they are more likely to have been disturbed through bioturbation), so I also halve the weighting given to the 0 cm sample.

I begin by assuming a zero surface erosion-rate (the presence of desert varnish on rare large boulders suggests that only small amounts of erosion have occurred) and solving for the best-fit exposure age and inheritance. The best match between

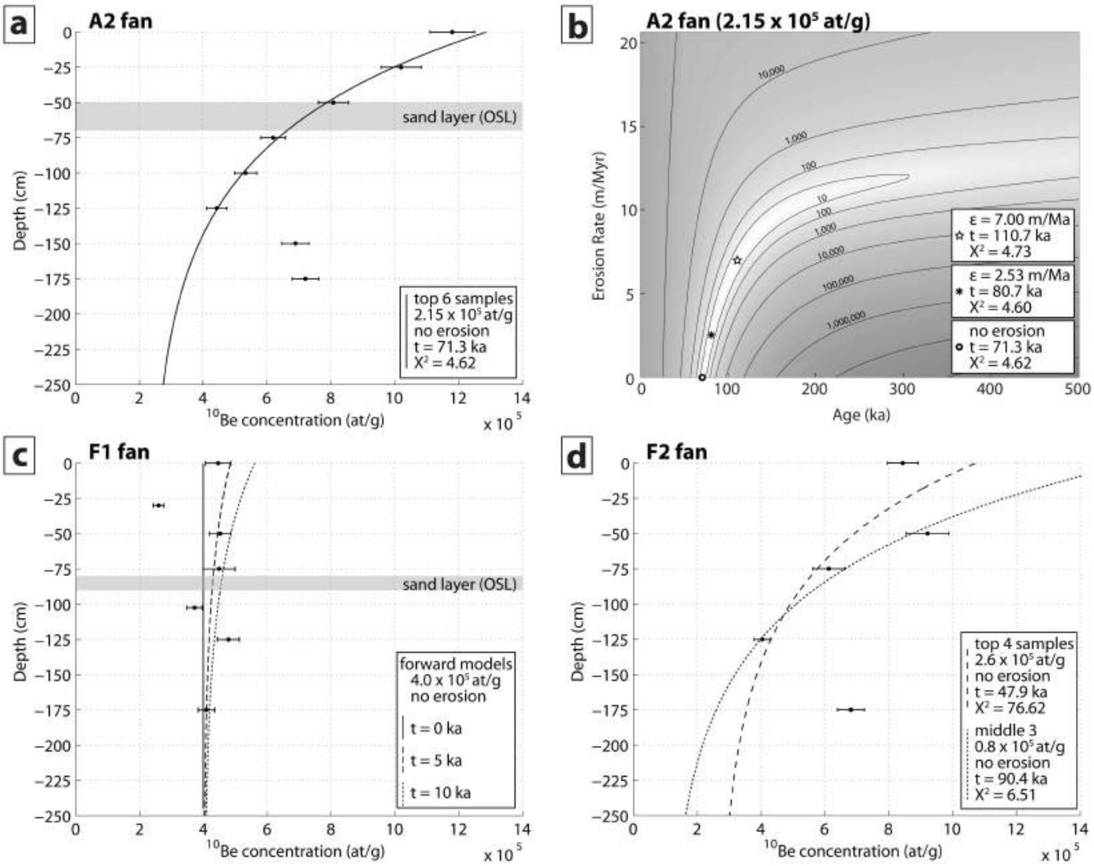

Figure 3.9: (a) Vertical profile of ^{10}Be concentrations (averaged over many clasts) through the A2 fan, with horizontal bars showing analytical errors at the 1σ level. The curved line represents the best-fit modelled distribution under the assumption of no erosion and discounting the lowest two samples (see text for details). (b) Plot of χ^2 values for a range of erosion rates and ages, using an inherited ^{10}Be concentration of 2.15×10^{5} atoms g^{-1}. The curved trough in χ^2 values demonstrates a clear trade-off in χ^2 between age and erosion rate. The circle represents the minimum age (using no erosion); the asterisk represents the overall best-fit age and erosion rate; and the star represents the best-fit age for a fixed erosion rate of 7 m Ma^{-1} (Vassallo et al., 2005). (c) Vertical profile of ^{10}Be through the F1 fan. Although I do not model this data, I do show forward-modelled distributions for ages of 0 ka, 5 ka and 10 ka. (d) Vertical profile of ^{10}Be through the F2 fan. Best-fit modelled distributions for the shallowest four samples and the middle three samples are shown as dashed and dotted lines, respectively. However, the wide scatter prevents us from establishing an exposure age for this surface.

observed and modelled concentrations (with $\chi^2 = 4.62$) is for an age of 71.3 ka and an inheritance of 2.15×10^{5} atoms g^{-1} (Fig. 3.9a). Because I have assumed no erosion, this estimate should be treated as a minimum age for the F2 fan.

The data is then modelled again, but with the erosion rate free to vary. Using an inherited component of 2.15×10^{5} atoms g^{-1}, the best match between observed and modelled concentrations (with $\chi^2 = 4.60$) is given by an erosion rate of 2.5 m Ma^{-1} and an age of 80.7 ka (because this model distribution lies very close to the 71.3 ka profile, I do not plot it separately on Fig. 3.9a). A good fit to the data can also be achieved at even greater ages, using higher erosion rates. This is demonstrated by a contour plot of χ^2 values for a range of ages and erosion rates (Fig. 3.9b); the pronounced trough of low χ^2 values demonstrates a strong trade-off between the two parameters. Interestingly, if I constrain the erosion rate to 7 ± 1 m Ma^{-1} – the value calculated for fans at similar elevations in the Gobi Altai (Vassallo et al., 2005) – a good fit to the data (with $\chi^2 = 4.73$) can be provided by ages of ∼100–120 ka (the star on Fig. 3.9b corresponds to an erosion rate of 7 m Ma^{-1} and an age of 110.7 ka). This would place A2 close in age to a number of fans in the Gobi Altai that are dated at ∼120 ka (Vassallo et al., 2005; Ritz et al., 2006), offering the possibility that periods of fan aggradation can be correlated over wide areas of Mongolia, presumably under the influence of climate.

From these arguments, it is clear that the precise age cannot be determined without better constraint on the erosion rate. From now on I will use the 71.3 ka figure as a minimum estimate of the exposure age, although it is worth reiterating that by allowing realistic rates of erosion, ages of up to about ∼120 ka are also permissible.

F1 fan profile

In general, the sediment exposed in the F1 pit closely resembles that of A2. Also like A2, a layer of soft sand is exposed in one of the F1 pit walls, at a depth of 80-90 cm. The F1 pit also contains a distinctive layer of larger cobbles, up to about 10 cm in diameter, at 30 cm depth.

F1 shows no clear decrease in average ^{10}Be concentration with depth, and all but one measurement falls close to 4×10^{5} atoms g^{-1} (Fig. 3.9b). This implies that levels of ^{10}Be are dominated by the inherited component, with only small amounts of additional ^{10}Be produced since deposition. The 30 cm sample contains an anomalously low concentration, which may reflect the unusually large size (and presumably shorter transport times) of clasts within this particular horizon.

The fan is clearly much younger than A2 or F2, but analytical errors are too large and the data too scattered (even discounting the 30 cm sample) for us to precisely constrain this age. On Fig. 3.9c I plot forward modelled ^{10}Be profiles, for ages of 0 ka, 5 ka and 10 ka, each with an inheritance of 4.0×10^{5} atoms g^{-1} (the average ^{10}Be concentration in F1). The relatively poor fit of the 10 ka curve would suggest a younger exposure age, but the scatter in the data is too high to provide any further constraints.

F2 fan profile

The material exposed in the F2 pit is somewhat finer grained than in A2 or F1, comprising angular to sub-angular gravels with rare cobbles. Like the other pits the sediment shows only subtle stratification, and there are no clear paleosols. Clasts are again either mafic or granitic, but the latter material contains abundant K-feldspar and is significantly less quartz-rich than in the other pits (presumably this reflects the variability of the granitic source in the Jargalant-Nuruu mountains).

Only five of my F2 samples yield measurable ^{10}Be concentrations. These vary from a minimum of $\sim 4 \times 10^{5}$ atoms g^{-1} up to a maximum of $\sim 9 \times 10^{5}$ atoms g^{-1}, but there is no simple, exponential decay with depth. Modelling the shallowest four samples under assumptions of no erosion yields a best-fit age of 47.9 ka and inherited component of 2.6×10^{5} atoms g^{-1}, but there is a poor fit to the data (the dashed line on Fig. 3.9c). If I discount the 0 cm sample, which may be contaminated by recent material deposited on the fan surface, a much-improved fit can be found, corresponding to an age of 90.4 ka and an inheritance of 0.8 × 10 ^{5} atoms g^{-1} (the dotted line on Fig. 3.9c). However, because of the overall scatter in the F2 profile I use the modelled profiles as approximate guides only, and prefer not to assign an exposure age to the fan.

The ^{10}Be profiles from the A2 and F1 fans are consistent with a relatively small variation in the average inheritance through time (up to ∼1 × 10 ^{5} atoms g^{-1}, discounting the 30 cm cobble layer in F1). Erosion and transport conditions in the F2 catchment area at the time of its deposition were probably similar, so there are likely to be only small variations in its average inheritance, too. The large scatter in the F2 ^{10}Be concentrations is therefore best be explained by pulses of fan-building, with at least three separate stages of aggradation. There are no well-developed paleosols in the F2 pit; however, as with the A2 fan, any soil that developed following an earlier stages of fan-building was probably eroded when the next pulse of sediment was deposited.

3.3.3 Optically Stimulated Luminescence (OSL) dating

A brief introduction to OSL dating

Optically Stimulated Luminescence (OSL) provides an alternative and independent method of determining the age at which sediments were deposited (e.g. Huntley et al., 1985). OSL is normally used to date fine-grained loess deposits, but with careful site description and interpretation its applicability can be extended to coarse, alluvial sediment (e.g. Fattahi et al., 2006).

Subjected to natural radioactivity, electrons within quartz grains are displaced from their mineral lattices and become stored in nearby lattice defects. These trapped electrons are released during prolonged exposure to sunlight, but can begin to accumulate once the grains are buried. Stimulating samples of buried quartz with laser light in the laboratory releases the trapped electrons together with photons of light (OSL). By comparing this natural OSL with the luminescence signals produced after the material is given known laboratory radiation doses, the total radiation received during burial (or “paleodose”) can be established. Meanwhile the dose rate received during burial is determined using measurements of radioactive U, Th and K in the surrounding sediment and from estimates of cosmic radiation. The age at which this sediment was last exposed to sunlight is then calculated by dividing the paleodose by the dose rate.

Fine-grained fluvial or aeolian sediments are preferred for OSL dating, because they are more likely to have undergone prolonged exposure to sunlight during transport, thus resetting the luminescence clock prior to deposition; if the grains were not fully bleached before burial then the true age of deposition can be over-estimated. The coarse gravels and pebbles within the three ^{10}Be sample pits are therefore a poor choice of material for OSL dating. However, the A2 and F1 pits each contain a layer of homogeneous, soft sand. These layers – which lie between depths of 50–70 cm in A2 and 80–90 cm in F1 – are only exposed on one wall of the pit. This is consistent with a channelised shape, and I interpret them as having been deposited by small, low-energy channels within the fan system. If this interpretation is correct then grains are likely to have undergone significant exposure to sunlight during transport, opening up the possibility of dating their burial with OSL.

Sampling and laboratory procedures

The sand layers in the A2 and F1 sampling pits were targeted for OSL dating. To collect samples a fresh surface was cut into the exposed sand layer, into which a metal tube was inserted (I used steel food cans). The tube was removed and the open end covered with duct-tape to ensure as little light as possible reached the uppermost sediment inside. The tube was then packed tightly with more duct-tape to prevent the material inside from shifting during transport, and wrapped in several layers of opaque black plastic. I collected two such samples from the sand layer in A2, and one from that in F1.

Under subdued red light in the laboratory, the sediment from the top and bottom of each tube (which may have been exposed to some light during sampling) was removed for estimations of the dose-rates received during burial. U, Th and K were measured in the laboratory with ICP mass spectroscopy, and moisture contents were determined by drying at 40°C. The resulting alpha, beta and gamma dose rates were calculated using the conversion factors of Aitken (1985), Bell (1980) and Mejdahl (1979). Dose rates received from cosmic rays were determined using the formula of Prescott & Hutton (1988). The U, Th and K contents, cosmic-ray dose rate and total dose rate recieved during burial (in Gy ka^{-1}) of each sample are shown in Table 3.2.

Sediment from the central part of the tube was used to determine equivalent dose (D_e). Samples were wet-sieved and immersed in 1 N HCl and two days in H_2O_2 to eliminate carbonates and organics, respectively. Heavy minerals (>2.72 g cm^{-3}) were then removed in a heavy liquid separation and the remaining quartz grains etched in 48% HF, rinsed in distilled water and dry-sieved. The quartz fraction was mounted as a monolayer on 10 mm diameter aluminium discs using a silicon spray as an adhesive. Between eleven and fourteen such discs were prepared from each sample.

To calculate D_e values, the Single Aliquot Regeneration procedure was used (Murray & Wintle, 2000). For each sample, the natural luminescence signal is first measured. Next, the sample is zeroed through exposure to light and its luminescence response to a series of known laboratory irradiation doses is measured. The D_e is then read off a straight-line plot of dose-responses, using the value of the natural luminescence signal. A full description of the experimental condition is provided by Fattahi et al. (2007).

Weighted mean D_e values (in grays) and luminescence ages are shown in Table 3.2.

Individual aliquot D_e values (in seconds) are plotted in Fig. 3.10.

A2 fan

Two separate samples were collected from the sand layer in the A2 pit. For sample A2a, D_e values agree to within error for seven out of the eleven aliquots, producing a well-defined peak in dose distributions (Fig. 3.10a). The remaining four aliquots show significantly higher D_e values, suggesting that not all grains were completely reset before deposition. Using the weighted mean D_e (shown in Table 3.2), I determine a luminescence age of 18.8 ± 3.5 ka (with 1σ error bounds). D_e values from the fourteen aliquots from sample A2b are distributed in three clusters (Fig. 3.10b), but nevertheless provide a weighted mean D_e and age (19.8 ± 8.5 ka) consistent with that of A2a. Both luminescence ages from the A2 surface are significantly younger than even the minimum exposure age (71.3 ka) calculated from modelling ^{10}Be concentrations from the same pit (Fig. 3.9a); I discuss this discrepancy in Section 3.3.4.

F1 fan

Paleodoses for the F1 sample show an even spread between about 250–400 s, except for two aliquots that register significantly higher values (Fig. 3.10c). Using the weighted mean D_e I calculate a luminescence age of 6.3 ± 1.7 ka, consistent with the young ages expected from the distribution of ^{10}Be in the same pit.

Sample	*Equivalent dose (Gy)*	*K (%)*	*U (ppm)*	*Th (ppm)*	*Cosmic dose rate (Gy/ka)*	*Total dose rate (Gy/ka)*	*Age (ka)*
A2a	70.68 ± 12.37	2.806 ± 0.028	1.7 ± 0.052	5.6 ± 0.168	0.252 ± 0.135	3.76 ± 0.18	18.8 ± 3.5
A2b	73.38 ± 31.04	2.847 ± 0.028	1.4 ± 0.052	5.3 ± 0.168	0.252 ± 0.135	3.70 ± 0.18	19.8 ± 8.5
F1	28.75 ± 7.53	2.507 ± 0.028	4.3 ± 0.052	11.8 ± 0.168	0.243 ± 0.135	4.55 ± 0.18	6.3 ± 1.7

Table 3.2: Weighted mean equivalent doses for two samples from the A2 sampling pit and one from the F1 sampling pit, calculated from individual aliquot D_e values. Also displayed are measurements of radioactive K, U and Th, and estimates of the cosmic dose rate; these values are used to calculate the total dose rate received by each sample during burial. The final column shows OSL ages, determined by dividing the weighted mean equivalent dose by the dose rate received during burial. All errors are shown at the 1σ level.

3.3.4 Slip-rate calculations

Here I discuss the discrepancy between the A2 minimum exposure age (71.3 ka) and the A2 burial ages (18.8 ± 3.5 ka and 19.8 ± 8.5 ka), and the implications of these age data for determining the fault slip-rate.

The calculated exposure age for the A2 fan relies on the assumption that the averaged inherited ^{10}Be component is constant within the six samples used in the inversion. However, if there was a fluctuation in the average inherited component as the fan was deposited, then the true exposure age could be different from that provided by my modelled distribution. However, this scenario is unlikely, because ^{10}Be concentrations in the young, F1 deposit suggest that the inheritance has remained relatively unchanged during the course of fan deposition (with the exception of the coarse, cobble layer at 30 cm).

The alternative interpretation for the discrepancy is that I have somehow underestimated the A2 burial age using OSL. This could have occurred if the sediment was partially bleached after burial, although there are no indications within the pit of bioturbation and only the ends of the sampling tube could have undergone any exposure during sampling. However, I cannot rule out the possibility that sediment shifted within the sampling tubes during transport, such that bleached grains at the tube ends were mixed in with the pristine material in the central part of the tubes (which was used for the OSL measurements). A final possibility is that my measurements of radioactive K, U and Th within my samples – from which I estimate the dose-rate received during burial – may not be representative of the sediment as a whole. This further uncertainty is not reflected within my error bounds, and may have lead to an under-estimation of the luminescence ages.

To calculate the slip-rate, I divide the 155 ± 30 m displacements of the older surfaces by estimates of the age of the A2 fan; because it is not immediately clear whether the cosmogenic ^{10}Be age or the OSL age is accurate, I use both estimates in

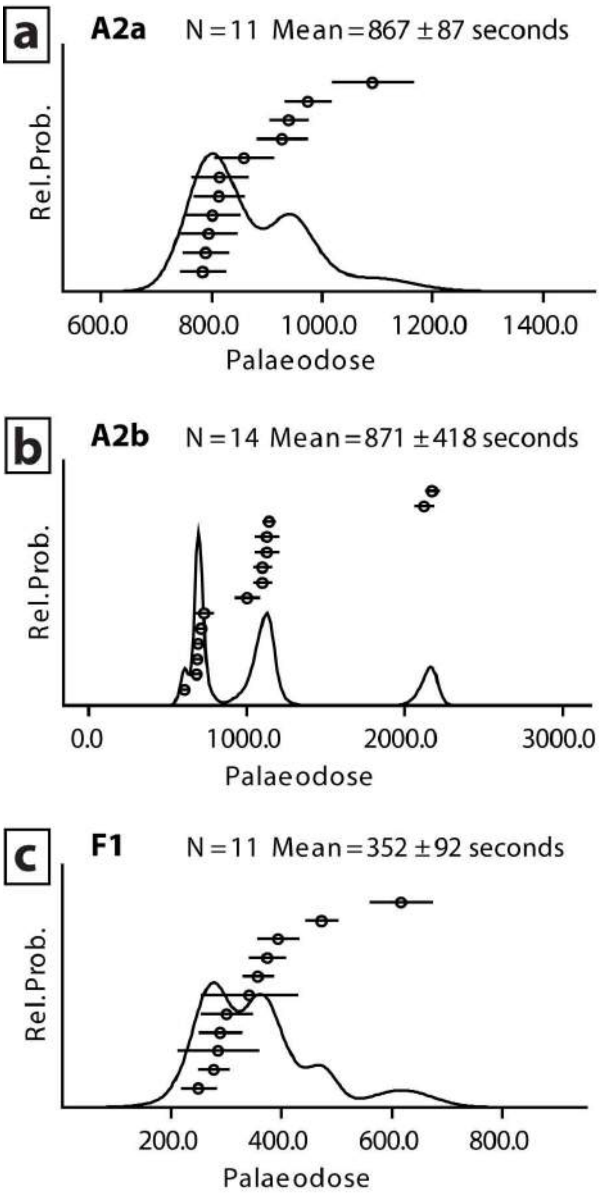

Figure 3.10: Equivalent dose distribution plots for OSL samples (a) A2a, (b) A2b and (c) F1. The x-axis represents the number of seconds of exposure to a known beta source (delivering $\sim$5 Gy min^{-1}) required to reproduce the natural OSL signal. There are N aliquots in each sample, and Mean is the weighted mean D_e for all these aliquots. D_e values for individual aliquots are displayed in rank order, with an overall probability density function superimposed on top. Error bars in individual aliquot D_e values are based on photon-counting statistics, an error in fitting a straight line through the dose-response plots, and a 1% systematic error.

my slip-rate calculations. On the one hand, the minimum exposure age for the A2 fan (71.3 ka) gives a maximum horizontal (right-lateral) slip-rate of 1.8–2.6 mm yr^{-1}, with a preferred value of 2.2 mm yr^{-1}. (As discussed in Section 3.3.2, if I consider an erosion rate of ~7 m Ma^{-1} (Vassallo et al., 2005) the age of the fan could be up to ~120 ka, so the slip-rate might conceivably be as low as 1.0–1.5 mm yr^{-1}). On the other hand, the luminescence age of sample A2a (18.8 ± 3.5 ka) provides a horizontal slip-rate of 5.6–12.1 mm yr^{-1}, with a preferred value of 8.2 mm yr^{-1}.

Assuming the 12 ± 2 m displacement of the F1–F2 riser dates from abandonment of the F1 surface, and using the luminescence age for sample F1 (6.3 ± 1.7 ka), I calculate a horizontal slip-rate of 1.3–3.0 mm yr^{-1}, with a preferred value of 1.9 mm yr^{-1}. Although I cannot be certain that the riser was completely reset before F1 abandonment, this figure is much closer to the ~2 mm yr^{-1} slip-rate calculated with the exposure age of the A2 fan than the ~8 mm yr^{-1} slip-rate calculated with its burial age. This would imply that the exposure age for the A2 fan is correct, and the luminescence age too young.

Finally, dividing the 0.4–0.8 m vertical displacement across the F1 scarp by the 6.3 ± 1.7 ka burial age provides a vertical slip-rate of $0.10\ ^{+0.07}_{-0.05}$ mm yr^{-1} across the fault.

3.4 Paleo-earthquake ruptures

I found clear paleo-earthquake ruptures on a section of the Har-Us-Nuur fault just south of the displaced alluvial fans studied in Section 3.3, presumably from the last event to have struck this section of the fault. These ruptures can also be seen in high-resolution ASTER and SPOT-5 images, where they appear as a series of lineations picked out either by snow drifts or dark vegetation. Field photographs of the ruptures are shown in Fig. 3.11. Where best preserved, they consist of a left-stepping, en echelon arrangement of ~N–S fissures, consistent with right-lateral

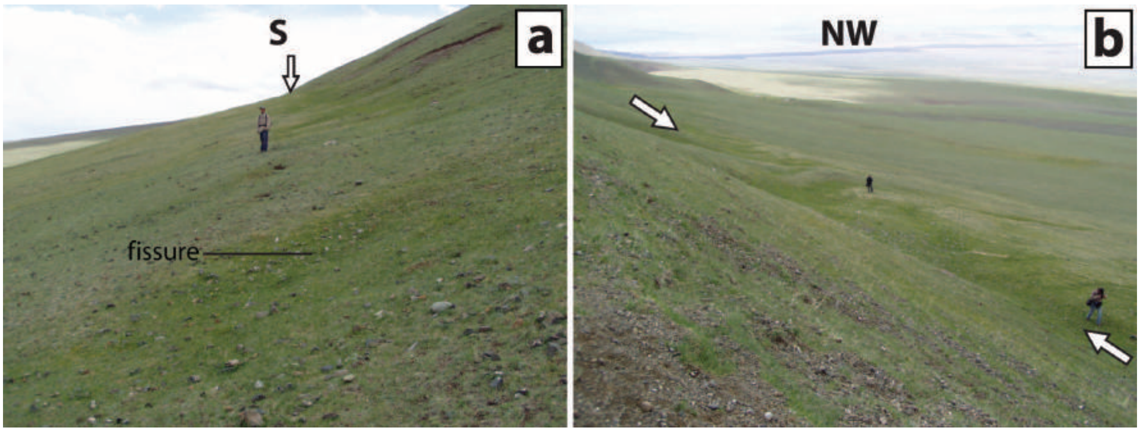

Figure 3.11: Photographs facing (a) ~S and (b) ~N of en echelon tension fissures at 47° 47' 20" N 92° 31' 58" E. The location of these fissures, and the overall extents of the paleo-earthquake ruptures, are shown on Fig. 3.1.

strike-slip along the ~NNW-SSE trending fault. The fissures are now largely infilled, but can be distinguished from the surrounding, unbroken ground by the slightly denser vegetation growing in them. They are typically ~5–15 m in length and 1.0–1.5 m wide, and their along-strike width, ~2–3 m, provides a rough indication of the amount of slip that occurred in the earthquake.

Records of 20th century seismicity – such as the Global CMT and Engdahl et al. (1998) catalogues – list no nearby large earthquakes, so the ruptures are likely to be more than 100 years old. Their overall level of preservation is similar, or perhaps somewhat better, than the ruptures dated at 870–980 years on the Jid fault (Walker et al., 2006). I therefore bracket the age of the Har-Us-Nuur ruptures at 100–900 years.

I mapped the ruptures for a total distance of 30 km along the Har-Us-Nuur fault (Fig. 3.1). This length-scale is consistent with the observed coseismic slip of ~2.5 m, giving a realistic slip:length ratio of 8.3×10^{-5} (Scholz, 1982). Using these values, assuming faulting extended to 15 km depth, and taking a shear modulus of 3×10^{10} Pa, I estimate a moment of ~3.63×10^{19} Nm and a moment magnitude (M_w) of ~7. Dividing the coseismic slip (2–3 m) by the slip-rate calculated from the A2 exposure age (2.2 ± 0.4 mm yr^{-1}) gives an average repeat interval of about 1100 $^{500}_{-400}$ years between earthquakes on this particular segment of the fault. If the slip-rate calculated from the A2 luminescence age (8.2 $^{+3.9}_{-2.6}$ mm yr^{-1}) is used instead, the average repeat interval would be about 300 $^{+200}_{-100}$ years.

3.5 Apatite fission track (AFT) analysis

The initiation of strike slip on the Har-Us-Nuur fault is linked to the onset of mountain-building within its restraining bends, including the Jargalant-Nuruu massif within this study area (Fig. 3.1). In this section I use apatite fission track data to examine the low-temperature thermal history of the Jargalant-Nuruu. Following an E–W transect across the central part of the range (at a latitude of ∼47° 40’) I collected eight bedrock samples from the up-thrown side of the Har-Us-Nuur fault (Fig. 3.1). The highest samples were collected from the uplifted peneplain surface at an elevation of 3502 m (around 300 m below the highest peak of Jargalant-Nuruu), whilst the lowest sample was taken from the foot of the range, at 2446 m. The exposed bedrock is generally metasedimentary, although two intrusions – one basic and one acidic – were also sampled (Table 3.3).

After crushing and sieving, conventional magnetic and heavy liquid separation techniques were used to search for the presence of apatite. Unfortunately only sam-

Sample	*Coordinates*	*Elevation*	*Description*	*Apatite?*	*Central age (Ma)*
1a	47° 39’ 45” N 92° 36’ 03” E	3502 m	basaltic dyke	no	-
1b	47° 39’ 45” N 92° 36’ 03” E	3502 m	meta-conglomerate	no	-
2	47° 39’ 55” N 92° 36’ 37” E	3187 m	meta-sedimentary	no	-
3	47° 40’ 07” N 92° 36’ 52” E	3165 m	meta-conglomerate	no	-
4	47° 40’ 07” N 92° 37’ 33” E	2868 m	felsic intrusion	5 grains	150 ± 22
5a	47° 40’ 13” N 92° 38’ 20” E	2565 m	conglomerate	no	-
5b	47° 40’ 13” N 92° 38’ 20” E	2560 m	conglomerate	no	-
6	47° 39’ 59” N 92° 39’ 01” E	2446 m	meta-siltstone	no	-

Table 3.3: Apatite fission-track samples, taken from a traverse of the eastern flank of Jargalant-Nuruu (see Fig. 3.1). The radial plot for Sample 4 is displayed in Fig. 3.12.

ple 4 – from an acidic intrusion at 2868 m elevation – contained any apatite at all, and then only five 80–500 μm grains. These grains were mounted in epoxy resin on glass slides, and then ground and polished them to an optical finish to expose internal grain surfaces; these were then etched with 5N HNO_3 for 20 s at 20°C to reveal spontaneous tracks. Mounts were fitted with muscovite external detectors and irradiated at the Garching reactor in Munich, with the Corning CN-5 glass dosimeter used to monitor the neutron flux. The external detectors were then etched in 40% HF for 20 min at 25°C, revealing the induced fission tracks. Track densities were measured with a Zeiss Axioplan optical microscope at 1,250× magnification using dry objective.

Fission-track ages were calibrated using the ζ method (Hurford & Green, 1983). A radial plot of data for individual grains is shown in Fig. 3.12. The χ^2 test shows that the spread in single-grain ages is within the normal range predicted by Poissonian statistics for a single age population. The central age (see Galbraith & Laslett, 1993), weighted for the different precisions of individual grains, is 150 ± 22 Ma.

Sample 4 therefore passed through the apatite partial annealing zone – between ~110°C and ~60°C (Green et al., 1986) – at some point during the late Jurassic or early Cretaceous. The central age is consistent with ages calculated by Vassallo (2006) for samples on nearby Baatar Hyarhan (192 ± 7 – 154 ± 10 Ma) and Ih Türgen Uul (136 ± 7 – 82 ± 7 Ma). It also agrees well with central ages for the Gobi Altai range further SE (Vassallo et al., 2007a), and probably relates to a major period of exhumation that affected the whole of western and central Mongolia during the late Mesozoic (Cunningham, 2001; Jolivet et al., 2007).

Unfortunately, my bedrock samples yielded too little apatite for us to constrain the timing of the most recent, late Cenozoic, period of uplift. I had hoped to complement the fission track analysis with apatite (U-Th)/He thermochronology, which has an even lower temperature partial retention zone (between ~80°C and ~40°C),

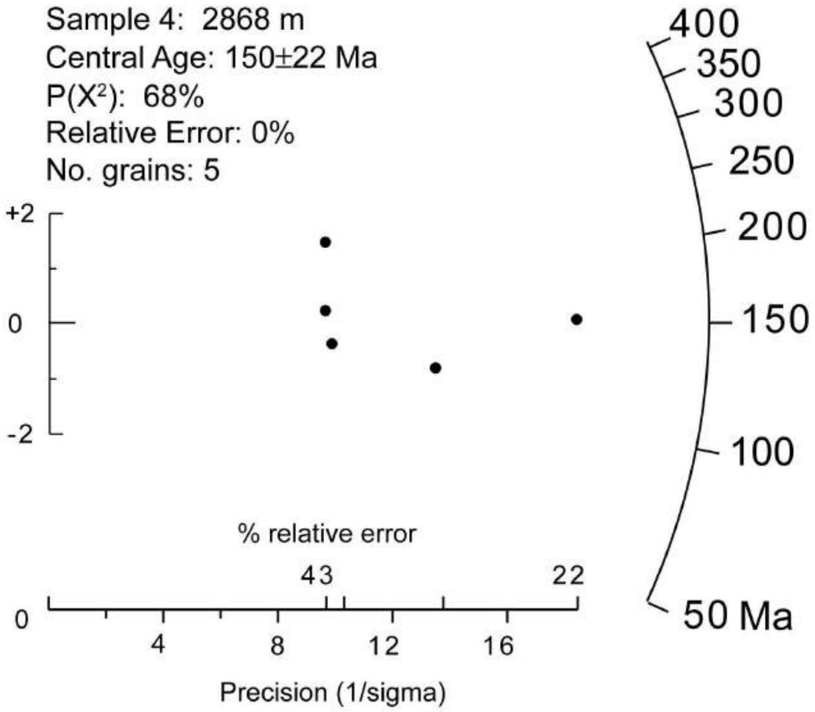

Figure 3.12: Radial plot of apatite fission track data for Sample 4 (see Galbraith & Laslett, 1993). The standardized error on single-grain ages is plotted on the *y*-axis, and the percentage of relative error on each single-grain age on the *x*-axis. Single-grain ages can be read by projecting a straight line from the origin of the left-hand (standardized error) scale, through the datapoint in question, to the radial scale on the right-hand side which represents the age in Ma. P(χ^2) is the probability of obtaining χ^2 value for n degrees of freedom, where n is the number of grains -1 (Galbraith, 1981). The central age (± 2σ) is a modal age, weighted for the different precisions of individual crystals (Galbraith & Laslett, 1993).

but this method requires greater concentrations of apatite than were present in my samples.

3.6 Discussion

Despite being unable to constrain the low-temperature thermal history of the Jargalant-Nuruu range, I can still provide a crude measure of the age of the Har-Us-Nuur fault by dividing the cumulative slip by the late Quaternary slip-rate. In this section I do this calculation, and then investigate implications for the evolution of faulting and topography across the Altai range.

At the alluvial fans studied in Section 3.3, the Har-Us-Nuur fault strikes ∼162° and has a horizontal slip-rate of 2.2 ± 0.4 mm yr^{-1} (according to my minimum exposure age). Adjacent to the highest part of the Jargalant-Nuruu range the fault strikes 148°, giving a shortening component of ∼0.4–0.6 mm yr^{-1}. Field observations constrain the fault dip to the range 50°–70° W, giving a vertical displacement rate of ∼0.5–1.7 mm yr^{-1} adjacent to the highest part of the range. At this rate, the 2000 m throw on the fault would be achieved in around 1.2–4.0 Ma.

Following the same arguments but assuming the A2 age of ∼120 ka age and a slip-rate of 1.0–1.5 mm yr^{-1}, the total throw would be achieved in 2.0–6.7 Ma. At the same time, if the OSL-derived slip-rate of $8.2\,^{+3.9}_{-2.6}$ mm yr^{-1} is correct, the total throw would be achieved in only ∼0.2–1.2 Ma.

Although these are crude estimates, they are significantly younger than initial India-related uplift in the Altai region as a whole, which is thought to date from the late Oligocene or early Miocene (∼28–5 Ma), as discussed in Chapter 1.3.4. This would suggest that active deformation migrated to the Har-Us-Nuur fault from elsewhere within the range.

The interior part of the Altai, which contains more continuous mountainous terrain than along the Har-Us-Nuur fault (Fig. 1.5), is an obvious choice for the focus of earlier deformation. If faults in this interior part of the range are, indeed, older, then they are likely to have rotated further about vertical axes in order to accommodate overall convergence; this is illustrated by the difference in strike between the 2003 Chuya earthquake in the interior Altai (∼WNW) and the 1931 Fu-Yun earthquake along the western margin of the range (∼NNW; Fig. 1.5). These rotations place older faults in the range interior at a higher angle to the regional convergence direction and gives them a relatively large component of shortening. Topography produced by this dip-slip component in turn increases the normal stresses acting on the faults and promotes the migration of deformation onto younger strike-slip faults with favourable orientations. New faults forming in high areas, where the topography is already elevated, would need to do more work against gravity in order to accommodate convergence than faults in low-lying regions. This highlights a possible mechanism for the migration of deformation onto faults in low areas at the range margins, such as the Har-Us-Nuur fault.

3.7 Conclusions

I date an abandoned alluvial fan, displaced right-laterally by ∼155 m along the Har-Us-Nuur fault in the eastern Mongolian Altai mountains, using vertical profiles of cosmogenic ^{10}Be and Optically Stimulated Luminescence. The first method provides a minimum age of ∼70 ka, but OSL yields an age of only ∼19 ka. These estimates yield right-lateral slip rates of ∼2 mm yr^{-1} and ∼8 mm yr^{-1}, respectively. However, an offset terrace riser preserved above a younger, ∼6 ka fan, provides a slip-rate of ∼1–3 mm yr^{-1}, more consistent with the ∼2 mm yr^{-1} estimate. Assuming this lower estimate is representative of the long-term slip, and using the ∼2 km vertical displacement of a Mesozoic peneplain as a marker of total strain, I date the onset of movement on the fault at 1–4 Ma. This age is probably younger that the initial uplift of the Altai, which dates from the late Oligocene or Miocene (28–5 Ma; e.g. Devyatkin, 1974, 1981; De Grave & Van den haute, 2002; Howard et al., 2003; Yuan et al., 2006). My results suggest that active deformation may be migrating away from the high, interior Altai, onto faults at the margins of the range, possibly because the older faults have rotated about vertical axes into orientations that require work to be done against gravity.

Chapter 4

Late Quaternary slip-rates at Baatar Hyarhan

4.1 Introduction

The specific focus of this chapter is active faulting around the margins of Baatar Hyarhan, a major massif in the south-eastern Altai (Fig. 1.5). Baatar Hyarhan is not associated with any of the major strike-slip faults in the Altai, and its uplift is instead accommodated by a series of thrust faults exposed along its margins and in the surrounding basins. Several of these thrusts break the surface, producing clear scarps through late Quaternary alluvial deposits. This contrasts with many other regions of continental thrusting, where shortening in the uppermost sedimentary layers is often taken up by folding, making it difficult to study the underlying "blind" thrusts using surface measurements (e.g. Yielding et al., 1981).

My first aim is to describe the contrasting styles of shortening around the margins of Baatar Hyarhan, and interpret how this faulting has evolved over time. In particular I make use of 2.5 m-pixel Satellite Pour l'Observation de la Terre (SPOT 5) data, which provides details that are difficult to uncover with lower-resolution images or fieldwork. A second aim is to test the applicability of optically stimulated luminescence (OSL) for dating alluvial deposits cut by the faults. Most slip-rate studies in Mongolia have relied on *in situ*-produced cosmogenic ^{10}Be for dating fan deposits (e.g. Ritz et al., 2006), but this method contains inherent assumptions (about the inherited level of ^{10}Be, its long-term production rate and the rate of erosion) and it is useful to test independent dating methods in a similar environment.

With OSL I calculate late Quaternary displacement rates on these thrust faults at Baatar Hyarhan – the first to be published anywhere in the Altai – allowing us to put the faults into a regional context. Another advantage of Baatar Hyarhan as a study area is that its long-term cooling history has already been determined through apatite fission-track and (U-Th)/He thermochronology (Vassallo, 2006). These results, summarised in Section 4.2.2, provide us with constraints on the initiation of uplift-related exhumation and permit the comparison between late Quaternary and geological rates of deformation.

As well as providing ages for fault slip-rate calculations, dating late Quaternary alluvial deposits yields important information about past climate. In the Qilian Shan mountains of north-eastern Tibet, major periods of strath terrace formation occurred at the transitions from cold and dry glacial periods to warmer and wetter interglacials (Pan et al., 2003). A similar climatic control on alluvial fan aggradation has also been proposed for the Gobi-Altai range, where pulses of fan building can be correlated over areas many tens of kilometers wide (Vassallo et al., 2005; Ritz et al., 2006). OSL dating will allow me to observe whether periods of alluvial fan and river terrace formation in the eastern Altai range correlate with those in neighbouring regions of central Asia.

4.2 Overview of Baatar Hyarhan and surrounding basins

Transpressional uplift along strike-slip faults may represent the dominant mode of mountain building in the Altai, but there are also a number of isolated massifs in the eastern part of the range that show clear thrust scarps through Quaternary deposits along their margins (some of these are labelled in Fig. 1.5). Baatar Hyarhan (also referred to as Baataryn Nuruu or Baatar Khairkhanii) is the southernmost of these massifs. It trends NW–SE, is around 100 km in length and up to 20 km wide, and reaches a maximum elevation of 3984 m, more than 2 km higher than the Zereg Basin ($\sim$1100 m) to the north-east and the Tsetseg Basin ($\sim$1700 m) to the south (Figs. 4.1a & 4.2a). In this section I provide an overview of the bedrock geology, uplift history and geomorphology of the range.

4.2.1 Bedrock geology

The bedrock of Baatar Hyarhan comprises Cambrian granite in the core of the range, surrounded by Paleozoic volcanics, metamorphics and sediments (Zaitsev et al., 1989). Because these rocks trend NW-SE there is little variation in bedrock lithology along the length of the range. The surface geology of the surrounding depressions primarily consists of Quaternary alluvium shed from Baatar Hyarhan and other nearby massifs. In addition, parts of the Zereg Basin contain low, NW-trending ridges, known locally as 'forebergs', that expose older Mesozoic and Tertiary sediments (Howard et al., 2003). Forebergs exist in a number of other places in Mongolia, especially along the Gobi-Altai range (in the southern part of the country) where they were first described (Florensov & Solonenko, 1963). Resulting from thrusting and folding of the Earth's surface in areas of thick alluvial cover, they form adjacent (and parallel) to range-bounding thrust or oblique-slip faults and are thought to represent the propagation of these faults into their forelands (e.g. Owen et al., 1997, 1999; Bayasgalan et al., 1999b). There are two sets of forebergs in the study area: one near the Bumbat Nuruu range, on the eastern side of the Zereg Basin (Fig. 4.2b), and one close to Baatar Hyarhan itself, on the southern side of the depression (Fig. 4.2c).

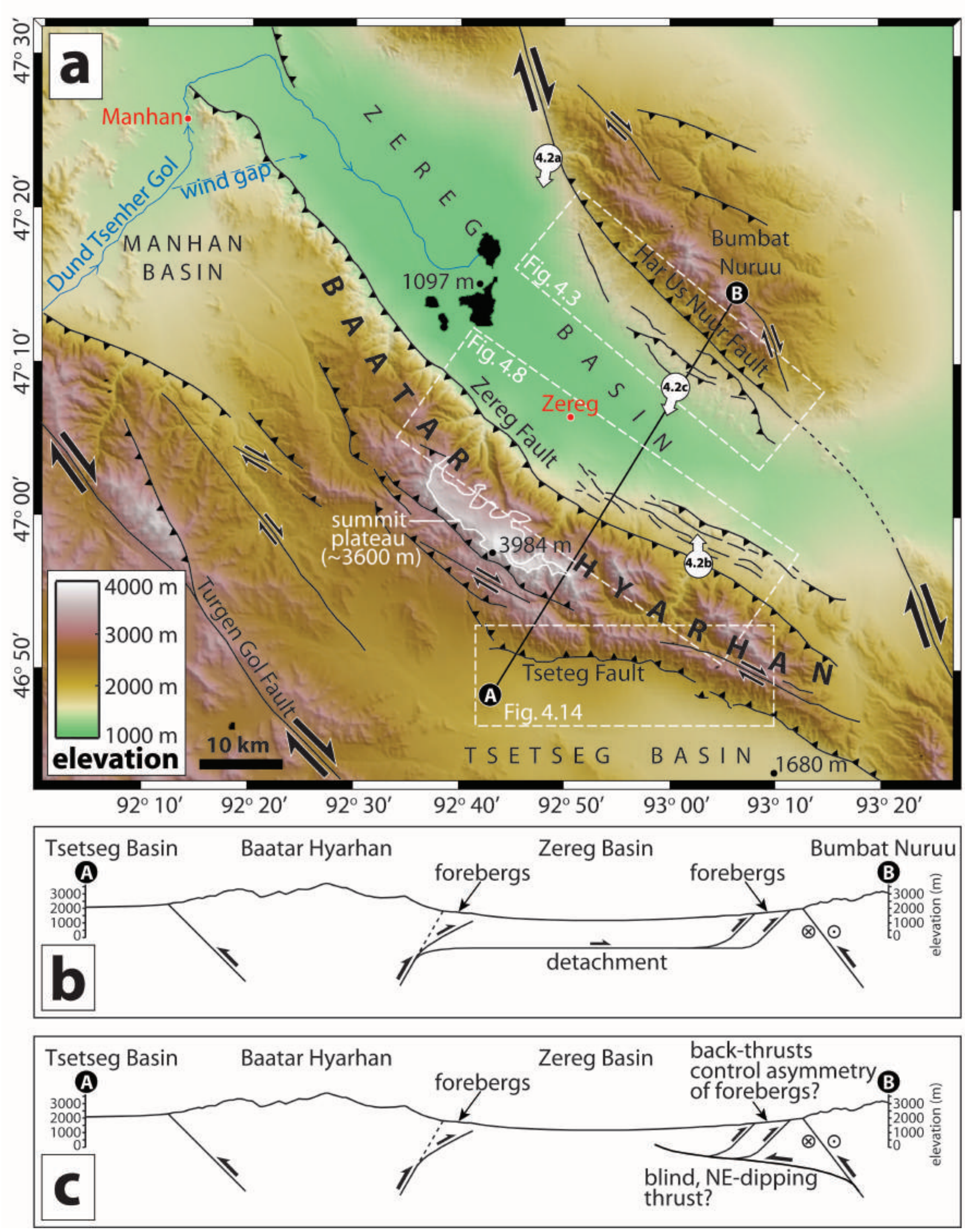

Figure 4.1: (a) SRTM topography and faults of the Baatar Hyarhan range and surrounding basins, displayed in the local UTM zone (46) projection (as are subsequent maps) and artificially sun-shaded from the NE. The location of the map is shown as a red, dashed box on Fig. 1.5. The dashed blue line shows a former course of the Dund Tsenher Gol river through what is now an air gap in the north-western part of the range. (b) Schematic cross-section through my study area. (c) Alternative interpretation, in which NE-verging folds in the eastern Zereg basin are controlled by back-thrusting above a blind, NE-dipping thrust. For reasons discussed in Section 4.3.1, I prefer the interpretation shown in (b).

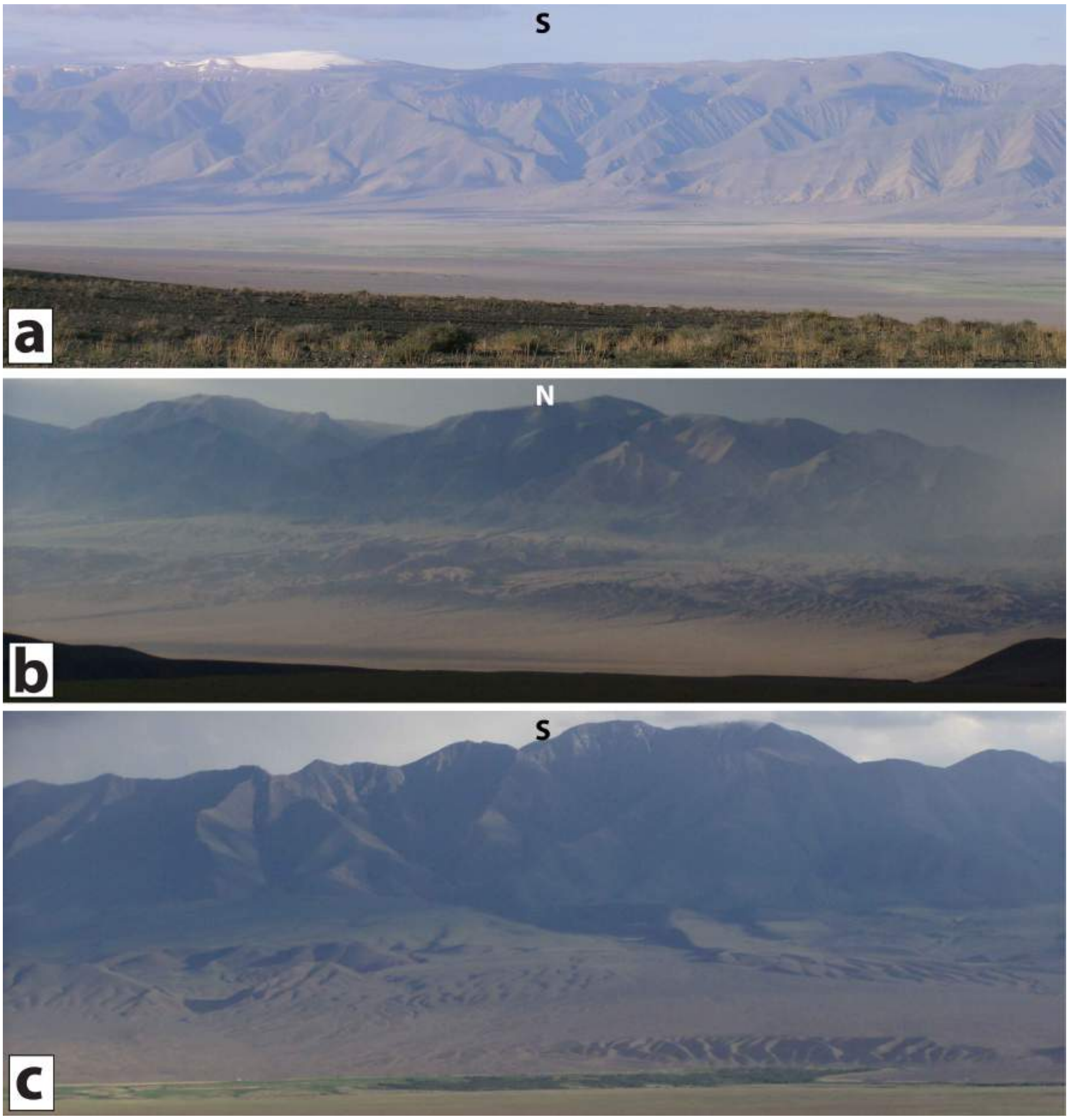

Figure 4.2: Field photographs of Baatar Hyarhan and nearby forebergs, taken from the locations plotted on Fig. 4.1a. (a) View S from 47°23’45”N 92°49’12”E, looking across the Zereg Basin (elevation $\sim$1100 m) towards the central Baatar Hyarhan massif with its flat summit peneplain and small glacier (at $\sim$3600 m). (b) View N from 46°57’06”N 93°02’53”E towards part of the E Zereg Basin forebergs, with the Bumbat Nuruu mountains behind. (c) View S from 47°08’06”N 93°00’42”E towards the western part of the S Zereg Basin forebergs, with SE Baatar Hyarhan behind. Note the sharper peaks and ridges of this part of the Baatar Hyarhan massif in comparison with the central part, shown in (a).

4.2.2 History of uplift

The cooling history of Baatar Hyarhan has been quantified through apatite fission-track (AFT) and (U-Th)/He measurements of bedrock samples from the Boorguinn Gol valley in the central section of the range (Vassallo, 2006; Fig. 4.8). AFT central ages range from 154–192 Ma, whilst those from analysis of (U-Th)/He range from 77–127 Ma. Temperature-time paths obtained by modelling this data confirm the late Mesozoic age of the summit plateau and place the latest, late Cenozoic stage of uplift at ∼5–1 Ma.

This is somewhat younger than an estimate of the onset of late Cenozoic uplift based on sedimentological grounds (Howard et al., 2003). Strata exposed in the S Zereg Basin forebergs show coarsening grain-sizes together with a switch to a south-westerly source during the Miocene (23–5 Ma). This may represent the earliest growth of Baatar Hyarhan, although there are uncertainties in the exact age of the material, as well as its origin (which might lie in ranges other than Baatar Hyarhan, such the mountains SW of the Tsetseg Basin).

4.2.3 Range geomorphology: lateral propagation?

The topographic characteristics of Baatar Hyarhan change notably along its length (Fig. 4.1a). The SE section (east of 92°50'E) is the most heavily eroded part of the massif, containing sharp peaks and ridges of up to ∼3500 m elevation, separated by deep, wide valleys. In contrast, the central section of the range (between 92°35'E and 92°50'E) contains a wide summit plateau at ∼3600 m elevation (Fig. 4.2a), part of the vast late Mesozoic peneplain surface observed throughout western and central Mongolia (Jolivet et al., 2007). In the final section of the massif (west of 92°35'E) the elevated topography – including remnants of the peneplain – gradually tails off towards the NW, dying out completely near the town of Manhan. Given that neither lithology nor climate varies significantly along the length of Baatar Hyarhan, the deep incision observed in the SE part of the range suggests that this area has been subjected to erosion for longer than the central and NW sections, where the peneplain is preserved.

Near Manhan, the Dund Tsenher Gol river flows round the north-western tip of the range on its way into the Zereg Basin (Fig. 4.1a). Around 12 km to the south a pronounced, linear depression (or wind-gap) indicates a probable former course of the river through what is now an uplifted part of the range. There are a number of possible reasons for the north-westwards shift in the course of the Dund Tsenher Gol river over time. It might either reflect the lateral growth of the Baatar Hyarhan from the SE towards the NW over time (Keller et al., 1998, 1999), or a lower uplift rate at the north-western end of the massif, or alternatively some past climatic change that reduced the river incision rate. Taken together with the lateral variation in the dissection of the summit peneplain, however, I support the view that the range has propagated from the SE towards the NW over time.

4.3 Active faulting

I now investigate variations in the style of shortening along the margins of Baatar Hyarhan, focusing on four contrasting sections of faulting. If the range has grown north-westwards over time (Section 4.2.3), then these changes help constrain how faulting in the region evolves over time. For three out of four sections I am also able to establish rates of uplift and horizontal shortening, using alluvial fans and river terraces as markers of fault slip and optically stimulated luminescence (OSL) to date these surfaces.

In Section 4.3.1, I study shortening across the forebergs in the eastern Zereg Basin; these trend parallel with the highest part of the massif, but lie about 20 km away to the NE. In Section 4.3.2 I focus on the forebergs in the southern Zereg Basin, which lie next to the most eroded (SE) part of Baatar Hyarhan (in this case no dateable material is found, so I do not provide constraints on rates of deformation). In Section 4.3.3 I investigate thrusting along the range-bounding Zereg fault, focusing on thrust scarps adjacent to the highest part of the range. Finally I switch my attention to the SW side of the range, studying the range-bounding Tsetseg fault in Section 4.3.4.

It should be noted that in all four study areas I primarily consider the reverse component of motion. There are no obvious indications in the geomorphology of a right-lateral strike-slip component to any of the main active thrusts, although given the tectonic setting I do not rule out there being one, in particular on the SW side of the range (discussed in 4.3.4).

4.3.1 Eastern Zereg Basin forebergs

The eastern Zereg Basin contains a series of foreberg hills in which Mesozoic and Tertiary sediments have been uplifted next to the SW margin of the Bumbat Nuruu mountains (Figs. 4.2b & 4.3). At first glance these hills resemble forebergs of Bumbat Nuruu, but a closer inspection reveals a series of fault and fold scarps that all face north-eastwards; furthermore, the main folds also verge towards the north-east. This provides strong evidence that the underlying thrusts dip south-west, towards Baatar Hyarhan (e.g. Howard et al., 2003).

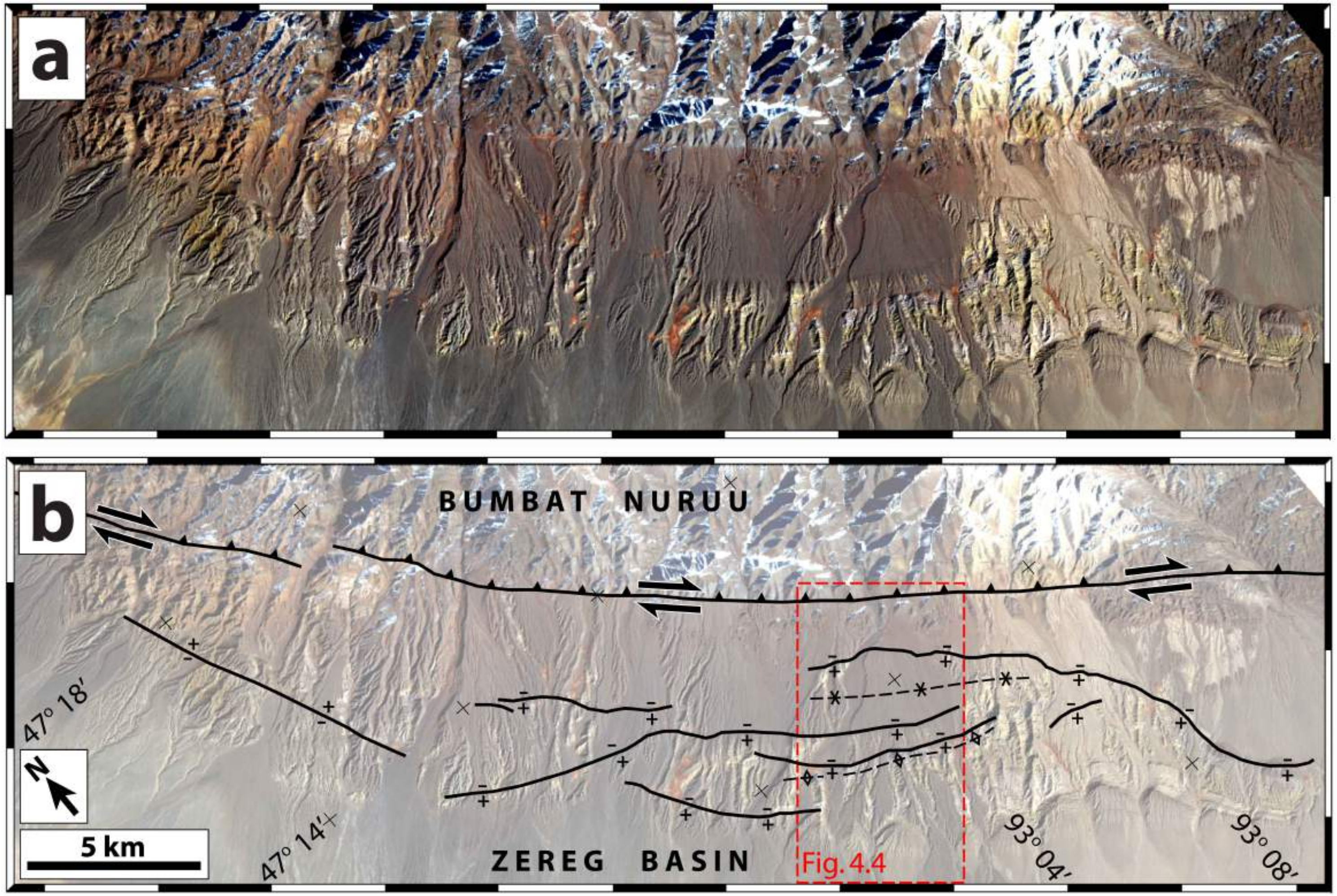

Figure 4.3: (a) ASTER image (15 m resolution; RGB 321) of the eastern Zereg Basin forebergs. The location of the map is shown as a dashed box on Fig. 4.1a. (b) The same view, with scarps plotted as thick solid lines (+/- indicates the sense of displacement) and fold axes as thin dashed lines.

Stratigraphy

Several perennial streams sourced from Bumbat Nuruu are actively incising into the forebergs, creating a badlands-style terrain in which the stratigraphy of the Mesozoic and Tertiary sediments is well exposed (Figs. 4.4 & 4.5a). This stratigraphy is described in detail by Howard et al. (2003), although there may be considerable uncertainties in the precise ages of the sediments, which were estimated using sometimes sparse fossil remains. The oldest strata are Lower Cretaceous, and consist of fine-grained lacustrine and floodplain deposits (divided into Yellow Sandstone and Red Bed units) sourced both from the NW and SE. This drainage was oriented axially to structures observed in and around the basin today, leading Howard et al. (2003) to suggest that the same faults were active in the Mesozoic, though with a normal sense of motion. For a short distance (150 m) of their mapped section, the authors trace a 20° angular unconformity between the Lower Cretaceous Red Bed unit and overlying Oligocene sandstones, which are the oldest Tertiary sediments exposed in the area. They suggest that this may represent the same erosion surface that is preserved as the flat summit plateaus of Baatar Hyarhan and other Altai massifs.

The Tertiary sediments coarsen upwards from the Oligocene sandstones into Miocene, Pliocene and Pleistocene conglomerates. Paleocurrent data show a switch from sources to the NW and SE (axial to local faults) to a source to the NE in the Miocene. Together with the coarsening in sedimentation, this suggests that Bumbat Nuruu (lying NE of the forebergs) began uplifting at this time. Quaternary fluvial and alluvial conglomerates were deposited unconformably over the Cretaceous and Tertiary strata, and are preserved today as abandoned river terraces and alluvial fans. There are three prominent levels of fill terrace in the central section of the forebergs, the area which I now focus on. I call these terraces EZ1, EZ2 and EZ3, in increasing order of age and elevation (Fig. 4.4b).

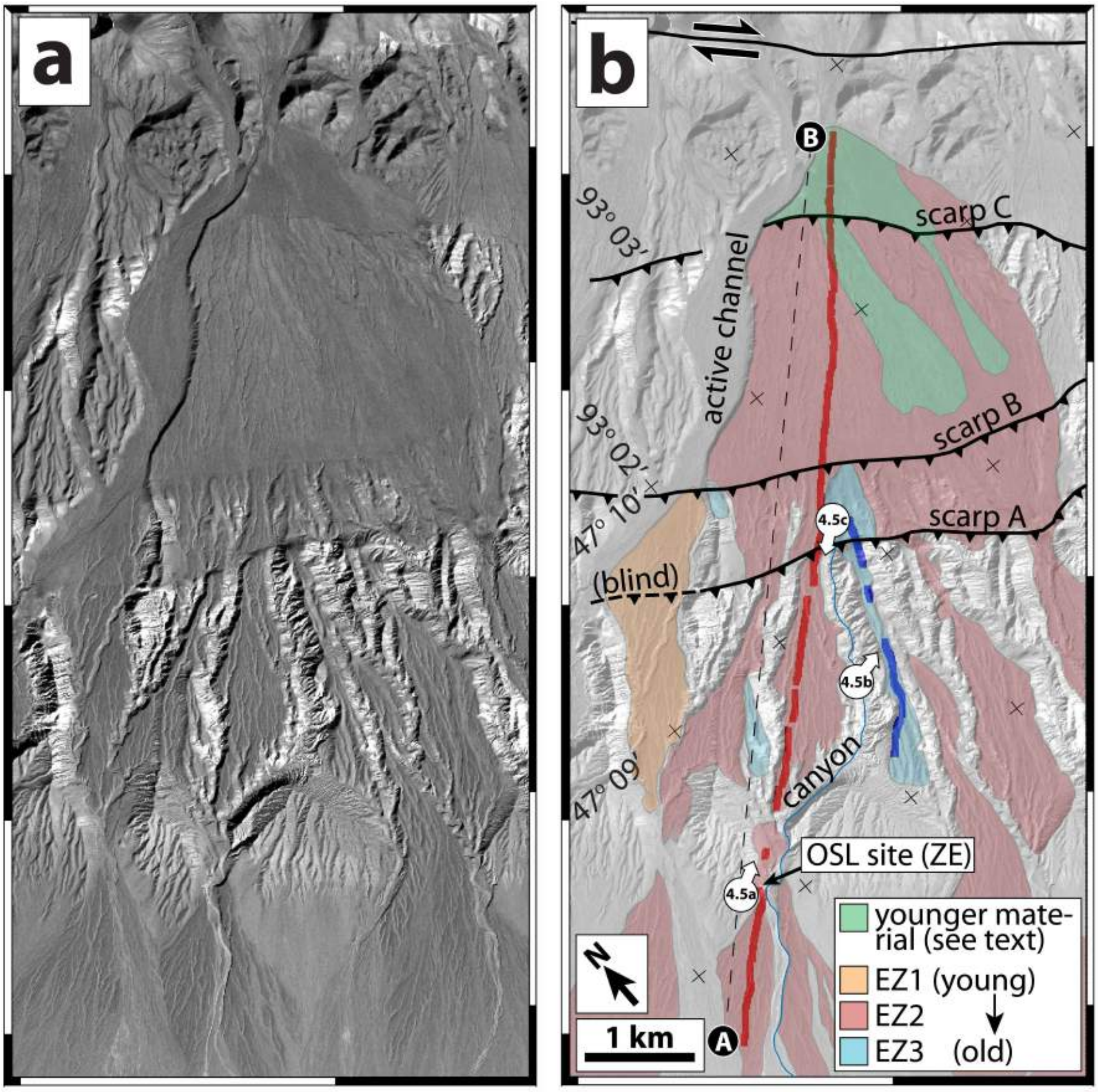

Figure 4.4: (a) SPOT 5 image (2.5 m resolution) of the central section of forebergs in the eastern Zereg Basin. The location of the map is shown as a dashed box on Fig. 4.3. (b) The same view, with Late Quaternary terrace levels and fault scarps superimposed. Cretaceous and Tertiary sediments are well exposed in the systems of canyons that lie between the preserved terrace remnants. The geology exposed in the canyon marked with a thin blue line is projected onto the line A–B and plotted in Fig. 4.6a. The small red and blue squares are points measured in differential GPS profiles of the EZ2 and EZ3 surfaces, respectively; elevations, again projected onto A–B, are plotted in Fig. 4.6b.

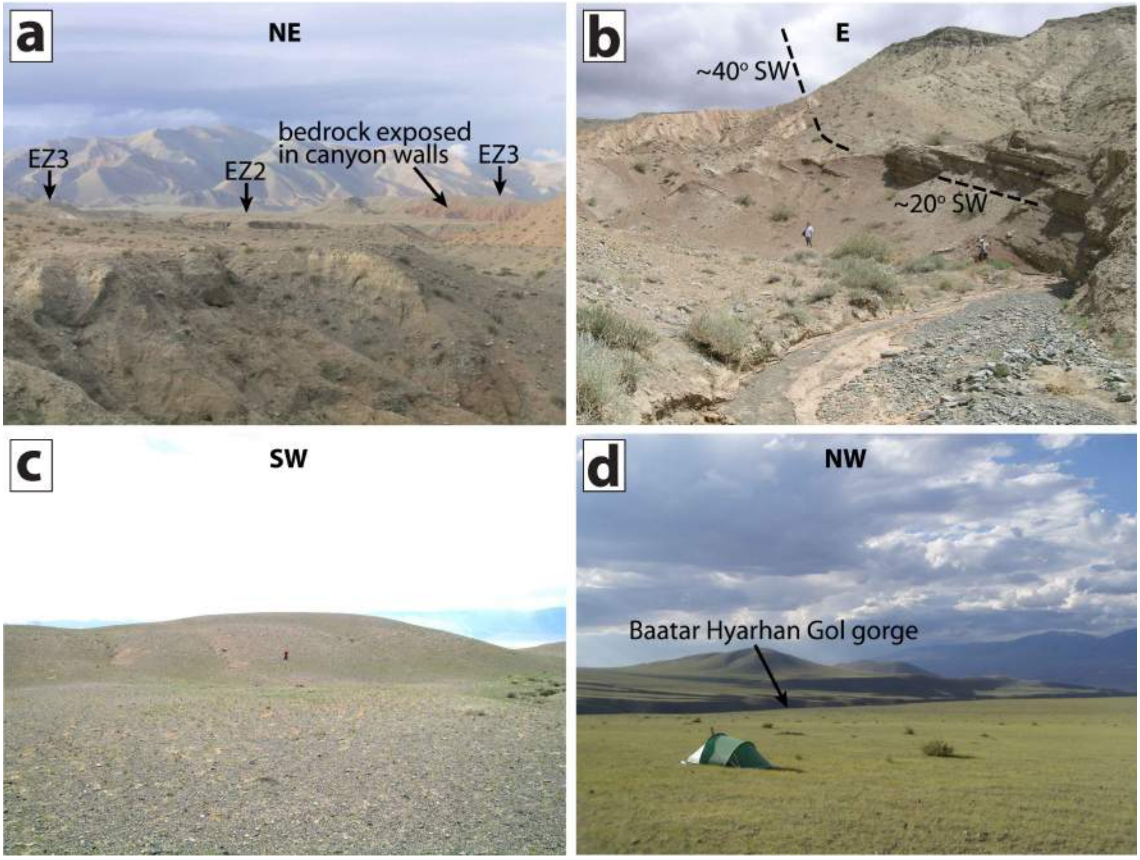

Figure 4.5: Photographs of forebergs in the Zereg Basin. (a) View NE from 47°08’06”N 93°00’42”E (see Fig. 4.4b) of badlands-style terrain in the E Zereg Basin forebergs, with the Bumbat Nuruu mountains in the distance. (b) View E from 47°08’37.1”N 93°02’14.7”E (see Fig. 4.4b), with two people for scale. Beds exposed in the canyon walls steepen sharply from ∼20° SW to 40° SW between the right and left-hand sides of the photograph. (c) View SW from 47°09’16.1”N 93°02’46.4”E (see Fig. 4.4b) of fault scarp A crossing the EZ2 terrace), with a person for scale. Note the relatively dense vegetation along the foot of the scarp. (d) View NW from 46°57’06”N 93°02’53”E (see Fig. 4.9b) of forebergs on the southern side of the Zereg depression. The foreground is the abandoned BG4 river terrace, while several other levels are picked out in the evening light on the far side of the Baatar Hyarhan Gol river. The mountains in the far distance (on the right-hand side of the photo) are the Bumbat Nuruu range.

Structure

Next I describe the geological structure across this same section of forebergs, using data from Howard et al. (2003) supplemented by my own measurements (taken from a narrow canyon plotted on Fig. 4.4b). The Cretaceous and Tertiary sediments are folded into a NE-verging anticline and syncline pair (Fig. 4.6a). Crossing the anticline I observe abrupt changes in the dip of these strata, starting with 0° in Quaternary alluvium at the SW edge of the forebergs and stepping progressively upwards to ∼20° SW (in the Pleistocene–Miocene conglomerates), ∼40° SW (in the Oligocene sandstones and the Cretaceous Red Bed unit) and ∼60–80° SW (in the Cretaceous Yellow Sandstone unit) as the core of the fold is approached (Fig. 4.5b). The NE limb of the anticline is initially overturned, before strata shallow out NE-wards into the syncline. The steep-sided canyons that expose the bedrock so well in the SW part of the geological cross-section do not extend as far NE as the syncline, so I extrapolate measurements taken by Howard et al. (2003) ∼2 km along strike to the SE (near 47°09'N 93°05'E). It is not clear whether the syncline contains abrupt changes in dip, similar to those observed in the anticline.

Three parallel, NE-facing scarps cross the Quaternary river terraces in the study area, each delineating a sharp change in the amount of river incision (Fig. 4.4). I refer to these as scarp A (in the south-west), B (in the centre) and C (in the north-east).

Scarp A is situated within a section of steep, 60–80° SW-dipping Cretaceous Yellow Sandstone strata close to the core of the anticline. Although I find no direct exposures of the scarp in cross-section, the strong NE-ward fold vergence suggests that it represents the surface expression of an active, SW-dipping thrust fault (Howard et al., 2003). I call this thrust 'fault A'. Along strike to the NW and SE it becomes blind, but the tightly-folded core of the anticline remains the same Yellow Sandstone unit. I assume, following the work of Howard et al. (2003), that the thrust propagated toward the surface from a detachment at the base of this unit. In this model, the anticline formed as a fault-propagation fold above the tip of this thrust, which has since broken through to the surface (Suppe & Medwedeff, 1990). I also consider the abrupt changes in the dip of sedimentary strata to reflect abrupt changes in the dip of the underlying thrust, consistent with the fault-bend folding model of Suppe (1983). This would suggest that the fault A soles into a flat detachment under the

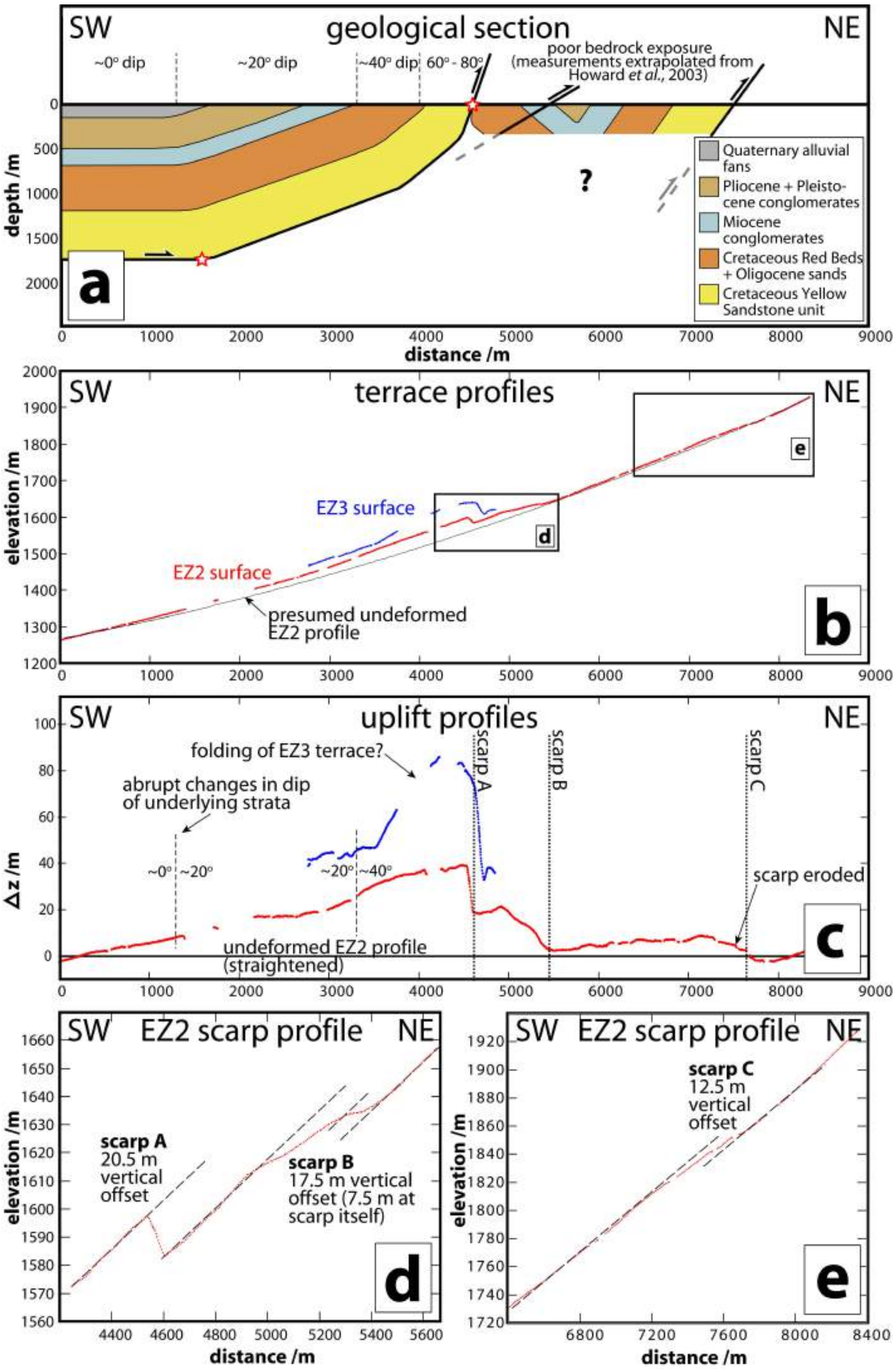

Figure 4.6: (a) Geological cross-section of the E Zereg Basin forebergs. Like Howard et al. (2003), I map the lower Cretaceous Red Bed unit and Oligocene sandstones together. Dip measurements are taken from a canyon (plotted as a thin blue line on Fig. 4.4b), except for the NE part where I extrapolate published data from Howard et al. (2003), taken near 47°09'N 93°05'E . All data are then projected onto the line A–B (plotted on Fig. 4.4b). The red stars show the 3.5 km and 6.5 km distances required to restore the base of the Yellow Sandstone unit along faults A and C, respectively. (b) Topographic profiles of EZ2 (red) and EZ3 (blue) fan surfaces, measured using differential GPS and also projected onto the line A–B (see Fig. 4.4b). (c) EZ2 uplift profile, calculated by subtracting the presumed undeformed profile from the observed heights. (d) & (e) Details of the topographic profiles across the scarps A, B and C.

Zereg Basin at depths of around 1.5–2 km (Figs. 4.1b & 4.6a).

Scarp B is situated about 1 km north-east of scarp A, probably within NE-dipping strata within the SW limb of the syncline. There is little bedrock exposure in this area and the scarp is not described by Howard et al. (2003). However, the same scarp can be followed on satellite imagery for a distance of ∼10 km north-west of the study area, and does not appear to outcrop within the same sedimentary unit along its whole length. This suggests that it represents another SW-dipping thrust ('fault B') – perhaps a shallow splay off fault A – rather than localised bedding-plane slip.

Scarp C is situated a further ∼2 km north-east of scarp B (in another area of poor bedrock exposure) and can be followed over a total distance of ∼15 km, finally ending in the far south-eastern section of forebergs. Although not exposed in cross-section within the study area, Howard et al. (2003) interpret it as a SW-dipping thrust ('fault C') based on their observations 2 km along strike to the NE, where it comes to the surface amongst Yellow Sandstones dipping ∼45–65° SW. The repetition of the Yellow Sandstone is most easily explained if fault C propogated to the surface along the base of this unit, perhaps from the same detachment under the Zereg Basin as fault A (Fig.4.6a).

Terrace profiles

Using differential GPS I produced topographic profiles of the preserved remnants of the EZ2 and EZ3 terraces. The position and elevation of a roving GPS receiver were measured relative to a second, stationary reciever. These relative heights are accurate to ∼5 cm. Profile points are plotted on Fig. 4.4b and the profiles themselves are shown in Fig. 4.6b, with EZ2 data in red and EZ3 in blue. The slope of the EZ2 terrace steepens from ∼3.4° at the SW end of the profile to ∼6.9° at the NE end. Fitting a quadratic line to data furthest from the faults (at the far SW and NE ends of the profile) provides an estimate of the original shape of the surface before deformation. Subtracting this presumed undeformed profile from the observed EZ2 and EZ3 surfaces gives a sense of the shape and magnitude of deformation that the terraces have undergone since abandonment (Fig. 4.6c). There are changes in the slope of both these profiles close to the places where the underlying strata suddenly steepen (from 0° to 20° and from 20° to 40° SW), supporting the notion that the abrupt changes in the dip of the exposed sediments reflect changes in the dip of the underlying thrust.

In addition, the EZ2 surface shows clear vertical displacements across scarps A and B (Fig. 4.6d). The former consists of a sharp, ∼20.5 m vertical offset (up to the SW). The latter consists of a further offset of ∼17.5 m, though of this only ∼7.5 m is preserved as a sharp offset at the scarp itself. The surface appears pristine, so this difference is unlikely to reflect erosion of the scarp; instead, the remaining 10 m vertical displacement might be achieved by folding of the hanging-wall sediments.

In the highest part of the topographic profile, there appears no abrupt displacement in EZ2 across the trace of scarp C (Fig. 4.6c). However, close inspection of SPOT imagery (made available to me only after I visited the study area) reveals that sections of this scarp, including the part I profiled, have been incised by more recent drainage systems and replaced with younger material (visible as darker areas in Fig. 4.4a and shaded in green in Fig. 4.4b). These younger deposits do not preserve the full deformation of the EZ2 surface, so to estimate the displacement of EZ2 I instead extrapolate slopes from a few hundred metres up and down-section from the eroded scarp. This yields a ∼12.5 m vertical offset of the EZ2 surface across the fault, up to the SW (Fig. 4.6e).

Late Quaternary displacement rates

Following the procedures outlined in Chapter 3 I sampled the EZ2 terrace for OSL dating. The sample (labelled ZE) comes from a 10 cm-thick sand body exposed ∼3 m below the surface of the terrace in the side of a gully, at 47°08'09.7"N 93°00'48.5"E (Fig. 4.4b). This is part of a much thicker sequence of sands and fine gravels (locally extensive over many tens of metres), buried beneath a single debris-flow deposit which forms the uppermost part of the terrace. Luminescence measurements were taken following the laboratory procedures described in Chapter 3. Individual aliquots show a well-defined peak in their measured equivalent doses (Fig. 4.7a). However, there is some spread to the data either side of this peak, which could signify incomplete bleaching of the sample prior to burial. Because of this uncertainty I use the weighted mean equivalent dose to calculate the burial age; this yields an age of 84.1 $\pm_{1\sigma}$ 9.4 ka (Table 4.1).

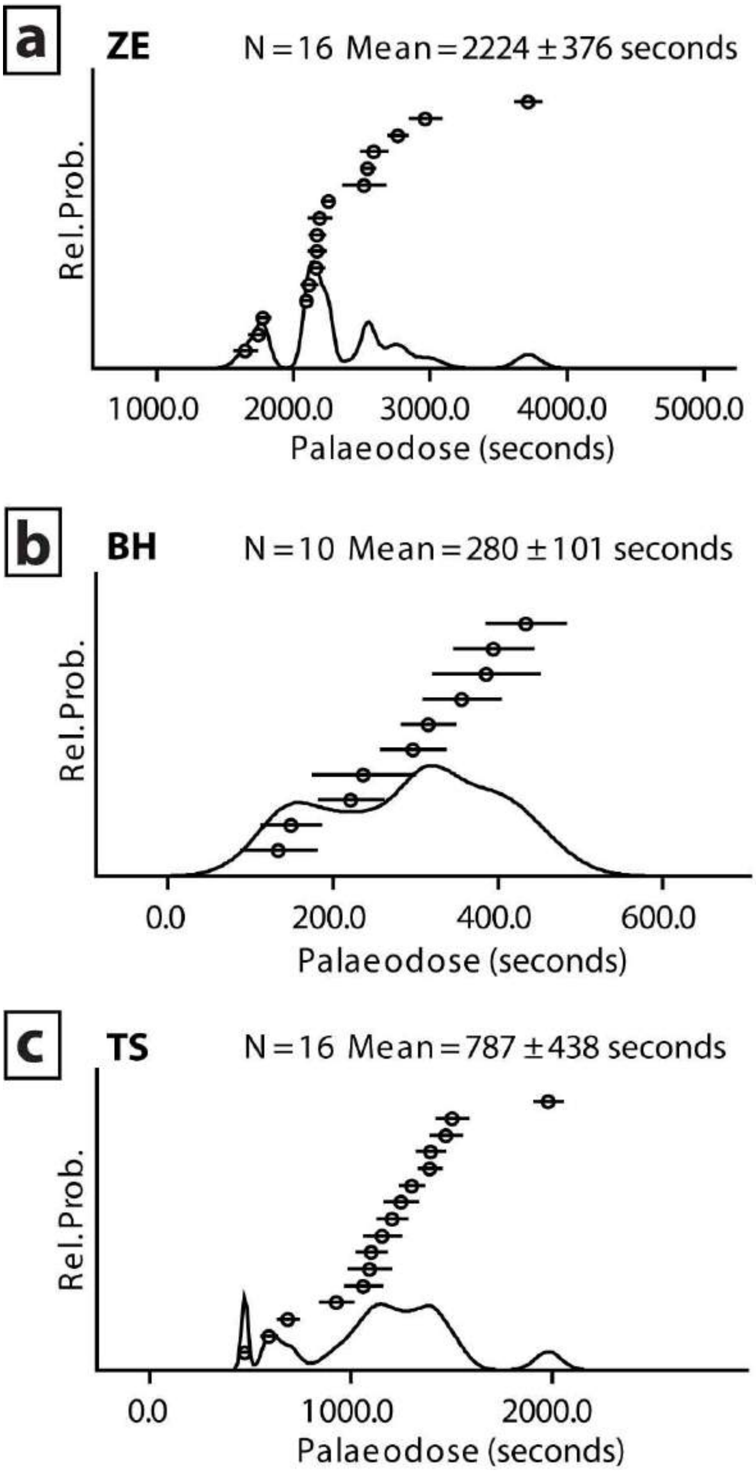

Figure 4.7: Equivalent dose distribution plots for OSL samples. The x-axis represents the number of seconds of exposure to a known beta source (delivering ~5 Gy min^{-1}) required to reproduce the natural luminescence signal. There are N aliquots in each sample, and Mean is the weighted mean D_e for all these aliquots. Individual aliquot D_e values are displayed in rank order, with probability density functions superimposed. For (a) ZE and (c) TS, D_e values form a well-defined peak; however, there is still a significant spread to the data, suggesting that bleaching of these samples was incomplete. For (b) BH, there is no clear peak to the dose distribution plot, so I cannot be certain that any of the aliquots were reset during transport prior to burial.

Sample	*Equivalent dose (Gy)*	*K (%)*	*U (ppm)*	*Th (ppm)*	*Cosmic dose rate (Gy/ka)*	*Total dose rate (Gy/ka)*	*Age (ka)*
ZE	188.29 ± 15.89	1.519 ± 0.028	1.4 ± 0.052	3.6 ± 0.168	0.181 ± 0.135	2.24 ± 0.15	84.1 ± 9.4
BH	22.93 ± 8.27	1.046 ± 0.028	0.7 ± 0.052	2.0 ± 0.168	0.284 ± 0.135	1.60 ± 0.14	14.3 ± 5.3
TS	64.46 ± 35.87	1.909 ± 0.028	2.1 ± 0.052	8.4 ± 0.168	0.288 ± 0.135	3.23 ± 0.16	20.0 ± 11.2

Table 4.1: Values used to calculate luminescence ages for the three fan surfaces. The errors are all 1σ. Sample ZE is taken from the eastern Zereg Basin forebergs (EZ2 surface), BH from the NE Baatar Hyarhan range-front (SZ1 surface) and TS from the SW Baatar Hyarhan range-front (NT1 surface).

Combining this age with the 20.5 m vertical scarp offset gives a vertical displacement rate of $0.24\ ^{+0.03}_{-0.02}$ mm yr^{-1} across fault A. The fault dip lies between 60 and 80° SW, giving a horizontal shortening rate of $0.09\ ^{+0.07}_{-0.05}$ mm yr^{-1} and a fault slip-rate of $0.26\ ^{+0.06}_{-0.04}$ mm yr^{-1}. The 17.5 m vertical offset across fault B yields a vertical displacement rate of $0.21\ ^{+0.02}_{-0.02}$ mm yr^{-1}. Using conservative bounds of 20–60° SW on the fault dip, the horizontal shortening rate is $0.25\ ^{+0.39}_{-0.14}$ mm yr^{-1} and the slip-rate is $0.32\ ^{+0.36}_{-0.10}$ mm yr^{-1}. Finally, a vertical scarp offset of 12.5 m and a dip of 45–65° SW gives a vertical displacement rate of $0.15\ ^{+0.02}_{-0.02}$ mm yr^{-1}, a horizontal shortening rate of $0.10\ ^{+0.07}_{-0.04}$ mm yr^{-1} and a sliprate of $0.18\ ^{+0.06}_{-0.04}$ mm yr^{-1} across fault C. These displacement rates are summarised in Table 4.2.

Fault name	*Fault dip*	*Offset (m)*	*Age (ka)*	*Displ. rates (mm yr^{-1})*		
				Vertical	*Horizontal*	*Fault slip*
Fault A	60–80°	20.5	84.1 ± 9.4	$0.24\ ^{+0.03}_{-0.02}$	$0.09\ ^{+0.07}_{-0.05}$	$0.26\ ^{+0.06}_{-0.04}$
Fault B	20–60°	17.5	84.1 ± 9.4	$0.21\ ^{+0.02}_{-0.02}$	$0.25\ ^{+0.39}_{-0.14}$	$0.32\ ^{+0.36}_{-0.10}$
Fault C	45–65°	12.5	84.1 ± 9.4	$0.15\ ^{+0.02}_{-0.02}$	$0.10\ ^{+0.07}_{-0.04}$	$0.18\ ^{+0.06}_{-0.04}$
Zereg Fault	50–70°	4.2–5.8	14.3 ± 5.3	$0.35\ ^{+0.29}_{-0.14}$	$0.20\ ^{+0.34}_{-0.12}$	$0.40\ ^{+0.44}_{-0.17}$
Tsetseg Fault	32–46°	2.5–3.3	20.0 ± 11.2	$0.15\ ^{+0.23}_{-0.07}$	$0.18\ ^{+0.42}_{-0.10}$	$0.23\ ^{+0.48}_{-0.12}$

Table 4.2: A summary of the rates of vertical and horizontal displacement and fault slip for the five thrusts studied in Section 4.3. Faults A, B and C are those studied in the eastern Zereg Basin (Section 4.3.1). *Offset* is the vertical offset of alluvial fans across the fault, and *age* is the luminescence age of these surfaces (with 1σ errors). The total shortening rate across the eastern Zereg Basin forebergs is equal to the sum of the slip-rates on faults A, B and C, as described in Section 4.3.1.

In my model, faults A, B and C sole into a detachment at the base of the Yellow Sandstone unit under the Zereg Basin (Figs. 4.1b & 4.6a). In this case, the total late Quaternary rate of slip on this detachment (and thus the total late Quaternary shortening across the E Zereg Basin) is the sum of the slip-rates on each fault, which is $0.76\ ^{+0.48}_{-0.17}$ mm yr^{-1}. This is a minimum estimate because a proportion of the slip on the detachment may not reach the surface on the thrusts, but could be accommodated instead by folding of the uppermost sediments.

Onset of faulting

I now consider the onset of deformation in the eastern Zereg Basin, using the geological cross-section in Fig. 4.6a to estimate the cumulative shortening on the three faults and the late Quaternary slip-rates to extrapolate back in time. Restoring the base of the Cretaceous Yellow Sandstone unit (Fig. 4.6a) there is around ∼3.5 km shortening on fault A and ∼6.5 km on fault C; these are minimum estimates, as they do not account for material removed at the surface by erosion. The structure of the middle part of the cross-section is too poorly understood to constrain the total shortening on fault B.

At the calculated late Quaternary rate of $0.76\ ^{+0.48}_{-0.17}$ mm yr^{-1}, and discounting folding, a minimum total shortening of ∼10 km would be achieved in 8–17 Ma. Because of uncertainties in my structural model at depth, as well as the assumption that late Quaternary slip-rates are representative over the longer-term, these should be considered only approximate ages. However, they do suggest that faulting in the eastern Zereg Basin is at least a few million years in age.

4.3.2 Southern Zereg Basin forebergs

There is a second line of forebergs on the southern side of the Zereg Basin, adjacent to the south-eastern section of Baatar Hyarhan (Figs. 4.2c & 4.8). Rivers and streams incising into these hills reveal deformed Mesozoic and Tertiary sediments, although there are fewer canyons and ravines than on the eastern side of the depression and the bedrock exposure is limited in comparison. The stratigraphy, which is described by Howard et al. (2003), consists of Lower Cretaceous red beds (fine-grained floodplain deposits sourced from the SE) and Miocene, Pliocene and Pleistocene alluvial fan conglomerates (sourced from the SW). As discussed in Section 4.2.2, the switch in paleocurrent direction and the coarsening in sedimentation may reflect the initial uplift of Baatar Hyarhan, or perhaps other mountains SW of the Tsetseg Basin. Quaternary fluvial and alluvial conglomerates deposited unconformably over the Cretaceous and Tertiary strata are preserved today as abandoned river terraces and alluvial fans.

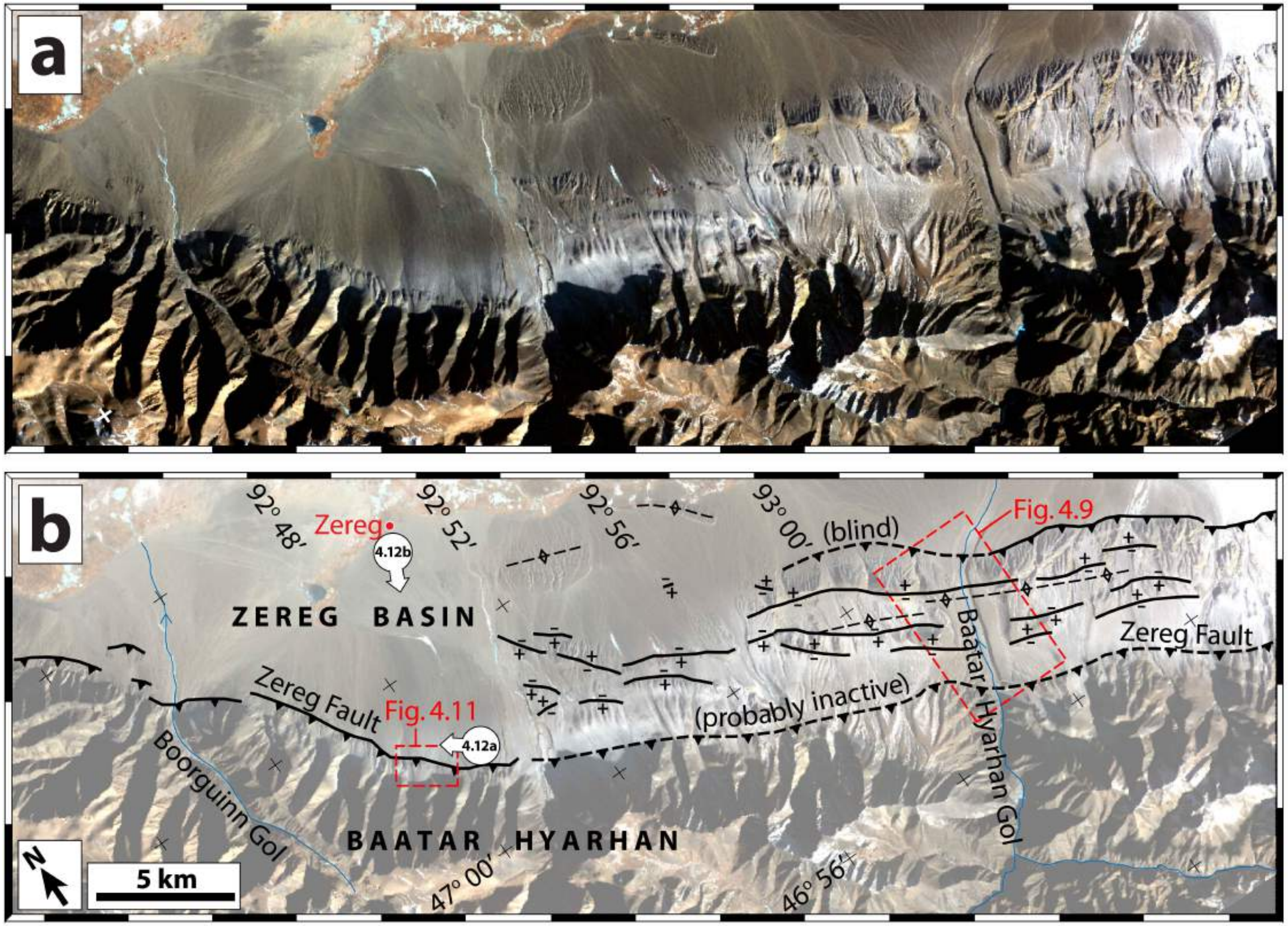

Figure 4.8: (a) ASTER image (RGB 321) showing faulting along the north-eastern margin of Baatar Hyarhan. The location of the map is shown as a dashed box on Fig. 4.1a. (b) The same view, with scarps plotted as thick solid lines (+/- indicates the sense of displacement) and fold axes as thin dashed lines. The eastern part of the Zereg fault, shown as a thick dashed line, looks degraded and may no longer be active.

The forebergs are bounded on the SW side by the Zereg fault, which in this section appears degraded and may no longer be active (Fig. 4.8). On the NE side of the forebergs an abrupt change in the amount of river incision marks the trace of an active, SW-dipping thrust, although west of the Baatar Hyarhan Gol river this fault is probably blind. Within the forebergs themselves the Cretaceous and Tertiary sediments are folded into a large anticline; like Howard et al. (2003), I interpret this as a fault propagation fold related to growth of the underlying thrust. In the central part of the forebergs (around the Baatar Hyarhan Gol river), dip measurements from Howard et al. (2003) and my own fieldwork show that this anticline verges northeastwards (Fig. 4.10a), although this sense of asymmetry appears to be reversed along strike to the NW. Numerous NE- and SW-facing scarps within the forebergs (Fig. 4.8) may represent bedding-plane slip and minor normal faulting associated with the growth of this anticline, although small thrusts and back-thrusts might also be present.

The Baatar Hyarhan Gol river, which drains much of the SE part of the range, cuts a prominent gorge through the forebergs (Figs. 4.5d & 4.9). Above it a prominent flight of abandoned river terraces are preserved (these are labelled BG1–BG8 on Fig. 4.9b). Using differential GPS I produced topographic profiles of the BG7 and BG4 terraces, as well as a prominent flood level preserved about a metre above the active stream bed (Fig. 4.10b). These three surfaces all show clear SW-facing scarps – with vertical displacements of around 20 m, 4.5 m and 3.0 m, respectively – at a distance of $\sim$3900 m along the profiles (and from the Zereg fault). This location coincides with the boundary between the Cretaceous red beds and Miocene conglomerates, and the scarp probably represents bedding-plane slip on this contact.

The BG4 terrace shows further evidence of folding (as would BG7, presumably, if it were more complete). I do not know the gradient at which BG4 was originally deposited; it may have been similar to that of the current Baatar Hyarhan Gol river

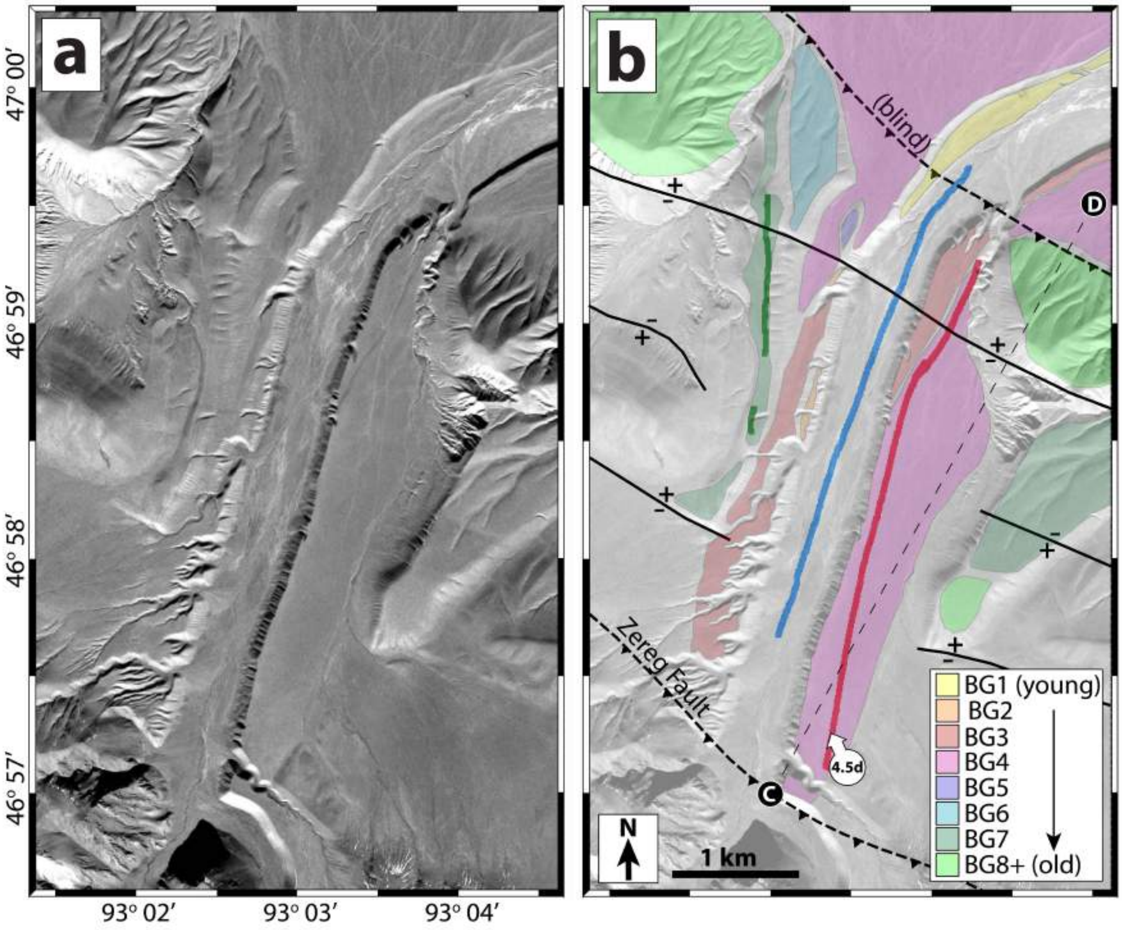

Figure 4.9: (a) SPOT 5 image of part of the forebergs in the southern Zereg Basin, where the Baatar Hyarhan Gol river exits the Baatar Hyarhan range. (b) The same view, with Late Quaternary terrace levels and fault scarps superimposed. The small green, red and blue squares are points measured in differential GPS profiles of the BG7, BG4 and abandoned Baatar Hyarhan Gol river bed surfaces, respectively; elevations are projected onto the line C–D and plotted in Fig. 4.10b.

bed, or perhaps steeper, if headward erosion into the peneplain has progressively lowered river gradients over time (Vassallo et al., 2007b). However, subtracting the slope of the current Baatar Hyarhan Gol river bed from the BG4 topographic profile provides at least an approximate indication of the shape of deformation the terrace has undergone since abandonment (Fig. 4.10c). Aside from the far SW end, where the BG4 surface is steep (and may actually be covered by small fan deposits derived from the slopes of Baatar Hyarhan), the maximum uplift is at a distance of 1000–

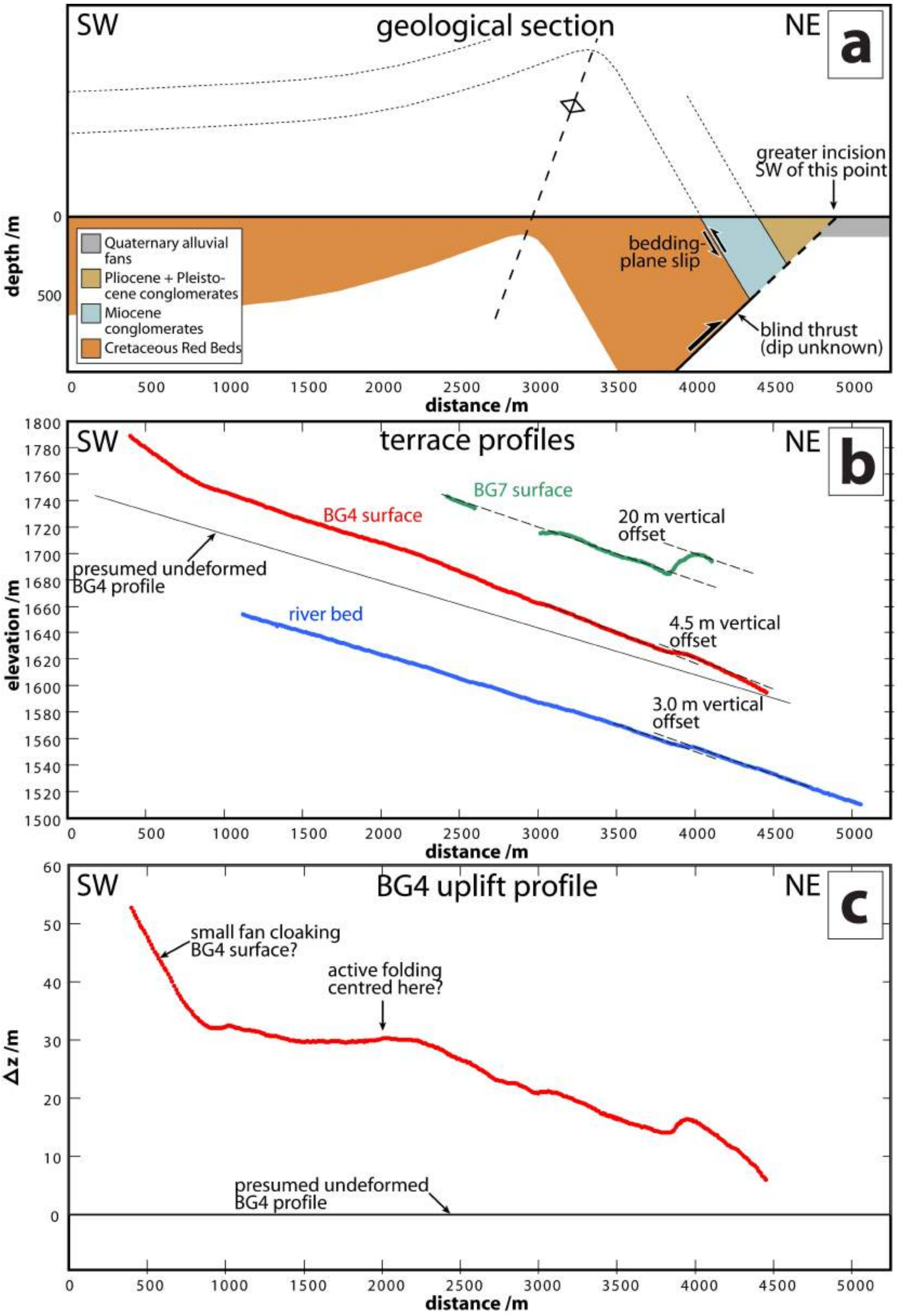

Figure 4.10: (a) Geological cross-section of the S Zereg Basin forebergs. Dip measurements are projected onto the line C–D (plotted on Fig. 4.9b). (b) Topographic profiles of the BG7 terrace (green), the BG4 terrace (red) and a prominent flood level of the Baatar Hyarhan Gol river bed (blue), all projected onto the line C–D (see Fig. 4.9b). (c) BG4 uplift profile, calculated by subtracting the presumed undeformed profile from the observed heights.

2000 m along the profile. This location is offset by 1–2 km from the mapped core of the anticline, although the geological cross-section is based on sparse bedrock exposure and so there are significant uncertainties in its exact shape.

I did not find any exposures where fine-grained sediments might be sampled for OSL dating of the terraces. The differential GPS profiles clearly show that folding (and, presumably, movement on the underlying thrust) occurred during the Late Quaternary, but I am unable to quantify the rates of deformation.

4.3.3 Zereg fault

I now shift my attention north-westwards along the Baatar Hyarhan range-front to the central section of the Zereg fault, adjacent to the highest part of the massif. Here, fresh NE-facing thrust scarps cut Quaternary alluvial fans deposited at the foot of the uplifting mountain range (Figs. 4.8, 4.11 & 4.12). These fans are now abandoned and streams flowing off Baatar Hyarhan actively incise into them. I found no fault exposures in river cuttings; however, because the scarps cross relatively steep fan deposits close to the range-front and have a fairly linear trace in map view, I infer that the fault dips quite steeply, perhaps ∼60° SW.

One of the clearest sections of faulting here is at 47°02'30"N 92°47'30"E (Figs. 4.11a & 4.12b). At this locality, at least two levels of abandoned terrace are observed. The youngest and best preserved (called SZ1) is shaded red in Fig. 4.11b; several small streams have incised into it, and recent debris-flows (consisting of scattered small boulders and gravels) coat the terrace surface close to these channels. There are also three isolated patches of an older terrace (or terraces), shaded in blue in Fig. 4.11b. I used differential GPS to produce six topographic profiles perpendicular to the trace of the fault – four across SZ1 and two across the older surfaces (Fig. 4.13). The SZ1 surface is displaced vertically by 4.2–5.8 m across the fault scarp (up to the SW). The older surfaces are not preserved NE of the fault trace so I can only estimate minimum

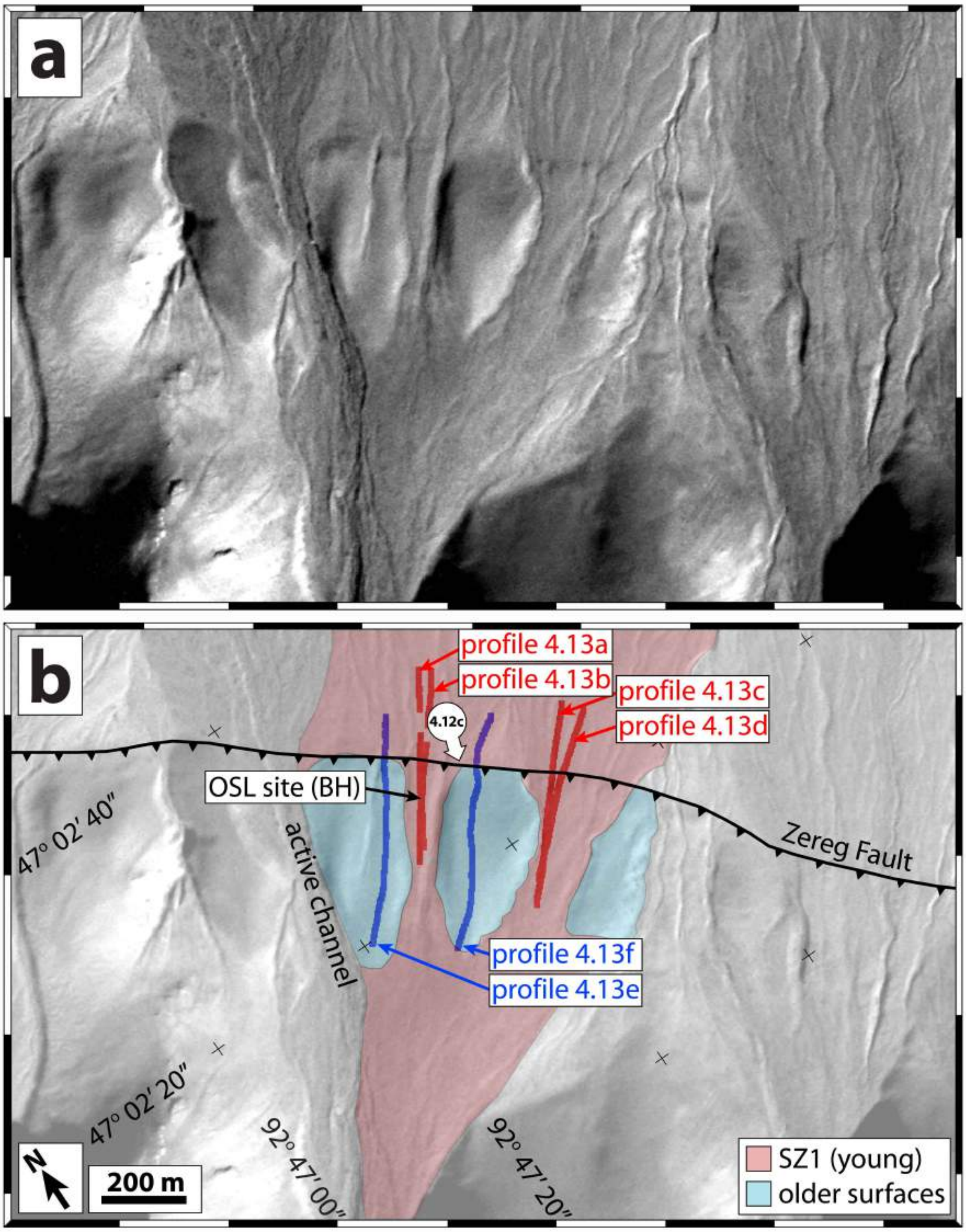

Figure 4.11: (a) SPOT 5 image of thrust scarps along the Zereg fault. The location of the map is shown as a dashed box on Fig. 4.8. (b) The same view, with terrace levels, fault scarps, exposed bedrock and differential GPS profile points superimposed.

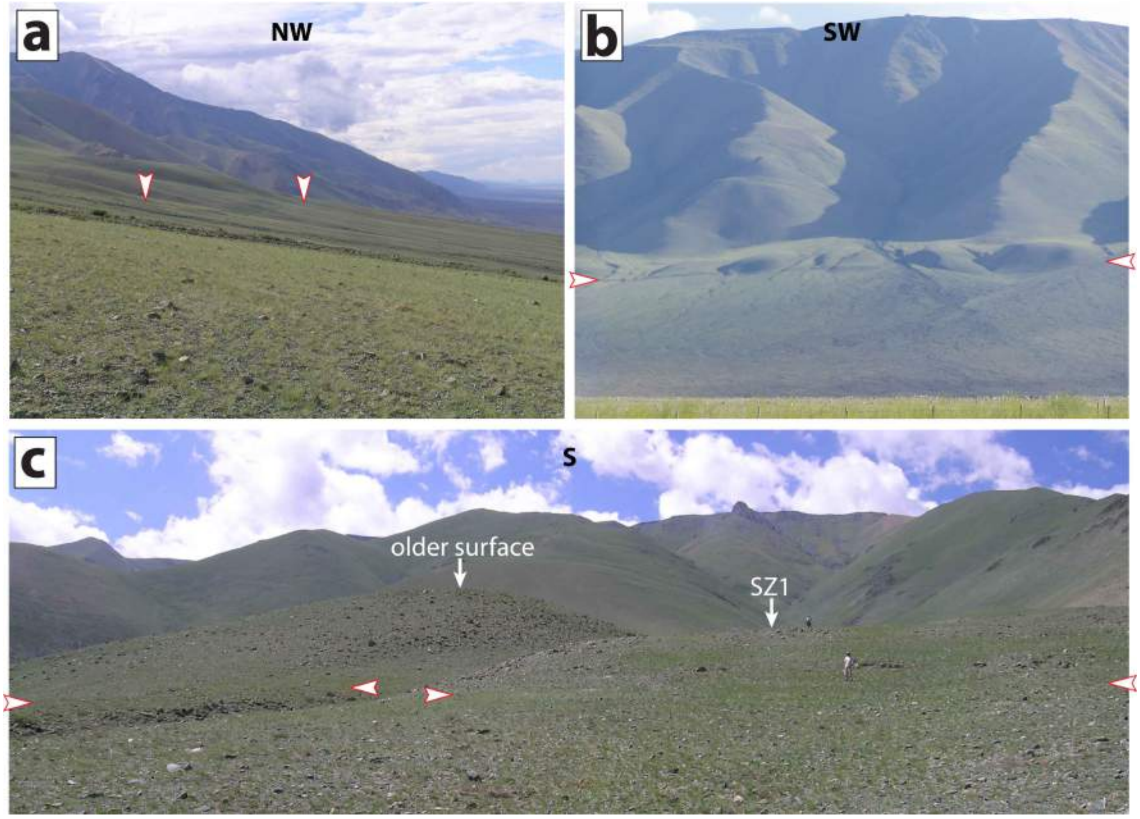

Figure 4.12: Photographs of the Zereg fault, with arrows picking out the base of thrust scarps. (a) View NW from 47°01’50.3”N 92°48’51.9”E (see Fig. 4.8); NE-facing thrust scarps can be seen in the middle distance, just to the left of centre. (b) View SW from near the town of Zereg (see Fig. 4.8) of the fault scarps described in Section 4.3.3. (c) Close up of part of these same fault scarps, facing S from ∼47°02’30”N 92°47’40”E (see Fig. 4.11b). Two people at the top and bottom of the scarp provide scale.

displacements; these are at least 8.7 m for the western patch, and 29.5 m for the central one. The large difference between these values suggests they are remnants of two separate surfaces.

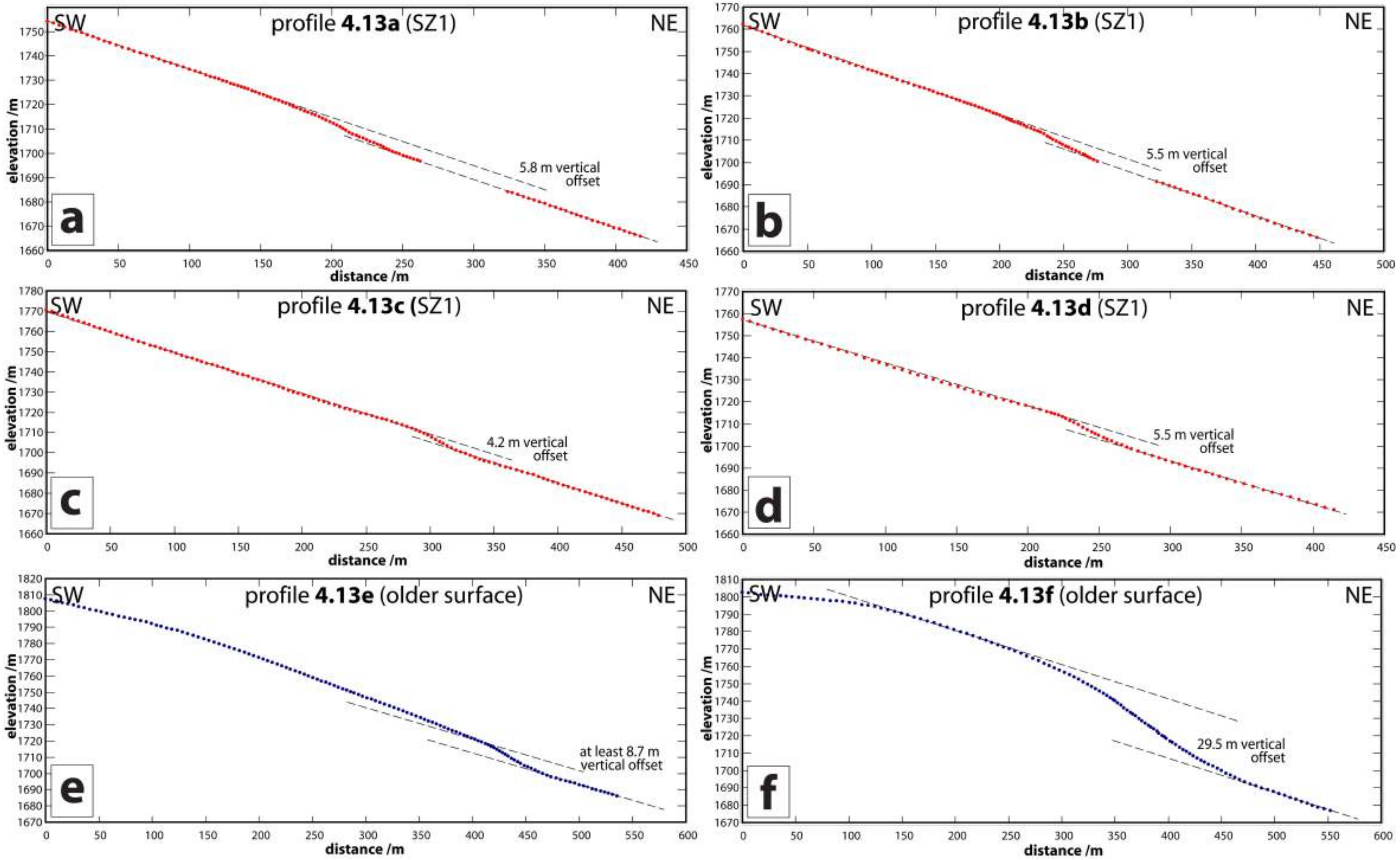

Figure 4.13: Topographic profiles of SZ1 fan (red) and older surfaces (blue), measured using differential GPS. Profile points are plotted on Fig. 4.11b.

Within this area there are no natural cuttings into the terrace deposits in which sediment suitable for OSL dating might easily be collected. Instead, a ∼1 m-deep pit was excavated in the SZ1 surface; its precise position (at 47°02'27.5"N 92°47'35.4"E) was chosen to avoid any of the small stream channels or recent debris-flows where there is a risk of dating material that postdates the terrace abandonment. The sediment exposed in the pit walls consists of 1–5 cm, angular gravels and a few larger clasts set in a fine-grained matrix. These high-energy deposits (possibly debris-flows) are not ideal for OSL sampling, because of the reduced chance of exposure to sunlight during transport; however, with the scarps positioned so close to the range-front lower-energy sediments may not be available at all.

The sediment exposed in the pit walls was too coarse to insert a tube and not cohesive enough to extract a large block, so I was not able to use the sampling methods outlined in Chapter 3. Instead, the pit was covered with canvas and plastic to ensure that sampling was done in darkness. Inside the pit, I widened one of the pit walls to remove any sediment that might have been exposed during digging. Using a sieve to remove larger clasts, loose, fine-grained matrix material was scraped from the widened pit wall (from a depth of about 50 cm) into light-protected bags. This sample is labelled BH.

Luminescence measurements were taken using the laboratory methods outlined in Chapter 3. The large spread in equivalent dose values means that it is not clear which (if any) of the aliquots were reset before burial (Fig. 4.7b), and the burial age of $14.3 \pm_{1\sigma} 5.3$ ka – again calculated using the weighted mean equivalent dose – should be treated with caution (Table 4.1). However, the burial age is within error of that of a fan surface on the opposite margin of Baatar Hyarhan (see Section 4.3.4), and is similar to exposure ages calculated for a number of surfaces flanking the Gobi Altai range in southern Mongolia (Vassallo et al., 2005; Ritz et al., 2006). Because of this, and given that one might expect alluvial sedimentation in the region to be pulsed (as it is in the Gobi-Altai), I am more confident that the burial age for SZ1 is correct. Combining the age with a vertical scarp offset of 5.0 ± 0.8 m gives a vertical displacement rate of $0.35\ ^{+0.29}_{-0.14}$ mm yr^{-1} across the range-front fault. Using a range of dips from 50° to 70° SW yields a horizontal shortening rate of $0.20\ ^{+0.34}_{-0.12}$ mm yr^{-1} and a slip-rate of $0.40\ ^{+0.44}_{-0.17}$ mm yr^{-1} (Table 4.2).

4.3.4 Tsetseg fault

Finally, I switch my attention to the south-western margin of the range, where Baatar Hyarhan overthrusts the Tsetseg Basin along the Tsetseg fault. Here, fresh S- or SW-facing thrust scarps cut Quaternary alluvial fans, either right at the the foot of the range or a short distance (up to ∼1 km) out into the depression (Fig. 4.14). North-west of ∼46°52'N 92°43'E the active faulting passes through hilly terrain between the Tsetseg and Manhan basins.

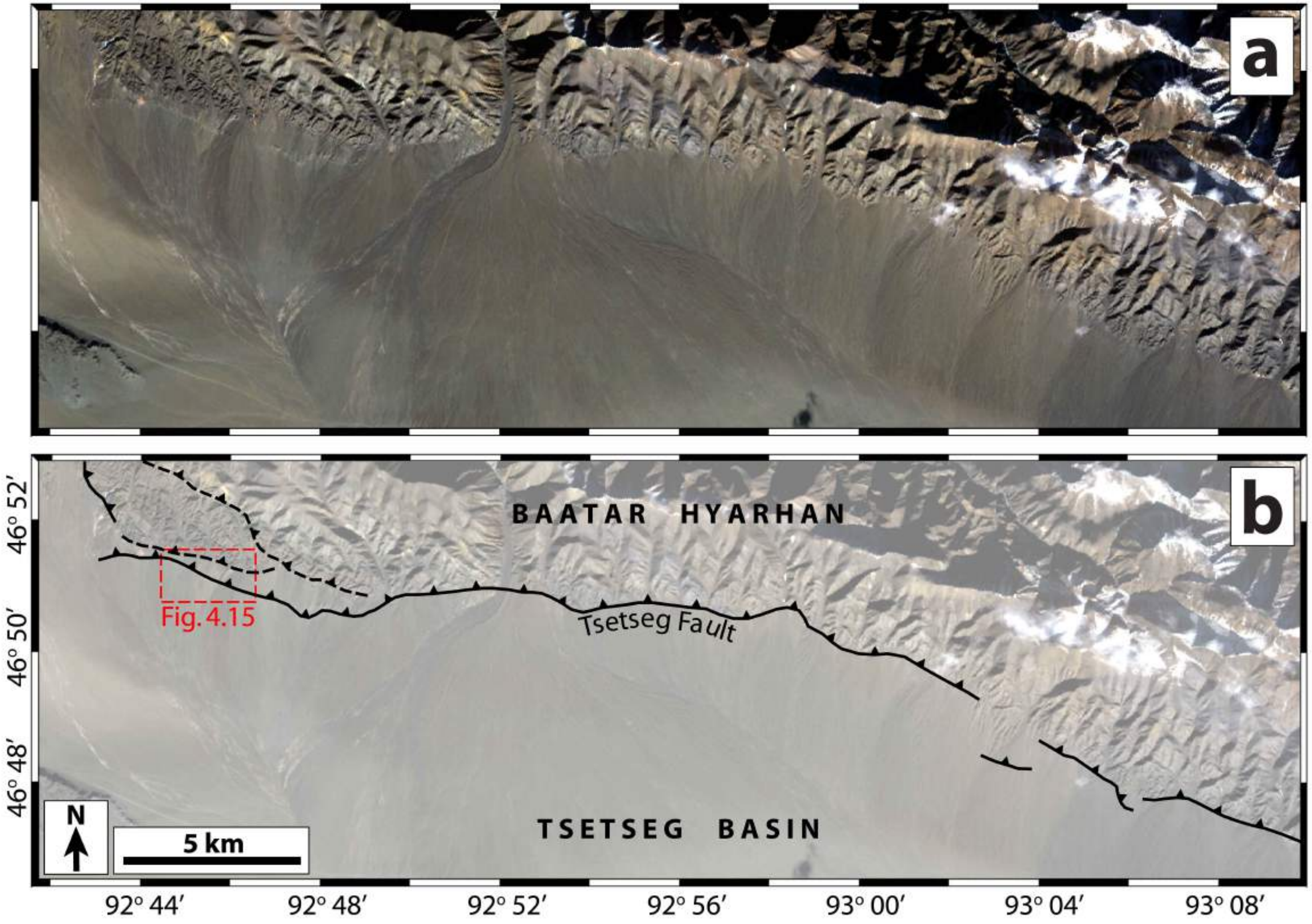

Figure 4.14: (a) ASTER image (RGB 321) showing the Tsetseg fault, along the south-western margin of Baatar Hyarhan. The location of the map is shown as a dashed box on Fig. 4.1a. (b) The same view with active faults scarps plotted as thick solid lines; the dashed lines are older faults, probably now inactive.

Perhaps the clearest scarps along the Tsetseg fault are at 46°51'N 92°56'E (Figs. 4.15a & 4.16a), where they cut abandoned and incised alluvial fans ∼500 m from the edge of the mountains. The same surfaces are not displaced across the range-front itself, which therefore appears to be inactive since fan abandonment. Again, there are no direct exposures of the fault in any river cuttings. However, striations and a ∼1 cm thick layer of fault gouge are observed on the underside of a granitic vein that outcrops in a series of small bedrock exposures very close to the trace of the active faulting (Fig. 4.16b). Striated surfaces dip 32–46° NNE, and the striations themselves indicate a small but significant component of right-lateral shear on the fault plane. In addition, schists, mylonites and volcanics (with a fabric dipping 40–70° N) exposed a few hundred metres north of the scarps are highly brecciated and foliated, indicating that the active faulting may follow the grain of an older shear zone.

Focusing on an alluvial fan (called NT1) rich in granite and thus easily distinguished by its light colour in SPOT imagery (Fig. 4.15b), I produced three topographic profiles across the fault with differential GPS (Fig. 4.17). The vertical displacement of NT1 across the scarp ranges from 2.5 to 3.3 m (up to the N). Following the procedures outlined in Chapter 3, I sampled the NT1 fan for OSL dating. This sample, labelled TS, was taken from a sand lens exposed in a stream cutting at 46°50'50.9"N 92°45'45.5"E, ∼75 cm below the surface (Fig. 4.16c).

To measure the luminescence I again employed the methods described in Chapter 3. Individual aliquot equivalent dose values form a broad peak (Fig. 4.7c), although the spread to this data suggests that bleaching was incomplete (as in Section 4.3.1). Using the weighted mean equivalent dose I attain a burial age of $20.0 \pm_{1\sigma} 11.2$ ka (Table 4.1). Combining this age with a vertical scarp offset of 2.9 ± 0.4 m gives a vertical displacement rate of $0.15\ ^{+0.23}_{-0.07}$ mm yr^{-1}. Using a fault dip of 39° ± 7° NNE, the horizontal shortening rate is $0.18\ ^{+0.42}_{-0.10}$ mm yr^{-1} and the slip-rate (neglecting the strike-slip component present in the striations) is

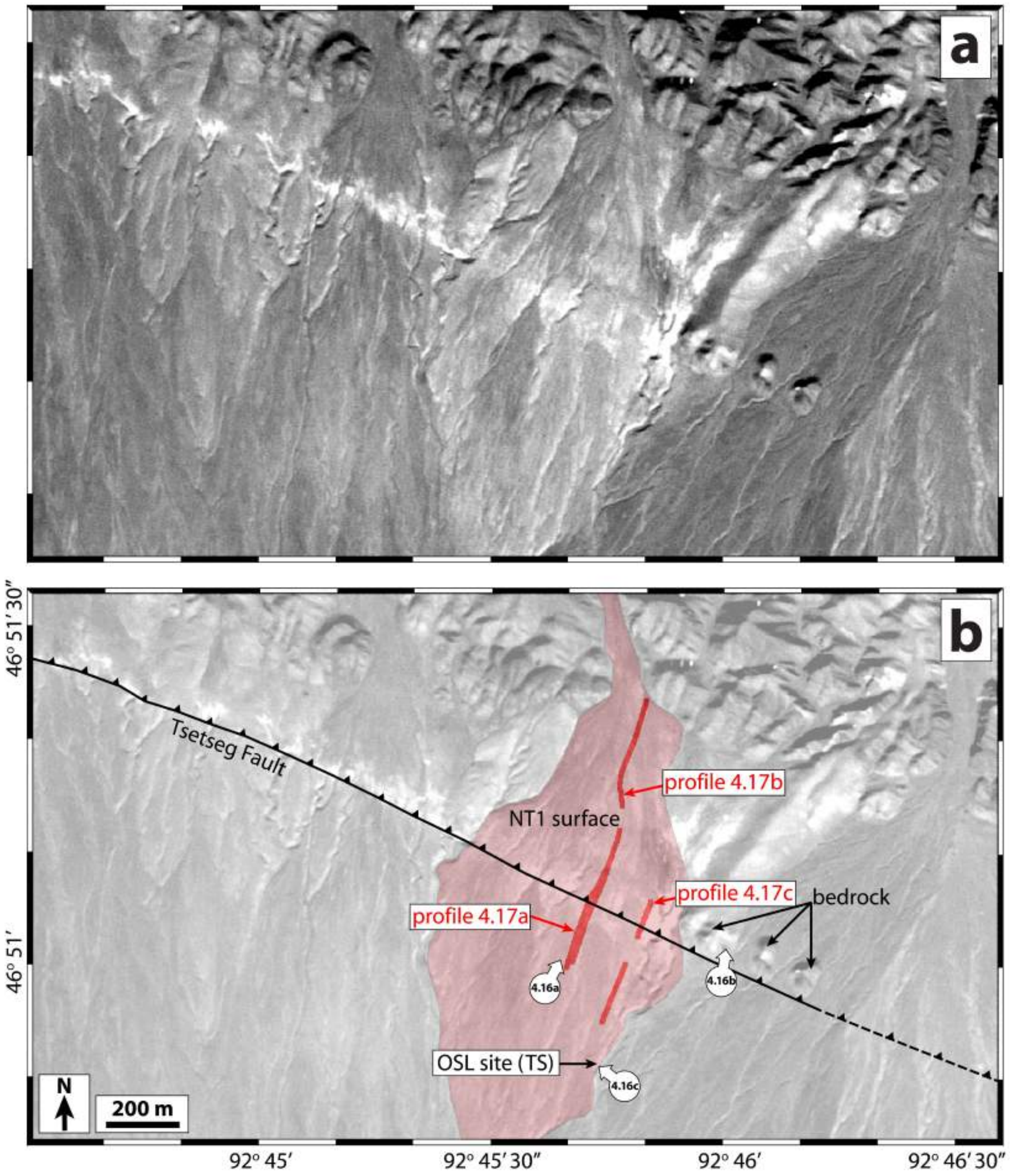

Figure 4.15: (a) SPOT 5 image of thrust scarps along the Tsetseg fault. The location of the map is shown as a dashed box on Fig. 4.14. (b) The same view, with the NT1 alluvial fan, fault scarps and differential GPS profile points superimposed.

$0.23\ ^{+0.48}_{-0.12}$ mm yr^{-1} (Table 4.2).

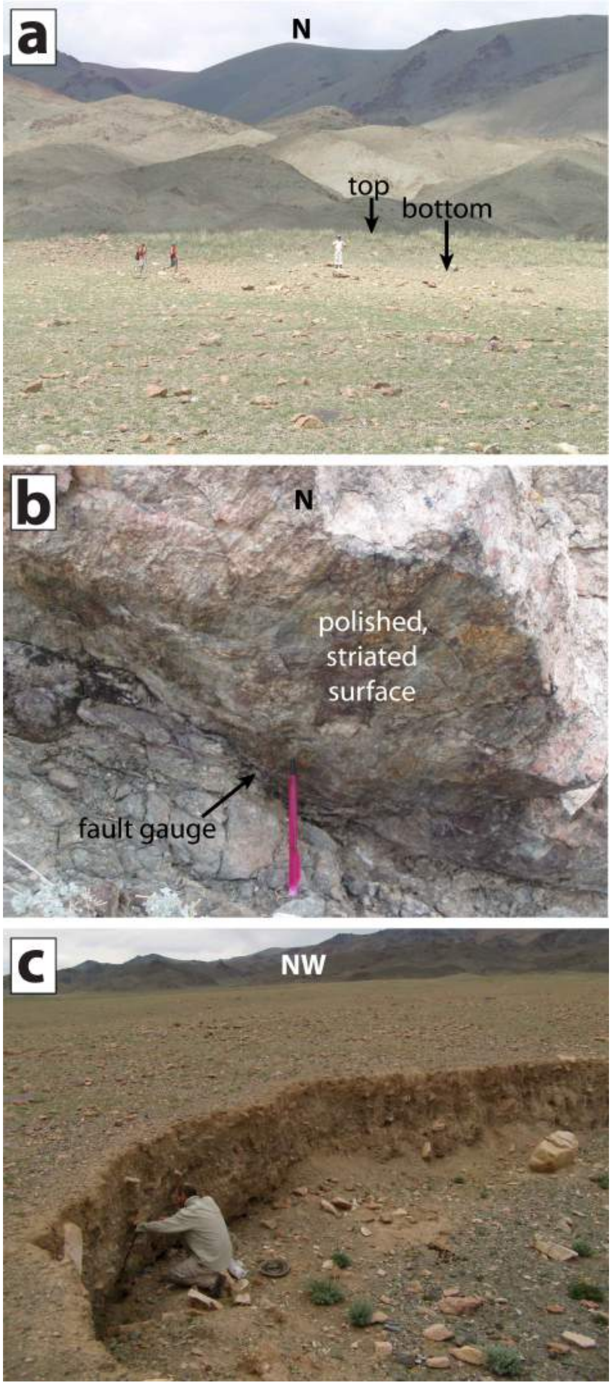

Figure 4.16: Photographs taken along the south-western margin of Baatar Hyarhan (see Fig. 4.15 for locations). (a) View N from ∼46°51’00”N 92°45’40”E of the thrust scarp cutting the NT1 surface; three people standing at the foot of scarp provide scale. (b) Striations and a 1 cm thickness of fault gouge exposed on the underside of a NNE-dipping granite vein at 46°51’01.4”N 92°46’02.6”E; the view is to the N with a pencil for scale. (c) Sampling the NT1 fan for OSL dating at 46°50’50.9”N 92°45’45.5”E; the view is to the NW.

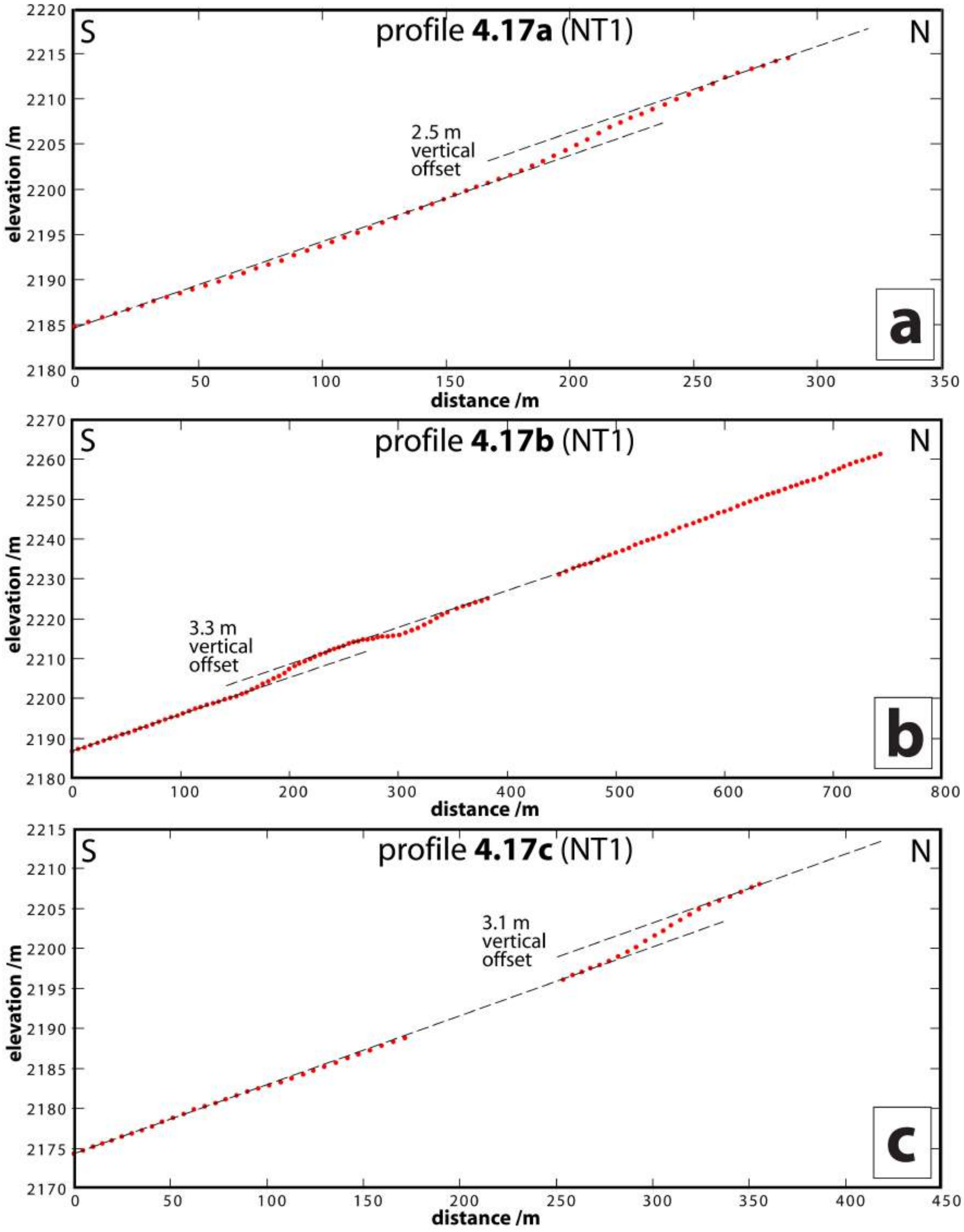

Figure 4.17: Topographic profiles of NT1 fan surface, measured using differential GPS. Profile points are plotted on Fig. 4.15b.

4.4 Discussion

4.4.1 OSL ages

One of the principal aims of this study was to investigate the applicability of OSL in dating alluvial sediments for slip-rate calculations. For all of the samples the extent to which the luminescence signal was reset prior to burial is unknown; because of this I use the weighted mean equivalent dose to calculate the OSL age, resulting in relatively large error bounds (particularly for the SZ1 surface). This uncertainty partly reflects the difficulty of finding suitable, fine-grained material so close to the active mountain-front. In addition, the measurements I took of radioactive K, U and Th concentrations – from which the dose-rate recieved during burial is estimated – may not be representative of the sediment as a whole. This adds a further uncertainty (one which is not reflected within the quoted error bounds), and the ages should therefore be treated as preliminary only. However, OSL still provides very useful bounds on the age of these alluvial deposits, especially given the rarity of organic material for radiocarbon dating and the uncertainties in erosion rates, long-term cosmogenic isotope production rates and inherited isotope concentrations that complicate exposure dating.

The OSL ages of the SZ1 and NT1 alluvial fans (14.3 $\pm_{1\sigma}$ 5.3 ka and 20.0 $\pm_{1\sigma}$ 11.2 ka, respectively) agree well with figures of 15–20 ka for fans in the Gobi Altai (Fig. 1.4a), calculated with *insitu*-produced ^{10}Be (Vassallo et al., 2005; Ritz et al., 2006). In addition, the OSL age of the EZ2 terrace (84.1 $\pm_{1\sigma}$ 9.4 ka) is close to a minimum age of 78 ± 11 ka established for a strath terrace in the Gobi Altai, again using ^{10}Be (Vassallo et al., 2007b). These results hint that major periods of alluvial fan and river terrace formation in the Altai range in western Mongolia may correlate with those in the Gobi Altai, 400–500 km to the south-east. However, the ages of many more surfaces must be determined if this idea is to be tested fully, especially given the uncertainties in both dating methods.

4.4.2 Late Quaternary vs Geological deformation rates

I now compare the late Quaternary vertical displacement rates across the Zereg and Tsetseg faults with long-term rates of range uplift, constrained by thermochronology and sedimentology (Section 4.2.2).

Before making this comparison, I must first consider the possibility that I am neglecting other active thrusts in the range interior. The clearest candidate for such a fault is a NE-dipping thrust just south of the summit plateau (plotted on Fig. 4.1a). However SPOT imagery reveals no fresh fault scarps along this thrust, and its contribution to the most recent uplift is likely to be negligible (I suspect that it results from an earlier stage of range uplift). Another two faults – one south of the summit plateau and one in the SE part of the range (Fig. 4.1a) – show apparent right-lateral drainage displacements, but are unlikely to contribute significantly to shortening and may not be active at all. I am therefore confident that my slip-rate estimates do indeed bracket the total late Quaternary vertical and horizontal displacement rates across the central part of the range.

According to the thermochronological work summarised in Section 4.2.2, the exhumation of bedrock exposed in Baatar Hyarhan (and presumably the uplift of the range above the surrounding depressions) started between 5 and 1 Ma (Vassallo, 2006). Coarse alluvial sedimentation at the foot of the range, also discussed in this section, points to an earlier initiation of uplift, some time in the Miocene (Howard et al., 2003). An age of 5 Ma minimises the discrepancy between these two estimates, and I use this value in my subsequent calculations.

To determine the long-term vertical displacement rates across the range-bounding faults, I use the late Mesozoic erosional surface as a marker. On Baatar Hyarhan itself the summit peneplain is at 3600 m elevation; erosion rates are probably low

(Jolivet et al., 2007) and for the purposes of the calculation can be ignored. In the central Zereg Basin (elevation ∼1100 m), the peneplain is covered by an estimated sediment thickness of ∼1500 m (see Fig. 4.6a), giving a total ∼4000 m vertical displacement. However, the marker may be deeper here than at the range-front, due to crustal flexure caused by the uplift of Baatar Hyarhan and Bumbat Nuruu and subsidence caused by the weight of late Cenozoic sediments shed into the basin; I therefore consider 4000 m a maximum estimate of the displacement across the Zereg fault itself. A minimum estimate of 1900 m is calculated by subtracting the elevation of the Zereg fault scarps (1700 m) from that of the summit peneplain (3600 m). The total offset across the Zereg fault is thus bracketed at 1900–4000 m. Using the same arguments (and assuming an equivalent sediment thickness) in the Tsetseg Basin, I bracket the total offset across the Tsetseg fault at 1400–3400 m.

Dividing these values by the age of 5 Ma gives long-term vertical displacement rates of ∼0.4–0.8 mm yr^{-1} and ∼0.3–0.7 mm yr^{-1} across the NE and SW margins of the range, respectively. In comparison, ∼20 ka displacement rates are 0.2–0.6 mm yr^{-1} across the Zereg fault and 0.1–0.4 mm yr^{-1} across the Tsetseg fault. The late Quaternary vertical displacement rates are therefore at the lower bounds of the geological rates.

Vertical rates of deformation may, therefore, have remained constant over the past ∼5 Ma (at 0.4–0.6 mm yr^{-1} across the Zereg fault and 0.3–0.4 mm yr^{-1} across the Tsetseg fault), but equally the late Quaternary rates might be lower than the geological ones. This possible discrepancy could be explained by the migration of some shortening away from the range-bounding faults and onto new structures in neighbouring low-lying areas, presumably in response to stresses generated by the raised topography. There are numerous other ∼4–4.5 km peaks across the Altai, but none that are higher; perhaps once these elevations are achieved the migration of fault activity away from the high areas is triggered. Certainly, there are many examples of similar behaviour in other parts of deforming Asia (e.g. Avouac et al., 1993; Bayasgalan et al., 1999b).

Geomorphic evidence from the SE section of Baatar Hyarhan supports the idea that active faulting has shifted away from the range-front into the southern Zereg Basin forebergs. However, the apparent slowing of vertical displacement rates alongside central Baatar Hyarhan cannot be explained by a switch in fault activity to the eastern Zereg Basin; my structural model implies at least 10 km overall shortening here, which (at the estimated late Quaternary rates) would be achieved in 8–17 Ma. This age could be reduced (and late Quaternary shortening rates increased) if some of the convergence across the forebergs is accommodated by folding not accounted for in my estimate, or if shortening was faster prior to ∼85 ka (the age of the EZ2 terrace). But the onset of deformation in the eastern Zereg Basin is still unlikely to be much younger than in the Baatar Hyarhan range itself; indeed, from the available data it is possible that the eastern Zereg Basin forebergs are similar in age, or even older, than Baatar Hyarhan. The forebergs cannot, therefore, be regarded simply as the latest phase of outward mountain growth.

There are other ways in which the possible discrepancy between ∼20 ka and ∼5 Ma year rates of range uplift could be accounted for. Feasible explanations include a shift in deformation to outside the area studied here, or a reduction in the overall rate of shortening across the Altai. Another possibility is that the sediment thickness in the Zereg Basin is lower than the figure suggested by my structural model, reducing the total throw on the range-front faults and, in turn, the long-term rates of range uplift. Equally if the preliminary OSL ages are too old (due to the problem of incomplete bleaching) then the late Quaternary rates should be higher. Clearly the uncertainties in my structural model and (in particular) OSL ages make it difficult to discriminate between these different interpretations.

4.4.3 Late Quaternary vs Decadal deformation rates

The relatively sparse GPS coverage in the Altai (Fig. 1.5) provides no direct measurement of shortening across Baatar Hyarhan on decadal timescales. Nevertheless it is useful to compare the late Quaternary horizontal displacement rates with GPS estimates of shortening across the whole Altai, in order to assess the contribution Baatar Hyarhan makes to this total convergence.

All three areas for which I have late Quaternary slip-rate estimates are adjacent to, or opposite, the central and highest part of Baatar Hyarhan. Adding up the horizontal displacement rates across these areas gives a total shortening rate of 0.7–2.4 mm yr^{-1}. The current rate of convergence across the whole Altai range, measured with GPS, is $\sim$7 mm yr^{-1} (Calais et al., 2003). Late Quaternary shortening across Baatar Hyarhan and the Zereg Basin thus makes up between one tenth and one third of this total. The majority of convergence is likely to be accommodated by the anticlockwise rotation of the dextral strike-slip faults and the slivers of crust between them.

4.5 Conclusion

I investigate a series of clear thrust scarps in late Quaternary alluvial deposits at the margins of Baatar Hyarhan, a major massif in the Mongolian Altai mountains. Optically Stimulated Luminescence (OSL) provides useful bounds on the age of these deposits, despite significant uncertainties in the extent to which each sample was bleached prior to burial. OSL ages of $\sim$15, $\sim$20 ka and $\sim$85 ka agree well with those of alluvial markers in the separate Gobi Altai range, suggesting that periods of fan and terrace formation may correlate over wide tracts of western Mongolia, presumably under the primary control of climate. I calculate $\sim$20 ka vertical displacement rates of 0.2–0.6 mm yr^{-1} and 0.1–0.4 mm yr^{-1} across the NE and SW margins of

Baatar Hyarhan, respectively. These results are at the lower end of long-term (5 Ma) estimates of vertical displacement rates across the same margins, which are ∼0.4–0.8 mm yr^{-1} and 0.3–0.7 mm yr^{-1}, respectively . The possible disparity between late Quaternary and geological rates could be explained if some shortening has migrated away from the range-bounding thrusts in response to stresses introduced by topography, although the large uncertainties in slip-rates prevent us from ruling out other possibilities. Today, the forebergs in the eastern Zereg Basin accommodate a large part of the active shortening across the study area. However, these are unlikely to be younger than Baatar Hyarhan itself and cannot be seen as simply the latest stage of outward mountain growth. Overall, thrust faulting around the Baatar Hyarhan massif and in the eastern Zereg Basin accommodates around 0.7–2.4 mm yr^{-1} of the overall ∼7 mm yr^{-1} convergence across the Altai mountains.

Chapter 5

The 2005 Qeshm Island earthquake (Iran)

5.1 Introduction

The Zagros mountains in southern Iran are one of the most seismically active regions in the Alpine-Himalayan belt, accommodating approximately one third of the N–S shortening between the Arabian plate and Eurasia, which is ∼25 mm/yr at 56° E (Sella et al., 2002; Vernant et al., 2004). Though strike-slip earthquakes have an important role in the central and western parts of the range, where convergence is oblique, seismicity in the Zagros is dominated by high-angle reverse faulting (Talebian & Jackson, 2004). These earthquakes only rarely rupture the surface (Walker et al., 2005); near-surface deformation is instead taken up by folding, which has produced the spectacular whaleback anticlines and synclines (often >100 km in length) that dominate the topography of the Simply Folded Belt, in the southwestern part of the Zagros (Fig. 5.1). There has long been a question as to whether there is a one-to-one correlation between these anticlines and steep, seismogenic reverse faults beneath them (e.g. Falcon, 1969; Jackson, 1980).

In some regions of continental shortening, a causal relationship between buried thrust faulting and surface folding is known to exist; coseismic fold growth above a blind thrust fault was first observed during the M_s 7.3 1980 El Asnam earthquake

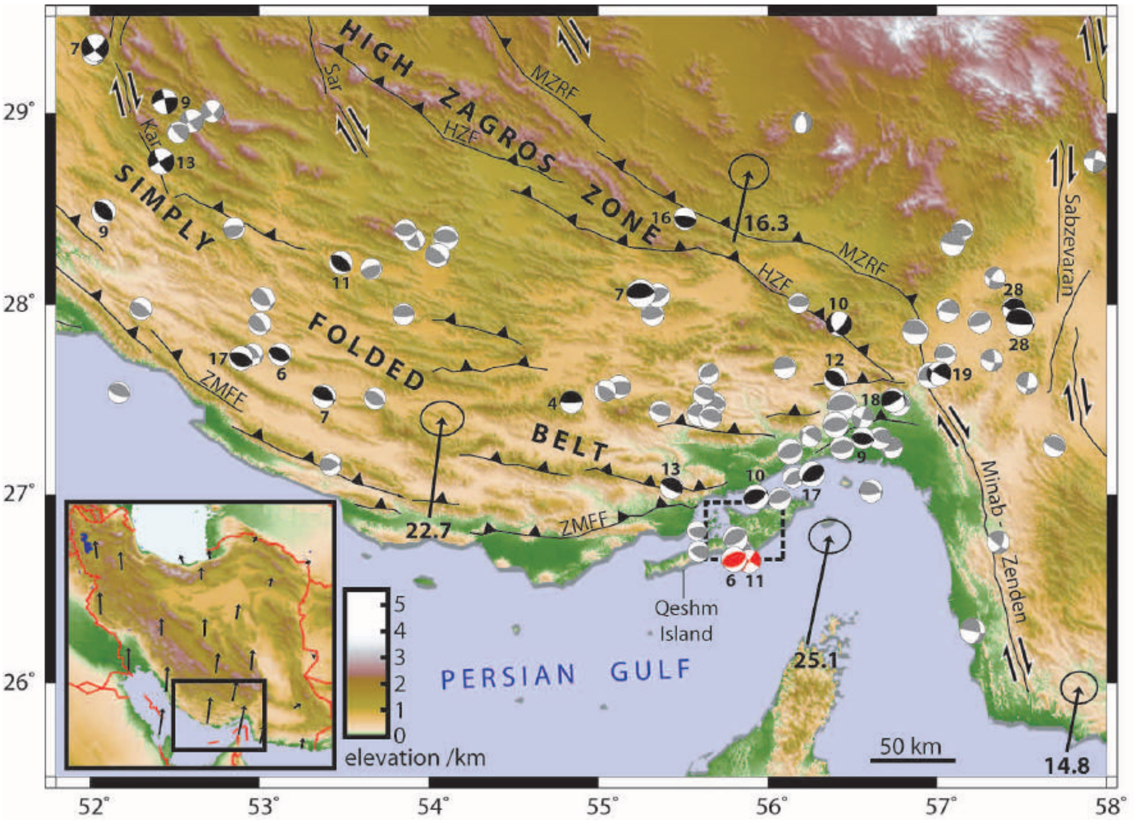

Figure 5.1: Shaded relief topography of the SE Zagros mountains in a Mercator projection. The inset shows the location of the map within Iran, with arrows representing GPS velocities relative to stable Eurasia (Vernant et al., 2004). In the main map, these same GPS velocities (mm/yr) are shown with 95% confidence ellipses. Grey focal mechanisms are Harvard CMT solutions (1976–2006). Black ones are bodywave solutions for earthquakes in the same period (as listed in Talebian & Jackson (2004)), with their centroid depths (in kilometers) next to them. The two red focal mechanisms are my preferred bodywave solutions for the 27 November 2005 M_w 6.0 Qeshm earthquake (centroid depth fixed to 6 km; see Section 5.3.3) and the M_w 5.4 aftershock. Black lines show major active faults; MZRF = Main Zagros Reverse Fault, HZF = High Zagros Fault, Kar = Karebas Fault, Sar = Sarvestan Fault, ZMFF = Zagros Mountain Front Fault. The dashed box over Qeshm island shows the extents of Figs. 5.2, 5.5, 5.7 & 11.

in Algeria (Yielding et al., 1981) and has since been demonstrated in eastern Iran (Berberian et al., 2000; Parsons et al., 2006; Walker et al., 2003), amongst other places. In the Zagros, however, it has been difficult to establish whether such a relationship exists. This is largely because of uncertainty in the extent to which the sedimentary cover is decoupled from its underlying basement by various décollement horizons, particularly in evaporites, that extend across large parts of the range.

Synthetic Aperture Radar interferometry (InSAR) can potentially help resolve this question. Coseismic surface displacements, imaged to subcentimetric precision with InSAR, can be compared with the location of surface folding; a strong link between the two would suggest that fold growth is controlled by faulting during earthquakes. However, since earthquakes were first studied using this method fifteen years ago, there have been very few events in the Zagros of sufficient magnitude for detailed interferometric analysis. Lohman & Simons (2005) use InSAR to locate four $M_w \sim 5$ earthquakes in the Zagros, but in each case interferograms in only one satellite line-of-sight direction are produced, providing little constraint on the mechanisms of such small events. The M_w 6.0 2005 November 27 Qeshm Island earthquake, however, provides one of the first opportunities to study the surface deformation of a large earthquake in the Zagros with InSAR. In this chapter, I combine radar interferometry with seismology and field observations to estimate the source characteristics of this earthquake and investigate the resulting surface displacements.

5.2 Overview of Qeshm Island

Qeshm Island lies in the eastern Persian Gulf, ∼10 km off the Iranian mainland (Fig. 5.1). It is ∼110 km in length but as little as ∼10 km wide, and trends ∼ENE, parallel with the mainland coast. The surface geology mainly comprises Neogene marls and sandstones, folded into prominent anticlines and synclines. Evaporites outcrop in the far western part of the island, where a prominent salt dome (Kuh-e-Namakdan) brings Cambrian Hormuz salt to the surface as a diapir. This is one of many similar salt domes in the Simply Folded Belt. On the adjacent mainland, Hormuz salt also outcrops in the cores of many whaleback anticlines. It is possible that the Qeshm island anticlines may also be cored with evaporites, although (Kuh-e-Namakdan aside) no salt is currently exposed at the surface. The depth to the basement on the island is not known specifically, but aeromagnetic surveys of the mainland Zagros (Morris, 1977) may offer a rough indication. Spectral analysis of these data reveals a basement depth of ∼16 km on the mainland just NW of Qeshm Island, while application of the half-slope method to individual magnetic anomalies yields depths of 10–17 km in the same area (Talebian, 2003). However, these estimates rely on long wavelength magnetic signals and locally there may be departures from this range.

Overall, Qeshm Island bears many geological and structural similarities with the adjacent mainland, and can thus be considered part of the Zagros Simply Folded Belt. Unusually, however, fold axes on Qeshm Island do not follow parallel trends. Instead, folds trending ∼E-W (Salakh anticline), ∼NE-SW (Ramkan syncline and Suza anticline) and ∼NW-SE (Laft anticline) converge to form a complicated structure in the central part of the island (Fig. 5.2).

Extensive marine terraces indicate that much of Qeshm island has been undergoing uplift during Quaternary times (Haghipour & Fontugne, 1993). The terraces comprise reef and beach deposits lying unconformably over Neogene sediments. As many as eighteen separate levels have been mapped, the oldest at 220 m altitude and the youngest in the current littoral zone. Uranium-series dating of aragonitic corals yields uplift rates of 0.2 mm/yr (Preusser et al., 2003). In the central part of the island, raised beaches along the coastlines near Shib Deraz, Suza, and north of Laft, indicate continuing uplift at the present day (Figs. 5.2 & 5.3a).

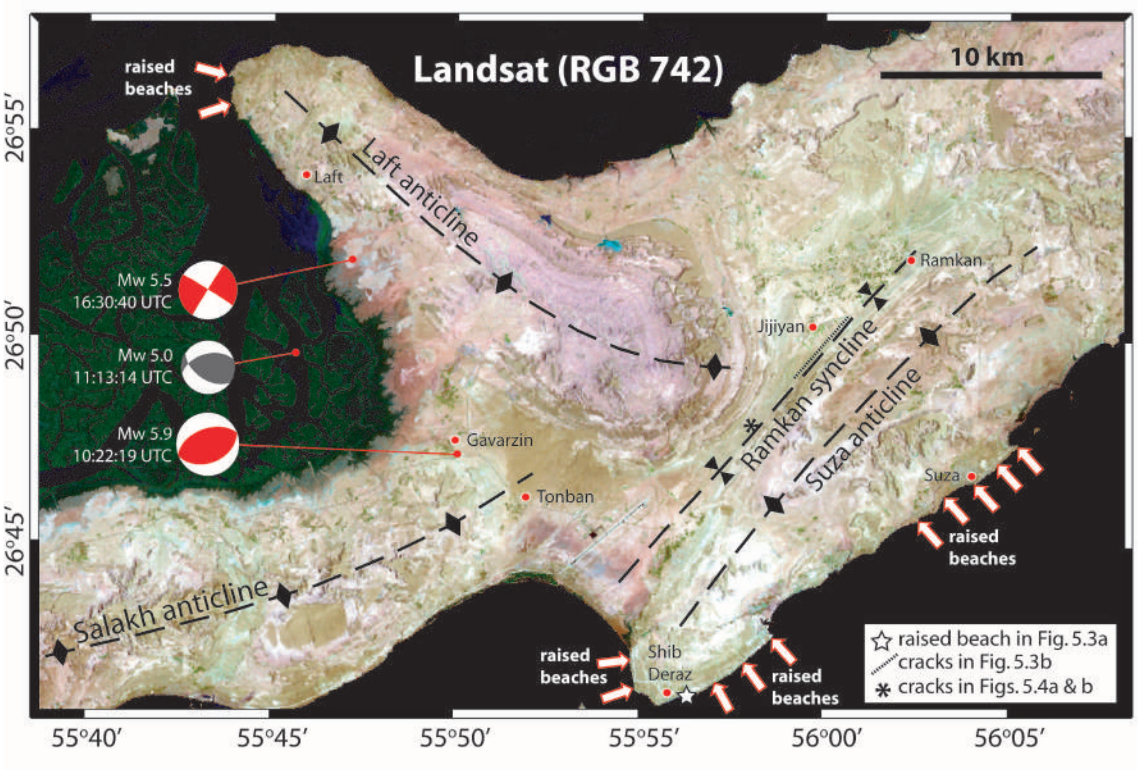

Figure 5.2: Landsat image (RGB 742) of central Qeshm island, displayed in the local UTM zone (40) projection (as are subsequent maps). The red focal mechanisms are our preferred bodywave solutions for the 27 November 2005 M_w 6.0 Qeshm Island earthquake and the M_w 5.4 aftershock, while the grey mechanism is the Harvard CMT solution for the M_w 5.0 aftershock. Red lines connect these earthquakes to their epicentres, as listed in the updated version of the Engdahl et al. (1998) catalogue; these are likely to be accurate to around ~10–15 km, from InSAR studies of other earthquakes in Iran (Talebian et al., 2004, 2006; Lohman & Simons, 2005; Parsons et al., 2006). Major fold axes are marked with dashed black lines. Red arrows point to parts of the Qeshm coastline that show evidence of active uplift, from Haghipour & Fontugne (1993). The star indicates the location of the photograph in Fig. 5.3a, the short dotted line represents the cracks in Fig. 5.3b, and the asterisk shows the location of the cracks in Figs. 5.4a & 5.4b.

5.3 The Qeshm Island earthquake

On 27 November 2005 at 10:22:19 UTC (13:52:19 local time), a M_w 6.0 earthquake struck Qeshm island. It destroyed the village of Tonban in the central part of the island, while several neighbouring settlements including Gavarzin and Jijyan were badly damaged. Overall, 13 people were killed and a further ~100 injured; these figures would probably have been higher had the earthquake not struck in the middle of the day, when many people were outdoors. Several aftershocks followed, including events of M_w 5.0 and 5.4 on the same day at 11:13:14 UTC and 16:30:40 UTC respectively.

In this section I begin by discussing field observations of ground deformation (made by Morteza Talebian, Manoucher Ghorashi and James Jackson) following the earthquake. I then produce ascending and descending-track interferograms spanning the earthquake; modelling these displacements using elastic dislocation theory, I attain a set of source parameters. I then model the earthquake and its largest aftershock with P and SH bodywaves to provide a second, independent set of source parameters.

5.3.1 Field observations

MG and MT visited Qeshm Island immediately after the earthquake; and returned in May 2006 with JJ. No coseismic surface ruptures were observed, nor were any reported by local people. However, two interesting surface deformational features were spotted, that may or may not have resulted from the Qeshm earthquake.

Firstly, parallel sets of cracks were seen in the north-western limb of the Ramkan syncline, close to the fold axis (Figs. 5.2 & 5.3b). Local people said these appeared after the earthquake. They are minor shortening features representing buckling or fracture of the top 2–3 cm of salt-encrusted soil. They can be followed for $\sim$3 km along a 040° trend, parallel with the strike of the bedding in the syncline but oblique to the E-W fault planes of our InSAR and bodywave models of the earthquake (see Sections 5.3.2 & 5.3.3). This suggests that the cracks are not a direct continuation of the faulting at depth. Instead, they are likely to represent flexural slip along bedding planes, possibly indicating the tightening of the Ramkan syncline during the earthquake. A similar style of surface deformation has been reported for some other reverse faulting earthquakes in Iran, such as the 1978 September 16 M_s 7.4

Figure 5.3: (a) View NE from 26° 41’ 22” N 55° 56’ 18” E (the star in Fig. 5.2), showing raised beaches, tilted gently seawards (to the SE), on the coastline east of Shib Deraz. (b) View SW from 26° 50’ 07” N 56° 00’ 35” E. These parallel sets of cracks, trending 040°, appeared after the Qeshm Island earthquake in the north-western limb of the Ramkan syncline (see dashed line in Fig. 5.2). The hills on the left of the picture are NW-dipping beds in the opposite limb of the same syncline.

Tabas earthquake (Berberian, 1979; Walker et al., 2003).

Secondly, a small set of cracks were seen futher south-west within the Ramkan syncline (Figs. 5.2, 5.4a & 5.4b). They are tensional fissures, only 100–200 m in length and trending 120°, oblique to both the local structure and to the fault planes of my earthquake models. Two of the cracks were observed during an earlier

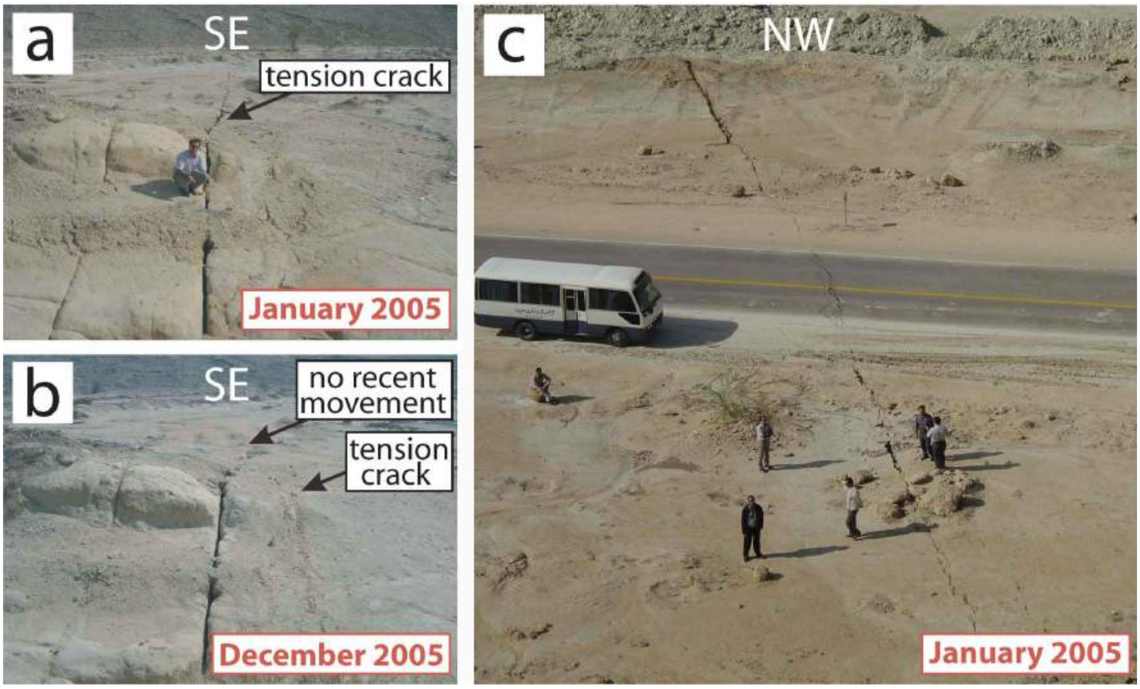

Figure 5.4: (a) Photo taken in January 2005, facing SE from 26° 47' 47" N 55° 58' 07" E (the asterisk in Fig. 5.2) of cracks trending 120°. (b) The same view in December 2005, shortly after the Qeshm Island earthquake. A new crack has appeared, 1 m to the SW of the earlier ones. This opening may or may not be a result of the earthquake; similar cracks appear and disappear frequently on Qeshm island. An example of these is shown in (c): photo taken in January 2005, facing NW from 26° 48' 22" N 55° 58' 04" E, ∼1 km north of (a). This tension fissure appeared approximately one year before the Qeshm Island earthquake; it trends 110° and has opened by ∼5 cm.

field trip in January 2005 (MT), several months before the earthquake (Fig. 5.4a). When the same locality was revisited shortly after the earthquake a third crack had appeared, 1 m south-west of the earlier cracks (Fig. 5.4b). However, this latest opening was not necessarily a result of the earthquake. Similar cracks appear and disappear frequently on Qeshm island, whether or not there have been earthquakes. Indeed, several others were observed in many different parts of the island in January 2005; one such example is shown in Fig. 5.4c. These cracks often follow pre-existing jointing, and may be related to sub-surface salt movement.

5.3.2 Synthetic Aperture Radar Interferometry (InSAR)

I use the JPL/Caltech ROI_PAC processing software (Rosen et al., 2004) and the Envisat ASAR data itemised in the top part of Table 5.1 to produce three interferograms spanning the earthquake. An initial orbital correction is made using Delft precise orbits (Scharroo & Viser, 1998), and the topographic phase contribution is removed using the 3-arcsecond (90 m) resolution Shuttle Radar Topographic Mission (SRTM) DEM (Farr & Kobrick, 2000). After smoothing the interferograms with a power spectrum filter (Goldstein & Werner, 1998), the phase data is unwrapped using the branch-cut algorithm (Goldstein et al., 1988). In contrast with the processing in Chapter 2 (where the deformation signal covers a large proportion of the interferograms), the orbital parameters are re-estimated empirically and a best-fit quadratic surface subtracted from the data.

Two of interferograms are constructed from descending track data with a centre-scene incidence angle of 23° (beam mode IS2), while the third is an ascending track interferogram with an incidence angle of 41° (beam mode IS6). Two out of three interferograms span 350 days, while one descending-track interferogram spans just 35 days.

Pass	*Mode*	i	*Track*	*Date 1*	*Orbit 1*	*Date 2*	*Orbit 2*	Δt *(days)*	$B_\perp$ *(m)*	H_a *(m)*
Desc.	IS2	23°	435	24-Nov-05	19527	29-Dec-05	20028	35	197	48
Desc.	IS2	23°	435	17-Feb-05	15519	02-Feb-06	20529	350	65	145
Asc.	IS6	41°	328	05-Jan-05	14911	21-Dec-05	19921	350	37	254
Desc.	IS2	23°	435	17-Jun-04	12012	24-Nov-05	19527	525	26	362
Desc.	IS2	23°	435	29-Dec-05	20028	09-Mar-06	21030	70	67	140

Table 5.1: Summary of Envisat data used to produce interferograms. *Mode* is the Envisat aquisition mode and i is the incidence angle at the centre of the image, measured from the vertical. The first image of each pair was acquired on Date 1, and the second on Date 2, separated by Δt days. The perpendicular baseline between the orbits in each pass is $B_\perp$ m., and the altitude of ambiguity H_a m. The top three interferograms span the earthquake; the bottom two cover periods before and after the earthquake, respectively.

The 350-day ascending-track interferogram is shown in Fig. 5.5a and the 350-day descending track interferogram in Fig. 5.5b. The 35-day descending-track interferogram looks very similar in shape to the 350-day one; for comparison it is shown later on (in Fig. 7a). They are displayed wrapped, adjacent fringes differing by 2.8 cm in line-of-sight (LOS) displacement. They each have excellent correlation over Qeshm island, which is low-lying and sparsely vegetated.

All three interferograms display a roughly elliptical pattern of fringes, elongated in an E-W orientation and containing displacements towards the satellite. In the ascending-track interferogram, maximum displacements are ∼14 cm (5 fringes) at 26° 49' N 55° 54' E. In the descending case, peak displacements are greater – ∼17 cm (6 fringes) in the 35-day interferogram and ∼20 cm (7 fringes) in the 350-day interferogram – and centred further east, at 26° 49' N 55° 56' E.

All three interferograms also display an area of displacements away from the satellites, centred on 26° 44' N 55° 54' E. The signal here is small, with one fringe (∼3 cm) in both descending-track interferograms and half a fringe (∼1.5 cm) in the ascending-track interferogram. However, because it lies in the same place and is of similar shape in all three interferograms, I am confident that it represents surface displacements, not atmospheric noise. The lack of a sharp division between displacements towards the satellite and those away from it indicates that whatever slip is occurring at depth does not reach the surface. The fringes are, however, most closely packed along an ∼ESE trend between 26° 47' N 55° 52' E and 26° 46' N 55° 55' E, suggesting that this is where the fault projects to the surface.

Together, these observations are consistent with slip on a buried, ∼N-dipping reverse fault. I illustrate this point by calculating displacements for a simple model fault (strike 270°, dip 45°, rake 90°, slip 1 m, length 8 km, top depth 4 km and bottom depth 8 km) in an elastic half-space (Okada, 1985; Funning et al., 2005). These are shown (unwrapped) in Fig. 5.6a. In each of the x, y and z components, the

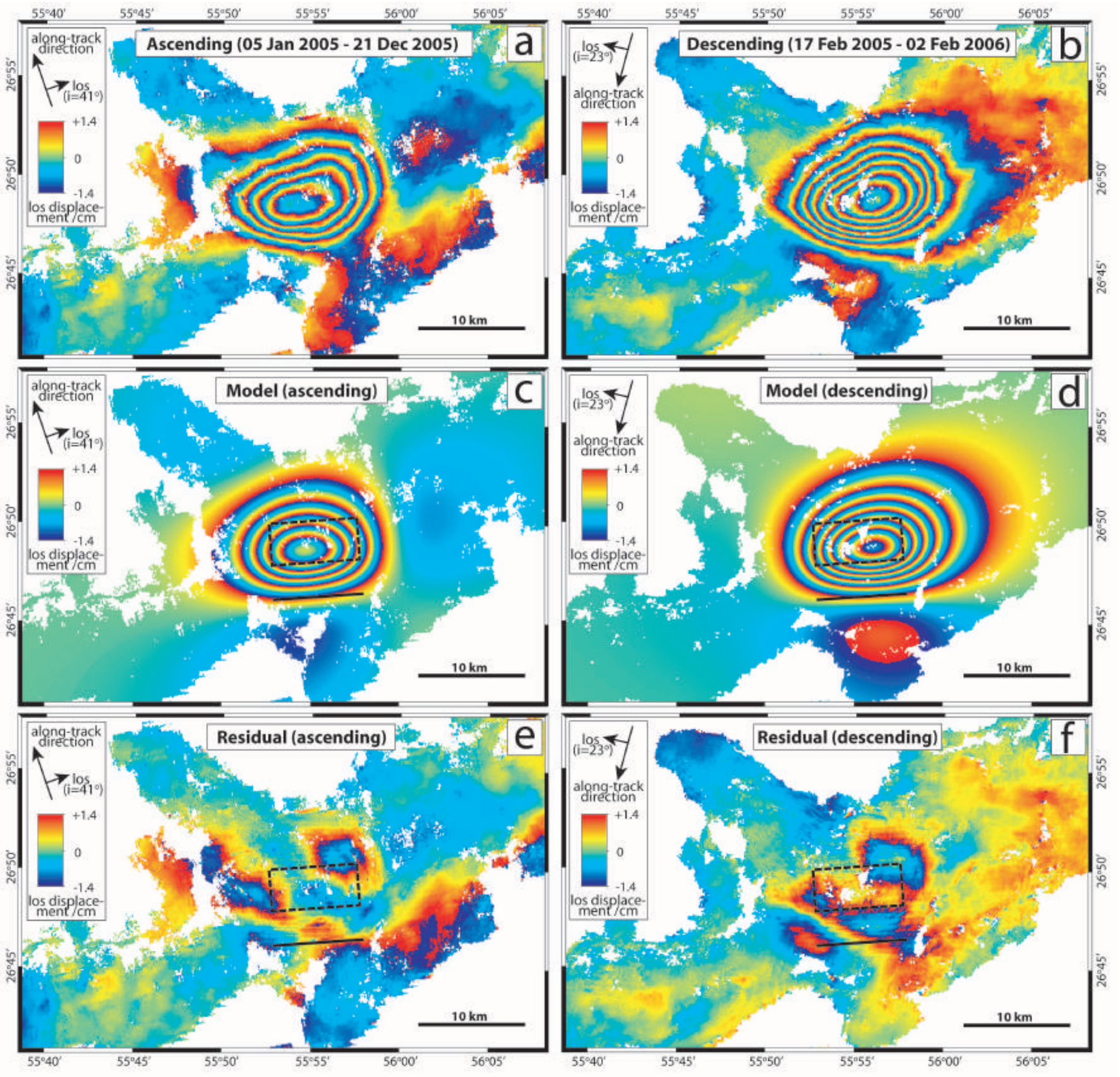

Figure 5.5: Top: 350-day (a) ascending-track and (b) descending-track interferograms spanning the earthquake. Middle: InSAR-derived model interferograms for (c) ascending and (d) descending cases (parameters in Table 2). Bottom: residuals left by subtracting the model interferogram from the observed one, for (e) ascending and (f) descending cases. All panels are shown wrapped with adjacent fringes differing by 2.8 cm in line-of-sight displacement. The dashed black box show the extents of the buried, north-dipping model fault plane in map view, while the thick black line is its projection at the surface.

majority of motion occurs north of the fault. Displacements are antisymmetic about a line perpendicular to the centre of the fault in the x component, but symmetric about the same line in y and z components.

Interferograms comprise the sum of x, y and z components of motion, each resolved onto the satellite LOS pointing vector (Fig. 5.6b). The z component dominates both interferograms, with the same sign in each case, but the signal is larger in the descending-track interferogram, with its steeper look angle. On the other hand, the y component contributes little to either interferogram; displacements in this direction are almost parallel with both ascending and descending satellite tracks. Finally, the x component is of the opposite sign in the ascending-track interferogram (where the horizontal component of the look direction is ∼E) than in the descending one (where it is ∼W). This moves the peak LOS displacements west in the ascending case, and east in the descending one. A north-dipping reverse fault can thus account for both the larger displacements in the descending-track interferograms, and the difference in the location of peak displacements in ascending and descending cases.

I now model the interferometric data to estimate the earthquake source parameters. I begin by reducing the number of data points in each interferogram from ∼2 million to ∼1000 using a quadtree decomposition algorithm (e.g. Jónsson et al., 2002). Giving the ascending-track displacements equal weighting to those of the two descending-track interferograms combined, I invert the data using a Powell minimization algorithm with multiple Monte Carlo restarts to avoid local minima (Wright et al., 1999). I solve for uniform slip on a rectangular fault plane in an elastic half-space (Okada, 1985), with an elastic shear modulus of 3.23×10^{10} Pa and a Poisson ratio of 0.25. The strike, dip, rake, amount of slip, latitude, longitude, length, and top and bottom depths are all allowed to vary in the inversion. To account for any residual orbital errors I also solve for best fit phase planes and static offsets.

The best-fit model fault parameters are given in Table 5.2, together with standard deviations calculated by inverting 100 datasets perturbed by realistic noise (Wright et al., 2003; Parsons et al., 2006). These show ∼0.9 m of almost pure reverse slip on a fault striking E-W and dipping ∼49° N. This relatively high angle is typical of reverse-faulting earthquakes in the Zagros, and may be inherited from normal

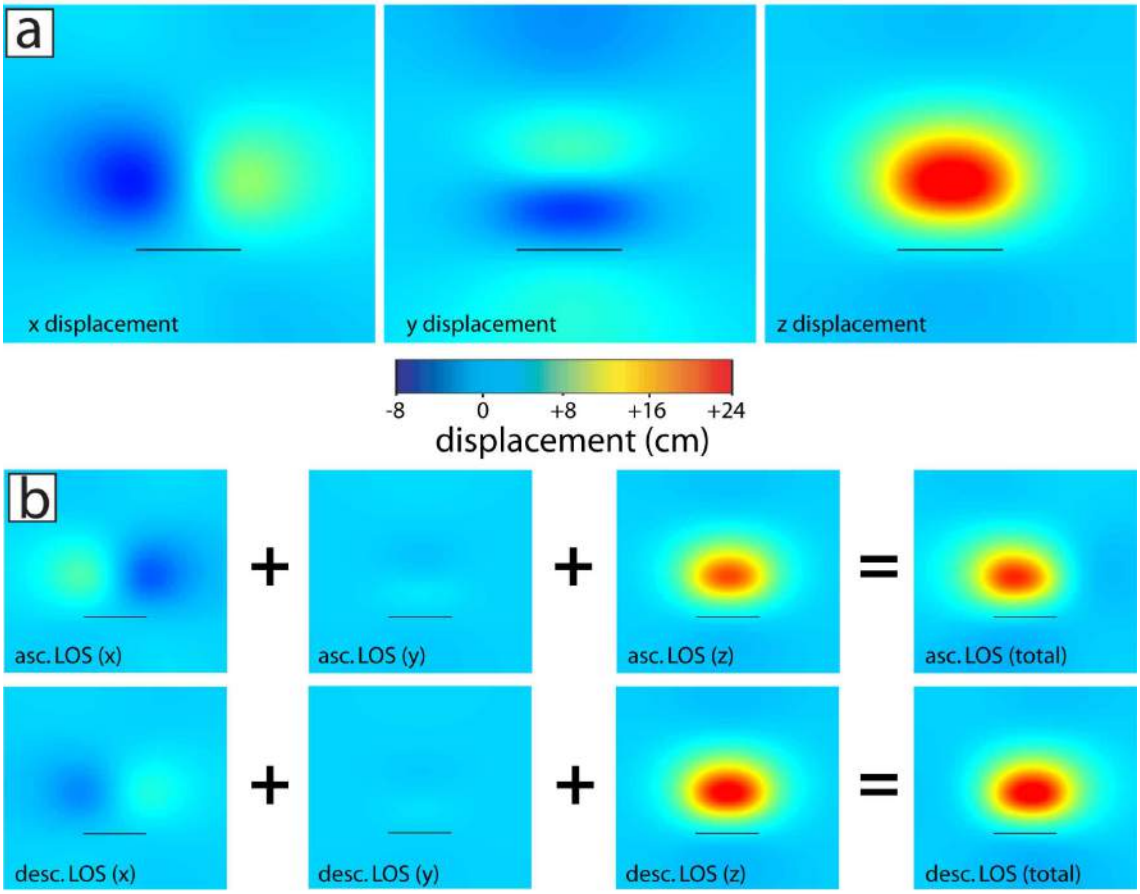

Figure 5.6: (a) Calculated x, y and z components of motion (unwrapped) for a simple N-dipping, buried reverse fault in an elastic half space. (b) The same displacements scaled by the satellite line-of-sight (LOS) pointing vectors in ascending (top) and descending (bottom) cases. These sum to produce the observed innterferograms. Figure adapted from Funning et al. (2005).

faulting in the stretched Arabian margin, reactivated under the present shortening regime (Jackson, 1980; Talebian & Jackson, 2004). The model fault plane extends from a maximum depth of ∼8 km up to ∼4 km beneath the surface. The depth to basement in the SE Zagros has been estimated from aeromagnetic data to be ∼10–17 km (Talebian, 2003), although locally there may be departures from this range. It would appear likely that the fault ruptured the sedimentary sequence, but it is not clear whether or not slip also occurred in the crystalline basement.

Model	*Strike*	*Dip*	*Rake*	*Slip (m)*	*Top (km)*	*Bottom (km)*	*Centroid (km)*	*Length (km)*	*Moment (Nm)*	M_w
InSAR	267° ±2	49° ±4	105° ±5	0.88 ±0.31	3.9 ±0.4	8.1 ±0.4	-	8.4 ±0.4	$1.27 \pm 0.07 \times 10^{18}$	6.0
bodywave	259°	50°	95°	-	-	-	9	-	0.71×10^{18}	5.9
bodywave	250°	50°	91°	-	-	-	6*	-	0.99×10^{18}	5.9
CMT	257°	39°	83°	-	-	-	12	-	1.03×10^{18}	5.9
USGS	249°	45°	91°	-	-	-	10	-	0.73×10^{18}	5.9

* depth fixed during inversion

Table 5.2: Fault plane parameters of the 2005 November 27 10:22:19 UTC earthquake from the inversion of interferometric data (with 1σ errors), from P & SH bodywave modelling, and as listed in the Harvard CMT and USGS catalogues. *Top* and *Bottom* refer to the top and bottom depths of the fault plane, and *Centroid* is the centroid depth. The first bodywave model is the minimum misfit solution; in the second I fixed the centroid depth to 6 km, the equivalent centroid depth of the InSAR model.

Model interferograms are shown in Fig. 5.5c (ascending-track) and Fig. 5.5d (descending-track), with residual interferograms (the difference between observed and model interferograms) in Fig. 5.5e (ascending-track) and Fig. 5.5f (descending-track). There is no more than one fringe present in the residuals, so in general my simple model reproduces the interferometric data well. However, in both ascending and descending cases there are ∼WNW-trending residuals above the western part of the model fault, suggesting a systematic misfit between data and model in this area.

These residuals may result from an ambiguity in the strike of the fault. This must account for both the overall E-W elongation of the elliptical pattern of displacements towards the satellite, and the ESE-WNW orientation of the most closely-packed fringes (where the fault projects to the surface). Uniform slip on a single, rectangular reverse fault cannot reproduce both of these trends; my model matches the E-W orientation of the ellipse successfully, but leaves residuals trending WNW where the fringes are most closely-packed in the interferograms. I find that a two-fault model, with an eastern segment striking ∼W and a western one striking ∼WNW, can reduce the residuals in this area. Allowing distributed slip on the model fault plane would also improve the overall fit to the data. However, for the purposes of this study the simple, uniform-slip, one-fault model reproduces the data sufficiently well.

Finally, I briefly discuss the difference between the 35-day and 350-day descending-track interferograms; these contain 6 fringes and 7 fringes of displacements towards the satellite, respectively (Fig. 5.7a & Fig. 5.5a). This difference is displayed in Fig. 5.7b, and may indicate a small amount of ground displacement either before or after the earthquake. To investigate further, I produce two more descending-track interferograms (using the data itemised in the bottom part of Table 5.2), spanning a ∼17 month pre-seismic period (Fig. 5.7c) and a ∼2 month post-seismic period (Fig. 7d). Both interferograms display small apparent displacements (less than one fringe) towards the satellite, centred close to the peak in the difference interferogram

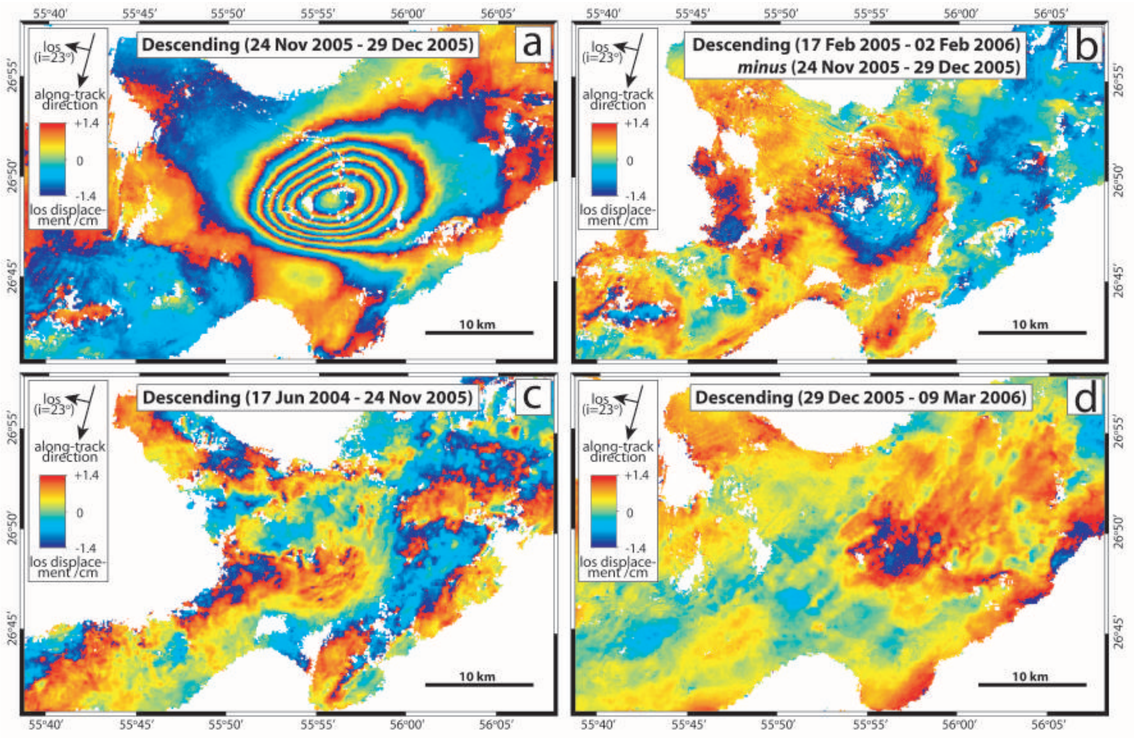

Figure 5.7: (a) 35-day descending-track interferogram, spanning the earthquake. (b) The difference between the 350-day and 35-day descending-track interferograms. (c) Descending-track interferogram spanning ~17 months prior to the earthquake. (d) Descending-track interferogram spanning ~2 months after the earthquake. All panels are shown wrapped with adjacent fringes differing by 2.8 cm in line-of-sight displacement.

(Fig. 5.7b) at 26° 49’ N 55° 56’ E. However, given the size of these signals it is difficult to demonstrate that these are real ground displacements, not atmospheric noise.

5.3.3 Teleseismic bodywave modelling

The M_w 6.0 and M_w 5.4 earthquakes were widely recorded by stations of the Global Digital Seismic Network (Butler et al., 2004). To avoid complications from the Earth’s crust and outer core, I use only those waveforms recorded in the distance range 30°–90°. I use the MT5 program (Zwick et al., 1994) to invert P and SH waveforms by a weighted least-squares method (McCaffrey & Abers, 1988), with a velocity model ($V_p = 6.0$ ms^{-1}, $V_s = 3.45$ ms^{-1} and $\rho = 2.78 \times 10^3$ kg/m^3)

that is consistent with the elastic parameters used in the interferometic modelling. Following the procedure of Molnar & Lyon-Caen (1989) I obtain the strike, dip, rake, centroid depth, seismic moment and source-time function of the best double-couple solutions.

The best-fit bodywave model for the larger event is displayed in Fig. 5.8; from the interferometry, it is clear that the north-dipping nodal plane represents the fault. Source parameters are listed in the second line of Table 5.2. In addition, I calculate approximate errors of ∼10° in strike, ∼5° in dip, ∼15° in rake and 0.2×10^{18} Nm in moment. These are estimated by fixing individual parameters to a range of values and inverting as previously, before comparing the resulting waveforms with those of the best-fit solution; they are not formal errors and so are excluded from Table 5.2. There are negligible differences in strike, dip and rake between the bodywave solution and the InSAR model. However, the bodywave moment is somewhat lower than the InSAR-derived moment, and the centroid depth (9 km) is deeper than the central point of the InSAR model fault (6 km).

To investigate these discrepancies I run a second bodywave inversion with the centroid depth fixed at 6 km (the equivalent centroid depth of the InSAR model). The fit of the P-waves in this fixed-depth model is very similar to that in the minimum-misfit solution. The fit of the S-waves is worse in the fixed-depth model only for those stations where the fit was poor anyhow; for the stations displaying a simple pulse, the fit is actually better. This improvement is shown in Fig. 5.9, and leads us to favour a centroid depth of 6 km. Furthermore, the moment of the fixed-depth bodywave model is now closer to that of the InSAR model and Harvard CMT mechanism, reflecting a negative trade-off between depth and moment in the seismic modelling; the strike, dip and rake have changed little from earlier minimum-misfit values. The source parameters of my favoured, fixed-depth model are listed on the third line of Table 5.2.

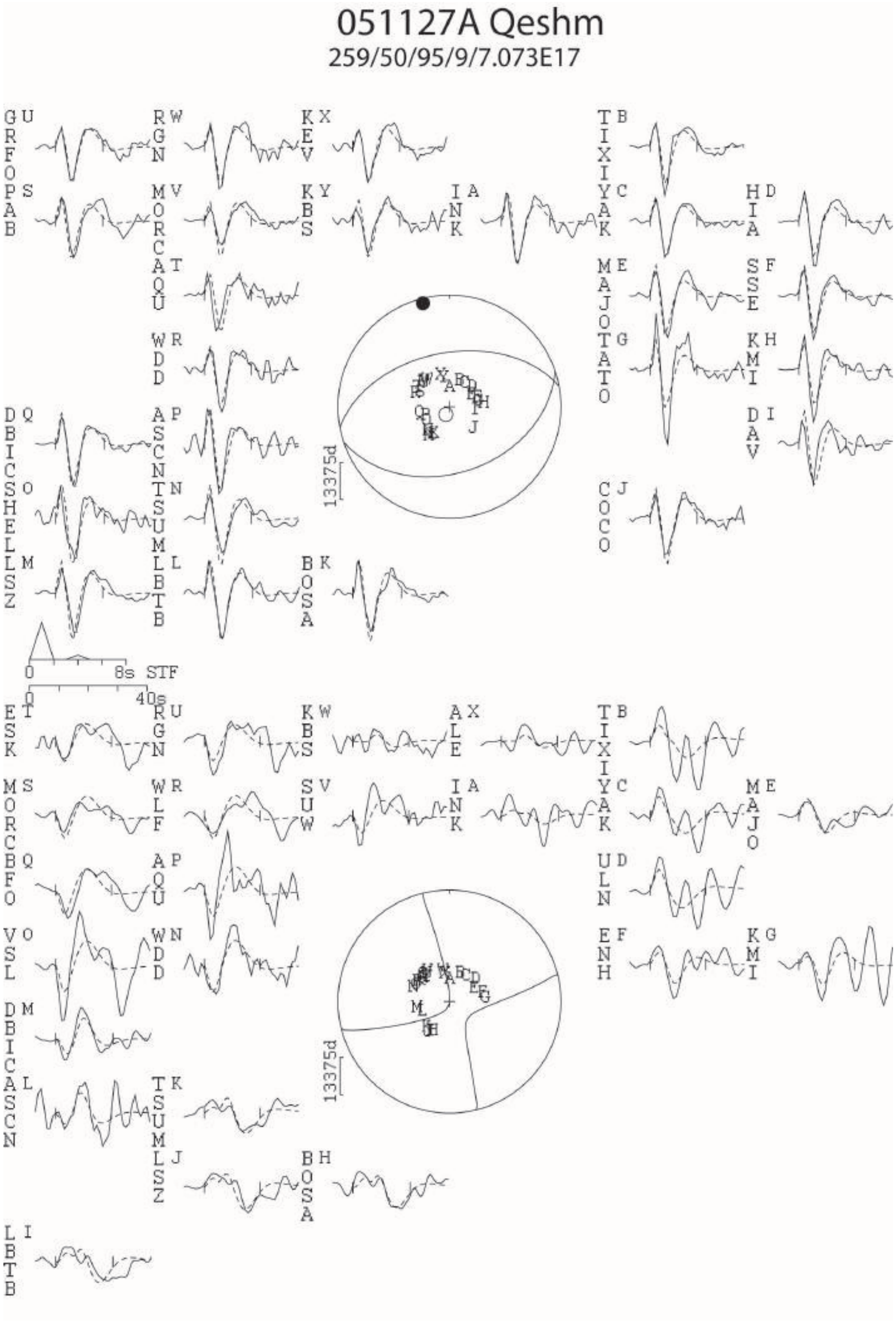

Figure 5.8: Minimum misfit solution for the 2005 November 27 10:22:19 UTC earthquake, calculated by inverting P and SH bodywaves for a point source in a half space of $V_p = 6.0$ ms^{-1}, $V_s = 3.45$ ms^{-1} and $\rho = 2.78 \times 10^3$ kg/m^3. The focal spheres show P (top) and SH (bottom) nodal planes in lower hemisphere projections; closed and open circles represent the P-axes and T-axes respectively. Numbers beneath the header line are strike, dip, rake, centroid depth (km) and moment (Nm) of the earthquake. Observed (solid) and synthetic (dashed) waveforms are plotted around the focal spheres; the inversion window is indicated by vertical ticks, station codes are written vertically and station positions denoted by capital letters. The STF is the source time function, and the scalebar below it (in seconds) is that of the waveforms.

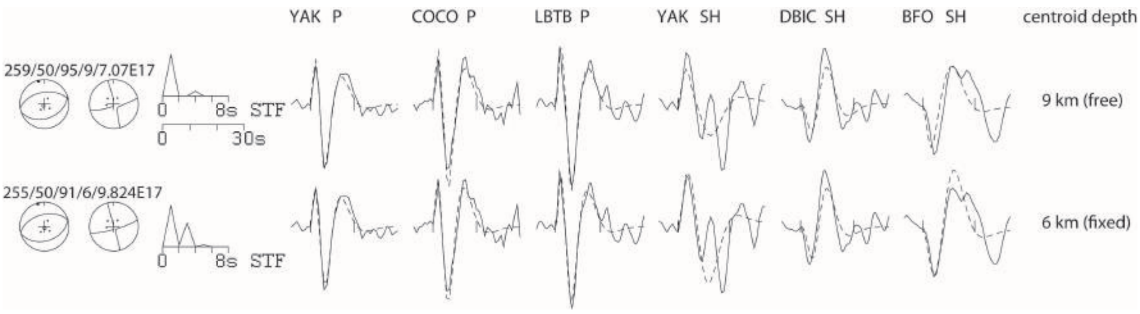

Figure 5.9: The match between real (solid line) and synthetic (dashed line) waveforms for a selection of three P and three SH stations, for the minimum misfit solution of the 10:22:19 UTC earthquake (top line) and a model in which the centroid depth was fixed to 6 km (second line). There is a similar match in the P waves for the two models; however, where SH stations show a simple pulse, such as YAK, DBIC and BFO, the 6 km solution matches the waveforms better than the minimum-misfit one. I therefore prefer the model with a depth of 6 km, which matches the equivalent centroid depth of the InSAR-derived model.

I do also consider an alternative possibility, that the mimimum-misfit bodywave centroid depth of 9 km is correct whilst interferometric modelling yields inaccurate top and bottom depths. However, when I produce model interferograms in which the equivalent centroid depth is fixed at 9 km, the fit to the data is significantly degraded. So whereas a centroid depth of 6 km is consistent with both seismic and interferometric data, a depth of 9 km is not.

The best-fit bodywave model for the smaller, 16:30:40 UTC event is shown in Fig. 5.10. Its source parameters (Table 5.3) are those of a pure strike-slip fault and lie very close to those of the Harvard CMT solution. Simple forward models of this bodywave solution shows that the earthquake is too small to have contributed significantly (more than one fringe) to the interferometric deformation. The interferograms cannot therefore help discriminate between NW- and SW-striking fault planes. Strike-slip faulting is rare in this part of the Zagros, and the aftershock may reflect tearing along the edge of the reverse fault. However, its slip vector (whichever nodal plane represents the fault) lies oblique to that of the earlier earthquake, so equally this might not be the case.

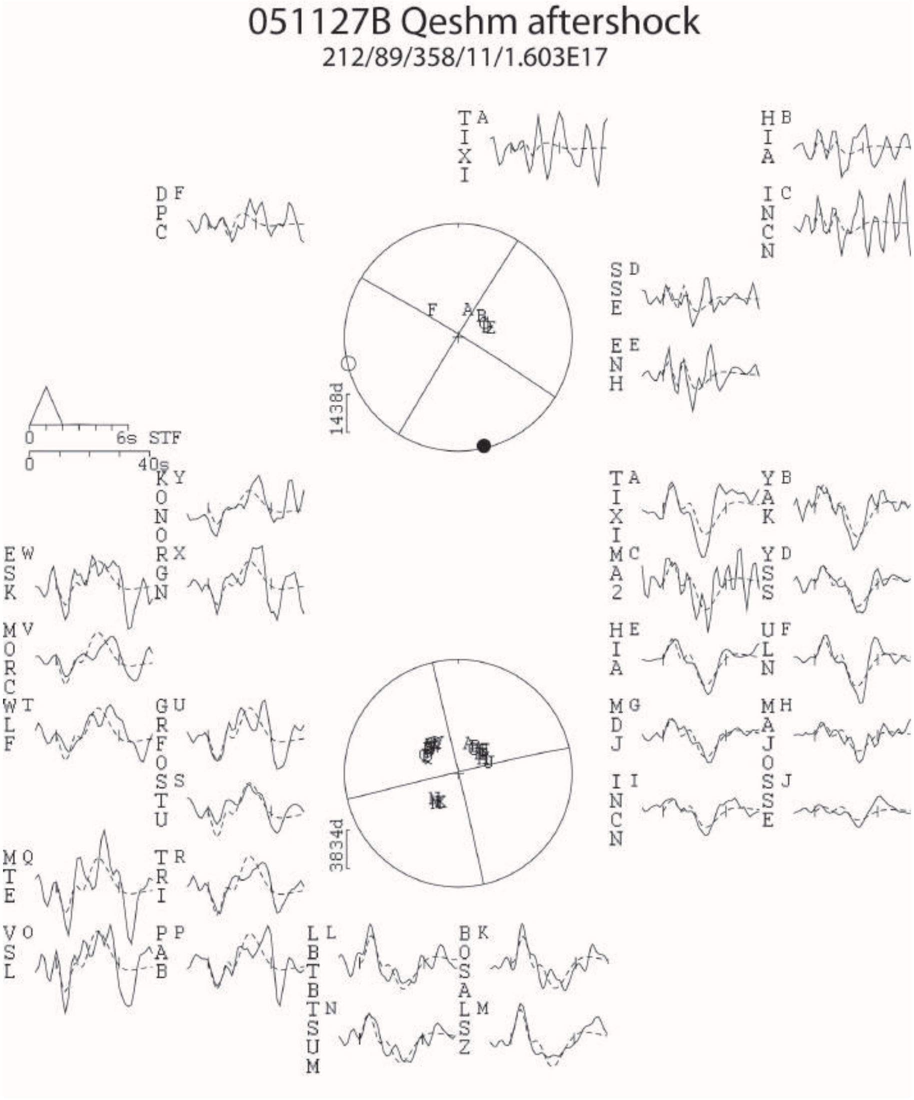

Figure 5.10: Minimum misfit solution for the 2005 November 27 16:30:40 UTC aftershock. The layout is the same as for Fig. 5.8.

Model	*Strike1*	*Dip1*	*Rake1*	*Strike2*	*Dip2*	*Rake2*	*Centroid*	*Moment (Nm)*	M_w
bodywave	212°	89°	358°	302°	88°	182°	11 km	1.60×10^{17}	5.4
CMT	218°	87°	358°	308°	88°	183°	12 km	2.13×10^{17}	5.5

Table 5.3: Source parameters of the 2005 November 27 16:30:40 UTC aftershock from P & SH bodywave modelling and as listed in the Harvard CMT catalogue. It is not clear which nodal plane (SW-striking or NW-striking) represents the fault.

5.4 Discussion

A number of simple models of folding exist, with varying degrees of involvement from faulting. In this section, I use the term ‘detachment fold’ to describe those which are completely decoupled from the underlying rock units. Detachment folds have little or no link with faulting, and grow aseismically by buckling in direct response to shortening. The term ‘forced fold’, on the other hand, is used to describe those which grow in direct response to faulting beneath them. Forced folds are typically asymmetric, and can be driven by the upwards propagation of thrust faults at depth or by thrusting of material over bends in the footwall ramp (e.g. Suppe, 1983).

In the Zagros Simply Folded Belt many whaleback anticlines have marginally steeper south-western limbs than north-eastern ones. This asymmetry has been used to imply forced folding above NE-dipping thrust or reverse faults (Falcon, 1974; McQuarrie, 2004). Furthermore, Ramsey et al. (2008) present geomorphological evidence that these same anticlines are segmented along length-scales that correspond with the length of faulting expected from the largest earthquakes observed in the Zagros, given simple earthquake scaling relationships; again, this is consistent with forced fold growth. However, others have argued that deformation in the Simply Folded Belt is better explained by detachment folding. Walpersdorf et al. (2006) use a discordance between shortening measured with GPS, which is concentrated within ∼100 km of the Persian Gulf coastline, and seismicity, which extends up to ∼200 km inland, to suggest decoupling of the sedimentary layers from the basement. Moreover, there are many actively growing folds in the Persian Gulf – hence the existence and continued uplift of islands such as Kish and Sheikh Shoeyb (Preusser et al., 2003) – even though there are very few recent, large earthquakes there.

Of course, it is possible that both models of folding are applicable to the Zagros, and some balanced cross-sections do indeed support a combination of forced folds and décollements (Blanc et al., 2003). But taken together, these studies do not conclusively support one type of folding over the other. I now consider whether the deformation observed during the Qeshm Island earthquake can help resolve this problem. In many ways, this earthquake is typical of those in the Zagros Simply Folded Belt: a M_w ∼6 reverse slip event on a steeply dipping (∼50°) fault plane. Furthermore, slip does not extend to the surface but is buried to ∼4 km depth.

I use the InSAR model source parameters to produce a map of uplift during the earthquake (Fig. 5.11). I compare this to the surface structure, displayed on a Landsat image of central Qeshm Island in Fig. 5.2. The greatest uplift (∼20 cm), directly above the model fault plane, occurs at the eastern end of the Laft anticline. Here, the fold axis bends E–W, roughly parallel with the model fault. This concurrence hints that the growth of this part of the Laft anticline might be controlled by the buried reverse fault which ruptured in the 2005 earthquake.

However, the pattern of uplift does not contour the Laft anticline but extends eastwards over significant portions of the NE-trending Ramkan syncline and Suza anticline. Together with the compressional cracks in Fig. 5.3b, this suggests that these neighbouring folds might also have tightened during the earthquake. The complication here is that only a fraction of the Ramkan and Suza folds uplifted during the earthquake; their long-term growth must be controlled by other factors. Equally, ∼1 cm coseismic subsidence south of the fault covers the south-western ends of these same two folds. This subsiding area lies very close to parts of the southern Qeshm coastline that are known to be uplifting over Quaternary timescales (Haghipour & Fontugne, 1993).

The faulting involved in the 2005 earthquake might then control the growth of the Laft anticline, but it bears no relation to the shape and long-term growth of neighbouring folds. This argument holds even if I project coseismic slip right up to the surface; if stresses in the top ∼4 km were to relax postseismically by folding along a narrow zone above the fault tip, as is observed above blind thrusts near

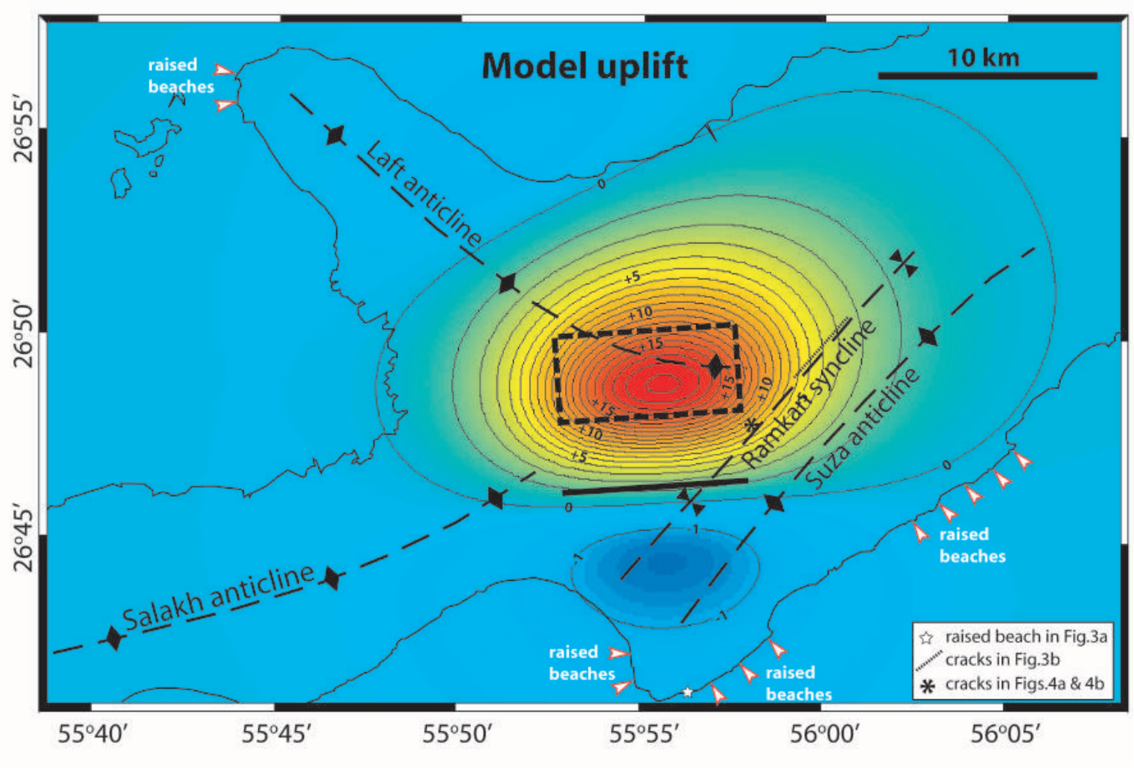

Figure 5.11: Coseismic uplift computed from the InSAR-derived earthquake model, with contours at 1 cm intervals. The area of positive uplift (up to ∼20 cm) is centred on the eastern end of the Laft anticline. The dotted black box show the extents of the buried, north-dipping model fault plane in map view, while the thick black line is its projection at the surface. Raised beaches and surface cracks are given the same symbols as in Fig. 5.2.

Los Angeles (Dolan et al., 2003), then the pattern of uplift would still fail to reflect long-term fold growth in central Qeshm Island. Of course, there may be other ways in which stresses in the region of folding above the seismogenic faults could relax; certainly there must be more going on than just repeated earthquakes, or the elastic limit would be reached in these uppermost sediments. However, assessing this may require measurements over much longer time periods.

The discordance between vertical motions caused by the earthquake and the pattern of long-term uplift prevents us from convincingly demonstrating a link between faulting and folding on Qeshm Island. Other factors must play a major part in local fold growth, although these could of course include other buried reverse faults. Folding in central Qeshm Island (with orthogonal fold axes) is clearly complicated, and it may take an earthquake in a simpler structural setting to reveal whether there is a one-on-one correlation between faulting and folding in the Zagros.

5.5 Conclusions

The M_w 6.0 Qeshm Island earthquake in the Zagros Simply Folded Belt involved reverse slip on a steep ($\sim$50°), north-dipping fault plane. Slip was restricted to depths of between $\sim$4 km and $\sim$8 km; the earthquake almost certainly ruptured the sedimentary sequence, but whether or not it also affected the uppermost basement is not clear. Coseismic uplift is centred on a prominent anticline, which grew by up to $\sim$20 cm during the earthquake. This implies that the growth of this particular fold is controlled by a reverse fault directly beneath it. However, the pattern of uplift is discordant with the long-term growth of neighbouring folds. On Qeshm Island at least, a simple connection between faulting and folding cannot be made.

Chapter 6

Concluding remarks

Although my thesis focuses on two separate study areas, a common thread is provided by my using results from several independent methods in parallel. To finish, I would like to briefly emphasize how it is the combining of varied techniques that offers the most insight into problems of continental deformation.

In Chapter 2, I demonstrated some of the difficulties in matching interferometric models of a clustered earthquake sequence with source mechanisms derived from seismology. Nevertheless, by helping to identify significant reverse faulting at the south-eastern end of the fault zone, InSAR-derived models lead to a direct improvement in the seismological source parameters for the largest earthquake (which, initially, had not included any reverse-faulting sub-event). Equally, the discrepancy between InSAR-derived fault parameters and those from seismology forced me to investigate more fully the limitations of my elastic dislocation modelling. The occurrence of the earthquakes close to paleomagnetic measurements of anticlockwise vertical-axis rotations appears to confirm the general kinematic description of Baljinnyam et al. (1993) and Bayasgalan et al. (2005).

In Chapter 3, I found a large discrepancy between an age provided by modelling vertical profiles of ^{10}Be and ages supported by luminescence measurements, highlighting the importance of using as many independent dating techniques on the same geomorphic feature as is possible. But despite the uncertainty in dating (and whichever of the resulting late Quaternary slip-rates is used), I show that the Har-Us-Nuur fault is probably much younger than the initial onset of India-related shortening in the Altai. This suggests that deformation has migrated to the range margins from the high, interior Altai. Considering that many of the faults in the Altai include significant reverse components, this temporal evolution is probably a result of the normal stresses introduced onto fault planes by raised topography.

Because of the scarcity of organic material in semi-arid environments like Mongolia, luminescence measurements provide a particularly useful alternative to exposure dating. Whether OSL can provide accurate ages even for relatively coarse alluvial deposits (such as at the Zereg Fault thrust scarps in Chapter 4) is something that is worth investigating in more detail, ideally with further tests against exposure ages. The slip-rates I calculated at Baatar Hyarhan are at the lower bounds of the geological (∼5 Ma) rates implied by thermochronology (Vassallo, 2006). If there is a difference between the two, it may again result from the migration of faulting away from high topography.

The pattern of uplift produced by the Qeshm Island earthquake (Chapter 5) – which was centred on a major anticline – initially appeared to support a direct link between buried reverse faulting and surface fold growth. It was geomorphic indicators of long-term uplift in an area that subsided during the earthquake that provided the main caution against this simple relationship. For this reason, the coastal part of the Zagros may be the best area in which to investigate this link – the presence of raised beaches (or, conversely, 'drowned' topography) allowing long-term vertical movements to be assessed. Since 2005, three other M_w 5.8–6.1 thrust earthquakes have struck the southern Zagros mountains – two of them, according to available epicentres, also on Qeshm Island (Fig. 6.1). If these occurred in a simpler structural setting than the orthogonal folds uplifted in the 2005 earthquake, then the relationship between faulting and folding could be tested with more confidence.

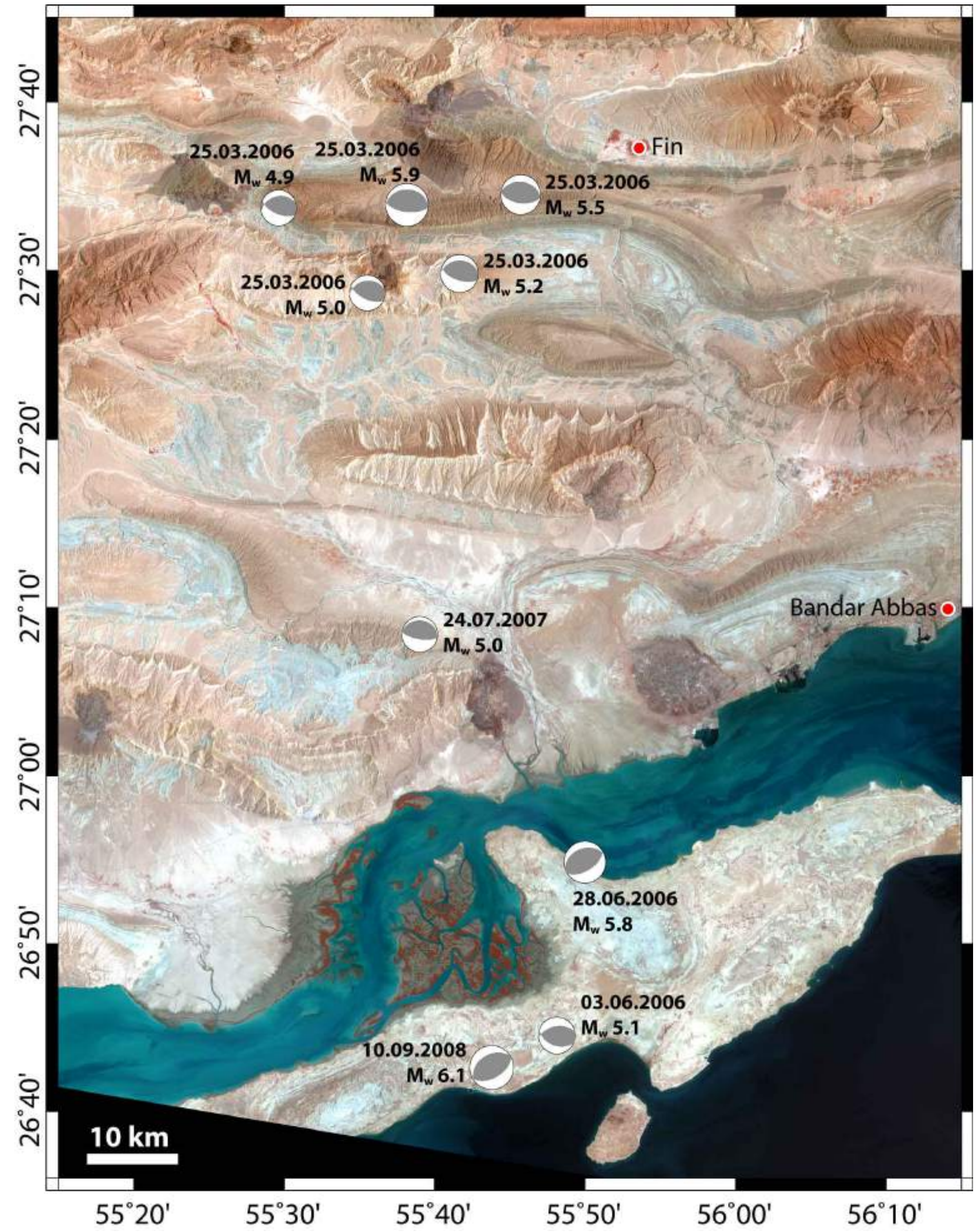

Figure 6.1: Landsat image (RGB 421) of the southern Zagros Simply Folded Belt, in a Mercator projection. Earthquake focal mechanisms, with dates and moment magnitudes, are from the Global CMT catalogue (December 2005 to September 2008). Apart from the 10 September 2008 event (which is at its CMT location), these earthquakes are plotted at relocated epicentres from an updated version of the Engdahl et al. (2006) catalogue, which are probably accurate to ∼10–15 km.

Bibliography

Aitken, M. J., 1985. *Thermoluminescence Dating*, Academic Press, London.

Anderson, R. S., Repka, J. L., & Dick, G. S., 1996. Explicit treatment of inheritance in dating depositional surfaces using in situ ^{10}Be and ^{26}Al, *Geology*, **24**, 47–51.

Arjannikova, A., Larroque, C., Ritz, J.-F., Déverchère, J., Stéphan, J.-F., Arjannikov, S., & San'kov, V., 2004. Geometry and kinematics of recent deformation in the Mondy-Tunka area (south-westernmost Baikal rift zone, Mongolia-Siberia), *Terra Nova*, **16**, 265–272.

Avouac, J.-P., Tapponnier, P., Bai, M., You, H., & Wang, G., 1993. Active thrusting and folding along the northern Tien Shan and Late Cenozoic rotation of the Tarim relative to Dzungaria and Kazakhstan, *J. Geophys. Res.*, **98**(B4), 6755–6804.

Badarch, G., Cunningham, W. D., & Windley, B. F., 2002. A new terrane subdivision for Mongolia: implications for the Phanerozoic crustal growth of Central Asia, *J. Asian Earth. Sci.*, **21**, 87–110.

Baljinnyam, I., Bayasgalan, A., Borisov, B. A., Cisternas, A., Dem'yanovich, M. G., Ganbaatar, L., Kochetkov, V. M., Kurushin, R. A., Molnar, P., Philip, H., & Vashchilov, Y. Y., 1993. Ruptures of Major Earthquakes and Active Deformation in Mongolia and Its Surroundings, *Geol. Soc. Am. Memoir*, **181**, 62 pp.

Bayasgalan, A., 1999. *Active tectonics of Mongolia*, Ph.D. thesis, University of Cambridge.

Bayasgalan, A. & Jackson, J., 1999. A re-assessment of the faulting in the 1967 Mogod earthquakes in Mongolia, *Geophys. J. Int.*, **138**, 784–800.

Bayasgalan, A., Jackson, J., Ritz, J.-F., & Carretier, S., 1999. Field examples of strike-slip fault terminations in Mongolia and their tectonic significance, *Tectonics*, **18**(3), 394–411.

Bayasgalan, A., Jackson, J., Ritz, J.-F., & Carretier, S., 1999. 'Forebergs', flower structures, and the development of large intra-continental strike-slip faults: the Gurvan Bogd fault system in Mongolia, *J. Struct. Geol.*, **21**, 1285–1302.

Bayasgalan, A., Jackson, J., & McKenzie, D., 2005. Lithosphere rheology and active tectonics in Mongolia: relations between earthquake source parameters, gravity and GPS measurements, *Geophys. J. Int.*, **163**, 1151–1179.

Bell, W. T., 1980. Alpha dose attenuation in quartz grains for thermoluminescence dating, *Ancient TL*, **12**, 4–8.

Berberian, M., 1979. Earthquake faulting and bedding thrust associated with the Tabas-e-Golshan (Iran) earthquake of September 16, 1978, *Bull. Seismol. Soc. Am.*, **69**, 1861–1887.

Berberian, M., Jackson, J. A., Qorashi, M., Khatib, M. M., Priestley, K., Talebian, M., & Ghafuri-Ashtiani, M., 1999. The 1997 May 10 Zirkuh (Qa'enat) earthquake (M_w 7.2): faulting along the Sistan suture zone of eastern Iran, *Geophys. J. Int.*, **136**, 671–694.

Berberian, M., Jackson, J. A., Qorashi, M., Talebian, M., Khatib, M., & Priestley, K., 2000. The 1994 Sefidabeh earthquakes in eastern Iran: blind thrusting and bedding-plane slip on a growing anticline, and active tectonics of the Sistan suture zone, *Geophys. J. Int.*, **142**, 283–299.

Bierman, P. R., Gillespie, A. R., & Caffee, M. W., 1995. Cosmogenic Ages for Earthquake Recurrence Intervals and Debris Flow Fan Deposition, Owens Valley, California, *Science*, **270**, 447–450.

Blanc, E. J.-P., Allen, M. B., Inger, S., & Hassani, H., 2003. Structural styles in the Zagros Simple Folded Zone, Iran, *J. Geol. Soc. London*, **160**, 401–412.

Braucher, R., Brown, E. T., Bourlès, D. L., & Colin, F., 2003. In situ produced ^{10}Be measurements at great depths: implications for production rates by fast muons, *Earth Planet. Sci. Lett.*, **211**, 251–258.

Brown, E. T., Bourlès, D. L., Raisbeck, G. M., Yiou, F., Clark Burchfiel, B., Molnar, P., Deng, Q., & Li, J., 1998. Estimation of slip rates in the southern Tien Shan using cosmic ray exposure dates of abandoned alluvial fans, *Geol. Soc. Am. Bull.*, **110**, 377–386.

Bürgmann, R., Rosen, P. A., & Fielding, E. J., 2000. Synthetic Aperture Radar interferometry to measure the Earth's surface topography and its deformation, *Ann. Rev. Earth. Planet. Sci.*, **28**, 169–209.

Butler, R., Lay, T., Creager, K., Earl, P., Fischer, K., Gaherty, J., Laske, G., Leith, B., Park, J., Ritzwoller, M., Tromp, J., & Wen, L., 2004. The Global Seismographic Network Surpasses Its Design Goal, *Eos Trans. AGU*, **85**, 225–229.

Calais, E., Vergnolle, M., San'kov, V., Lukhnev, A., Miroshnitchenko, A., Amarjargal, S., & Déverchère, J., 2003. GPS measurements of crustal deformation in the Baikal-Mongolia area (1994-2002): Implications for current kinematics of Asia, *J. Geophys. Res.*, **108**(B10), 2501.

Chen, Z., Burchfiel, B. C., Liu, Y., King, R. W., Royden, L. H., Tang, W., Wang, E., Zhao, J., & Zhang, X., 2000. Global Positioning System measurements from eastern Tibet and their implications for India/Eurasia intercontinental deformation, *J. Geophys. Res.*, **105**(B7), 16215–16228.

Chéry, J., Carretier, S., & Ritz, J.-F., 2001. Postseismic stress transfer explains time clustering of large earthquakes in Mongolia, *Earth Planet. Sci. Lett.*, **194**, 277–286.

Cunningham, D., 2001. Cenozoic normal faulting and regional doming in the southern Hangay region, Central Mongolia: implications for the origin of the Baikal rift province, *Tectonophys.*, **331**, 389–411.

Cunningham, D., 2005. Active intracontinental transpressional mountain building in the Mongolian Altai: Defining a new class of orogen, *Earth Planet. Sci. Lett.*, **240**, 436–444.

Cunningham, W. D., 1998. Lithospheric controls on late Cenozoic construction of the Mongolian Altai, *Tectonics*, **17**, 891–902.

Cunningham, W. D., Windley, B. F., Dorjnamjaa, D., Badamgarov, J., & Saandar, M., 1996. Late Cenozoic transpression in southwestern Mongolia and the Gobi Altai-Tien Shan connection, *Earth Planet. Sci. Lett.*, **140**, 67–81.

De Grave, J. & Van den haute, P., 2002. Denudation and cooling of the Late Teleskoye Region in the Altai Mountains (South Siberia) as revealed by apatite fission-track thermochronology, *Tectonophys.*, **349**, 145–159.

De Grave, J., Buslov, M. M., & Van den haute, P., 2007. Distant effects of India Eurasia convergence and Mesozoic intracontinental deformation in Central Asia: Constraints from apatite fission-track thermochronology, *J. Asian Earth. Sci.*, **29**, 188–204.

Dehandschutter, B., 2001. *Study of the structural evolution of continental basins in Altai, Central Asia*, Ph.D. thesis, Vrije Universiteit Brussel.

Delouis, B., Déverchère, J., Melnikova, V., Radziminovitch, N., Loncke, L., Larroque, C., Ritz, J.-F., & San'kov, V., 2002. A reappraisal of the 1950 (M_w 6.9) Mondy earthquake, Siberia, and its relationship to the strain pattern at the south-western end of the Baikal rift zone), *Terra Nova*, **14**, 491–500.

Delvaux, D., Theunissen, K., Van der Meer, R., & Berzin, N., 1995. Dynamics and paleostress of the Cenozoic Kurai-Chuya depression of Gorny-Altai (South Siberia): tectonic and climatic control, *Russ. Geol. Geophys*, **35**, 31–51.

Devyatkin, E. V., 1974. Structures and formational complexes of the Cenozoic activated stage (in Russian), in *Tectonics of the Mongolian People's Republic*, pp. 182–195, Nauka, Moscow.

Devyatkin, E. V., 1981. *The Cenozoic of Inner Asia (in Russian)*, Nauka, Moscow, Moscow.

Devyatkin, E. V., 2000. Inner Asia (in Russian), in *Recent Tectonics, Geodynamics, and Seismicity of North Eurasia*, pp. 92–100, Nauka, Moscow.

Dewey, J. W., 1972. Seismicity and tectonics of Western Venezuala, *Bull. Seismol. Soc. Am.*, **62**, 1711–1751.

Dolan, J. F., Christofferson, S. A., & Shaw, J. H., 2003. Recognition of Paleoearthquakes on the Puente Hills Blind Thrust Fault, California, *Science*, **300**, 115–118.

Douglas, A., 1967. Joint epicentre determination, *Nature*, **215**, 47–48.

Dricker, I. G., Roecker, S. W., Vinnik, L. P., Rogozhin, E. A., & Makeyeva, L. I., 2002. Upper-mantle anisotropy beneath the Altai-Sayan region of central Asia, *Phys. Earth Planet. Inter.*, **131**, 205–223.

Engdahl, E. R., van der Hilst, R. D., & Buland, R., 1998. Global teleseismic earthquake relocation from improved travel times and procedures for depth determination, *Bull. Seismol. Soc. Am.*, **88**, 722–743.

Engdahl, R. E., Jackson, J. A., Myers, S. C., Bergman, E. A., & Priestley, K., 2006. Relocation and assessment of seismicity in the Iran region, *Geophys. J. Int.*, **167**, 761–778.

England, P. & Molnar, P., 1997. The field of crustal velocity in Asia calculated from Quaternary rates of slip on faults, *Geophys. J. Int.*, **130**, 551–582.

England, P. & Molnar, P., 1997. Active Deformation of Asia: From Kinematics to Dynamics, *Science*, **278**, 647–650.

Falcon, N. L., 1969. Problems of the relationship between surface structure and deep displacements illustrated by the Zagros Range, in *Time and Place in Orogeny*, Special Publications No. 3, pp. 9–21, Geological Society of London.

Falcon, N. L., 1974. Southern Iran: Zagros Mountains, in *Mesozoic-Cenozoic orogenic belts*, Special Publications No. 4, pp. 199–211, Geological Society of London.

Farr, T. G. & Kobrick, M., 2000. Shuttle Radar Topography Mission produces a wealth of data, *Eos Trans. AGU*, **81**, 583–585.

Farr, T. G., Rosen, P. A., Caro, E., Crippen, R., Duren, R., Hensley, S., Kobrick, M., Paller, M., Rodriguez, E., Roth, L., Seal, D., Shaffer, S., Shimada, J., Umland, J., Werner, M., Oskin, M., Burbank, D., & Alsdorf, D., 2007. The Shuttle Radar Topography Mission, *Rev. Geophys.*, **45**, RG2004.

Fattahi, M., Walker, R., Hollingsworth, J., Bahroudi, A., Nazari, H., Talebian, M., Armitage, S., & Stokes, S., 2006. Holocene slip-rate on the Sabzevar thrust fault, NE Iran, determined using optically stimulated luminescence (OSL), *Earth Planet. Sci. Lett.*, **245**, 673–684.

Fattahi, M., Walker, R. T., Khatib, M. M., Dolati, A., & Bahroudi, A., 2007. Slip-rate estimate and past earthquakes on the Doruneh fault, eastern Iran, *Geophys. J. Int.*, **168**, 691–709.

Florensov, N. A. & Solonenko, V. P., 1963. *The Gobi-Altay earthquake (in Russian)*, Academika Nauk USSR, Moscow, (English translation, U.S. Department of Commerce, Washington, D.C., 1965).

Fraser, H. J., 1935. Experimental study of the porosity and permeability of clastic sediments, *J. Geol.*, **43**, 910–1010.

Funning, G. J., Parsons, B., Wright, T. J., Jackson, J. A., & Fielding, E. J., 2005. Surface displacements and source parameters of the 2003 Bam (Iran) earthquake from Envisat advanced synthetic aperture radar imagery, *J. Geophys. Res.*, **110**, B09406.

Funning, G. J., Parsons, B., & Wright, T. J., 2007. Fault slip in the 1997 Manyi, Tibet earthquake from linear elastic modelling of InSAR displacements, *Geophys. J. Int.*, **169**, 988–1008.

Gabriel, A. K., Goldstein, R. M., & Zebker, H. A., 1989. Mapping small elevation changes over large areas – differential radar interferometry, *J. Geophys. Res.*, **94**, 9183–9191.

Galbraith, R. F., 1981. On statistical models for fission track counts, *Math. Geol.*, **13**, 471–478.

Galbraith, R. F. & Laslett, G. M., 1993. Statistical models for mixed fission-track ages, *Nucl. Tracks Rad. Meas.*, **21**, 459–470.

Gens, R. & Van Genderen, J. L., 1996. SAR interferometry – issues, techniques, applications, *Int. J. Remote Sensing*, **17**, 1803–1835.

Goldstein, R. M. & Werner, C. L., 1998. Radar interferogram filtering for geophysical applications, *Geophys. Res. Lett.*, **25**, 4035–4038.

Goldstein, R. M., Zebker, H. A., & Werner, C. L., 1988. Satellite radar interferometry: Two-dimensional phase unwrapping, *Radio Science*, **23**, 713–720.

Green, P. F., Duddy, I. R., Gleadow, A. J. W., Tinegate, P. R., & Laslett, G. M., 1986. Thermal annealing of fission tracks in apatite: 1. A qualitative description, *Chem. Geol.*, **59**, 237–253.

Haghipour, A. & Fontugne, M., 1993. Quaternary uplift of Qeshm Island (Iran) , *Comptes Rendus de l'Académie des Sciences*, **317**, 419–424.

Howard, J. P., Cunningham, W. D., Davies, S. J., Dijkstra, A. H., & Badarch, G., 2003. The stratigraphic and structural evolution of the dzereg basin, western mongolia: clastic sedimentation, transpressional faulting and basin destruction in an intraplate, intracontinental setting, *Basin. Res.*, **15**, 45–72.

Howard, J. P., Cunningham, W. D., & Davies, S. J., 2006. Competing processes of clastic deposition and compartmentalized inversion in an actively evolving transpressional basin, western mongolia, *J. Geol. Soc. London*, **163**, 657–670.

Huntley, D. J., Godfrey-Smith, D. I., & Thewalt, M. L. W., 1985. Optical dating of sediments, *Nature*, **313**, 105–107.

Hurford, A. J. & Green, P. F., 1983. The zeta age calibration of fission track dating, *Chem. Geol.*, **1**, 285–317.

Jackson, J. & McKenzie, D., 1988. The relationship between plate motions and seismic moment tensors, and the rates of active deformation in the Mediterranean and Middle East, *Geophys. J. Int.*, **93**, 45–73.

Jackson, J., Bouchon, M., Fielding, E., Funning, G., Ghorashi, M., Hatzfeld, D., Nazari, H., Parsons, B., Priestley, K., Talebian, M., Tatar, M., Walker, R., & Wright, T., 2006. Seismotectonic, rupture process, and earthquake-hazard aspects of the 2003 December 26 Bam, Iran, earthquake, *Geophys. J. Int.*, **166**, 1270–1292.

Jackson, J. A., 1980. Reactivation of basement faults and crustal shortening in orogenic belts, *Nature*, **283**, 343–346.

Jolivet, M., Ritz, J.-F., Vassallo, R., Larroque, C., Braucher, R., Todbileg, M., Chauvet, A., Sue, C., Arnaud, N., De Vicente, R., Arzhanikova, A., & Arzhanikov, S., 2007. Mongolian summits: An uplifted, flat, old but still preserved erosion surface, *Geology*, **35**, 871–874.

Jónsson, S., Zebker, H., Segall, P., & Amelung, F., 2002. Fault Slip Distribution of the 1999 M_w 7.1 Hector Mine, California, Earthquake, Estimated from Satellite Radar and GPS Measurements, *Bull. Seismol. Soc. Am.*, **92**, 1377–1389.

Keller, E. A., Zepeda, R. L., Rockwell, T. K., Ku, T. L., & Dinklage, W. S., 1998. Active tectonics at Wheeler Ridge, Southern San Joaquin Valley, California, *Geol. Soc. Am. Bull.*, **110**, 298–310.

Keller, E. A., Gurrola, L., & Tierney, T. E., 1999. Geomorphic criteria to determine direction of lateral propagation of reverse faulting and folding, *Geology*, **27**, 515–518.

Khil'ko, S. D., Kurushin, R. A., Kochetkov, V. M., Baljinnyam, I., & Monkoo, D., 1985. Strong earthquakes, paleoseismological and macroseismic data (in Russian), in *Earthquakes and the Basis for Seismic Zoning of Mongolia*, Transactions 41, The Joint Soviet-Mongolian Scientific Geological Research Expedition, pp. 19–83, Moscow, Nauka, 19–83.

Kurushin, R. A., Bayasgalan, A., Ölziybat, M., Enhtuvshin, B., Molnar, P., Bayarsayhan, C., Hudnut, K. W., & Lin, J., 1997. The Surface Rupture of the 1957 Gobi-Altay, Mongolia, Earthquake, *Geol. Soc. Am. Memoir*, **320**, 143 pp.

Lohman, R. B. & Simons, M., 2005. Locations of selected small earthquakes in the Zagros mountains, *Geochem. Geophys. Geosyst.*, **6**, Q03001.

Maden, C., Anastasi, P. A. F., Dougans, A., Freeman, S. P. H. T., Kitchen, R., Klody, G., Schnabel, C., Sundquist, M., Vanner, K., & Xu, S., 2007. SUERC AMS ion detection, *Nucl. Instr. Methods Phys. Res. B*, **259**, 131–139.

Massonnet, D. & Feigl, K. L., 1998. Radar interferometry and its application to changes in the earth's surface, *Rev. Geophys.*, **364**, 138–142.

Massonnet, D., Rossi, M., Carmona, C., Adragna, F., Peltzer, G., Feigl, K., & Rabaute, T., 1993. The displacement field of the Landers earthquake mapped by radar interferometry, *Nature*, **36**, 441–500.

McCaffrey, R. & Abers, G., 1988. SYN3: A Program for Inversion of Teleseismic Body Wave Forms on Microcomputers, Air force geophysical laboratory technical report, Hanscomb Air Force Base, Massachusetts.

McKenzie, D., 1972. Active Tectonics of the Mediterranean Region, *Geophys. J. Int.*, **30**, 109–185.

McQuarrie, N., 2004. Crustal scale geometry of the Zagros fold-thrust belt, Iran, *J. Struct. Geol.*, **26**, 519–535.

Mejdahl, V., 1979. Thermoluminescence dating: beta-dose attenuation in quartz grains, *Archaeometry*, **21**, 61–72.

Michel, R., Avouac, J.-P., & Taboury, J., 1999. Measuring ground displacements from SAR amplitude images: application to the Landers earthquake, *Geophys. Res. Lett.*, **26**, 875–878.

Molnar, P., 1988. Continental tectonics in the aftermath of plate tectonics, *Nature*, **335**, 131–137.

Molnar, P. & Lyon-Caen, H., 1989. Fault plane solutions of earthquakes and active tectonics of the Tibetan Plateau and its margins, *Geophys. J. Int.*, **99**, 123–154.

Molnar, P. & Qidong, D., 1984. Faulting associated with large earthquakes and the average rate of deformation in central and eastern Asia, *J. Geophys. Res.*, **89**, 6203–6228.

Molnar, P. & Tapponnier, P., 1975. Cenozoic Tectonics of Asia: Effects of a Continental Collision, *Science*, **189**, 419–426.

Morris, P., 1977. Basement structure as suggested by aeromagnetic surveys in SW Iran, Internal report, Oil Serivce Company of Iran.

Murray, A. S. & Wintle, A. G., 2000. Luminescence dating of quartz using an improved single-aliquot regenerative-dose protocol, *Radiation Measurements*, **32**, 57–73.

Nishiizumi, K., 2002. ^{10}Be, ^{26}Al, ^{36}Cl and ^{41}Ca standards, in *Abstracts of the Ninth International Conference on Accelerator Mass Spectrometry (AMS-9), Nagoya, Japan*.

Nishiizumi, K., Arnold, J. R., Lal, D., Klein, J., & Middleton, R., 1986. Production of Be-10 and Al-26 by cosmic rays in terrestrial quartz in situ and implications for erosion rates, *Nature*, **319**, 134–136.

Nishiizumi, K., Imamura, M., Caffee, M. W., Southon, J. R., Finkel, R. C., & McAninch, J., 2007. Absolute calibration of ^{10}Be AMS standards, *Nucl. Instr. Methods Phys. Res. B*, **258**, 403–413.

Okada, Y., 1985. Surface deformation due to shear and tensile faults in a half-space, *Bull. Seismol. Soc. Am.*, **75**, 1135–1154.

Okal, E. A., 1977. The July 9 and 23, 1905, Mongolian earthquakes: A surface wave investigation, *Earth Planet. Sci. Lett.*, **34**, 326–331.

Owen, L. A., Windley, B. F., Cunningham, W. D., , Badamgarav, J., & Dorjnamjaa, D., 1997. Quaternary alluvial fans in the Gobi of southern Mongolia: evidence for neotectonics and climate change, *J. Quat. Sci.*, **12**, 239–252.

Owen, L. A., Cunningham, D., Richards, B. W. M., Rhodes, E., Windley, B. F., Dorjnamjaa, D., & Badamgarav, J., 1999. Timing of formation of forebergs in the northeastern Gobi Altai, Mongolia: implications for estimating mountain uplift rates and earthquake recurrence intervals, *J. Geol. Soc. London*, **156**, 457–464.

Pan, B., Burbank, D., Wang, Y., Wu, G., Li, J., & Guan, Q., 2003. A 900 k.y. record of strath terrace formation during glacial-interglacial transitions in northwest China, *Geology*, **31**, 957–960.

Parsons, B., Wright, T., Rowe, P., Andrews, J., Jackson, J., Walker, R., Khatib, M., Talebian, M., Bergman, E., & Engdahl, E. R., 2006. The 1994 Sefidabeh (eastern Iran) earthquakes revisited: new evidence from satellite radar interferometry and carbonate dating about the growth of an active fold above a blind thrust fault, *Geophys. J. Int.*, **164**, 202–217.

Petit, C., Déverchère, J., Calais, E., San'kov, V., & Fairhead, D., 2002. Deep structure and mechanical behavior of the lithosphere in the Hangai-Hövsgöl region, Mongolia: new constraints from gravity modeling, *Earth Planet. Sci. Lett.*, **197**, 133–149.

Pollitz, F., Vergnolle, M., & Calais, E., 2003. Fault interaction and stress triggering of twentieth century earthquakes in Mongolia, *J. Geophys. Res.*, **108**(B10), 2503.

Prentice, C. S., Kendrick, K., Berryman, K., Bayasgalan, A., Ritz, J. F., & Spencer, J. Q., 2002. Prehistoric ruptures of the Gurvan Bulag fault, Gobi Altay, Mongolia, *J. Geophys. Res.*, **107**(B12), 2321.

Prescott, J. R. & Hutton, J. T., 1988. Cosmic ray and gamma ray dosimetry for TL and ESR , *Nucl. Tracks Rad. Meas.*, **14**, 223–227.

Preusser, F., Radtke, U., Fontugne, M., Haghipour, A., Hilgers, A., Kasper, H. U., Nazari, H., & Pirazzoli, P. A., 2003. ESR dating of raised coral reefs from Kish Island, Persian Gulf, *Quat. Sci. Rev.*, **22**, 1317–1322.

Ramsey, L. A., Walker, R. T., & Jackson, J. A., 2008. Fold evolution and drainage development in the Zagros mountains of Fars province, SE Iran, *Basin. Res.*, **20**, 23–48.

Repka, J. L., Anderson, R. S., & Finkel, R. C., 1997. Cosmogenic dating of fluvial terraces, Fremont River, Utah, *Earth Planet. Sci. Lett.*, **152**, 59–73.

Ritz, J. F., Brown, E. T., Bourlès, D. L., Philip, H., Schlupp, A., Raisbeck, G. M., Yiou, F., & Enkhtuvshin, B., 1995. Slip rates along active faults estimated with cosmic-ray exposure dates: Application to the Bogd fault, Gobi-Altaï, Mongolia, *Geology*, **23**, 1019–1022.

Ritz, J.-F., Vassallo, R., Braucher, R., Brown, E. T., Carretier, S., & Bourlès, D. L., 2006. Using in situ-produced ^{10}Be to quantify active tectonics in the Gurvan Bogd mountain range (Gobi-Altay, Mongolia), in *In Situ-Produced Cosmogenic Nuclides and Quantification of Geological Processes*, Special Papers No. 415, pp. 87–110, Geological Society of America, 87–110.

Ritz, J.-F., Prentice, C. S., Braucher, R., Marco, S., Vassallo, R., Chauvet, A., Rizza, M., Ulziibat, M., Baatarsuren, G., Demberel, S., Todbileg, M., Ulzibat, M., Bayanmunkh, B., Schwartz, D., Michelot, J., & Massault, M., 2007. Earthquake Geology of the Bogd Fault, Gobi Altay, Mongolia, *AGU Fall Meeting Abstracts*, p. B1362.

Rodriguez, E., Morris, C. S., & Belz, J. E., 2006. A global assessment of the SRTM performance, *Photogrammetric Engineering and Remote Sensing*, **72**, 249–260.

Rogozhin, E. A., Bogachkin, B. M., Nechaev, Y. V., Platonova, S. G., Chichagov, V. P., & Chichagova, O. A., 1998. Paleoseismological investigations on the territory of Russian (Gornyi) Altai, *J. Earthquake. Prediction Res.*, **7**, 391–413.

Rogozhin, E. A., Bogachkin, B. M., Nechaev, Y. V., Platonova, S. G., Chichagova, O. A., & Chichagov, V. P., 1998. New evidence of strong earthquakes in the Mountainous Altai Region, *Izvestia, Phys. Solid Earth*, **34**, 244–250.

Rogozhin, E. A., Ovsyuchenko, A. N., Geodakov, A. R., & Platonova, S. G., 2003. A strong earthquake of 2003 in Gornyi Altai, *Russ. J. Earth Sci.*, **5**, 439–454.

Rosen, P. A., Henley, S., Peltzer, G., & Simons, M., 2004. Update Repeat Orbit Interferometry Package Released, *Eos Trans. AGU*, **85**, 47.

Ryerson, F. J., Tapponnier, P., Finkel, R. C., Mériaux, A.-S., Van der Woerd, J., Lasserre, C., Chevalier, M.-L., Xu, X., Li, H., & King, G. C. P., 2006. Applications of morphochronology to the active tectonics of Tibet, in *In Situ-Produced Cosmogenic Nuclides and Quantification of Geological Processes*, Special Papers No. 415, pp. 61–86, Geological Society of America, 61–86.

Scharroo, R. & Viser, P., 1998. Precise orbit determination and gravity field improvement for the ERS satellites, *J. Geophys. Res.*, **103**, 8113–8127.

Schlupp, A. & Cisternas, A., 2007. Source history of the 1905 great Mongolian earthquakes (Tsetserleg, Bolnay), *Geophys. J. Int.*, **169**, 1115–1131.

Schnabel, C., Reinhardt, L., Barrows, T. T., Bishop, P., Davidson, A., Fifield, L. K., Freeman, S., Kim, J. Y., Maden, C., & Xu, S., 2007. Inter-comparison in ^{10}Be analysis starting from pre-purified quartz, *Nucl. Instr. Methods Phys. Res. B*, **259**, 571–575.

Scholz, C. H., 1982. Scaling laws for large earthquakes: consequences for physical models, *Bull. Seismol. Soc. Am.*, **72**, 1–14.

Sella, G. F., Dixon, T. H., & Mao, A., 2002. REVEL: A model for Recent plate velocities from space geodesy, *J. Geophys. Res.*, **107**(B4), 2081.

Sengör, A. M. C., Natal'in, B. A., & Burtman, V. S., 1993. Evolution of the Altaid tectonic collage and Palaeozoic crustal growth in Eurasia, *Nature*, **364**, 299–307.

Shi, J., Feng, X., Ge, S., Yang, Z., Bo, M., & Hu, J., 1984. The Fu-Yun earthquake fault zone in Xinjiang, China (in Chinese), in *Continental seismicity and earthquake prediction*, Beijing Seismology Press, 325–346.

Siame, L., Bellier, O., Braucher, R., Sébrier, M., Cushing, M., Bourlès, D., Hamelin, B., Baroux, E., de Voogd, B., Raisbeck, G., & Yiou, F., 2004. Local erosion rates versus active tectonics: cosmic ray exposure modelling in Provence (south-east France), *Earth Planet. Sci. Lett.*, **220**, 345–364.

Stein, R. S. & King, G. C. P., 1984. Seismic Potential Revealed by Surface Folding: 1983 Coalinga, California, Earthquake, *Science*, **224**, 869–872.

Stone, J. O., 2000. Air pressure and cosmogenic isotope production, *J. Geophys. Res.*, **105**(B10), 23753–23760.

Suppe, J., 1983. Geometry and kinematics of fault-bend folding, *Amer. J. Sci.*, **283**, 684–721.

Suppe, J. & Medwedeff, D. A., 1990. Geometry and kinematics of fault-propogation folding, *Eclogae Geol. Helvetiae*, **83**, 409–454.

Talebian, M., 2003. *Active faulting in the Zagros mountains of Iran*, Ph.D. thesis, University of Cambridge.

Talebian, M. & Jackson, J., 2004. A reappraisal of earthquake focal mechanisms and active shortening in the Zagros mountains of Iran, *Geophys. J. Int.*, **156**, 506–526.

Talebian, M., Fielding, E. J., Funning, G. J., Ghorashi, M., Jackson, J., Nazari, H., Parsons, B., Priestley, K., Rosen, P. A., Walker, R., & Wright, T. J., 2004. The 2003 Bam (Iran) earthquake: Rupture of a blind strike-slip fault, *Geophys. Res. Lett.*, **31**, L11611.

Talebian, M., Biggs, J., Bolourchi, M., Copley, A., Ghassemi, A., Ghorashi, M., Hollingsworth, J., Jackson, J., Nissen, E., Oveisi, B., Parsons, B., Priestley, K., & Saiidi, A., 2006. The Dahuiyeh (Zarand) earthquake of 2005 February 22 in central Iran: reactivation of an intramountain reverse fault, *Geophys. J. Int.*, **164**, 137–148.

Tapponnier, P. & Molnar, P., 1979. Active faulting and Cenozoic tectonics of the Tien Shan, Mongolia, and Baykal regions, *J. Geophys. Res.*, **84**, 3425–3459.

Thatcher, W., 1995. Microplate versus continuum descriptions of active tectonic deformation, *J. Geophys. Res.*, **100**, 3885–3894.

Thatcher, W., 2007. Microplate model for the present-day deformation of Tibet, *J. Geophys. Res.*, **112**, B01401.

Thomas, J. C., Lanza, R., Kazansky, A., Zykin, V., Semakov, N., Mitrokhin, D., & Delvaux, D., 2002. Paleomagnetic study of Cenozoic sediments from the Zaisan basin (SE Kazakhstan) and the Chuya depression (Siberian Altai): tectonic implications for central Asia, *Tectonophys.*, **351**, 119–137.

Vassallo, R., 2006. *Chronologie et évolution des reliefs dans la région de Mongolie-Sibérie: Approche morphotectonique et géochronologique (in French)*, Ph.D. thesis, Université Montpellier 2.

Vassallo, R., Ritz, J. F., Braucher, R., & Carretier, S., 2005. Dating faulted alluvial fans with cosmogenic ^{10}Be in the Gurvan Bogd mountain range (Gobi-Altay, Mongolia): climatic and tectonic implications, *Terra Nova*, **17**, 278–285.

Vassallo, R., Jolivet, M., Ritz, J.-F., Braucher, R., Larroque, C., Sue, C., Todbileg, M., & Javkhlanbold, D., 2007. Uplift age and rates of the Gurvan Bogd system (Gobi-Altay) by apatite fission track analysis, *Earth Planet. Sci. Lett.*, **259**, 333–346.

Vassallo, R., Ritz, J.-F., Braucher, R., Jolivet, M., Carretier, S., Larroque, C., Chauvet, A., Sue, C., Todbileg, M., Bourlès, D., Arzhannikova, A., & Arzhannikov, S., 2007. Transpressional tectonics and stream terraces of the Gobi-Altay, Mongolia, *Tectonics*, **26**, TC5013.

Vernant, P., Nilforoushan, F., Hatzfeld, D., Abbassi, M. R., Vigny, C., Masson, F., Nankali, H., Martinod, J., Ashtiani, A., Bayer, R., Tavakoli, F., & Chéry, J., 2004. Present-day crustal deformation and plate kinematics in the Middle East constrained by GPS measurements in Iran and northern Oman, *Geophys. J. Int.*, **157**, 381–398.

Walker, R., Jackson, J., & Baker, C., 2003. Surface expression of thrust faulting in eastern Iran: source parameters and surface deformation of the 1978 Tabas and 1968 Ferdows earthquake sequences, *Geophys. J. Int.*, **152**, 749–765.

Walker, R. T., Andalibi, M. J., Gheitanchi, M. R., Jackson, J. A., Karegar, S., & Priestley, K., 2005. Seismological and field observations from the 1990 November 6 Furg (Hormozgan) earthquake: a rare case of surface rupture in the Zagros mountains of Iran, *Geophys. J. Int.*, **163**, 567–579.

Walker, R. T., Bayasgalan, A., Carson, R., Hazlett, R., McCarthy, L., Mischler, J., Molor, E., Sarantsetseg, P., Smith, L., Tsogtbadrakh, B., & Tsolmon, G., 2006. Geomorphology and structure of the Jid right-lateral strike-slip fault in the Mongolian Altay mountains, *J. Struct. Geol.*, **28**, 1607–1622.

Walker, R. T., Nissen, E., Molor, E., & Bayasgalan, A., 2007. Reinterpretation of the active faulting in central Mongolia, *Geology*, **35**, 759–762.

Walker, R. T., Molor, E., Fox, M., & Bayasgalan, A., 2008. Active tectonics of an apparently aseismic region: distributed active strike-slip faulting in the Hangay Mountains of central Mongolia, *Geophys. J. Int.*, **174**, 1121–1137.

Walpersdorf, A., Hatzfeld, D., Nankali, H., Tavakoli, F., Nilforoushan, F., Tatar, M., Vernant, P., Chéry, J., & Masson, F., 2006. Difference in the GPS deformation pattern of North and Central Zagros (Iran), *Geophys. J. Int.*, **167**, 1077–1088.

Wang, Q., Zhang, P.-Z., Freymueller, J. T., Bilham, R., Larson, K. M., Lai, X., You, X., Niu, Z., Wu, J., Li, Y., Liu, J., Yang, Z., & Chen, Q., 2001. Present-Day Crustal Deformation in China Constrained by Global Positioning System Measurements, *Science*, **294**, 574–578.

Wilson, P., Bentley, M. J., Schnabel, C., Clark, R., & Xu, S., 2008. Stone run (block stream) formation in the Falkland Islands over several cold stages, deduced from cosmogenic isotope (^{10}Be and ^{26}Al) surface exposure dating, *J. Quat. Sci.*, **23**, 461–473.

Windley, B. F. & Allen, M. B., 1993. Mongolian plateau: Evidence for a late Cenozoic mantle plume under central Asia, *Geology*, **21**, 295–298.

Wright, T. J., Parsons, B. E., Jackson, J. A., Haynes, M., Fielding, E. J., England, P. C., & Clarke, P. J., 1999. Source parameters of the 1 October 1995 Dinar (Turkey) earthquake from SAR interferometry and seismic bodywave modelling, *Earth Planet. Sci. Lett.*, **172**, 23–37.

Wright, T. J., Lu, Z., & Wicks, C., 2003. Source model for the M_w 6.7, 23 October 2002, Nenana Mountain Earthquake (Alaska) from InSAR, *Geophys. Res. Lett.*, **30**(18), 1974.

Yielding, G., Jackson, J. A., King, G. C. P., Sinvhal, H., Vita-Finzi, C., & Wood, R. M., 1981. Relations between surface deformation, fault geometry, seismicity, and rupture characteristics during the El Asnam (Algeria) earthquake of 10 October 1980, *Earth Planet. Sci. Lett.*, **56**, 287–304.

Yuan, W., Carter, A., Dong, J., & Bao, Z., 2006. Mesozoic-Tertiary exhumation history of the Altai Mountains, northern Xinjiang, China: New constraints from apatite fission track data, *Tectonophys.*, **412**, 183–193.

Zaitsev, N. S., Kovalenko, V. I., Luvsandansan, B., Lutchiski, I. V., & Yarmolyuk, V. V., 1989. Geological map of the People's Republic of Mongolia, 1/500,000, Academy of Sciences, People's Republic of Mongolia.

Zhang, P., 1982. *Surface ruptures associated with the 1931 Fu-Yun, northwestern China, earthquake (in Chinese)*, Master's thesis, Chinese University of Science and Technology.

Zwick, P., McCaffrey, R., & Abers, G., 1994. MT5 Program, *IASPEI Software Library*, **4**.